A Novel Method for Vibration Analysis of the Tire-Vehicle System via Frequency Based Substructuring

Matthew Clontz

Dissertation submitted to the Faculty of the

Virginia Polytechnic Institute and State University

in partial fulfillment of the requirements for the degree of

Doctor of Philosophy

in

Mechanical Engineering

Saied Taheri, Chair

Mehdi Ahmadian

Corina Sandu

Daniel J. Stilwell

Pablo A. Tarazaga

May 2nd, 2018

Blacksburg, VA

Keywords: Quarter Car, Frequency Based Substructuring, Decoupling, Tire, Suspension, Tire Design, Rigid Ring Tire, Vibration, Ride Comfort, Small-Scale.

A Novel Method for Vibration Analysis of the Tire-Vehicle System via Frequency Based Substructuring

Matthew Clontz

Abstract

Noise and vibration transmitted through the tire and suspension system are strong indicators of overall vehicle ride quality. Often, during the tire design process, target specifications are used to achieve the desired ride performance. To validate the design, subjective evaluations are performed by expert drivers. These evaluations are usually done on a test track and are both quite expensive and time consuming due to the several experimental sets of tires that must be manufactured, installed, and then tested on the target vehicle. In order to evaluate the performance, expert drivers tune themselves to the frequency response of the tire/vehicle combination. Provided the right models exist, this evaluation can also be achieved in a laboratory.

The research presented here is a method which utilizes the principles of frequency based substructuring (FBS) to separate or combine frequency response data for the tire and suspension. This method allows for the possibility of combining high fidelity tire models with analytical or experimental suspension data in order to obtain an overall response of the combined system without requiring an experimental setup or comprehensive simulations. Though high fidelity models are not combined with experimental data in the present work, these coupling/decoupling techniques are applied independently to several quarter car models of varying complexity and to experimental data. These models range from a simplified spring-mass model to a generalized 3D model including rotation. Further, decoupling techniques were applied to simulations of a rigid

ring tire model, which allows for inclusion of nonlinearities present in the tire subsystem and provides meaningful information for a loaded tire. By reducing the need for time consuming simulations and experiments, this research has the potential to significantly reduce the time and cost associated with tire design for ride performance.

In order to validate the process experimentally, a small-scale quarter car test rig was developed. This novel setup was specifically designed for the challenges associated with the testing necessary to apply FBS techniques to the tire and suspension systems. The small-scale quarter car system was then used to validate both the models and the testing processes unique to this application. By validating the coupling/decoupling process for the first time on the tire/vehicle system with experimental data, this research can potentially improve the current process of tire design for ride performance.

A Novel Method for Vibration Analysis of the Tire-Vehicle System via Frequency Based Substructuring

Matthew Clontz

General Audience Abstract

Noise and vibration transmitted through the tire and suspension system of a vehicle strongly influence the comfort of passengers. Often, during the tire design process, target specifications are used to achieve the desired vibrational characteristics. Subjective evaluations are then performed by expert drivers in order to validate the tire design. These evaluations are usually done on a test track and are both quite expensive and time consuming due to the several experimental sets of tires that must be manufactured, installed, then tested on the target vehicle.

The research presented here utilizes techniques from the field of Dynamic Substructuring which allow frequency data for the tire and suspension systems to be separated or combined. This method allows for the possibility of combining high fidelity tire models with analytical or experimental suspension data in order to obtain an overall response of the combined system without requiring an experimental setup or comprehensive simulations. Several analytical tire and suspension models were developed for this work and the process of separating/combining the frequency data was performed. Then, a small scale test system was developed and used to establish experimental procedures to collect the data necessary to carry out the Dynamic Substructuring techniques. Finally, the process was validated by repeating the process of separating/combing the frequency properties of the experimental data.

Dedication

To my wife, Lauren, whose love and support made this all possible.

Acknowledgements

I am extremely grateful to my advisor, Dr. Saied Taheri, for all of the guidance and support which he provided to me over the course of my studies. In addition to fostering my passion for vehicle dynamics, I am also thankful for his encouragement and advice on matters outside of my research, in my personal life. Without his help, I would not be where I am today.

I would also like to thank Dr. Pablo Tarazaga and Dr. Sriram Malladi for their assistance. They both were very generous with advice and with the time they spent answering my many questions. Their advice, along with Dr. Tarazaga's gracious sharing of resources helped to make this work possible.

Finally, I want to thank all of my committee members: Dr. Mehdi Ahmadian, Dr. Corina Sandu, Dr. Dan Stilwell, and Dr. Pablo Tarazaga. Their time and feedback helped to improve my work and make me a better researcher. I am truly grateful for all of the assistance and support I have received throughout the course of my work.

Contents

List of Figures

List of Tables

Chapter 1 - Introduction

Ride comfort and handling (or road holding) are two of the most important functional performance areas in the design of tires and suspensions. Ride comfort can be broken down further into effects from noise and from vibration. In the present context, vibration refers to higher amplitude vibrations which occur at lower frequencies which more strongly affect the body of the passengers, whereas noise refers to higher frequency vibrations which cause auditory discomfort. The main source of noise passed through a tire/suspension system in passenger cars arises from tire and road surface properties [1]. In this context, the road surface is viewed as the excitation with the tire/suspension as a filtering mechanism between the input and the passenger.

Effects on ride comfort from noise and vibration are both due to system vibrations, but generally belong to separate frequency ranges. “Vibration” is typically considered to be approximately from 0 – 25 Hz, while noise is considered to be anywhere from 25 – 20,000 Hz, and harshness is a subjective quality generally considered to be in the 0-70 Hz range [2]. For decades, most ride comfort research was centered on subjective testing and categorizing [3] [4] [5] [6] [7] [8] [9]. However, starting in the 1980’s, there was an increased interest in developing objective, analytical

methods [10] [5] [11] [12] [13] [14]. The work presented in this dissertation is an effort to develop an aid to such objective methods.

Further than just an aid to subjective methods, the present research could benefit industry processes. During tire design or tire selection process, vibration target specifications are a primary focus. Traditional industry methods typically involve experimental testing of the tire-vehicle system under consideration. Experimental testing is a time consuming process in general, but is especially so for tire design where a new prototype may be required for each test. The methods presented in this research, to mathematically separate or combine vibrational effects from the tire and suspension, have the potential to significantly shorten tire design and selection processes.

In the present work, a method to mathematically couple or decouple frequency response data from the tire and suspension is developed through frequency based substructuring (FBS) techniques. Due to the complexity of changes in vibrational properties when two systems are coupled together, individually analyzing the tire and suspension is not sufficient in the tire selection or design processes. Through the proposed method, this challenge is overcome by the inherent inclusion of information on how the two systems are joined. These techniques not only have the potential to shorten design and testing times, but also allow for better understanding of the mechanism of noise/vibration transmission and damping in passenger cars.

1.1 Problem Statement

Transmission of vibration from the road surface to the passengers of the vehicle is of primary interest to researchers and industry alike. However, the transmission path from the road to the passenger is complex due to the various subsystems involved and the interactions between them. Though there is a great body of research on vibration transmission and the response of the

passengers to vibration, there has not been much work done on the interaction of the various subsystems involved. One way to study the interaction between the various vehicle subsystems is through the concepts of dynamic substructuring.

The current work aims to develop a method to couple or decouple the dynamics of the tire and suspension using frequency based substructuring (FBS) techniques. Successful application of this method will allow tire or suspension models to be combined with experimental data in order to give the overall response of the tire-vehicle system. The ability to obtain an approximate response without the need for extensive simulations or testing presents the possibility for significantly reducing the time required for tire design or tire selection.

1.2 Contributions

The specific contributions of this work are:

Analytical:

- Developed formulation for several quarter car models, suitable for application of coupling/decoupling procedures
- Developed a decoupling formulation for a generalized quarter car system
- Investigated effects of tire stiffness nonlinearity and its role in the decoupling process
    - Developed procedure to address nonlinearity from the tire subsystem
- Developed simulations for rigid ring tire model and nonlinear small-scale tire model

Experimental

- Development of experimental FBS process specific to vehicle vibration analysis and tuning
- Designed a small-scale quarter car test system from 1/5 scale vehicle

- Designed and developed experimental setup capable of specific testing requirements for decoupling
    - Test setup also capable of typical “road input” excitation and excitation directly to unsprung mass

1.3 Organization

This dissertation is organized into six chapters. **Chapter 2 – Background** consists of a literature review on frequency based substructuring (FBS) as well as the modal/vibrational testing of tires and suspensions. The FBS Section contains a complete derivation of the original method along with a summary of the important theoretical and experimental advancements. The “Modal Testing of Tires and Suspensions” Section gives a brief overview of modal analysis, followed by an in depth review of modal testing and analysis performed specifically on tires and suspensions.

Chapter 3 – Analytical Development details the various analytical models upon which FBS decoupling was performed. The analytical models are presented in order of increasing complexity: 1) a two degree of freedom (DOF) quarter car model with one coupling DOF; 2) a generalized quarter car model with three coupling DOFs located at a single point; and 3) a generalized quarter car model with nine coupling DOFs located at three points.

In **Chapter 4 – Experimental Design and Setup**, the various test setups are discussed in detail. The full-scale quarter car rig and its various components are detailed. Then, a brief overview of various design improvements is given before and explanation of why work on the full-scale rig was suspended. Motivation for the development of a small-scale quarter car test rig is given, followed by a detailed description of the design and construction of the test setup.

All results are presented and discussed in **Chapter 5 – Results and Validation**. This chapter begins with the application of the methods developed in this work to numerically populated, analytical models. Next, simulations are performed for a rigid ring tire model with nonlinear stiffness elements and the previous process is repeated. Similar results are shown for the small-scale system. Finally, the experimental setup of the small-scale system is analyzed and the coupling/decoupling processes are validated on experimental data.

The final chapter, **Chapter 6 – Conclusions and Future Work**, summarizes the work presented in this document. Major conclusions of the present work are stated and potential future directions of the research are suggested.

Chapter 2 - Background

The background and literature review for this document is organized into two distinct sections: Frequency Based Substructuring and Modal Testing of Tires and Suspensions. Each section contains information which is relevant to both the analytical developments and to the techniques which are important to the experimental applications of the current work. A list of relevant parameters for the present chapter is shown below.

$\boldsymbol{M}$	Mass matrix
$\boldsymbol{C}$	Damping matrix
$\boldsymbol{K}$	Stiffness matrix
$\boldsymbol{x}$	Displacement vector
$\boldsymbol{f}$	External forcing function
$\boldsymbol{g}$	Internal forcing function (between coupled DOFs)
$\boldsymbol{B}$	Signed Boolean matrix which operates on the coupling DOFs
$\boldsymbol{L}$	Signed Boolean matrix relating to either compatibility or equilibrium conditions
$\boldsymbol{q}$	Generalized set of DOFs
$\boldsymbol{\lambda}$	Lagrange multipliers corresponding to the equilibrium condition
$\boldsymbol{Z}$	Dynamic stiffness matrix
$\boldsymbol{Y}$	Receptance FRF matrix
$\boldsymbol{Y}_{ic}^{B}$	Receptance FRF matrix for substructure “B” between internal, “i,” and coupled, “c,” DOFs
$\boldsymbol{x}_{c}^{A}$	Displacement for coupled, “c,” DOFs for substructure “A”

The above parameters are listed in approximate order of appearance. Other variables may be introduced in the text, but will be introduced and explained as they arise.

2.1 Frequency Based Substructuring

Dynamic substructuring (DS) is a process by which the dynamics of a complex system are analyzed by breaking the system down into separate components and analyzed individually. The dynamic information for the components can then be coupled together to form the assembled system, or a component can be decoupled from the assembled system. The standard formulation for DS in frequency domain was first developed in the 1980s. Due to limitations in measurement and computational power, interest in the field declined. With the increase in experimental and computational capabilities which became available by the early 2000s, the structural dynamic community showed a renewed interest in DS techniques. Since that time, a variety of improved formulations for both coupling and decoupling have been investigated. Additionally, the emphasis of DS in experimental applications has driven research into difficulties and subsequent improvements to experimental practices (i.e. for rotations, error propagation, etc.). This review article presents the fundamental theory and mathematical background of dynamic substructuring in the frequency domain, which is then followed by a discussion of the theoretical and experimental improvements from the past decade.

2.1.1 FBS Introduction

The concept of breaking down a complex problem into multiple, but simple problems is not a new idea. It has been used throughout history in widely varying fields ranging from military applications to mathematics and engineering. Dynamic substructuring is a process that utilizes the concept of breaking down a complex mechanical system into components or “substructures.” There are several main advantages or reasons that one might use dynamic substructuring in place of global system analysis, such as: the ability to analyze large or complex systems on a component

basis, ease of isolating and identifying local dynamic behavior, and the ability to combine dynamic information from different sources (i.e. FEA and experimental) [15].

In general, dynamic substructuring can be thought of in terms of either coupling or decoupling substructures in the physical, modal or frequency domains. The next section will give a brief overview of the theory associated with dynamic substructuring coupling or decoupling in each domain. While all the same information is theoretically present in each domain, analyses in each are carried out differently and each have different advantages. After the next section, the remainder of the chapter will focus on substructuring in the frequency domain.

Dynamic substructuring in the frequency domain is often called "frequency based substructuring" (FBS). The classical FBS method was developed by Jetmundsen et al [16]. A decade later, the basic theory of FBS was well established, but the method was often troubled by experimental difficulties. Additionally, with the limit in computation power available in the late 20^{th} century, many complex structures of interest were unable to be modeled numerically. However, due to an increase in computing power and testing capabilities available in the 21^{st} century, there has been a renewed interest in FBS since the mid 2000's [17].

After a brief overview of dynamic substructuring in the three domains, the remainder of the chapter will focus on coupling or decoupling procedures in the frequency domain. First, the remaining sections of the present chapter will provide a brief history of FBS methods and the associated mathematical background. With the FBS formulations presented, recent improvements to the theory and/or application of FBS methods will be discussed along with other substructuring formulations. The chapter will conclude with a brief discussion of potential use of FBS methods in vehicle dynamic applications and opportunities for future work.

2.1.2 Substructuring in the Physical and Frequency Domains

As mentioned previously, dynamic substructuring can be formulated in physical, modal, and frequency domains. Although each domain theoretically contains the same mathematical information, the formulation in each can be quite different in practice. Corresponding to the differences in application, formulations in each domain have distinct differences and advantages. The remainder of this section will give a brief overview of the formulation in each domain as presented by De Klerk et al. Figure 1 shows the general relationship between the different domains:

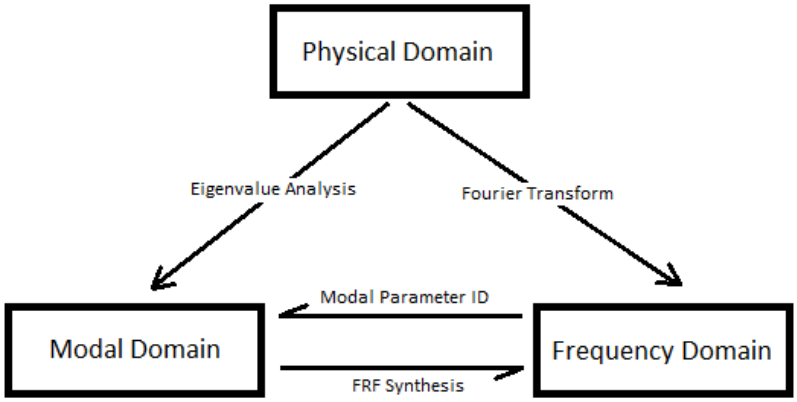

Figure 1: Relationship of system dynamics between the three domains.

This figure also indirectly shows certain limitations that arise between substructuring in the various domains. For instance, when moving to the modal domain, certain information may be inherently lost due to the need to use a finite number of modes. This loss of information and other issues with the specific domains will be addressed in the corresponding parts of this section.

Before dynamic substructuring in each specific domain can be discussed, several important details must first be presented. By definition, a substructure is a structure that interacts with other adjacent structures within some assembly or system. Regardless of what method is used to couple (or

decouple) a structure, there are two conditions which must always be met between coupled structures:

1) The "**compatibility condition**" requires that any coupled substructures have compatible displacements at the interface. This condition is equivalent to two substructures remaining joined at their connection or "interface point," which intuitively makes sense in a physical perspective.
2) The "**equilibrium condition**" requires that the forces on the substructure interfaces to be in equilibrium. Again, this condition makes sense in a physical perspective as it corresponds to a force balance for the given interface point.

Generally, there are two types of assembly methods to determine the characteristics of the coupled system. These assembly methods are termed "primal" or "dual" depending on the choice of unknowns. A primal assembly is one in which displacements are treated as unknown, while a dual assembly is one in which forces are treated as unknown. There are also assembly methods that treat both forces and displacements as unknowns either separately or in some combination. Primal and dual methods can be used in each domain and will be discussed the following subsections.

2.1.2.1 Physical Domain

A structure is described in the physical domain by its mass, stiffness, and damping characteristics. In the typical way, the equations of motion of a discretized dynamic subsystem (s) can be written as:

$$\boldsymbol{M}^{(s)}\ddot{\boldsymbol{x}}^{(s)}(t) + \boldsymbol{C}^{(s)}\dot{\boldsymbol{x}}^{(s)}(t) + \boldsymbol{K}^{(s)}\boldsymbol{x}^{(s)}(t) = \boldsymbol{f}^{(s)}(t) + \boldsymbol{g}^{(s)}(t) \quad (1)$$

Where $\boldsymbol{M}^{(s)}$, $\boldsymbol{C}^{(s)}$, and $\boldsymbol{K}^{(s)}$ are mass, damping, and stiffness matrices respectively; $\boldsymbol{x}^{(s)}$ is a vector of displacements (or degrees of freedom), $\boldsymbol{f}^{(s)}$ is a vector of external forces, and $\boldsymbol{g}^{(s)}$ is a vector of

connecting forces with other substructures. It is important to note that Equation (1) is for one specific substructure of an assembly, (*s*). It is also important to note that the system described in Equation (1) is assumed to be a linear, time-invariant (LTI) system. Within this framework, the external force vector can be viewed as constraining forces for the previously mentioned necessary conditions (compatibility and equilibrium).

There have been methods developed for nonlinear or time variant systems in recent years, but no standard set of methods has been established yet [18] [19]. The lack of a standard, nonlinear method can be attributed to the difficulty of generalizing nonlinear systems. As such, the present work will focus on the well-established, linear system methods.

In the more general case, where we have *n* substructures that are coupled in an assembly, we can write the system as:

$$\boldsymbol{M}\ddot{\boldsymbol{x}} + \boldsymbol{C}\dot{\boldsymbol{x}} + \boldsymbol{K}\boldsymbol{x} = \boldsymbol{f} + \boldsymbol{g} \tag{2}$$

Where $\boldsymbol{M}$, $\boldsymbol{C}$, and $\boldsymbol{K}$ are now block diagonal matrices, while $\boldsymbol{f}$, $\boldsymbol{g}$, and $\boldsymbol{x}$ are now columns of vectors consisting of components from each substructure. Note that $\boldsymbol{f}$, $\boldsymbol{g}$, and $\boldsymbol{x}$ are still time dependent though the notation has been dropped in the interest of simplicity. The terms of Equation (2) can be written more specifically as follows:

$$\boldsymbol{M} \triangleq diag\left(\boldsymbol{M}^{(1)}, \boldsymbol{M}^{(2)}, \dots, \boldsymbol{M}^{(n)}\right) = \begin{bmatrix} \boldsymbol{M}^{(1)} & \cdots & \cdot \\ \vdots & \ddots & \vdots \\ \cdot & \cdots & \boldsymbol{M}^{(n)} \end{bmatrix}$$

$$\boldsymbol{C} \triangleq diag\left(\boldsymbol{C}^{(1)}, \boldsymbol{C}^{(2)}, \dots, \boldsymbol{C}^{(n)}\right) \qquad \text{and} \qquad \boldsymbol{K} \triangleq diag\left(\boldsymbol{K}^{(1)}, \boldsymbol{K}^{(2)}, \dots, \boldsymbol{K}^{(n)}\right)$$

$$\boldsymbol{x} = \begin{bmatrix} \boldsymbol{x}^{(1)} \\ \vdots \\ \boldsymbol{x}^{(n)} \end{bmatrix}, \quad \boldsymbol{f} = \begin{bmatrix} \boldsymbol{f}^{(1)} \\ \vdots \\ \boldsymbol{f}^{(n)} \end{bmatrix}, \quad \boldsymbol{g} = \begin{bmatrix} \boldsymbol{g}^{(1)} \\ \vdots \\ \boldsymbol{g}^{(n)} \end{bmatrix}$$

From the expressions for the block diagonal matrices, it is important to note that all of the off-diagonal terms are zero. In this context, by "zero," we mean that the off-diagonal terms are matrices of corresponding size and full of zeros.

With the generalized form of the equations of motion as shown in Equation (2), the compatibility condition is expressed as:

$$\boldsymbol{Bx} = \mathbf{0} \tag{3}$$

Where $\boldsymbol{B}$ is a signed Boolean matrix which operates on the interface degrees of freedom (i.e. DOFs involved in coupling). The matrix $\boldsymbol{B}$ is essentially a matrix which denotes the connections between the entire set of DOFs. A more comprehensive discussion of this matrix is given in [15]. However, it is worth noting here that $\boldsymbol{B}$ may not be Boolean if certain other conditions are applied to the interfaces. These non-Boolean cases are beyond the scope of the present work, but the following discussion is still valid for those cases.

The equilibrium condition can similarly be written as:

$$\boldsymbol{L}^T\boldsymbol{g} = \mathbf{0} \tag{4}$$

Where $\boldsymbol{L}$ is a different Boolean matrix designed to localize the interface DOFs of each substructure from the global, dual set of DOFs. Equation (4) states that the resultant force must be zero when the dual connection forces are summed at a given interface point. In reality, the equilibrium condition is being applied for a discretized system and thus will result in an "equilibrium error" when applied to the actual continuous system. For the purposes of this work, Equation (4) will be treated as enforcing exact equilibrium.

Continuing with the brief overview of the physical domain formulation [15], we can now write the complete system of equations as:

$$\begin{cases} \boldsymbol{M\ddot{x} + C\dot{x} + Kx = f + g} \\ \boldsymbol{Bx = 0} \\ \boldsymbol{L^T g = 0} \end{cases} \tag{5}$$

Recall that the system of Equation (5) is for any number of structures (we specified this number as *n*). Using Equation (5), a formulation for the coupled structure can be obtained in either a primal or dual manner.

2.1.2.2 Physical Domain: Primal Formulation

In a primal formulation, interfaces forces are eliminated as unknowns, thus allowing the system to be coupled by using the compatibility condition. A unique set of interface degrees of freedom must be defined, which is expressed mathematically as:

$$\boldsymbol{x = Lq} \tag{6}$$

Where x and L are as previously defined and q is the unique set of interface DOFs. By definition, Equation (6) indicates that the substructure DOFs ($\boldsymbol{x}$) are obtained using the unique set which, in turn, implies that the compatibility condition will be satisfied for any set $\boldsymbol{q}$. This can be understood mathematically by:

$$\boldsymbol{Bx = BLq = 0} \qquad \forall\, \boldsymbol{q}$$

This relationship implies that L is actually the null space of B or vice versa. One useful result of this property is that only one Boolean matrix needs to be formulated in the assembly process of calculation the response of the coupled system. For more details on this property see De Klerk et al (2008).

Since the choice of the unique set $\boldsymbol{q}$ automatically satisfies the compatibility condition in Equation (5), we can substitute Equation (6) into Equation (5) to obtain a reduced system:

$$\begin{cases} \boldsymbol{ML\ddot{q} + CL\dot{q} + KLq = f + g} \\ \boldsymbol{L^T g = 0} \end{cases}$$

The $\boldsymbol{g}$ term can be eliminated from the equations of motion by premultiplying by $\boldsymbol{L^T}$. A new set of system matrices can be assembled to simplify the primal assembled system:

$$\begin{cases} \boldsymbol{\widetilde{M} \triangleq L^T ML} \\ \boldsymbol{\widetilde{C} \triangleq L^T CL} \\ \boldsymbol{\widetilde{K} \triangleq L^T KL} \\ \boldsymbol{\tilde{f} \triangleq L^T fL} \end{cases}$$

The above set of matrices completes the reduction of the original system from Equation (5) to:

$$\boldsymbol{\widetilde{M}\ddot{q} + \widetilde{C}\dot{q} + \widetilde{K}q = \tilde{f}} \tag{7}$$

The concepts which were applied to obtain Equation (7) will later be used again to obtain a similar primal formulation in the frequency domain.

2.1.2.3 Physical Domain: Dual Formulation

In contrast to the primal formulation, the dual formulation eliminates the displacements as unknowns and the assembly is solved using the equilibrium condition. Corresponding to the choice of eliminating displacements as unknowns, the dual formulation retains the full set of global DOFs. This statement is best explained by a walkthrough of the dual assembly procedure. First, interface forces are chosen in the form:

$$\boldsymbol{g = -B^T \lambda}$$

Where $\boldsymbol{\lambda}$ are Lagrange multipliers which correspond physically to the interface for intensities. Due to the construction of the Boolean matrix $\boldsymbol{B}$, this choice of form for the interface forces ensures that each force will be balanced by a corresponding force in the opposite direction for any given interface DOF.

The equilibrium condition can then be rewritten as follows.

$$\boldsymbol{L}^T\boldsymbol{g} = -\boldsymbol{L}^T\boldsymbol{B}^T\boldsymbol{\lambda} = \boldsymbol{0}$$

Recall that it was previously stated that L and B were actually null spaces for each other which implies that the above condition is automatically satisfied. As in the primal formulation, the system of Equation (5) can be reduced to the following:

$$\begin{cases} \boldsymbol{M}\ddot{\boldsymbol{x}} + \boldsymbol{C}\dot{\boldsymbol{x}} + \boldsymbol{K}\boldsymbol{x} + \boldsymbol{B}^T\boldsymbol{\lambda} = \boldsymbol{f} \\ \boldsymbol{B}\boldsymbol{x} = \boldsymbol{0} \end{cases}$$

This expression of the dual formulation in the physical domain can finally be shown in the following block matrix representation:

$$\begin{bmatrix} \boldsymbol{M} & \boldsymbol{0} \\ \boldsymbol{0} & \boldsymbol{0} \end{bmatrix} \begin{bmatrix} \ddot{\boldsymbol{x}} \\ \ddot{\boldsymbol{\lambda}} \end{bmatrix} + \begin{bmatrix} \boldsymbol{C} & \boldsymbol{0} \\ \boldsymbol{0} & \boldsymbol{0} \end{bmatrix} \begin{bmatrix} \dot{\boldsymbol{x}} \\ \dot{\boldsymbol{\lambda}} \end{bmatrix} + \begin{bmatrix} \boldsymbol{K} & \boldsymbol{B}^T \\ \boldsymbol{B} & \boldsymbol{0} \end{bmatrix} \begin{bmatrix} \boldsymbol{x} \\ \boldsymbol{\lambda} \end{bmatrix} = \begin{bmatrix} \boldsymbol{f} \\ \boldsymbol{0} \end{bmatrix} \tag{8}$$

This concludes the discussion of dynamic substructuring or decoupling in the physical domain. Though the remainder of the chapter will focus on frequency based substructuring (FBS), the principals and processes presented in this section will appear again throughout. The following section includes a brief history of the FBS method and its extensions as well as a mathematical background of said methods.

2.1.3 History and Mathematical Background of FBS Methods

The FBS method in its currently recognized form was first presented in the 1980's by Jetmundsen et al. The method was described as "a generalized frequency domain substructure synthesis methodology" with the application of using the new method to analyze helicopter airframe vibration. Before the FBS methodology is discussed, the necessary mathematical background and notation will be presented. Other names for the FBS method include: impedance based substructuring, receptance coupling (or modelling), and admittance coupling (or modelling).

2.1.3.1 FBS Background Math and Notation

Recall from the previous section that Equation (2) describes the equations of motion of the given system in the physical domain. Equation (2) is repeated here for convenience:

$$\boldsymbol{M\ddot{x} + C\dot{x} + Kx = f + g} \tag{2}$$

As in the original FBS method proposed by Jetmundsen et al, the interface force vector, g, is omitted in the following mathematical discussion. With $\boldsymbol{g}$ omitted, Equation (2) can be transformed into the frequency domain using a Fourier transform:

$$[-\omega^2\boldsymbol{M} + j\omega\boldsymbol{C} + \boldsymbol{K}]\boldsymbol{x}(\omega) = \boldsymbol{f}(\omega) \tag{9}$$

Where the left hand side of Equation (9) defines the dynamic stiffness matrix, $\boldsymbol{Z}$, so that the system may be written in a condensed form as:

$$\boldsymbol{Z}(\omega)\boldsymbol{x}(\omega) = \boldsymbol{f}(\omega) \tag{10}$$

It is worth noting that the impedance matrix, $\boldsymbol{Z}$, is also often referred to as the dynamic stiffness. We can define an additional matrix:

$$\boldsymbol{Y} = \boldsymbol{Z}^{-1} \tag{11}$$

Here, the notation of frequency dependence has been dropped in the interest of clarity. The matrix $\boldsymbol{Y}$ is often referred to as the receptance (or admittance) matrix [20]. Alternatively, for velocity and acceleration, similar matrices are termed mobility or accelerance, respectively. Though some differences exist between substructuring with receptance, mobility, and accelerance matrices, the following derivation for a simplified system holds for all three. We can rewrite Equation (10) using the mobility matrix in place of the impedance so that it appears as:

$$\boldsymbol{x} = \boldsymbol{Y}\boldsymbol{f} \tag{12}$$

It is useful to view the system as having the form of Equations (10) or (12) as opposed to the expanded form in Equation (9). Mass, stiffness, and damping matrices are not generally known or easily formulated for complex systems. On the other hand, it is much easier and there are well established methods for obtaining receptances or mobilities through modal testing [20].

2.1.3.2 Simplified FBS Formulation

Many academic papers and even textbooks that address dynamic substructuring skip over portions of the background math and derivations that may be non-obvious to a given reader. In the interest of being thorough, that background math will be presented here. Figure 2 displays the simplest case of coupling between two structures in which the structures are couple by a single DOF.

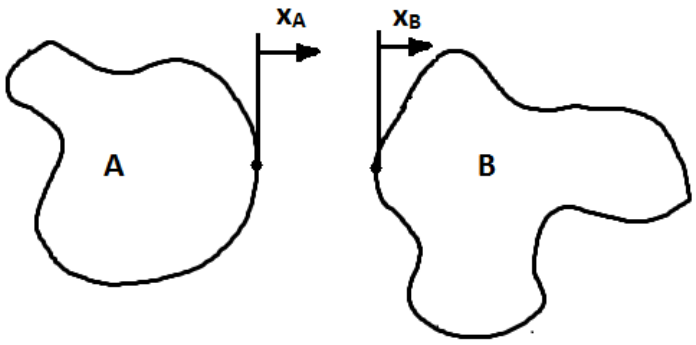

Figure 2: Arbitrary structures, A and B, coupled by a single coordinate, x_A and x_B, on each structure

In Figure 2, A and B represent two arbitrary structures that are coupled by a single coordinate to form a new structure that will be called C. In the form of Equation (12), we can write:

$$\boldsymbol{x}_A = \boldsymbol{Y}_A \boldsymbol{f}_A \qquad \text{and} \qquad \boldsymbol{x}_B = \boldsymbol{Y}_B \boldsymbol{f}_B$$

The compatibility and equilibrium conditions can be applied at the connection point between substructures A and B:

$$\boldsymbol{x}_C = \boldsymbol{x}_A = \boldsymbol{x}_B \tag{13}$$

$$\boldsymbol{F}_C = \boldsymbol{F}_A + \boldsymbol{F}_B \tag{14}$$

Which yields the following after some manipulation:

$$\boldsymbol{Y}_C^{-1} = \boldsymbol{Y}_A^{-1} + \boldsymbol{Y}_B^{-1} \tag{15}$$

Equation (15) can be extended to a system in which there are several DOFs involved in the coupling procedure. However, no additional internal DOFs are included in this analysis. Conceptually, Equation (15) will give the FRF properties of the coupled system as a combination of the two independent subsystems. It is important to note that Equation (15) could be written in terms of dynamic stiffnesses rather than receptances (i.e. using $\boldsymbol{Z}$ as opposed to $\boldsymbol{Y}^{-1}$). For the

following analysis, we will use the receptances rather than dynamic stiffnesses, but when the analysis is extended to include multiple DOFs, which may or may not be involved in the coupling, the dynamic stiffness method becomes much more straightforward algebraically.

As we proceed with the analysis in terms of receptances, there is a major limitation of the form of Equation (15) that must be addressed. Even for this simplified representation, the current form requires three matrix inversions. Matrix inverse operations are computationally expensive and can end up magnifying errors within the data as they are carried out. The form of Equation (15) can be changed through the following steps, as derived in [20], to reduce the number of necessary matrix inversions.

$$\begin{aligned} \boldsymbol{Y}_C^{-1} &= \boldsymbol{Y}_A^{-1} + \boldsymbol{Y}_B^{-1} \\ &= \boldsymbol{Y}_A^{-1}(\boldsymbol{I} + \boldsymbol{Y}_A\boldsymbol{Y}_B^{-1}) \\ &= \boldsymbol{Y}_A^{-1}(\boldsymbol{Y}_B + \boldsymbol{Y}_A)\boldsymbol{Y}_B^{-1} \end{aligned}$$

Which clearly yields:

$$\boldsymbol{Y}_C = \boldsymbol{Y}_B(\boldsymbol{Y}_B + \boldsymbol{Y}_A)^{-1}\boldsymbol{Y}_A \tag{16}$$

Equation (16) is much more efficient than Equation (15) from a computation standpoint. We can rearrange Equation (16) to obtain yet another version that is more useful for modification purposes:

$$\begin{aligned} \boldsymbol{Y}_C &= \boldsymbol{Y}_B(\boldsymbol{Y}_B + \boldsymbol{Y}_A)^{-1}\boldsymbol{Y}_A \\ &= (\boldsymbol{Y}_A + \boldsymbol{Y}_B - \boldsymbol{Y}_A)(\boldsymbol{Y}_B + \boldsymbol{Y}_A)^{-1}\boldsymbol{Y}_A \\ &= (\boldsymbol{Y}_A + \boldsymbol{Y}_B)(\boldsymbol{Y}_B + \boldsymbol{Y}_A)^{-1}\boldsymbol{Y}_A - \boldsymbol{Y}_A(\boldsymbol{Y}_B + \boldsymbol{Y}_A)^{-1}\boldsymbol{Y}_A \\ &= \boldsymbol{I}\boldsymbol{Y}_A - \boldsymbol{Y}_A(\boldsymbol{Y}_B + \boldsymbol{Y}_A)^{-1}\boldsymbol{Y}_A \end{aligned}$$

From which we arrive at the final desired form of:

$$\boldsymbol{Y}_C = \boldsymbol{Y}_A - \boldsymbol{Y}_A(\boldsymbol{Y}_B + \boldsymbol{Y}_A)^{-1}\boldsymbol{Y}_A \tag{17}$$

Which is considered the most useful form for structural modification purposes [20].

2.1.3.3 Generalized FBS Formulation

The preceding analysis for the simplified system can readily be extended to the more general case of subsystems with arbitrarily large numbers of DOFs and coupled at any number of those DOFs. In such a case, we can partition the receptance matrix into portions which correspond to the coupling DOFs and those that do not:

$$\boldsymbol{Y}_A = \begin{bmatrix} \boldsymbol{Y}_{ii}^A & \boldsymbol{Y}_{ic}^A \\ \boldsymbol{Y}_{ci}^A & \boldsymbol{Y}_{cc}^A \end{bmatrix} \tag{18}$$

$$\boldsymbol{Y}_B = \begin{bmatrix} \boldsymbol{Y}_{ii}^B & \boldsymbol{Y}_{ic}^B \\ \boldsymbol{Y}_{ci}^B & \boldsymbol{Y}_{cc}^B \end{bmatrix} \tag{19}$$

Where the subscripts denote the specific receptance and the superscript denotes the substructure from which the receptance originates. For example,

- $\boldsymbol{Y}_{ii}^A$ denotes the partition of the receptance matrix for the internal (uncoupled) DOFs on substructure A
- $\boldsymbol{Y}_{ic}^A$ denotes the cross-partition of the interface/internal (i.e. coupled and uncoupled) receptances
- $\boldsymbol{Y}_{cc}^A$ denotes the partition of the interface (coupling) receptances from substructure A

It is worth noting that there are corresponding impedance matrices ($\boldsymbol{Z}$) for each receptance. Using the receptances as defined in Equations (18) and (19), we can write out an expanded form of Equation (12):

$$\begin{Bmatrix} \boldsymbol{x}_i^A \\ \boldsymbol{x}_c^A \end{Bmatrix} = \begin{bmatrix} \boldsymbol{Y}_{ii}^A & \boldsymbol{Y}_{ic}^A \\ \boldsymbol{Y}_{ci}^A & \boldsymbol{Y}_{cc}^A \end{bmatrix} \begin{Bmatrix} \boldsymbol{f}_i^A \\ \boldsymbol{f}_c^A \end{Bmatrix} \tag{20}$$

$$\begin{Bmatrix} \boldsymbol{x}_i^B \\ \boldsymbol{x}_c^B \end{Bmatrix} = \begin{bmatrix} \boldsymbol{Y}_{ii}^B & \boldsymbol{Y}_{ic}^B \\ \boldsymbol{Y}_{ci}^B & \boldsymbol{Y}_{cc}^B \end{bmatrix} \begin{Bmatrix} \boldsymbol{f}_i^B \\ \boldsymbol{f}_c^B \end{Bmatrix} \tag{21}$$

With the formulation of Equations (20) and (21), we can then partition the coordinates of the FRF matrix of the coupled structure into three regions [21]:

1. Interior DOFs of substructure A, thus forward denoted with a subscript “a”
2. Interior DOFs of substructure B, thus forward denoted with a subscript “b”
3. The coupling DOFs of both substructures, thus forward denoted with a subscript “c”

With these three specific regions defined, the FRF for the complete system can be written as:

$$\begin{Bmatrix} \boldsymbol{X}_a \\ \boldsymbol{X}_c \\ \boldsymbol{X}_b \end{Bmatrix} = \begin{bmatrix} \boldsymbol{Y}_{aa} & \boldsymbol{Y}_{ac} & \boldsymbol{Y}_{ab} \\ \boldsymbol{Y}_{ca} & \boldsymbol{Y}_{cc} & \boldsymbol{Y}_{cb} \\ \boldsymbol{Y}_{ba} & \boldsymbol{Y}_{bc} & \boldsymbol{Y}_{bb} \end{bmatrix} \begin{Bmatrix} \boldsymbol{F}_a \\ \boldsymbol{F}_c \\ \boldsymbol{F}_b \end{Bmatrix} \tag{22}$$

Where the $\boldsymbol{X}$‘s and $\boldsymbol{F}$’s are column vectors and the receptance block matrix will be called $\boldsymbol{Y}^C$. Simplifying the notation and expressing compatibility and equilibrium requirements we arrive at the following:

$$\boldsymbol{X}_a = \boldsymbol{x}_i^A \tag{23}$$

$$\boldsymbol{X}_{\boldsymbol{b}} = \boldsymbol{x}_i^A \tag{24}$$

$$\boldsymbol{X}_c = \boldsymbol{x}_c^A = \boldsymbol{x}_c^B \tag{25}$$

$$\boldsymbol{F}_c = \boldsymbol{f}_c^A + \boldsymbol{f}_c^B \tag{26}$$

$$\boldsymbol{F}_a = \boldsymbol{f}_i^A \tag{27}$$

$$\boldsymbol{F_b} = \boldsymbol{f}_i^B \tag{28}$$

Where the compatibility and equilibrium conditions are represented by Equations (25) and (26), respectively. Going back to Equations (20) and (21), we can expand the $\boldsymbol{x}_c^A$ and $\boldsymbol{x}_c^B$ terms to find:

$$\boldsymbol{x}_c^A = \boldsymbol{Y}_{ci}^A \boldsymbol{f}_i^A + \boldsymbol{Y}_{cc}^A \boldsymbol{f}_c^A \tag{29}$$

$$\boldsymbol{x}_c^B = \boldsymbol{Y}_{ci}^B \boldsymbol{f}_i^B + \boldsymbol{Y}_{cc}^B \boldsymbol{f}_c^B \tag{30}$$

Then, using the compatibility condition of Equation (25) we arrive at a relationship between $\boldsymbol{f}_c^A$ and $\boldsymbol{f}_c^B$:

$$\boldsymbol{f}_c^B = \boldsymbol{Y}_{cc}^{B\ -1}(\boldsymbol{Y}_{cc}^A \boldsymbol{f}_c^A + \boldsymbol{Y}_{ci}^A \boldsymbol{f}_i^A - \boldsymbol{Y}_{ci}^B \boldsymbol{f}_i^B) \tag{31}$$

By utilizing the equilibrium condition of Equation (26), along with Equations (27), (28), (29), and (30), the compatibility condition can be written as:

$$\boldsymbol{x}_c^A = \boldsymbol{Y}_{ci}^A \boldsymbol{F}_a + \boldsymbol{Y}_{cc}^A \boldsymbol{f}_c^A \tag{32}$$

$$\boldsymbol{x}_c^A = \boldsymbol{X}_c = \boldsymbol{Y}_{ca} \boldsymbol{F}_a + \boldsymbol{Y}_{cc}(\boldsymbol{f}_c^A + \boldsymbol{f}_c^B) + \boldsymbol{Y}_{cb} \boldsymbol{F}_b \tag{33}$$

Substituting Equation (31) into (33) and then setting Equations (32) and (33) equal to each other produces the following after some simplification:

$$\boldsymbol{Y}_{ci}^A \boldsymbol{F}_a + \boldsymbol{Y}_{cc}^A \boldsymbol{f}_c^A = \tag{34}$$

$$= \left(\boldsymbol{Y}_{ca} + \boldsymbol{Y}_{cc}{\boldsymbol{Y}_{cc}^{B}}^{-1}\boldsymbol{Y}_{ci}^{A}\right)\boldsymbol{F}_{a} + \left(\boldsymbol{Y}_{cc} + \boldsymbol{Y}_{cc}{\boldsymbol{Y}_{cc}^{B}}^{-1}\boldsymbol{Y}_{cc}^{A}\right)\boldsymbol{f}_{c}^{A} + \left(\boldsymbol{Y}_{cb} - \boldsymbol{Y}_{cc}{\boldsymbol{Y}_{cc}^{B}}^{-1}\boldsymbol{Y}_{ci}^{B}\right)\boldsymbol{F}_{B}$$

The corresponding force terms from each side of Equation (34) are then set equal to each other such that we arrive at the following:

$$\boldsymbol{Y}_{cc} + \boldsymbol{Y}_{cc}{\boldsymbol{Y}_{cc}^{B}}^{-1}\boldsymbol{Y}_{cc}^{A} = \boldsymbol{Y}_{cc}^{A} \tag{35}$$

$$\boldsymbol{Y}_{ca} + \boldsymbol{Y}_{cc}{\boldsymbol{Y}_{cc}^{B}}^{-1}\boldsymbol{Y}_{ci}^{A} = \boldsymbol{Y}_{ci}^{A} \tag{36}$$

$$\boldsymbol{Y}_{cb} - \boldsymbol{Y}_{cc}{\boldsymbol{Y}_{cc}^{B}}^{-1}\boldsymbol{Y}_{ci}^{B} = \boldsymbol{0} \tag{37}$$

Equations (35)-(37) can be solved for the $\boldsymbol{Y}_{cc}$ term in the following steps:

$$\boldsymbol{Y}_{cc}(\boldsymbol{I} + {\boldsymbol{Y}_{cc}^{B}}^{-1}\boldsymbol{Y}_{cc}^{A}) = \boldsymbol{Y}_{cc}^{A}$$

$$\boldsymbol{Y}_{cc} = \boldsymbol{Y}_{cc}^{A}\left(\boldsymbol{I} + {\boldsymbol{Y}_{cc}^{B}}^{-1}\boldsymbol{Y}_{cc}^{A}\right)^{-1}$$

$$\boldsymbol{Y}_{cc} = \boldsymbol{Y}_{cc}^{A}\left({\boldsymbol{Y}_{cc}^{B}}^{-1}\left(\boldsymbol{Y}_{cc}^{B}\boldsymbol{I} + \boldsymbol{Y}_{cc}^{B}{\boldsymbol{Y}_{cc}^{B}}^{-1}\boldsymbol{Y}_{cc}^{A}\right)\right)^{-1}$$

$$\boldsymbol{Y}_{cc} = \boldsymbol{Y}_{cc}^{A}(\boldsymbol{Y}_{cc}^{B} + \boldsymbol{Y}_{cc}^{A})^{-1}\boldsymbol{Y}_{cc}^{B} = \boldsymbol{Y}_{cc}^{B}(\boldsymbol{Y}_{cc}^{B} + \boldsymbol{Y}_{cc}^{A})^{-1}\boldsymbol{Y}_{cc}^{A}$$

Note that the terms of the final expression for $\boldsymbol{Y}_{cc}$ can be can be rearranged in either order since the matrices are all symmetric in theory. Then, through the steps described for the simplified coupling problem, the final expression for $\boldsymbol{Y}_{cc}$ can be put in the form of Equation (17):

$$\boldsymbol{Y}_{cc} = \boldsymbol{Y}_{cc}^{A} + \boldsymbol{Y}_{cc}^{A}(\boldsymbol{Y}_{cc}^{B} + \boldsymbol{Y}_{cc}^{A})^{-1}\boldsymbol{Y}_{cc}^{A} \tag{38}$$

Equation (38) is then used to solve Equations (36) and (37) for $\boldsymbol{Y}_{ca}$ and $\boldsymbol{Y}_{cb}$ respectively. The remainder of the entries of the $\boldsymbol{Y}^{C}$ receptance block matrix are found through similar applications

of (23)-(28). It is worth noting that $\boldsymbol{Y}_{ca}$ is the transpose of $\boldsymbol{Y}_{ac}$, $\boldsymbol{Y}_{ba}$ is the transpose of $\boldsymbol{Y}_{ab}$, and so on for the other entries of $\boldsymbol{Y}^{C}$.

The remainder of the receptance terms for $\boldsymbol{Y}^{C}$ are shown in Equations (39)-(44):

$$\boldsymbol{Y}_{aa} = \boldsymbol{Y}_{ii}^{A} - \boldsymbol{Y}_{ic}^{A}(\boldsymbol{Y}_{cc}^{A} + \boldsymbol{Y}_{cc}^{B})^{-1}\boldsymbol{Y}_{ci}^{A} \tag{39}$$

$$\boldsymbol{Y}_{ab} = \boldsymbol{Y}_{ic}^{A}(\boldsymbol{Y}_{cc}^{A} + \boldsymbol{Y}_{cc}^{B})^{-1}\boldsymbol{Y}_{ci}^{B} \tag{40}$$

$$\boldsymbol{Y}_{bb} = \boldsymbol{Y}_{ii}^{B} - \boldsymbol{Y}_{ic}^{B}(\boldsymbol{Y}_{cc}^{A} + \boldsymbol{Y}_{cc}^{B})^{-1}\boldsymbol{Y}_{ci}^{B} \tag{41}$$

$$\boldsymbol{Y}_{ba} = \boldsymbol{Y}_{ic}^{B}(\boldsymbol{Y}_{cc}^{A} + \boldsymbol{Y}_{cc}^{B})^{-1}\boldsymbol{Y}_{ci}^{A} \tag{42}$$

$$\boldsymbol{Y}_{ca} = [\boldsymbol{Y}_{ac}]^{T} = \boldsymbol{Y}_{ci}^{A} - \boldsymbol{Y}_{cc}^{A}(\boldsymbol{Y}_{cc}^{A} + \boldsymbol{Y}_{cc}^{B})^{-1}\boldsymbol{Y}_{ci}^{A} \tag{43}$$

$$\boldsymbol{Y}_{cb} = [\boldsymbol{Y}_{bc}]^{T} = \boldsymbol{Y}_{cc}^{A}(\boldsymbol{Y}_{cc}^{A} + \boldsymbol{Y}_{cc}^{B})^{-1}\boldsymbol{Y}_{ci}^{B} \tag{44}$$

Equations (38)-(44) can then be reassembled into the canonical form of the FBS method as developed by Jetmundsen et al [16] and shown in Equation(45).

$$\boldsymbol{Y}^{C} = \begin{bmatrix} \boldsymbol{Y}_{aa} & \boldsymbol{Y}_{ac} & \boldsymbol{Y}_{ab} \\ \boldsymbol{Y}_{ca} & \boldsymbol{Y}_{cc} & \boldsymbol{Y}_{cb} \\ \boldsymbol{Y}_{ba} & \boldsymbol{Y}_{bc} & \boldsymbol{Y}_{bb} \end{bmatrix} = \begin{bmatrix} \boldsymbol{Y}_{ii}^{A} & \boldsymbol{Y}_{ic}^{A} & \boldsymbol{0} \\ \boldsymbol{Y}_{ci}^{A} & \boldsymbol{Y}_{cc}^{A} & \boldsymbol{0} \\ \boldsymbol{0} & \boldsymbol{0} & \boldsymbol{Y}_{ii}^{B} \end{bmatrix} - \begin{bmatrix} \boldsymbol{Y}_{ic}^{A} \\ \boldsymbol{Y}_{cc}^{A} \\ -\boldsymbol{Y}_{ic}^{B} \end{bmatrix} (\boldsymbol{Y}_{cc}^{A} + \boldsymbol{Y}_{cc}^{B})^{-1} \begin{bmatrix} \boldsymbol{Y}_{ic}^{A} \\ \boldsymbol{Y}_{cc}^{A} \\ -\boldsymbol{Y}_{ic}^{B} \end{bmatrix}^{T} \tag{45}$$

Equation (45) is the form of the FBS method that most commonly appears throughout literature and has served as the basis for many improvements to the method.

2.1.3.4 Application of FBS to Multiple Substructures

Though the FBS method as presented here is for the coupling of two substructures, the concept can be extended to include an arbitrarily large number of substructures. As discussed in [22], the

problem of coupling multiple substructures through the FBS method can be described by a simple example consisting of only three substructures. Figure 3 demonstrates the general concept.

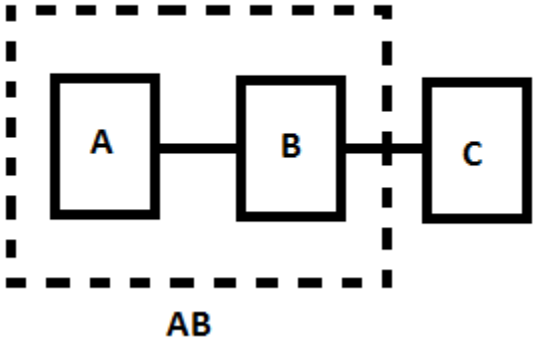

Figure 3: Three substructures to be coupled together. First, substructures A and B are coupled. Then, the combined substructure AB is couple with C.

As shown in Figure 3, substructures A and B are first coupled to each other and then the combined substructure, AB, is coupled to C. In this way, the FBS method can be extend to an arbitrarily large number of substructures [22]. This same concept can also be applied to decoupling as shown in [23]. However, if substructure C was also coupled to A, or if all three substructures shared a coupling point, the process would no longer be as straightforward as presented here.

2.1.3.5 Generalized Receptance Coupling

A more generalized formulation of FBS was presented in [24]. The method was termed the "generalized receptance method" or "GRC" and was a physically and mathematically generalized version of the classical FBS/receptance method. In fact, the classical FBS method of Jetmundsen [16] is a special case of GRC [25] [26]. However, most future work focused on either improvements to the classical FBS method, or entirely different coupling formulations such as in [23]. Thus, the mathematical formulation of GRC will not be presented here.

2.1.3.6 Lagrange Multiplier Frequency Based Substructuring (LM FBS)

De Klerk et al [23] use the dual formulation to improve the base FBS method through the inclusion of Lagrange multipliers. The dual assembly in the physical domain was introduced in a previous section, where a Lagrange multiplier term was introduced to enforce the equilibrium condition. The following analysis similarly uses Lagrange multipliers in the frequency domain.

With the inclusion of the Lagrange multipliers, the local equilibrium equations can be written in the frequency domain as:

$$\boldsymbol{ZX} + \boldsymbol{B}^T\boldsymbol{\lambda} = \boldsymbol{F} \tag{46}$$

Recall that $\boldsymbol{Z}$ is the dynamic stiffness (impedance could be used alternatively), $\boldsymbol{X}$ is the vector of displacements, $\boldsymbol{B}$ is the Boolean mapping matrix as previously defined, $\boldsymbol{\lambda}$ is a vector of Lagrange multipliers, and $\boldsymbol{F}$ is a vector containing the internal and interface forces.

The compatibility condition is expressed as:

$$\boldsymbol{BU} = \boldsymbol{0} \tag{47}$$

Where the Boolean matrix is constructed in theory to satisfy this equation. The transpose of this Boolean mapping matrix is used in Equation (46) to define on which DOFs the connecting forces, $\boldsymbol{\lambda}$, will be applied.

The behavior of the complete system in the dual assembly formulation is described, as follows, by combining Equations (46) and (47):

$$\begin{bmatrix} \boldsymbol{Z} & \boldsymbol{B}^T \\ \boldsymbol{B} & \boldsymbol{0} \end{bmatrix} \begin{Bmatrix} \boldsymbol{U} \\ \boldsymbol{\lambda} \end{Bmatrix} = \begin{Bmatrix} \boldsymbol{F} \\ \boldsymbol{0} \end{Bmatrix} \tag{48}$$

Solving the first row of Equation (48), the equilibrium equations, for $\boldsymbol{X}$ we find:

$$\boldsymbol{U} = \boldsymbol{Y}(\boldsymbol{F} - \boldsymbol{B}^T\boldsymbol{\lambda}) \tag{49}$$

Where, as before, $\boldsymbol{Y}$ is the receptance (or admittance) and is the inverse of the dynamic stiffness, $\boldsymbol{Z}$. Equation (49) can then be substituted into the second line of Equation (48), the compatibility equations, to obtain an expression for $\boldsymbol{\lambda}$:

$$\boldsymbol{\lambda} = (\boldsymbol{B}\boldsymbol{Y}\boldsymbol{B}^T)^{-1}\boldsymbol{B}\boldsymbol{Y}\boldsymbol{F} \tag{50}$$

Equation (50) can then be substituted back into Equation (49) to obtain an expression for $\boldsymbol{X}$ independent of $\boldsymbol{\lambda}$:

$$\boldsymbol{U} = \boldsymbol{Y}(\boldsymbol{I} - \boldsymbol{B}^T(\boldsymbol{B}\boldsymbol{Y}\boldsymbol{B}^T)^{-1}\boldsymbol{B}\boldsymbol{Y})\boldsymbol{F} \tag{51}$$

This formulation is mathematically equivalent to the classical FBS formulation. A full discussion and comparison of the two methods to demonstrate the equivalence is shown in [23]. Essentially, the only difference between the two methods is the point during the analysis in which the interface degrees of freedom are no longer considered for both coupled substructures. The choice is predetermined in the classical FBS method, whereas the LM FBS method allows the user to make the choice later on in the analysis. The classical method eliminates the interface DOFs when not all information about the assembled system is known.

The ability to choose on which substructure the interface DOFs are retained provides the primary advantage of the LM FBS method over the classical FBS method. The user can then choose whichever set of FRFs contain a lower or less significant level of noise and, therefore, improve the quality of the coupled FRF.

With these FBS coupling methods described, our discussion will now turn to substructure decoupling in the frequency domain.

2.1.3.7 Decoupling Theory and Applications

Decoupling theory arose out of the need to describe the dynamics of a system or subsystem which may be difficult or impossible to measure through normal means. Examples of these types of systems are those that are very small, delicate, rotating, or potentially hazardous [27]. Some of the difficulties associated with these types of systems can be addressed through the use of non-contact testing methods such as laser Doppler vibrometry. However, non-contact methods come with their own difficulties and may still not be appropriate for the types of systems mentioned previously. Thus, decoupling theory and experimental application has still been an area of interest in recent years.

Substructure decoupling techniques can be generally classified as either "inverse coupling" techniques or "direct decoupling techniques" [28] [29]. Inverse coupling works by rearranging the equations for coupling so that one of the substructures is isolated and treated as unknown instead of the coupled structure. Most commonly, the FBS (or impedance) methods are used in inverse coupling [27] [30] [31].

On the other hand, direct decoupling uses a "fictitious substructure" which is added to the assembled system. This fictitious substructure is exactly the negative of the residual substructure which is defined as the substructure of the overall assembly which can be measured independently. This procedure starts from what is known as the 3-field formulation, so named for the sets of equations describing the system: one set to express the dynamic balance of the assembled system and of the fictitious substructure separately, one set to enforce compatibility at the interface DOFs, and one set to enforce equilibrium at the interface DOFs [29].

Either a primal or a dual approach can be used to carry out direct decoupling (primal and dual approach concepts are outlined in the mathematical background section). Compatibility and equilibrium conditions can be required either at only the coupling DOFs, or at coupling DOFs and additional internal DOFs of the residual substructure. We define a "standard interface" to be when the conditions are enforced at only the coupling DOFs, an "extended interface" to be when all coupling and some internal DOFs are included, and a "mixed interface" to only include some coupling DOFs and some internal DOFs [28] [29].

The following subsections present the standard methods for both inverse coupling and direct decoupling.

2.1.3.7.1 Inverse Coupling – Re-structuring of FBS method for decoupling

With the background math presented in the preceding sections, the most apparent method for decoupling structures is carried out through a restructuring of the FBS formulation. Recall the final formulation of the FBS methodology shown in Equation (45). The most upper left corner of the $\boldsymbol{Y}^{C}$ receptance matrix is also described by Equation (39). According to Ind [27] this equation can be reorganized to yield:

$$\boldsymbol{Y}_{cc}^{B} = \boldsymbol{Y}_{ci}^{A}\left(\boldsymbol{Y}_{ii}^{A} - \boldsymbol{Y}_{aa}\right)^{-1}\boldsymbol{Y}_{ic}^{A} - \boldsymbol{Y}_{cc}^{A} \tag{52}$$

Equation (52) shows that the FRFs of the uncoupled structure B can be determined by measurements made on structure A while the two structures are coupled. The equation also implies that for the FRFs of B to be determined, we must know the relationships between the remote excitation DOFs and the coupling DOFs for the structure A when it is not coupled to B. These "relationships" are described by the terms with superscript "A" in Equation (52).

Through similar analysis, the lower most left corner of the $\mathbf{Y}^{C}$ receptance matrix (also described by Equation (41)) can be rearranged as:

$$\boldsymbol{Y}_{ic}^{B} = \boldsymbol{Y}_{ba}[\boldsymbol{Y}_{ci}^{A}]^{-1}(\boldsymbol{Y}_{cc}^{B} - \boldsymbol{Y}_{cc}^{A}) \tag{53}$$

Where the $\boldsymbol{Y}_{cc}^{B}$ term can be substituted in from Equation (52). This analysis shows that the uncoupled FRFs of the structure B at DOFs remote from the coupling location can be found without direct measurement.

It is important to note that neither the auto FRF matrix ($\boldsymbol{Y}_{cc}^{A}$) nor the cross matrix ($\boldsymbol{Y}_{ba}$) need to be measured fully for Equations (52) and (53) respectively. The details of this reduction in necessary measurements effectively makes the measurement phase of any experiment less demanding and are discussed more fully in [27] [32].

Although Equations (52) and (53) are for the decoupling of structures, they were derived from the FBS (or impedance) method formulation. Thus, they are subject to the same issues encountered during the coupling procedures. The most common difficulties of decoupling using the previously described equations are listed briefly as follows and in more detail in [27]:

1) The coupling matrices which are to be inverted become singular due to ill conditioning of the data (i.e. signal noise and stiffness/damping properties at the measurement site)
2) Large order matrices are more susceptible to ill conditioning. With 6 DOFs needed at each connection point to have a full FRF matrix, a relatively small number of connection points can result in a large order matrix.
3) If any rotational DOFs are active in the coupling/decoupling, they need to be included in the FRF matrix. At the time of the publication of [27], measurement of rotational DOFs

was still notoriously difficult. However, more work on the subject has been done in recent years and will be discussed later.

4) Modal truncation may occur if FRFs are synthesized from a modal database. This is often referred to as a "residual" problem, due to the residual dynamics truncated in the modal data. Like the rotational DOFs, this is an area in which further work has been done and will be discussed later.

Despite these difficulties, the decoupling method of Equations (52) and (53) does have some advantages over its coupling counterpart. These advantages primarily come from the ability to control certain aspects of the test through the design of the test fixture. Some of the advantages are control over the number of connection points, flexibility properties of one of the structures, and the location of the measurement points on the testing fixture [27].

D'Ambrogio et al [33] explored a similar approach, using impedance matrices instead of receptance. Furthermore, [33] shows that the decoupling equation is the same whether it is derived using impedances or mobilities, so long as only the coupling DOFs are used. However, if additional internal DOFs are included as well, the derivation of the decoupling equations is different depending on if impedance or mobility matrices are used.

2.1.3.7.2 Direct Decoupling

As with previous mathematical descriptions in this chapter, we will assume that two substructures, A and B, are coupled to form the assembled system, C. For the following descriptions of direct decoupling using the primal formulation, we will treat B as the residual substructure. It is important to note that the substructure B can be an individual substructure or an assembly of other

substructures. With B as the known substructure, it is our goal to extract the FRF of A from the coupled system, C, by cancelling out the dynamic effects of the residual substructure.

This cancelling out of the residual substructure is accomplished by adding a fictitious substructure to the coupled system. The fictitious substructure must have a dynamic stiffness equal to the negative of the residual substructure and must satisfy the compatibility and equilibrium conditions. The combined system of the coupled structure and the fictitious substructure can be expressed in block diagonal format as [29]:

$$\begin{bmatrix} \boldsymbol{Z}^C & \mathbf{0} \\ \mathbf{0} & -\boldsymbol{Z}^B \end{bmatrix} \begin{Bmatrix} \boldsymbol{x}^C \\ \boldsymbol{x}^B \end{Bmatrix} = \begin{Bmatrix} \boldsymbol{f}^C \\ \boldsymbol{f}^B \end{Bmatrix} + \begin{Bmatrix} \boldsymbol{g}^C \\ \boldsymbol{g}^B \end{Bmatrix} \tag{54}$$

Where, as previously, $\boldsymbol{f}$ corresponds to the external forces, $\boldsymbol{g}$ corresponds to the forces at the interfaces, $\boldsymbol{Z}$ is the dynamic stiffness, $\boldsymbol{x}$ is displacement, and the superscripts denote the corresponding structure.

This formulation implies that the interface between the fictitious substructure and the coupled system includes all of the internal DOFs of the residual substructure in addition to the coupling DOFs between the original substructures, A and B. However, it is not necessary to consider all of these DOFs to carry out the process. It is possible to decouple the system by considering only the coupling DOFs. Thus, the number of DOFs used when adding the fictitious substructure just has to be greater than or equal to the number of coupling DOFs between A and B. According to [29], there exist 3 options for these interface DOFs:

1) The “standard interface” which includes only the coupling DOFs between A and B
2) The “extended interface” which is the standard interface with the addition of a subset of internal DOFs from the residual subsystem

3) The “mixed interface” which includes a subset of the original coupling DOFs and a subset of the internal DOFs from the residual substructure

Each interface has advantages and disadvantages depending upon the situation in which they are applied. For instance, as discussed later in the section on rotational DOFs, the mixed interface can be used to avoid including any rotational DOFs for which data is not available.

Regardless of which interface is used, the compatibility condition implies that any pair of matching DOFs between the coupled system and the residual substructure must have the same displacement. In other words, if we have matching DOFs x_k^C and x_l^B, where x_k^C is DOF number “k” on the coupled system and x_l^B is DOF “l” on the residual substructure, then:

$$x_k^C - x_l^B = 0$$

We can express the compatibility condition more generally as:

$$[\boldsymbol{B}_C^C \quad \boldsymbol{B}_C^B] \begin{Bmatrix} \boldsymbol{x}^C \\ \boldsymbol{x}^B \end{Bmatrix} = \mathbf{0} \tag{55}$$

Where $\boldsymbol{B_C}$ is a signed Boolean matrix (with the subscript “C” referring to the compatibility condition) partitioned into portions corresponding to the coupled system, C, and the residual substructure, B. Each row of $\boldsymbol{B_C}$ corresponds to a pair of matching DOFs.

The equilibrium condition implies that the connecting forces at any pair of matching DOFs must sum to zero. Thus, if g_k^C and g_l^B are interface forces at DOF “k” on C and DOF “l” on B, then:

$$g_k^C + g_l^B = 0$$

Additionally, the interface force for any DOF which does not belong to the equilibrium interface must be equal to zero. In other words, if "m" is an arbitrary DOF on either C or B and is not part of the equilibrium interface, then:

$$g_m^C = 0 \qquad or \qquad g_m^B = 0$$

The equilibrium conditions can be more generally expressed as:

$$\begin{bmatrix} \boldsymbol{L}_E^C \\ \boldsymbol{L}_E^B \end{bmatrix}^T \begin{Bmatrix} \boldsymbol{g}^C \\ \boldsymbol{g}^B \end{Bmatrix} = \boldsymbol{0} \tag{56}$$

Where the matrix $\boldsymbol{L}_E = [\boldsymbol{L}_E^C \quad \boldsymbol{L}_E^B]$ is a Boolean localization matrix which is partitioned into portions corresponding to the coupled system, C, and the residual substructure, B. The subscript "E" specifies that the Boolean matrix is for the equilibrium condition.

Equations (54)-(56) together make up the previously mentioned 3-field formulation. With the 3-field formulation to use as a starting point, the following subsections present the primal and dual formulations for direct decoupling.

2.1.3.7.2.1 Direct Decoupling – Primal Formulation

The primal formulation is defined for direct decoupling in the same way as for coupling in the physical domain (see Equation (6)). Though the two presentations are mathematically equivalent, the primal formulation is defined again in this section to show it in partitioned form.

The primal formulation is based off of the definition of a unique set of DOFs:

$$\begin{Bmatrix} \boldsymbol{x}^C \\ \boldsymbol{x}^B \end{Bmatrix} = \begin{bmatrix} \boldsymbol{L}_C^C \\ \boldsymbol{L}_C^B \end{bmatrix} \{\boldsymbol{q}\} \tag{57}$$

Where $\boldsymbol{q}$ is the unique set of DOFs and $\boldsymbol{L}_C$ is a localization matrix (similar to $\boldsymbol{L}_E$) with the subscript "C" denoting that this matrix will be used in the compatibility condition.

The compatibility is satisfied for any $\boldsymbol{q}$ since, by definition, $\boldsymbol{q}$ is a unique set of DOFs. This concept can be shown mathematically as:

$$[\boldsymbol{B}_C^C \quad \boldsymbol{B}_C^B] \begin{Bmatrix} \boldsymbol{x}^C \\ \boldsymbol{x}^B \end{Bmatrix} = [\boldsymbol{B}_C^C \quad \boldsymbol{B}_C^B] \begin{bmatrix} \boldsymbol{L}_C^C \\ \boldsymbol{L}_C^B \end{bmatrix} \{\boldsymbol{q}\} = \boldsymbol{0} \qquad \forall \boldsymbol{q} \tag{58}$$

Which implies:

$$[\boldsymbol{B}_C^C \quad \boldsymbol{B}_C^B] \begin{bmatrix} \boldsymbol{L}_C^C \\ \boldsymbol{L}_C^B \end{bmatrix} = \boldsymbol{0} \qquad or \qquad \begin{bmatrix} \boldsymbol{L}_C^C \\ \boldsymbol{L}_C^B \end{bmatrix}^T [\boldsymbol{B}_C^C \quad \boldsymbol{B}_C^B]^T = \boldsymbol{0} \tag{59}$$

Equation (59) shows that $\boldsymbol{L}_C$ is the null space of $\boldsymbol{B}_C$ and, equivalently, $\boldsymbol{B}_C{}^T$ is the null space of $\boldsymbol{L}_C{}^T$

.

With the compatibility condition (Equation (55)) satisfied, the 3-field formulation reduces to:

$$\begin{cases} \begin{bmatrix} \boldsymbol{Z}^C & \boldsymbol{0} \\ \boldsymbol{0} & -\boldsymbol{Z}^B \end{bmatrix} \begin{bmatrix} \boldsymbol{L}_C^C \\ \boldsymbol{L}_C^B \end{bmatrix} \{\boldsymbol{q}\} = \begin{Bmatrix} \boldsymbol{f}^C \\ \boldsymbol{f}^B \end{Bmatrix} + \begin{Bmatrix} \boldsymbol{g}^C \\ \boldsymbol{g}^B \end{Bmatrix} \\ \begin{bmatrix} \boldsymbol{L}_E^C \\ \boldsymbol{L}_E^B \end{bmatrix}^T \begin{Bmatrix} \boldsymbol{g}^C \\ \boldsymbol{g}^B \end{Bmatrix} = \boldsymbol{0} \end{cases} \tag{60}$$

(56)

Following the derivation of [29], we pre-multiply Equation (60) by $\boldsymbol{L}_E{}^T$ and use Equation (56) to reduce the formulation to:

$$\begin{bmatrix} \boldsymbol{L}_E^C \\ \boldsymbol{L}_E^B \end{bmatrix}^T \begin{bmatrix} \boldsymbol{Z}^C & \boldsymbol{0} \\ \boldsymbol{0} & -\boldsymbol{Z}^B \end{bmatrix} \begin{bmatrix} \boldsymbol{L}_C^C \\ \boldsymbol{L}_C^B \end{bmatrix} \{\boldsymbol{q}\} = \begin{bmatrix} \boldsymbol{L}_E^C \\ \boldsymbol{L}_E^B \end{bmatrix}^T \begin{Bmatrix} \boldsymbol{f}^C \\ \boldsymbol{f}^B \end{Bmatrix} \tag{61}$$

Which rearranges to yield:

$$\{\boldsymbol{q}\} = \left(\begin{bmatrix} \boldsymbol{L}_E^C \\ \boldsymbol{L}_E^B \end{bmatrix}^T \begin{bmatrix} \boldsymbol{Z}^C & \boldsymbol{0} \\ \boldsymbol{0} & -\boldsymbol{Z}^B \end{bmatrix} \begin{bmatrix} \boldsymbol{L}_C^C \\ \boldsymbol{L}_C^B \end{bmatrix} \right)^+ \begin{bmatrix} \boldsymbol{L}_E^C \\ \boldsymbol{L}_E^B \end{bmatrix}^T \begin{Bmatrix} \boldsymbol{f}^C \\ \boldsymbol{f}^B \end{Bmatrix} \tag{62}$$

Where the superscript "+" refers to what is called the "generalized inverse," or the "pseudoinverse." The pseudoinverse is an "inverse-like" operation that, unlike a standard inversion, can be used for an over determined matrix. In this case, a Moore-Penrose pseudoinverse will be used.

According to [29], in order to obtain a determined or over-determined matrix for the primal formulation, we must have:

$$N_C \geq N_E > n_c \tag{63}$$

Where N_C is the number of compatibility interface DOFs, N_E is the number of equilibrium interface DOFs, and n_c is the number of DOFs coupled between substructures A and B. If $N_C > N_E$, then Equation (61) is satisfied by $\boldsymbol{q}$ only in a minimum square sense (i.e. is not satisfied exactly). However, due to the nature of the primal formulation, the compatibility conditions is satisfied exactly by $\boldsymbol{q}$.

Finally, the FRF for the unknown substructure, A, can be found from Equation (62) as:

$$\boldsymbol{Y}^A = \left(\begin{bmatrix} \boldsymbol{L}_E^C \\ \boldsymbol{L}_E^B \end{bmatrix}^T \begin{bmatrix} \boldsymbol{Z}^C & \boldsymbol{0} \\ \boldsymbol{0} & -\boldsymbol{Z}^B \end{bmatrix} \begin{bmatrix} \boldsymbol{L}_C^C \\ \boldsymbol{L}_C^B \end{bmatrix} \right)^+ \begin{bmatrix} \boldsymbol{L}_E^C \\ \boldsymbol{L}_E^B \end{bmatrix}^T \tag{64}$$

$$\boldsymbol{Y}^A = ([\boldsymbol{L}_E^C]^T \boldsymbol{Z}^C \boldsymbol{L}_C^C - [\boldsymbol{L}_E^B]^T \boldsymbol{Z}^B \boldsymbol{L}_C^B)^+ [[\boldsymbol{L}_E^C]^T \quad [\boldsymbol{L}_E^B]^T] \tag{65}$$

Equation (64) and (65) conclude our derivation of the primal formulation for direct decoupling. Additionally, if the extended interface is used, $\boldsymbol{Y}^A$ will contain some rows and columns which correspond to the internal DOFs of the residual substructure, B. These entries from the residual

substructure are meaningless and should thus be discarded along with the duplicate entries for the interface DOFs during subsequent analysis. There are other derivations for decoupling via the primal formulations, such as that described in [34]. However, the differences for most of these formulations are minor and so they will not be presented independently here.

2.1.3.7.2.2 Direct Decoupling – Dual Formulation

In contrast to the primal formulation, the total set of DOFs is retained in the dual formulation. Thus, each interface DOFs is present in the formulation as many times as there are substructures connected at that interface point. The dual formulation also differs from the primal formulation in that the equilibrium condition is strictly enforced as opposed to the compatibility condition in the primal formulation. In other words, if we continue with the same notation as in the previous section:

$$g_k^C + g_l^B = 0$$

Which can be satisfied by the choice:

$$g_k^C = -\lambda \qquad and \qquad g_l^B = \lambda$$

Where k and l are arbitrary, coupled DOFs on the coupled system and residual substructure respectively. This enforcement of the equilibrium condition can be written more generally for the entire system as:

$$\begin{Bmatrix} \boldsymbol{g}^C \\ \boldsymbol{g}^B \end{Bmatrix} = -\begin{bmatrix} [\boldsymbol{B}_E^C]^T \\ [\boldsymbol{B}_E^B]^T \end{bmatrix} \{\boldsymbol{\lambda}\} \tag{66}$$

Where $\boldsymbol{\lambda}$ is a vector of Lagrange multipliers corresponding the interface force intensity and $\boldsymbol{B}_E$ is a signed Boolean matrix which satisfies Equation (66) by construction. With this formulation, the equilibrium condition of Equation (56) can be rewritten as:

$$\begin{bmatrix} \boldsymbol{L}_E^C \\ \boldsymbol{L}_E^B \end{bmatrix}^T \begin{Bmatrix} \boldsymbol{g}^C \\ \boldsymbol{g}^B \end{Bmatrix} = -\begin{bmatrix} \boldsymbol{L}_E^C \\ \boldsymbol{L}_E^B \end{bmatrix}^T \begin{bmatrix} [\boldsymbol{B}_E^C]^T \\ [\boldsymbol{B}_E^B]^T \end{bmatrix} \{\boldsymbol{\lambda}\} = \boldsymbol{0} \tag{67}$$

Similar to the primal formulation, $\boldsymbol{B}_E{}^T$ is the nullspace of $\boldsymbol{L}_E{}^T$, and $\boldsymbol{L}_E$ is the nullspace of $\boldsymbol{B}_E$. With the equilibrium condition (Equation (56)) satisfied, the 3-field formulation reduces to:

$$\begin{cases} \begin{bmatrix} \boldsymbol{Z}^C & \boldsymbol{0} \\ \boldsymbol{0} & -\boldsymbol{Z}^B \end{bmatrix} \begin{Bmatrix} \boldsymbol{x}^C \\ \boldsymbol{x}^B \end{Bmatrix} + \begin{bmatrix} [\boldsymbol{B}_E^C]^T \\ [\boldsymbol{B}_E^B]^T \end{bmatrix} \{\boldsymbol{\lambda}\} = \begin{Bmatrix} \boldsymbol{f}^C \\ \boldsymbol{f}^B \end{Bmatrix} \\ [\boldsymbol{B}_C^C \quad \boldsymbol{B}_C^B] \begin{Bmatrix} \boldsymbol{x}^C \\ \boldsymbol{x}^B \end{Bmatrix} = \boldsymbol{0} \end{cases} \tag{68}$$

(55)

An expression for $\boldsymbol{\lambda}$ can be found by solving Equation (68) for the displacements, $\boldsymbol{x}$, and substituting into Equation (55) [28]. The resulting expression is:

$$\{\boldsymbol{\lambda}\} = \left([\boldsymbol{B}_C^C \quad \boldsymbol{B}_C^B] \begin{bmatrix} \boldsymbol{Z}^C & \boldsymbol{0} \\ \boldsymbol{0} & -\boldsymbol{Z}^B \end{bmatrix}^{-1} \begin{bmatrix} [\boldsymbol{B}_E^C]^T \\ [\boldsymbol{B}_E^B]^T \end{bmatrix} \right)^+ [\boldsymbol{B}_C^C \quad \boldsymbol{B}_C^B] \begin{bmatrix} \boldsymbol{Z}^C & \boldsymbol{0} \\ \boldsymbol{0} & -\boldsymbol{Z}^B \end{bmatrix}^{-1} \begin{Bmatrix} \boldsymbol{f}^C \\ \boldsymbol{f}^B \end{Bmatrix} \tag{69}$$

Where again, the "+" superscript denotes the generalized or pseudo inverse.

As with the primal formulation, Equation (63) must be satisfied to obtain a determined or over-determined matrix to carry out the generalized inverse. For the dual formulation if $N_C > N_E$, then the compatibility conditions (Equation (55)) are only satisfied approximately. However, the equilibrium conditions are satisfied exactly by the construction of the dual formulation.

By substituting the expression for $\boldsymbol{\lambda}$ (Equation (69)) into Equation (68), we can obtain an expression for $\boldsymbol{x}$ in the form:

$$\begin{Bmatrix}\boldsymbol{x}^C\\ \boldsymbol{x}^B\end{Bmatrix} = \begin{bmatrix}\boldsymbol{Z}^C & \boldsymbol{0}\\ \boldsymbol{0} & -\boldsymbol{Z}^B\end{bmatrix}^{-1} - \begin{bmatrix}\boldsymbol{Z}^C & \boldsymbol{0}\\ \boldsymbol{0} & -\boldsymbol{Z}^B\end{bmatrix}^{-1}\begin{bmatrix}[\boldsymbol{B}_E^C]^T\\ [\boldsymbol{B}_E^B]^T\end{bmatrix}\times \\ \times\left([\boldsymbol{B}_C^C \quad \boldsymbol{B}_C^B]\begin{bmatrix}\boldsymbol{Z}^C & \boldsymbol{0}\\ \boldsymbol{0} & -\boldsymbol{Z}^B\end{bmatrix}^{-1}\begin{bmatrix}[\boldsymbol{B}_E^C]^T\\ [\boldsymbol{B}_E^B]^T\end{bmatrix}\right)^{+}[\boldsymbol{B}_C^C \quad \boldsymbol{B}_C^B]\begin{bmatrix}\boldsymbol{Z}^C & \boldsymbol{0}\\ \boldsymbol{0} & -\boldsymbol{Z}^B\end{bmatrix}^{-1}\begin{Bmatrix}\boldsymbol{f}^C\\ \boldsymbol{f}^B\end{Bmatrix} \tag{70}$$

Where the "×" symbols are used to denote matrix multiplication where one entire expression will not fit on a single line. If we recall that the receptance, $\boldsymbol{Y}$, is the inverse of the dynamic stiffness and assume that Equation (70) is of the form:

$$\boldsymbol{x} = \boldsymbol{Y}\boldsymbol{f}$$

then Equation (70) provides the receptance FRF matrix for the unknown substructure, A:

$$\boldsymbol{Y}^A = \begin{bmatrix}\boldsymbol{Y}^C & \boldsymbol{0}\\ \boldsymbol{0} & -\boldsymbol{Y}^B\end{bmatrix} - \begin{bmatrix}\boldsymbol{Y}^C & \boldsymbol{0}\\ \boldsymbol{0} & -\boldsymbol{Y}^B\end{bmatrix}\begin{bmatrix}[\boldsymbol{B}_E^C]^T\\ [\boldsymbol{B}_E^B]^T\end{bmatrix}\times \\ \times\left([\boldsymbol{B}_C^C \quad \boldsymbol{B}_C^B]\begin{bmatrix}\boldsymbol{Y}^C & \boldsymbol{0}\\ \boldsymbol{0} & -\boldsymbol{Y}^B\end{bmatrix}\begin{bmatrix}[\boldsymbol{B}_E^C]^T\\ [\boldsymbol{B}_E^B]^T\end{bmatrix}\right)^{+}[\boldsymbol{B}_C^C \quad \boldsymbol{B}_C^B]\begin{bmatrix}\boldsymbol{Y}^C & \boldsymbol{0}\\ \boldsymbol{0} & -\boldsymbol{Y}^B\end{bmatrix} \tag{71}$$

Note that Equation (71), the dual formulation for direct decoupling, all rows and columns in $\boldsymbol{Y}^{\mathrm{A}}$ which correspond to the interface DOFs appear twice (once for the coupled system and once for the residual substructure). As with the primal formulation, if the extended interface is used, $\boldsymbol{Y}^{\mathrm{A}}$ will contain some rows and columns which correspond to the internal DOFs of the residual substructure, B. Again, these entries are meaningless and should thus be discarded along with the duplicate entries for the interface DOFs during subsequent analysis.

This concludes our derivation of the dual formulation for direct decoupling. An alternative approach to the derivation of the dual formulation was presented by Voormeeren et al [34]. Since the end result of the two approaches is the same, the alternative derivation will not be presented here, but can be found in [34] ('a dual approach"). This method for decoupling via the dual formulation is mathematically equivalent to the LM FBS method for dynamic substructure proposed by [23] (Equation (70) compared to (71)). However, the derivation in the context of decoupling will be useful as we continue our discussion into improvements for decoupling methods using experimental data.

2.1.3.7.2.3 Comparison of direct decoupling through primal and dual formulations

We conclude our discussion of primal and dual formulations for direct decoupling with a comparison of the methods. The receptance of the unknown substructure can be rewritten from Equation 46 in condensed form as:

$$\boldsymbol{Y}_P^A = (\boldsymbol{L}_E^T\, \boldsymbol{Z}\, \boldsymbol{L}_C)^+ \boldsymbol{L}_E^T \tag{72}$$

Where the subscript "P" specifies that the receptance is according to the primal formulation. If N_C=N_E (number of compatibility and equilibrium interface points are equal), then a standard inversion can be used in place of the pseudoinverse, and Equation (72) can be rearranged to yield:

$$(\boldsymbol{L}_E^T\, \boldsymbol{Z}\, \boldsymbol{L}_C)\boldsymbol{Y}_P^A = \boldsymbol{L}_E^T \tag{73}$$

Similarly, the dual formulation of Equation (71) can be displayed in condensed form as:

$$\boldsymbol{Y}_D^A = \boldsymbol{Y} - \boldsymbol{Y}\, \boldsymbol{B}_E^T(\boldsymbol{B}_C \boldsymbol{Y}\, \boldsymbol{B}_E^T)^{-1} \boldsymbol{B}_C\, \boldsymbol{Y} \tag{74}$$

Where the subscript "D" specifies accordance to the dual formulation. The pseudoinverse has been replaced again by the standard inverse which implies that we are assuming $N_C=N_E$. Pre-multiplication of Equation (74) by $\boldsymbol{Z}$ and $\boldsymbol{L}_E^T$ (in order) yields:

$$\boldsymbol{L}_E^T\,\boldsymbol{Z}\,\boldsymbol{Y}_D^A = \boldsymbol{L}_E^T - \boldsymbol{L}_E^T\,\boldsymbol{B}_E^T(\boldsymbol{B}_C\boldsymbol{Y}\,\boldsymbol{B}_E^T)^{-1}\boldsymbol{B}_C\,\boldsymbol{Y} \tag{75}$$

Recall from the previous section that $\boldsymbol{B}_E^T$ is the nullspace of $\boldsymbol{L}_E^T$:

$$\boldsymbol{L}_E^T\boldsymbol{B}_E^T = \boldsymbol{0}$$

Thus Equation (75) is simplified to:

$$\boldsymbol{L}_E^T\,\boldsymbol{Z}\,\boldsymbol{Y}_D^A = \boldsymbol{L}_E^T \tag{76}$$

A comparison of Equation (73) and (76) shows that:

$$\boldsymbol{Y}_D^A = \boldsymbol{L}_C\boldsymbol{Y}_P^A \tag{77}$$

Equation (77) shows that if $N_C=N_E$, then the primal and dual formulations are equivalent. However, due to the definition of the pseudoinverse (shown in the primal formulation section), Equation (76) cannot be obtained for an overdetermined system. Thus, if $N_C>N_E$, the primal and dual formulations will produce different results [29].

2.1.3.7.3 Decoupling via the Hybrid Formulation

More recently, another method for decoupling has been developed which can be thought of as a combination of the primal and dual formulations [35]. This combined method has been termed the "direct hybrid assembly" or the "hybrid formulation for decoupling." Like the primal and dual formulations, the hybrid formulation is a method of direct decoupling, where a fictitious

substructure is added to the coupled system to cancel out the dynamic effects of the residual substructure.

As mentioned previously, if the extended interface is used with primal or dual formulations, the equilibrium or compatibility conditions, respectively, may only be satisfied in a least square sense. In contrast, the hybrid formulation satisfies both the compatibility and equilibrium conditions exactly, regardless of interface choice. The direct hybrid assembly begins the same as the primal formulation for direct decoupling:

$$\begin{Bmatrix} \boldsymbol{x}^C \\ \boldsymbol{x}^B \end{Bmatrix} = \begin{bmatrix} \boldsymbol{L}_C^C \\ \boldsymbol{L}_C^B \end{bmatrix} \{\boldsymbol{q}\} \tag{57}$$

$$[\boldsymbol{B}_C^C \quad \boldsymbol{B}_C^B] \begin{Bmatrix} \boldsymbol{x}^C \\ \boldsymbol{x}^B \end{Bmatrix} = [\boldsymbol{B}_C^C \quad \boldsymbol{B}_C^B] \begin{bmatrix} \boldsymbol{L}_C^C \\ \boldsymbol{L}_C^B \end{bmatrix} \{\boldsymbol{q}\} = \boldsymbol{0} \qquad \forall \boldsymbol{q} \tag{58}$$

Recall that $\boldsymbol{q}$ is a unique set of DOFs, $\boldsymbol{L}_C$ is a Boolean localization matrix, and $\boldsymbol{B}_C$ is a signed Boolean matrix defining the coupled DOFs. By definition, this choice guarantees the compatibility condition is satisfied exactly. It is then possible to also satisfy the equilibrium exactly by proceeding in the fashion of the dual formulation. The connecting forces are written as:

$$\begin{bmatrix} \boldsymbol{L}_C^C \\ \boldsymbol{L}_C^B \end{bmatrix} \{\boldsymbol{q}\} + \begin{bmatrix} \boldsymbol{Y}^C & \boldsymbol{0} \\ \boldsymbol{0} & -\boldsymbol{Y}^B \end{bmatrix} \begin{bmatrix} [\boldsymbol{B}_E^C]^T \\ [\boldsymbol{B}_E^B]^T \end{bmatrix} \{\boldsymbol{\lambda}\} = \begin{bmatrix} \boldsymbol{Y}^C & \boldsymbol{0} \\ \boldsymbol{0} & -\boldsymbol{Y}^B \end{bmatrix} \begin{Bmatrix} \boldsymbol{f}^C \\ \boldsymbol{f}^B \end{Bmatrix} \tag{78}$$

Which can be shown in condensed form as:

$$\boldsymbol{L}_C \boldsymbol{q} + \boldsymbol{Y} \boldsymbol{B}_E^T \{\boldsymbol{\lambda}\} = \boldsymbol{Y} \boldsymbol{f} \tag{79}$$

If $\boldsymbol{q}$ and $\boldsymbol{\lambda}$ are gathered into a single vector, the generalized inverse can be used to arrive at:

$$\begin{Bmatrix} \boldsymbol{q} \\ \boldsymbol{\lambda} \end{Bmatrix} = [\boldsymbol{L}_C \quad \boldsymbol{Y}\boldsymbol{B}_E^T]^+ \boldsymbol{Y}\boldsymbol{f} \tag{80}$$

Note that for the generalized inverse operation, the matrix must be determined or overdetermined which requires $N_C \geq N_E \geq n_C$ (where N_C is number of interface DOFs where compatibility is enforced, N_E is the same for equilibrium respectively, and n_C is the actual number of coupling DOFs). If $N_C > N_E$, Equation 60 is only satisfied in a minimum square sense, while compatibility and equilibrium are satisfied exactly.

Equation (80) can be rewritten in a more physically intuitive form as:

$$\begin{Bmatrix} \boldsymbol{q} \\ \boldsymbol{\lambda} \end{Bmatrix} = \begin{bmatrix} \boldsymbol{Y}^A \\ \boldsymbol{T} \end{bmatrix} \boldsymbol{f} \tag{81}$$

Where $\boldsymbol{Y}^A$ is the FRF matrix of the unknown subsystem and $\boldsymbol{T}$ is the transmissibility between the external forces and the connecting force intensities, $\boldsymbol{\lambda}$.

In this hybrid formulation, columns of $\boldsymbol{Y}^A$ corresponding to equilibrium interface DOFs appear twice. Also, $\boldsymbol{Y}^A$ contains rows and columns corresponding to the residual substructure when an extended interface is used. These rows and columns are meaningless in the context of the FRF of the unknown substructure and so should be discarded during analysis along with redundant entries.

In [35], D'Ambrogio et al go on to show that hybrid and dual formulations are mathematically equivalent if $N_C = N_E$. However, if $N_C \neq N_E$ the two formulations provide different results. Based on a simple case study performed in [35], in cases where the two formulations gave different results, there was no clear indication of one method producing better results than the other.

2.1.3.8 Experimental Difficulties and Improved Techniques

In recent years, much research has been conducted on experimental coupling and decoupling. More specifically, researchers have worked to discover issues that arise during the coupling/decoupling process and develop methods to correct for these issues. A few of the main issues that will be addressed in the following sections are: ill conditioning of matrices, spurious peaks in the coupled/decoupled FRFs, inclusion of rotational DOFs, and uncertainty propagation from measured to calculated FRFs. The methods presented in the following subsections were chosen to demonstrate the variety techniques used to address the previously mentioned difficulties.

2.1.3.8.1 Improved Techniques for Coupling Using Experimentally measured FRFs

Although the concepts of substructure coupling used in the FBS method by Jetmundsen et al [16] were direct and well established, the benefit of the process was overshadowed by practical problems during experimental implementation. Around the same time the FBS method was developed by Jetmundsen et al, techniques to improve FBS-like coupling methods were being investigated by Leuridan [36]. These techniques fell generally into two categories: preprocessing of measured FRFs and use of the pseudo inverse in place of the direct inverse.

2.1.3.8.2 Preprocessing of Measured FRFs

It is well known in the field of dynamic substructuring that the matrix to be inverted tends to be ill conditioned in the neighborhood of the resonant frequencies. Additionally, the matrix being inverted (Equation (45)) should be symmetric for structures that satisfy reciprocity. Leuridan proposes that these two issues can be remedied through FRF smoothing and symmetrization respectively.

Though both smoothing and symmetrization showed improvement over the base coupling method, Leuridan found that the improvement due to smoothing was much less significant than that due to symmetrization. Since Leuridan's technique for smoothing did not offer a significant improvement, it will not be discussed in the present work.

The method of symmetrization proposed by Leuridan is based on principal component analysis of each pair of reciprocal FRFs. In this method, the principal component is normalized to give a symmetrized approximation for the pair of FRFs.

$$\widehat{\boldsymbol{y}}_{ij}(\boldsymbol{\omega}_k) = \widehat{\boldsymbol{y}}_{ij}(\boldsymbol{\omega}_k) = \frac{1}{\sqrt{2}}\boldsymbol{y}'_{ij}(\boldsymbol{\omega}_k) \tag{82}$$

Where $\widehat{\boldsymbol{y}}_{ij}$ is an approximation of the FRF between DOFs i and j for an arbitrary substructure and $\boldsymbol{y}'_{ij}$ is the corresponding principal component. This transformation symmetrization is derived using a unitary transformation matrix in the process of principal component analysis and is discussed in more detail in [36].

2.1.3.8.2.1 Use of the Pseudo Inverse

As mentioned previously, the matrix to be inverted in the coupling process is often ill conditioned in the neighborhood of resonant frequencies. Thus, the matrix often ends up being singular or "close to singular," where "close to singular" is a relative term measured by the condition number of the matrix. In such circumstances, the pseudo inverse (or "generalized inverse") can be used in place of the direct inverse.

There are many forms of pseudo inverses so the operation may be derived and used differently in the different sections of this chapter. In each case that a different pseudo inverse is used, it will be

fully described in the corresponding section. In Leuridan's work, the pseudo inverse is defined as follows. Suppose we have the system:

$$\boldsymbol{y} = \boldsymbol{W}\boldsymbol{z} \tag{83}$$

Where $\boldsymbol{z}$ is the vector solution of an equation with $\boldsymbol{W}$ as a coefficient matrix. If $\boldsymbol{W}$ is singular or close to singular, we can calculate the solution as:

$$\boldsymbol{z} = \boldsymbol{W}^{+}\boldsymbol{y} \tag{84}$$

Where the "+" superscript denotes the pseudo inverse. This form of the pseudo inverse is derived from [37]:

$$\begin{aligned} \boldsymbol{W} &= [\boldsymbol{U}][\boldsymbol{\Delta}][\boldsymbol{V}]^{\boldsymbol{h}} \\ \boldsymbol{W}^{+} &= [\boldsymbol{V}]_{\boldsymbol{r}}[\boldsymbol{\Delta}]_{\boldsymbol{r}}[\boldsymbol{U}]_{\boldsymbol{r}}^{\boldsymbol{h}} \end{aligned} \tag{85}$$

The subscript "r" refers to the matrix $\boldsymbol{\Delta}$ reduced to important singular values of $\boldsymbol{W}$, and the corresponding left and right singular vectors in $\boldsymbol{U}$ and $\boldsymbol{V}$. "Importance" is measured by comparing the singular values to the largest singular value. It is also worth noting that the superscript "h" denotes the conjugate transpose of the matrix and brackets have been included on these matrices solely in the interest of clarity.

When calculated using this pseudo inverse, $\boldsymbol{z}$ is also a solution that satisfies:

$$\boldsymbol{y} = \boldsymbol{W}\boldsymbol{z}, \;\; \|\boldsymbol{z}\| = minimum \tag{86}$$

Or, in other words, $\boldsymbol{z}$ is the minimum norm least squares solution.

In summary, if the above pseudo inverse is used in the coupling equation, we are actually calculating the solution to the coupling problem that is realized with minimum effort. Leuridan found that the use of this pseudo inverse significantly improved that accuracy of the calculated FRF of the couple systems, especially in the areas of the resonant frequencies.

2.1.3.8.3 Reduction of FRF Order by means of SVD

As discussed previously, experimentally measured FRFs can tend to be ill conditioned in the neighborhoods of resonant frequencies due to the influence of noise. Ill conditioned matrices do not work well in the coupling process and produce noisy and sometimes incorrect coupled FRFs. The pseudo inverse technique described in the previous subsection can be considered a data reduction technique in the spatial domain and has been shown to be valid for handling inversion of ill conditioned matrices.

The work done by Otte et al [38] presents an extension of the work done by Leuridan on the singular value decomposition (SVD) based pseudo inverse. This extension is a more general strategy for data reduction in the spatial domain with a strong emphasis on physical significance in terms of the compatibility and equilibrium constraints.

Recall the matrix to be inverted in the FBS method from Equation (45):

$$(\boldsymbol{Y}_{cc}^{A} + \boldsymbol{Y}_{cc}^{B})^{-1} = \boldsymbol{G}^{-1}$$

Where the combination of the two FRF matrices has been denoted as $\boldsymbol{G}$ to simplify the following derivation. The objective of using a SVD is to force the smallest singular values of $\boldsymbol{G}$ to zero. Forcing the smallest singular values to zero is equivalent to imposing physical constraints on the coupling DOFs on both substructures, A and B.

Conceptually, the j-th column of an FRF matrix can be thought of as a deflection vector due to a unit force input on the j-th reference DOF. With that concept in mind, each column of $\boldsymbol{G}$ can be considered to be the vector sum of the deflections at the coupling DOFs on substructures A and B. The SVD of FRF $\boldsymbol{G}$ can then be written as:

$$\boldsymbol{G} = [\boldsymbol{U}][\boldsymbol{\Delta}][\boldsymbol{V}]^{\boldsymbol{h}} \tag{87}$$

Where, as in the previous subsection, Δ is a matrix of singular values of $\boldsymbol{G}$, while $\boldsymbol{U}$ and $\boldsymbol{V}$ are the corresponding left and right singular vectors and are both unitary matrices. Again, brackets have been included on these matrices solely in the interest of clarity. We define a new matrix:

$$\boldsymbol{G'} = [\boldsymbol{G}][\boldsymbol{V}] = [\boldsymbol{U}][\boldsymbol{\Delta}] \tag{88}$$

From which Equation (87) can be rewritten as:

$$\boldsymbol{G} = [\boldsymbol{G'}][\boldsymbol{V}]^{\boldsymbol{h}} \tag{89}$$

Alternatively, $\boldsymbol{Y}_{cc}^{A}$ and $\boldsymbol{Y}_{cc}^{A}$ can be reduced separately, though the method results in a more severe data reduction than the procedure described in Equations (87)-(89). Further work done by Otte et al [38] makes use of the pseudo inverse and symmetrization techniques by Leuridan [36]. Overall, the method by Otte et al was shown to provide fair approximations of large FRF matrices with high modal density.

2.1.3.8.4 A filter to remove coupling anomalies

Perhaps the biggest challenge in carrying out FBS coupling or decoupling is extreme sensitivity to noise. As such, there have been many methods developed to reduce this sensitivity. Imregun et al [39] addressed this sensitivity by first performing modal analysis on the data and then synthesizing FRFs from the modal model. Leuridan [36] and Otte et al [38], used data reduction and

symmetrization techniques. In a further effort to reduce the sensitivity of the admittance method to noise, Carne et al [40] developed a conditioning filter to "clean up" the FRF matrices while minimally affecting them.

The motivation for the development of this conditioning filter came from the observation that the imaginary part of the driving point FRF was negative for some frequency range. These negative values for the imaginary part of the FRF imply that the system either has negative damping or that the FRF does not fit the prescribed analytical models [40]. A full derivation of the filter can be found in [40], while only the final formulation is presented here.

We can express a FRF matrix as a combination of real and imaginary parts:

$$\boldsymbol{Y} = \boldsymbol{Y}_r + j\boldsymbol{Y}_i \tag{90}$$

Where Y_r and Y_i are the real and imaginary components of Y, respectively, and the frequency dependence has been omitted from the equation. Additionally, Y_r and Y_i are both real and symmetric matrices. We can then view Y_i in the following form using the standard eigenvalue decomposition for symmetric matrices:

$$\boldsymbol{Y}_i = \sum_{m=1}^{p} \lambda_m \psi_m \psi_m^T \tag{91}$$

Where $\lambda_1,\ldots, \lambda_p$ are eigenvalues and $\psi_1,\ldots, \psi_p$ are the corresponding orthonormal eigenvectors of Y_i. Again, the frequency dependence of Y_I, λ, and ψ has been omitted for convenience. None of the eigenvalues can be negative if Y_i is to be at least positive semi-definite. Thus, a filter is defined as follows in order to force all eigenvalues to be non-negative:

$$\tilde{\lambda}_m = \begin{cases} \lambda_m & if \quad \lambda_m \geq 0 \\ 0 & if \quad \lambda_m < 0 \end{cases} \tag{92}$$

Equation (90) can now be rewritten to include the filtered eigenvalue decomposition for H_i:

$$\widetilde{\boldsymbol{Y}} = \boldsymbol{Y}_r + j \sum_{m=1}^{p} \tilde{\lambda}_m \psi_m \psi_m^T \tag{93}$$

This filtered version of the FRF matrix now has all eigenvalues corresponding to the imaginary part as greater than or equal to zero (in other words, imag($\widetilde{\boldsymbol{Y}}$) is positive semi-definite). Essentially, the application of this filter performs an eigenvalue decomposition and then re-synthesizes the matrix after deleting all contributions due to negative eigenvalues. Carne named this filter the "DeComposition Data" filter, or the DCD filter. Carne then proceeds to give an example of the experimental application of the filter which can be found in [40]. In summary, the filter appeared to remove the anomalies present in the decoupled FRF that were due to the negative eigenvalues.

2.1.3.8.5 Negative Mass after Decoupling

Decoupled FRFs can sometimes exhibit physically unrealizable phenomena due to errors in the measured FRFs. For example, the imaginary part of the driving point FRF must always be positive as found in [40], or else spurious peaks can appear in the decoupled FRF. Similarly, in the modal domain it is possible to obtain a system representation which does not have a positive definite mass matrix after decoupling. This problem in the modal domain most often occurs when subtracting one flexible structure from another [41] [42] [43].

Since coupling or decoupling procedures are often used in a hybrid format with measured data and FEA data, and since most FEA packages only allow for positive definite mass matrices, the negative mass error can cripple the process. Additionally, as with the work by Carne et al, Allen

et al found that the negative entries of the mass matrix in the modal domain can cause spurious peaks in the decoupled FRFs.

In [44], Allen et al developed an analytical method in the modal domain to determine which modes are contributing to each negative eigenvalue of the decoupled system. This method was based on the modal decoupling method of [42] and on Effective Independence which is discussed more thoroughly in [45]. A simple example showed that a zero or slightly negative mass can sometimes have physical relevance [42], while in other cases, the negative mass may indicate that the modal basis for the residual subsystem is not adequate to span the motion observed on the coupled system.

In later work, Allen et al expanded upon the work of [44] and developed metrics to determine the cause of indefinite mass or stiffness matrices after decoupling [46]. Though these methods developed in [44] [42] [46] have relevance in frequency domain, they are formulated in the modal domain. Thus, in the interest of keeping the focus of this work on FRF based coupling, the exact mathematical formulations will not be presented.

2.1.3.8.6 Variability Improvement of Key Inaccurate Node Groups (VIKING)

The exact causes for these errors that lead to incorrect results after decoupling are often not all known, and even when the cause is known, the current solutions are often specific to one certain type of error. Nicgorski et al [47] developed a method for conditioning measured FRF data to improve the results of decoupling. The method uses a combination of approaches and is referred to as variability improvement of key inaccurate node groups, or VIKING.

The VIKING method consists of three steps which can be summarized as: 1) testing, 2) data smoothing, and 3) data completion/FRF synthesis. These steps are summarized in following subsections, while a more thorough discussion can be found in [47].

2.1.3.8.6.1 Testing

Lower-order flexible mode shapes are obtained from a physical structure through testing and modal parameter estimation. For VIKING, measurements are taken at all interface DOFs, as well as any other internal DOFs of interest. There must be enough DOFs tested such that the mode shapes within the frequency range of interest can be well described.

2.1.3.8.6.2 Data Smoothing

A coordinate orthogonality check is used to determine which DOFs have large contributions to the orthogonality of the test mode shapes under investigation. “Good” measured DOFs are then selected on a mode-by-mode basis, where a “good” DOF is defined as one with a large contribution to orthogonality. Any DOFs which have a small contribution to orthogonality are omitted to create a reduced a-space representation of the given mode shape.

After the coordinate orthogonality check is used to reduce the representation of the mode shapes, a FE model is developed for the structure of interest and a full-space eigensolution is performed. A modal assurance criterion (MAC) and a pseudo-orthogonality check (POC) are used to determine which FE mode shapes are most correlated to the test data. A more in depth description of MAC and POC can be found in [47]. The shapes that are most correlated are then selected for use in the data smoothing.

With the “good” mode shapes determined, the system equivalent reduction expansion process (SEREP), originally developed by O’Callahan et al [48], is utilized next. A SEREP expansion matrix from the FE model, which relates the “good” test data to the full set of test DOFs, is created for each mode shape. In the context of VIKING, the SEREP expansion matrix contains as many FE shapes as there are test shapes. The “good” set of test DOFs is expanded to the full set of test

DOFs using the SEREP expansion matrix. This expansion process smooths out the experimentally determined mode shapes for use with FBS coupling or decoupling.

During the SEREP implementation, test mode shape information is expanded. This is possible because the test mode shape information can be described by linear combinations of the FE mode shapes within the SEREP matrix. Since anomalies in the experimentally determined mode shapes cannot be described by a linear combination of FEA mode shapes, the SEREP expansion smooths the anomalies and conditions the data to be better suited for use in FBS.

The data smoothing step concludes with another check using MAC and POC. This check ensures that the shapes smoothed by SEREP still correlate well to the experimentally obtained mode shapes. High correlation with MAC and POC are important because the goal of the VIKING process is to preserve the characteristics of the test data while removing variance from the mode shapes.

2.1.3.8.6.3 Data Completion and FRF Synthesis

Since the previous two steps are limited to a finite number of modes, it is necessary to address complications which arise from test-based residual compensation terms [49]. The VIKING method addresses these complications by appending rigid body modes and higher order numerical modes from the FE model in order to complete the dataset. By including a sufficient number of numeric modes, the VIKING method avoids truncation errors that sometimes arise during the transition from modal to frequency domains. These FE modes are assigned a modal damping value typical for the structure being tested. Finally, FRF synthesis is performed and the FRFs are then used in FBS coupling or decoupling.

It is important to note that, though VIKING makes extensive use of the modal domain, it is still considered to be a type of FBS method since the end goal is synthesize FRFs suitable for decoupling. The VIKING method effectively addresses issues such as drive point measurement adequacy, inability to measure exact location of measurement, cross measurements, and measurement noise.

2.1.3.8.7 Uncertainty Quantification

Voormeeren et al developed a method to quantify the expected error in coupled FRF based on measured uncertainties in the measured substructure FRFs [50] [34]. The formulation presented by Voormeeren was developed for systems coupled by the LM FBS method as presented by De Klerk et al [23] and summarized earlier in the current chapter. The main goal of the work was to answer the question of how uncertainties propagate through the coupling process.

The steps through which uncertainty propagates in the coupling process can be generally be described in two steps. First, uncertainty propagates from the measured time domain signals to the substructure FRFs. Second, uncertainty in the substructure FRFs propagate to the FRF for the coupled system. Based on this general knowledge, Voormeeren et al addressed the problem from a statistical point of view.

In [17] it was found that the random influences on a real life substructure closely obey a Gaussian distribution. Voormeeren et al used knowledge of statistical techniques for Gaussian distributions along with first order Taylor approximations to develop a method which describes uncertainty propagation from substructure FRFs to the final, coupled FRF [50] [34]. The method was validated via Monte Carlo simulations that produced almost identical results for small input uncertainties (2% on magnitude and 1^{o} on phase). However, for the example used for validation, the Voormeeren

method only took 3 seconds of CPU time as compared to over 300 seconds for the Monte Carlo Simulation.

Additionally, Voormeeren et al investigated how uncertainty propagates between FRFs of different substructures. The findings can be summarized as follows.

2.1.3.8.7.1 Internal-to-Coupling FRFs

When uncertainty is present in an internal-to-coupling FRF, the accuracy of all coupled FRFs associated with the considered input DOF will be affected. More specifically, the uncertainty will propagate from this coupling DOF to the internal DOFs of all substructures coupled at that point.

2.1.3.8.7.2 Coupling-to-Coupling FRFs

For coupling-to-coupling FRFs, the uncertainty always propagates into the FRFs of each substructure coupled at that particular DOF. For lightly damped structures, this can lead to spurious peaks in the FRF of the coupled system.

2.1.3.8.7.3 Internal-to-Internal FRFs

Uncertainty located purely in the internal substructure FRFs does not propagate to other FRFs after coupling. These uncertainties do not propagate due to the fact that the FRFs do not participate in the interface flexibility matrix. In other words, the uncertainties for the internal DOFs do not affect the coupled FRF because they do not "communicate" with the other FRFs during the process.

Though the process was developed for coupling via the LM FBS method, the standard FBS method was shown to have the exact same uncertainty propagation behavior. For either FBS method, it was shown that small uncertainties in the substructure FRFs of lightly damped substructures could

lead to large discrepancies in the coupled FRFs. For the specific example in [50] [34], errors of 2% in substructure FRFs were shown to grow as large as 70% in the coupled FRF.

2.1.3.8.7.4 Uncertainty Propagation in Decoupling

In [50] the same general procedure was used to determine how uncertainty propagates in the decoupling process. The analysis for decoupling uses the same basic procedures and statistical methods as those used for coupling. Voormeeren et al applied these techniques to both inverse coupling and direct decoupling methods to observe differences in error magnification. It was found that direct decoupling magnified error by a factor of 5 to 10 times less than inverse coupling (a factor of 15 for direct versus a factor of about 100 for inverse). These results intuitively make sense based on the knowledge that direct decoupling can incorporate additional internal DOFs and thus satisfy one of the conditions in only a minimum square sense.

2.1.3.8.7.5 Other Uncertainty Propagation Methods

In recent years, various other methods have been investigated to address uncertainty propagation through frequency response and dynamic substructuring. Covariance based methods were developed in [51] [23] [52]. Compared to methods by Voormeeren et al [50] [34], these covariance based methods break down in the vicinity of isolated resonances and anti-resonances. Despite that limitation, for a simple example, the covariance method of [51] showed less than 2% deviation from the Monte Carlo simulations at the first 25 elastic modes.

2.1.3.8.8 Rotational DOFs

One of the biggest challenges in experimental dynamic substructuring is the measurement or use of rotational degrees of freedom (RDOFs). A variety of different methods have been investigated in recent years, ranging from techniques to extract rotational information to techniques centered

on avoiding the use of RDOFs entirely. Some of the more prominent methods for dealing with RDOFs will be summarized in the following subsections. It is worth noting that the methods which are formulated in the modal domain can usually still be applied in frequency domain substructuring.

2.1.3.8.8.1 System Equivalent Reduction Expansion Process (SEREP)

Though the system equivalent reduction expansion process (SEREP) was found to provide advantages in a number of areas of modal testing, it was originally formulated to estimate rotational degrees of freedom from experimental modal data [48]. In the context of dynamic substructuring, SEREP implementation has both advantages and disadvantages. When used as an expansion technique, SEREP creates expanded modes as a linear combination of analytical modes. In turn, this expansion by linear combination smooths the measured data in some sense. A major drawback of using SEREP expansion is that a high quality FE model is required for the process to be effective.

2.1.3.8.8.2 Static Expansion

A local model of the substructure of interest can be considered in the static expansion of a local interface model [53] [54]. This local model of the substructure the interface region common to both models (i.e. the coupling DOFs). While the mathematical representation of this static expansion can be found in [55], the method can be summarized as follows.

Guyan condensation is used on the measured DOFs of the substructure of interest. It is important to note that the Guyan transformation only provides meaningful results if the dynamics at the unmeasured points are negligible. With the simplified representation from the Guyan condensation, another transformation matrix can be used along with the experimental mode shapes

to obtain the expanded mode shapes at the coupling DOFs. This technique can be improved significantly if the measured data is smoothed to reduce errors before the transformation is applied.

Compared to SEREP, this static expansion provides an advantage in that a detailed FE model of the entire substructure is not needed. Instead, only a model of the substructure in the region of the interface is needed [55]. However, the accuracy of the static expansion process is dependent upon the DOFs that are chosen for the reduced system model and the frequencies/mode shapes are not guaranteed to match the original model [48].

2.1.3.8.8.3 Equivalent Multi-Point Connection (EMPC)

When two substructures are considered to be connected rigidly at a single point, compatibility and equilibrium conditions involve both translational (displacement/force) and rotational (rotation/moment) quantities. For these rigidly connected substructures, neglecting RDOFs provides meaningless results if coupling is assumed to occur at a single point. Thus, the equivalent multi-point connection (EMPC) method was developed to account for rotational dynamics by assuming that coupling occurs at several closely spaced points [56] [57] [17] [33] [58].

For the EMPC method, when two coupled substructures experience bending motion, coupling can be assumed to occur in the joint region at three closely spaced points. The points cannot be in a straight line, otherwise the necessary range of rotations and moments may not be covered. Thus, the most common selection of coupling DOFs for the EMPC method are the vertices of a triangle, as shown in Figure 4.

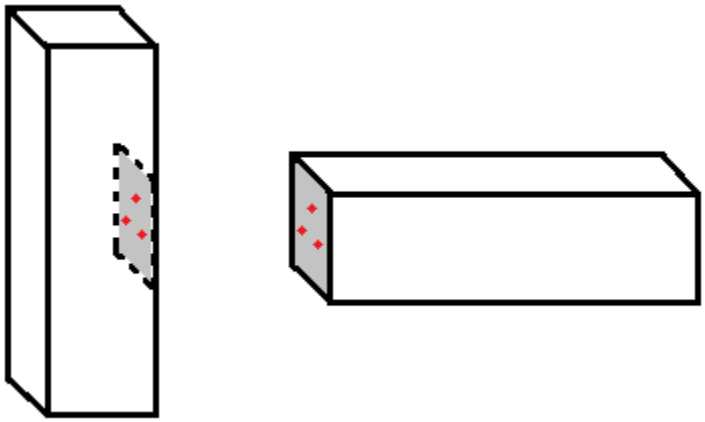

Figure 4: Graphical representation of the EMPC method. The three dots in the shaded regions represent measurement points

The EMPC method continues with the assumption that only orthogonal forces are transmitted through the selected coupling points. The combination of forces from these points gives resultant forces and moments that approximate the real dynamics at the coupling interface. The use of only translational DOFs at the coupling points provides reasonably acceptable results, in terms of displacement and rotation compatibility, as long as the joint region lies approximately in a single plane. The average displacement and rotation of the interface can be implicitly obtained from the displacements at the three coupling points [55].

One important limitation to the EMPC method is the ratio of the distance between the assumed coupling points and the frequency of interest. The distance between the points must be greater than a quarter of the maximum involved wavelength. Otherwise, the joint region is no longer approximated by a plane and the accuracy of the procedure decreases.

In [56], an extension of the EMPC method was developed to help reduce the effect of errors made in the measurement of the substructure interface. The extension is essentially a filtration method which separates and removes the effects of residual modes from what is considered to be the

dominant set of modes. The filtration method also allows to determine if the number interface flexibility modes considered dominant is valid.

2.1.3.8.8.4 Transmission simulator

The transmission simulator method is also referred to as the modal constraint for fixture and subsystem (MCFS) method [43] [59]. This method is conceptually similar to the EMPC method in how it accounts for RDOFs. Both methods use a set of translational DOFs spaced around the coupling interface to include estimates of rotational actions. Aside from the similarities with respect to RDOFs, the two methods are very different.

A fixture dubbed the "transmission simulator" is mounted to an experimental substructure with the exact same joint properties (geometry and material) that the substructure will experience as part of the assembled system. By including the joints in the experimental substructure, measurements automatically include the dynamics of the joints. Additionally, the transmission simulator gives locations to mount sensors or input forces where the connection point of the substructures might not (for example, bolted connections) [60] [59] [61].

Once measurements are taken, the transmission simulator fixture is subtracted from the substructures, which can be either analytical or experimental. This subtraction is done via standard modal or frequency based decoupling procedures [59]. With the fixture dynamics subtracted, the substructure FRFs are ready to be coupled together. In the context of RDOFs, the substructure FRFs contain rotational information relevant to how the two substructure will be coupled together.

2.1.3.8.8.5 RDOFs in Decoupling

Until recently, it was believed that all of the issues associated with RDOFs in coupling procedures also appeared in decoupling procedures. D'Ambrogio et al [35] found that the effects of RDOFs,

which depend on how the substructures are coupled, were already included in the FRF measurements of the assembled system. The use of a mixed interface in decoupling allows for the exclusion of unwanted coupling DOFs in favor of additional internal DOFs in experimental application.

The concept of replacing rotational coupling DOFs was tested using a simplified test structure of two coupled beams. Results from decoupling with the mixed interface with no RDOFs were comparable to those using an extended interface, with only slight frequency shifts at resonances and anti-resonances (due to curve fitting). Thus, the theory was supported that rotational information is inherently included in the FRF measurements of the assembled system and RDOFs can be excluded from the decoupling procedure. Since this discovery was relatively recent, there have yet to be many other studies to support these findings.

2.1.3.9 Alternative Substructuring Formulations

In recent years, the majority of work done in experimental substructuring has been focused in either modal or FRF based methods. However, there exist some techniques that do not approach the coupling/decoupling problem in the typical modal or frequency manners. Since the focus of this work is on frequency based methods, only a general overview (with no mathematical formulation) will be given on these alternate formulations.

2.1.3.9.1 State Space

Sjovall et al [30] call upon developments in frequency based substructure, modal substructuring, joint identification, and structural modification to address the decoupling problem in the context of system identification. After system identification, the state space models of the assembled system and the residual substructure are used in the reconstruction of their corresponding FRFs.

The FRFs are then used in decoupling procedure similar to the dual formulation for direct decoupling.

2.1.3.9.2 Impulse Based Substructuring

The impulse based substructuring (IBS) method can be described as a time domain formulation of dynamic substructuring in the frequency domain. More specifically, the IBS method is a transposition of the LM-FBS method [23] to the time domain [62]. The assembly process of the IBS method computes the time response on a substructure basis by evaluating the convolution product between the impulse response functions and the applied forces. These applied forces included the interface forces used to satisfy equilibrium and compatibility.

When compared to FBS, the IBS method has several distinct advantages, such as: no approximation to full time integration is made, time discretization error can be controlled, Fourier transforms are avoided when results are desired in the time domain, potential to deal with nonlinear structures, and processes that are generally less computationally expensive. Despite these advantages, IBS is often used more for impact loading cases, while FBS is used in a wide range of applications.

2.1.3.9.3 Base Excitation

Standard formulations for FBS methods assume that the input to the system is a force input. Cesnik et al [63] approached the substructuring problem from a different perspective, base excitation. This method takes the equations of motion for base excitation in the physical domain and applies the same concepts to the pre-existing structural modification using response functions (SMURF) method [64]. The advantages of this technique are that it can be used to compute displacement transmissibility and stress response functions.

2.1.3.9.4 Interface Force Identification

Most of the common FBS methods rely on knowledge (either analytical or experimental) of the residual substructure in order to decouple it from the assembled system. In an effort to reduce the need for a model of the residual substructure, a new type of FBS method was developed based on experimental identification of interface forces [65].

Since interface forces cannot be measured directly in most cases, the method includes a step to estimate these forces [30] [50]. These interface forces are then treated as excitation forces to one of the substructures and the system is then solved by more typical FBS methods [65].

2.1.3.9.5 Real Time Hybrid Substructuring (RTHS) as Feedback Control

Real time hybrid substructuring (RTHS), sometimes also referred to as "real time hybrid simulation" or "real time dynamic substructuring," is still a relatively new method of dynamic substructuring made possible by improvements in computational power, signal processing, and actuation capabilities. In the typical way of dynamic substructuring, RTHS treats a coupled system as a known (residual) substructure and an unknown substructure. The residual substructure is simulated in real time either analytically or numerically, while the actual unknown substructure is measured with the necessary sensors.

The simulated and tested substructures pass displacement and force signals to each other through a network of sensors and actuators. Typically, the physical substructure is the system of interest, while the simulated substructure is an analytical or numerical model of a system which is either well known or difficult to implement physically. In some ways, RTHS is conceptually similar to hardware-in-the-loop (HIL) concepts commonly used when certain components are either difficult to model or difficult to incorporate experimentally.

There has been much work done with RTHS in recent years [66] [67] [68] [69] [70]. However, only the formulation developed by Botelho and Christenson [71] will be discussed here. Botelho and Christenson found that RHTS was mathematically equivalent to feedback control. In the formulation, the residual substructure (which is being simulated) acts as the controller and the unknown substructure (which is being measured) acts as the plant. This setup requires actuators to be connected to the unknown substructure to provide the interface forces and displacements calculated by the simulation of the residual substructure.

The work showed that the coupled response due to a force input on the residual substructure resembled the closed-loop response for reference tracking. On the other hand, the coupled response due to a force input on the unknown substructure was found to resemble the closed-loop response for disturbance rejection [71]. This formulation of RTHS as feedback control shows the potential of applying feedback theory and techniques to both RTHS and traditional dynamic substructuring.

2.1.3.10 Test Structures

There are many difficulties that arise when carrying out experimental FBS coupling or decoupling, such as those mentioned in the previous section. Due to these difficulties, a need has arisen for versatile benchmark test structures to investigate causes and potential solutions to the difficulties.

In recent years, several different benchmark test structures have been proposed. Though some of the end goals of these test structures are similar, they are not all designed for the same purposes. For instance, some structures have been designed to improve testing results, while other structures have been designed to benchmark and validate the various proposed improvements to experimental substructuring. Thus, some of these test structure designs differ radically from each other. Only

two test structures which represent common designs and goals will be present here, along with brief summaries of the goals associated with each test structure.

2.1.3.10.1 Benchmark Test Structure for Experimental DS

Van der Valk et al compiled a list of requirements for the desired test structure to account for the difficulties commonly encountered during experimental dynamic substructuring. These requirements can be found in full in [72] and summarized as follows.

A broad range of possible connections should be available to connect the test structure to different substructures as well as to passive and active components such as springs or actuators. The first flexible mode of the system should be above 50 Hz in order to be well separated from the rigid body modes. There should be an area that can be assumed to be rigid or can be made rigid to allow for the use of the EMPC method for determining rotations [17]. Materials that have environmentally dependent behavior (temperature, humidity, etc.) and materials that are susceptible to aging should be avoided to increase the reproducibility of results. Finally, the cost per piece of the test structure should be low so that destructive testing, such as welding, can be conducted in a practical manner.

From this list of requirements, Van der Valk et al concluded that the benchmark test structure should be a simple setup and demonstrate linear behavior so that it can be modeled and measured easily. The final design is shown in [72], but a brief description will be given here. The structure is made from a single sheet of 5mm stainless steel and can be manufactured using only laser cutting and machinal bending. The simplicity of the creation of the structure keeps the cost low and thus allows for destructive testing. Additionally, the spacing of connection points and the material properties of the stainless steel support the rigidity assumption necessary to use the EMPC method.

The FE model of the test structure was validated by comparing it to experimental data obtained on the actual structure. The comparison showed MAC values of greater than 93% and a maximum difference of 1.4% in eigenfrequencies. This close correlation between the FE model and the actual structure provides a number of benefits such as the ability to use FE model data in substructuring. Furthermore, the structure contains a portion rigid enough (a 93% rigidity factor as defined in [72]) to account for rotations via the EMPC method.

2.1.3.10.2 Lumped Parameter Benchmark Test Structure

Some issues of experimental substructuring are not well known or cannot be fully investigated using only simulated experiments. In order to better understand these issues, Culla et al developed a lumped parameter benchmark test structure [73] [74]. Additionally, this test structure was used to test methods which were designed to improve experimental substructuring results.

The test structure is termed “lumped parameter” due to the lumped masses and springs used to construct it. A lumped parameter system is attractive for benchmarking because of its relative simplicity when compared to a distributed parameter system. Furthermore, the ability to isolate and change certain portions of the test structure makes it easier to observe changes in results of dynamic substructuring due to changes in independent substructures.

The concept of using lumped parameter systems to test and validate experimental substructuring techniques has been explored previously [34] [75]. However, in those cases, tests were simulated without a lumped parameter structure being tested in the real world.

The first version of the test structure developed by Culla et al consists of several lumped masses connected either rigidly or by springs [73] [74]. This first version had the masses translate horizontally on rigid guide rails. These guide rails were intended to restrict rotation and lateral

displacement. The concept was not implemented effectively due to difficulties ensuring that the guide rails were exactly parallel. A full description with accompanying images of the actual test setup can be found in [73]

In an effort to eliminate the errors from the first version, Culla et al developed a second version of the test structure without guide rails. All masses, connections, and springs were kept the same, but the structure was rotated so that the masses would translate in the vertical direction in respect to the ground. With this orientation, the guide rails are no longer necessary to support the masses and were thus be omitted from the design. However, there are some drawbacks to this second version as well. More specifically, without the guide rails, the masses may experience some small rotations or lateral translations. Again, a full description of the test structure is presented in [73].

Culla et al used the second version of the test structure to conduct coupling and decoupling tests. These tests were used to validate current substructuring techniques and investigate other experimental difficulties that may not appear in simulations.

2.1.3.11 Vehicle Specific Applications

Several researchers have already used dynamic substructuring techniques in a variety of land vehicle applications. Among a variety of works, some of the notable applications include: coupling of individually modeled tread blocks to evaluate acoustic properties [76], coupling of subframes to the vehicle body [77], coupling of the individual components of a rear axle system, and even vibration transmission in train bogie assemblies [30]. One similarity that all of these vehicle dynamics applications share, is that they all pertain to coupling components together. For instance, a simplified lumped parameter model for passenger vehicle was coupled to the vehicle body in [78] and [79].

In this context, it is the goal of the authors to apply frequency domain decoupling procedures to passenger vehicle suspension system. In particular, the procedures described in the preceding sections will be used to decouple the components of a quarter-car system both analytically and experimentally.

2.2 Modal Testing of Tires and Suspensions

Central to the concept of experimental frequency based substructuring (FBS) is the carrying out of modal testing. This chapter will present the basics of modal analysis and testing followed by the documented specific applications to passenger car tires and suspensions. The chapter is not intended to be a thorough discussion of modal analysis or modal testing, but rather a high level overview/review for the reader who is already familiar with modal concepts.

2.2.1 Brief Overview of Concepts – Modal Analysis

At the basest level, modal analysis is the study of the dynamic properties of a system with respect to system vibrations. More specifically, these dynamic properties are often in the form of frequencies and the corresponding shapes of the natural vibrations of a given system. These frequencies (natural frequencies) and shapes (mode shapes) depend on a variety of factors such as: material properties, physical shape, connections to other structures, and environmental effects.

Perhaps the most intuitive demonstration of the concept of natural frequencies and mode shapes is through the discussion of a theoretical example of a string in tension with two fixed ends (also known as fixed-fixed boundary conditions). Many resources exist for the theoretical derivation

and experimental validation for the fixed-fixed string, so only an overview of the results will be presented here [97]. Figure 5 displays the first four mode shapes of the fixed-fixed string.

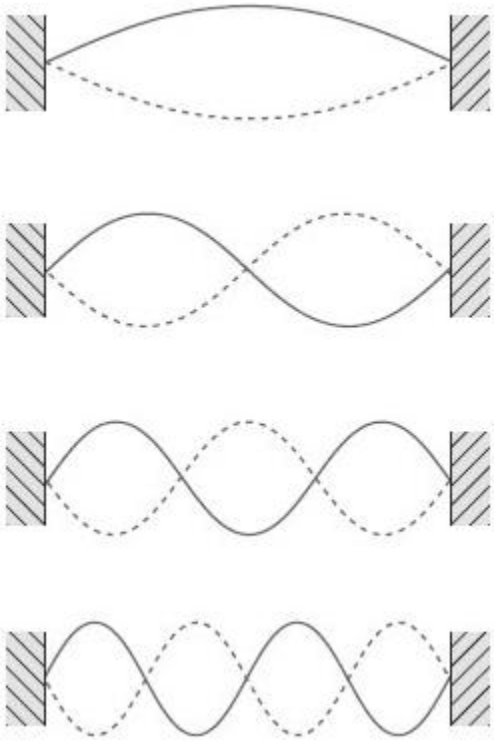

Figure 5: First four mode shapes of a fixed-fixed string

The mode shapes of Figure 5 each correspond to a natural frequency which is the slowest for the first mode and increases for each subsequent mode. Unless excited specifically at one of these natural frequencies, the vibration response of the string will appear as some combination of all present mode shapes. In reality, there are an infinite number off mode shapes for any given system. However, only a certain number of these modes have a high enough energy content, or are considered “dominant” enough to have a noticeable effect on the response of the system. Thus, it is common practice to only consider frequencies and mode shapes up to a certain threshold: either a frequency threshold or an energy threshold depending on the application.

2.2.2 Brief Overview of Concepts – Modal Testing

In contrast with the analytical/theoretical analysis discussed in the previous section, experimental modal analysis depends heavily on the quality of the testing procedures. There are a number of factors paramount to the success of modal testing, such as: measurement locations, excitation method, frequency range of excitation, and boundary conditions. The considerations for each of these factors will be discussed in more detail in the following sub sections.

2.2.2.1 Measurement Locations

The locations at which system response is measured during modal testing determine which modes and corresponding frequencies can be detected. A portion of Figure 5 is repeated in Figure 6 to emphasize the importance of measurement locations.

Figure 6: Demonstration of the importance of measurement locations. The orange X's mark the node points of the third mode of the fixed-fixed string.

The orange X's in Figure 6 mark the "node points" of the third mode of the fixed-fixed string. The node points mark area of zero displacement for the given mode of the string model. For a two dimensional system, the areas of zero displacement will appear as node lines as opposed to the points. If measurements are taken at one of the nodal locations, the corresponding mode will not appear (or will not appear correctly) in the experimental modal analysis.

It is important to note that the concept of nodal lines applies only to normal modes and not complex modes. Normal (or "real") modes are characterized by all portions of the structure moving in phase or 180^{o} out of phase and can be thought of as standing waves. In contrast, complex modes can

have any phase relationship between parts of the structure and can be thought of as travelling waves. Since the structure is moving in phase for normal modes, all portions of the structure reach their maxima at the same instance which gives rise to the node lines. On the other hand, since complex modes can have any phase relationship, the portions of the structure do not reach their maxima simultaneously and node lines do not appear [20].

For a given structure, the damping distribution determines whether the modes will be normal or complex. Specifically structures with light/negligible damping or structures with proportional damping will have normal modes. While structures with localized damping have complex modes [98].

With nodal lines and normal vs. complex modes in mind, later sections of this chapter will analyze the modal properties of tires and suspensions to determine the ideal measurement locations.

2.2.2.2 Excitation Method

Excitation methods for modal testing can be generally classified into two categories: contacting and non-contacting. These two categories can then be broken down even further into the different types of mechanisms used to achieve the excitation.

2.2.2.2.1 Contact Excitation

The two most common contacting methods of excitation are hammers and shakers. A general overview of hammers and shakers will be given here, while a more complete discussion can be found in [20].

Hammers are the popular choice for many testing applications due to the relative simplicity of the excitation setup. The tip of the hammer is equipped with a force transducer to record the input (during the hit) and accelerometers are placed at the locations of interest across the structure under

examination. Although simple, using a hammer strike as the method of excitation is not always the best choice. The frequency range of the input from the hammer is limited by the duration of the impact, which is in turn effected by the material of the test structure, the hardness of the hammer tip, and the weight of the hammer head. Thus, if the duration of the impact is too high, the input excitation may not have adequate frequency content to excite all the modes of interest. Additionally, for more heavily damped systems, the energy imparted to the test structure from the hammer strike may not be sufficient to produce measureable response at the points of interest. It is for the aforementioned reasons that excitation via shaker is sometimes the better option.

In the context of modal testing, a shaker is a mechanism which provides some vibratory input to the structure under investigation, often in the form of "shaking." There are a variety of shaker types that are commonly employed for modal testing, such as mechanical, electromagnetic, or electrohydraulic [20]. Each of these types of shakers has its own advantages and disadvantages, but all share one thing in common: they provide greater control over the method of excitation than the hammer.

Two challenges that must be overcome for shaker excitation are mass loading of the test structure and the potential to cause resisting moments/forces from the input mechanism. These challenges are most often addressed by the use of a "stinger." A stinger is a relatively slender rod which connects the shaker to the test structure and often connects somehow to a force transducer. However, the use of a stinger gives rise which must be accounted for. If the rod is too long or too flexible, then it can introduce effects of its own resonances into the measurements and pollute the data from the test structure. Thus, the stinger is kept as short as possible and stiff in the direction of excitation while relatively flexible in all other directions.

Depending on the specific application and the specific structure under observation, there are a number of different input types which are commonly used. Specifically, the inputs can be either continuous or transient. Continuous excitations include those such as sinusoidal inputs or random excitation among others, while transient excitations include “pulse” and “chirp” inputs.

2.2.2.2.2 Non-Contact Excitation

The development of non-contact excitation methods has been driven by the need to test delicate and/or small structures. The field of micro-electronics begets a particular interest in such testing methods since nearly all of the involved electronic components are both small and delicate. There are several types of well documented non-contact excitation methods which will be presented in this section.

Magnetic excitation can be applied if the structure under investigation is magnetic or if a magnetic strip is attached at the desired excitation point. An electromagnet can then be positioned to apply a controllable force on said excitation point [20]. Acoustic excitation from a loudspeaker can be applied to the structure or surface of interest, but the method suffers from several drawbacks. Namely, it is difficult to supply sufficient energy from the air to the wall and, since the exact input force may not be known, it is difficult (if not impossible) to obtain the true FRF. However, the frequency spectrum and amplitude of vibrations can still be observed from the test object [99]. Two other methods that suffer from some of the same difficulties as acoustic excitation are electrical pulse exciation [100] and laser pulse excitation [101]. The final non-contact excitation method which will be presented here is one that addresses some of the drawbacks of the aforementioned methods. Pneumatic excitation works by hitting the test object with a jet of air which exerts some force. The magnitude of the force can be measured by the change in momentum of the air stream and thus, the FRF of the system can be measured [102].

2.2.2.3 Excitation Frequency

The frequency range of interest for the structure under observation is typically known to the experimenter prior to testing. In the case that the frequency range of interest is not known, more thorough and exhaustive tests must be conducted. When the range is known, the difficulty in testing lies with selecting the proper testing procedures which will provide meaningful information across the entire range.

The various excitation methods discussed in the previous section become important again in the context of the provided frequency range. For instance, as mentioned previously, the frequency band excited during a hammer impact is inversely proportional to the duration of impact. Similarly, for any type of shaker induced excitation (sine sweep, pulse, chirp, noise, etc.), the frequency band in which adequate energy is supplied to the structure must meet the requirement set forth by the range of interest. In summary, this frequency band of excitation can be limited by the choice of excitation, the specific equipment used to achieve said excitation, and the test setup.

2.2.2.4 Boundary Conditions

One of the most important decisions during the modal testing process is whether to test a structure in a “free” condition or a “grounded” condition. In this context, a free boundary condition means that the test object is not attached rigidly to any other structure and is effectively suspended “freely” in space. In contrast, a grounded boundary condition is where select locations on the test object are attempted to be fixed to some “ground” or sufficiently rigid structure.

2.2.2.4.1 Free Boundary Condition

In theory, a freely supported structure will exhibit six rigid body modes (three translational and three rotational) which are solely determined by inertial properties and occur at a frequency of 0

Hz. In reality, it is not possible to provide a truly free support and thus the rigid body modes will have non-zero natural frequencies. Since the test object must be held in some way, the best approximation of a free condition is to support the structure on some "soft" suspension. The requirement of a "soft" suspension system arises from the necessity to keep the rigid body modes low in relation to the lowest bending mode. A typical goal is to keep the highest rigid body mode less than 10 to 20 percent of the lowest bending mode [20]. If the suspension is too stiff, the rigid body modes will be high enough to pollute the experimental data and cause errors in the region of the bending modes.

Another precaution to ensure minimal effect of the suspension on the test object is to attach the supports at or near the nodal points of the mode (or modes) in question. Doing so helps to reduce the dampening effects of the supports since these nodal points have theoretically zero displacements at the mode of interest.

Conducting a modal test on a freely supported structure may not always be the best choice for a give object and circumstance, thus the following section will address the concept of modal testing on a grounded structure.

2.2.2.4.2 Grounded Boundary Condition

Grounded (or fixed) boundary conditions are easy to apply in theoretical analysis. All that is required is to keep the grounded coordinates fixed at zero so that the boundary does not translate or rotate. However, like the freely supported structure, the grounded boundary condition does not actually exist in practice. The best approximation is to fix the test structure to a base or foundation which is sufficiently rigid to allow negligible movement at the boundary. To a certain extent, the ability to provide such a reliable approximation is dependent upon the characteristics of the test

object. For example, it is relatively easy to approximate grounded boundaries on thin wire when compared to the difficulty of adequately grounding a steel I-beam.

One method to ensure more accurate grounded/fixed boundary condition is to first examine the mobility FRF of the proposed based structure over the frequency range of interest. If the base structure has a mobility much lower than that of the test structure (at the points of attachment), then the base structure can be assumed to provide a "reasonably grounded" boundary [20]. Another, more recent, method to address interactions at constrained boundaries is to attach the test object to some relatively simple component with analytically or theoretically known dynamics. Thus, once the tests are completed, the decoupling techniques discussed previously in this chapter can be applied to separate the dynamics of the known structure from those of the test object. An example of this concept is in the Transmission Simulator which was also discussed previously in this chapter [42, 59, 60].

The preceding sections are my no means intended to provide a comprehensive discussion on the vast field of modal testing and analysis. Instead, they are intended to provide the reader with at least a qualitative introduction to modal concepts. The following sections will present the modal testing and analysis work which has been done specifically on tires and suspension.

2.2.3 Types of Tire Tests

On the subject of the support method for the tire during modal testing, much work has been done on both free and fixed supports. While both methods introduce additional modes into the system, the rigid body modes that are introduced through the use of a freely suspend tire typically occur at very low frequencies (less than 5 Hz) and thus pollute the measurements of the other modes less than those additional modes introduced by fixed supports [103].

If hammer excitation is used, one option to increase the input frequency bandwidth is to attach a small, rigid metal plate to the impact point on the tire. Even with this increased rigidity, hammer tests were shown to have limited bandwidth and poor coherence [104].

2.2.3.1 Loaded Tire

By necessity, tests on a loaded tire are performed with the tire support/boundary condition as fixed. It is worth noting that performing modal analysis on a loaded, and thus deformed tire, will provide different results than for a free tire in terms of both frequency response and mode shapes [104]. Under free circumstances, a tire has two duplicate mode shapes at each frequency. For loaded conditions, there still exist two mode shapes at each frequency, but they are distinctly different from each other. Specifically, there is one symmetric and one anti-symmetric mode shape for the loaded tire [105].

Loading the tire causes the natural frequencies to ride and the associated modal damping ratios to decrease [105]. This change is conceptually similar to how the frequencies and damping changes when inflation pressure is increased.

2.2.3.2 Free (Unloaded) Tire

The testing of an unloaded tire allows for the choice of applying either fixed/grounded or free supports.

In [106] tests were conducted in radial, tangential, and “side” (lateral) directions and the corresponding mode shapes were reported. The tests were repeated on a tire with 3 different rims and the effects of the rim weight on tire natural frequency were recorded. These results are perhaps the most applicable to the current work since we are interested in vibrations in all 3 directions. For certain cases there were some measurements taken at interior points on the rim, but not many.

It was found that the rim weight only had significant impact on the lower order modes of the tire: R1, T0, T1, S0, and S1 [106]. This behavior suggests that the natural frequencies of the rim are relatively far away from those of the tire as would be expected due to the macroscopic material properties. Intuitively, the natural frequencies of the tire in the radial direction increase with increasing tire pressure (increased rigidity, decreased damping). Other work, done by Yam et al [107] found that the amplitude of rim vibrations were less than 10 percent of those experienced by the tire carcass.

There is a specific mode related to the cavity of the tire, called the "Cavity mode," which does not vary with increasing tire pressure [106] [107]. This mode does not vary because it is primarily dependent on the shape of the tire in contrast to the other modes.

Tests carried out with excitation in the tangential (longitudinal direction) demonstrated similar natural frequencies across the present modes. However, the magnitude of the vibration of these modes due to the tangential excitation was considerably less than that due to radial excitation [107].

To prevent the shaker and stinger from altering the dynamics of the tire, some researchers have even freely suspended the shaker [108].

2.2.3.3 Rolling

Due to the difficulty in determining the excitation force input from the road surface to a rolling tire, operational modal analysis (OMA) is often used in place of traditional modal analysis [109].

2.2.3.4 Static

For a sine sweep/dwell, the length of data segment in each frame is determined by the frequency bandwidth of analysis and the corresponding sampling time. In [104], Guan et al separated the

frequency range of interest into three sub-ranges in order to ensure that enough excitation energy was input into the system at each frequency. Not only did this technique improve the signal to noise ratio (SNR), it also reduced aliasing without the need for special equipment or filters.

The concepts introduced in this chapter, particularly those relating to FBS, will be put to use in the following chapter, **Chapter 3 – Analytical Development.**

Chapter 3 – Analytical Development

The following chapter presents a method to mathematically separate the vibrational properties of the tire and the suspension in order to further understand the mechanism of vibration transmission between the two. The frequency based substructuring (FBS) techniques of Chapter 1 will be used to decouple the tire subsystem from the suspension subsystem. In this chapter, these FBS techniques are applied first to decouple the equations of motion of a simple quarter car system as a proof of concept. Then, a more generalized approach is taken which will be applicable to experimental data.

3.1 Simplified Quarter-Car Model – Coupled at a Single Degree of Freedom

In this derivation, the system under investigation is a quarter car system. The first step in deriving a full FBS formulation for decoupling the suspension and tire is to use a simplified quarter car model with a single coupled degree of freedom. Before using FBS methods, the system can be coupled or decoupled analytically using the equations of motion. Figure 7 shows the simplified model used in this derivation.

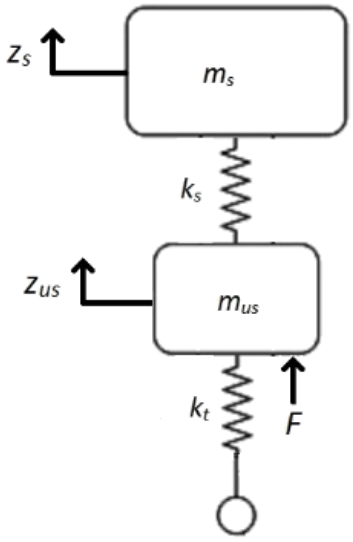

Figure 7: Simplified quarter car model used for initial FBS decoupling formulation

This simple model consists of two lumped masses (sprung and unsprung mass) with some associated stiffness and negligible damping. The equations of motion for this model are shown in Equations (94) and (95):

$$m_s\ddot{z}_s + k_s(z_s - z_{us}) = 0 \tag{94}$$

$$m_{us}\ddot{z}_{us} - k_s(z_s - z_{us}) + k_t z_{us} = F \tag{95}$$

Where m_S is the sprung mass, z_S is the sprung mass displacement, m_{US} is the unsprung mass, z_{US} is the unsprung mass displacement, k_t is the tire stiffness, k_S is the suspension stiffness, and F is the force input. The time dependence of the displacements has been omitted in Equations (94) and (95) for brevity.

By transforming the system to the frequency domain and rearranging the terms, we arrive at Equations (96) and (97):

$$z_s = \frac{k_s}{k_s - m_s\omega^2} z_{us} \tag{96}$$

$$z_{us} = \frac{k_s - m_s\omega^2}{m_s m_{us}\omega^4 - \big((m_s + m_{us})k_s + m_s k_t\big)\omega^2 + k_s k_t} F \tag{97}$$

Where the displacements are now in the frequency domain, and the constants the same as previously.

The system of Figure 7 can then be broken down into two component subsystems. Figure 8 shows one of these subsystems as it will be treated in this derivation.

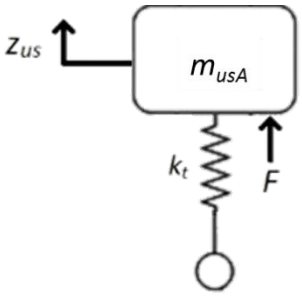

Figure 8: Tire subsystem denoted as "subsystem A"

To split up the quarter car system, the unsprung mass will be split into a part associated with the tire and a part associated with the suspension. Figure 8 shows the subsystem which corresponds to the tire portion of the unsprung mass and will be denoted as "subsystem A." As with the system from Figure 7, an equation of motion for subsystem A was derived and then transformed into the frequency domain, shown in Equations (98) and (99):

$$m_{usA}\ddot{z}_{us} + k_t z_{us} = F \tag{98}$$

$$z_{us} = \frac{1}{k_t - m_{usA}\omega^2} F \tag{99}$$

The second subsystem, “subsystem B,” contains the sprung mass and portion of the unsprung mass associated with the suspension. Subsystem B is shown in Figure 9.

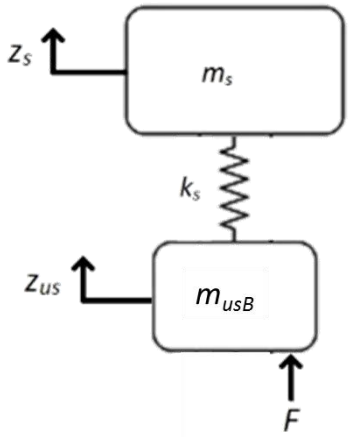

Figure 9: Suspension subsystem denoted as “subsystem B”

For subsystem B, the equations of motion associated with the sprung mass are the same as for the assembled system of Figure 7. Thus, the motion of the sprung mass is still fully described by Equations (94) and (96). As with subsystem A, the equations of motion associated with the portion of the unsprung mass in subsystem B are shown in Equations (100) and (101):

$$m_{usB}\ddot{z}_{us} - k_s(z_s - z_{us}) = F \tag{100}$$

$$z_{us} = \frac{k_s - m_s\omega^2}{m_s m_{usB}\omega^4 - (m_s + m_{usB})\omega^2} F \tag{101}$$

With all the equations of motion defined in both time and frequency domains, the next step is to employ the actual FBS techniques. Recall Equation (15) which displays the simplest, single degree of freedom (SDOF) formulation for FBS coupling as presented by [20].

$$Y^{C^{-1}} = Y^{A^{-1}} + Y^{B^{-1}} \tag{15}$$

Which can be rearranged to yield:

$$Y^C = \left(Y^{A^{-1}} + Y^{B^{-1}}\right)^{-1}$$

Where Y^C is the receptance FRF for the coupled system (Figure 7), Y^A is the receptance for subsystem A (Figure 8), and Y^B is the receptance for subsystem B (Figure 9). Specifically, these are the receptances for the unsprung mass and are found by dividing the frequency domain displacement by the force input. The expression for each receptance are shown in Equations (102) - (104):

$$Y^Q = Y^C = \frac{z_{us}}{F} = \frac{k_s - m_s\omega^2}{m_s m_{us}\omega^4 - \left((m_s + m_{us})k_s + m_s k_t\right)\omega^2 + k_s k_t} \tag{102}$$

$$Y^t = Y^A = \frac{z_{us}}{F} = \frac{1}{k_t - m_{usA}\omega^2} \tag{103}$$

$$Y^s = Y^B = \frac{z_{us}}{F} = \frac{k_s - m_s\omega^2}{m_s m_{usB}\omega^4 - (m_s + m_{usB})\omega^2} \tag{104}$$

Where Y^Q, Y^t and Y^s have been included in Equations (103) and (104) to reinforce that these receptances belong to the quarter-car system (C), tire subsystem (A), and suspension subsystem (B) respectively. These superscripts will be used throughout the remainder of this chapter.

The question now becomes, does the coupling process of Equation (15) result in Equation (102) when the expressions are put in for the subsystem receptances (Equations (103) and (104))?

$$Y^{A^{-1}} + Y^{B^{-1}} = \frac{m_s m_{usB}\omega^4 - (m_s + m_{usB})\omega^2}{k_s - m_s\omega^2} + \frac{k_t - m_{usA}\omega^2}{1} \times \frac{k_s - m_s\omega^2}{k_s - m_s\omega^2}$$

$$= \frac{m_s(m_{usA} + m_{usB})\omega^4 - \left((m_s + m_{usA} + m_{usB}) + m_s k_t\right)\omega^2 + k_s k_t}{k_s - m_s\omega^2}$$

Taking into account that:

$$m_{us} = m_{usA} + m_{usB}$$

We finally arrive at:

$$Y^C = \left(Y^{A^{-1}} + Y^{B^{-1}}\right)^{-1} = \left(\frac{m_s m_{us}\omega^4 - \left((m_s + m_{us}) + m_s k_t\right)\omega^2 + k_s k_t}{k_s - \mathrm{m_s}\omega^2}\right)^{-1}$$

Which matches up with the originally derived receptance for the coupled system as shown in Equation (102). This corroboration of results supports the use of FBS decoupling for the simplified quarter car system. Though this example was shown for coupling the two substructures together, it is apparent that Equation (15) could be rearranged for this simplified system and allow for decoupling one of the substructures from the combined system.

3.1.1 Simple Quarter Car – Direct Decoupling Dual Formulation

The simplified method of using Equation (15) for decoupling has many drawbacks including trouble dealing with ill conditioned matrices and a lack of generalization. In recent years, newer formulations for FBS decoupling have been developed such as inverse coupling [27] [30] [31] and direct decoupling [29] [23] [34].

Though full descriptions can be found in the previously mentioned references, a brief summary will be provided here. In inverse coupling the coupling equations are rearranged to subtract the known subsystem ("residual" subsystem) from the coupled system to obtain information about the unknown subsystem. In contrast, direct decoupling consists of adding to the coupled system a "fictitious" substructure with the exact opposite dynamics of the residual subsystem.

Direct decoupling can then be broken down further into primal and dual formulations. While a full description can be found in [29], another summary will be presented here. The primal formulation exactly satisfies the compatibility (displacement) conditions between the substructure, but may only satisfy the equilibrium (force) conditions in a least squares sense. On the other hand, the dual formulation exactly satisfies the equilibrium condition, but may only satisfy the compatibility condition in the least squares sense. Whether the condition is satisfied in a least squares sense or not depends on the selection of interface DOFs used, again described fully in [29].

The final form of direct decoupling via the primal formulation is shown in Equation (64):

$$\boldsymbol{Y}^{A} = \left(\begin{bmatrix} \boldsymbol{L}_E^C \\ \boldsymbol{L}_E^B \end{bmatrix}^T \begin{bmatrix} \boldsymbol{Z}^C & \boldsymbol{0} \\ \boldsymbol{0} & -\boldsymbol{Z}^B \end{bmatrix} \begin{bmatrix} \boldsymbol{L}_C^C \\ \boldsymbol{L}_C^B \end{bmatrix} \right)^{+} \begin{bmatrix} \boldsymbol{L}_E^C \\ \boldsymbol{L}_E^B \end{bmatrix}^T \tag{64}$$

Which can be rewritten in terms of the quarter-car system superscripts used for this analysis as:

$$\boldsymbol{Y}^{t} = \left(\begin{bmatrix} \boldsymbol{L}_E^Q \\ \boldsymbol{L}_E^S \end{bmatrix}^T \begin{bmatrix} \boldsymbol{Z}^Q & \boldsymbol{0} \\ \boldsymbol{0} & -\boldsymbol{Z}^S \end{bmatrix} \begin{bmatrix} \boldsymbol{L}_C^Q \\ \boldsymbol{L}_C^S \end{bmatrix} \right)^{+} \begin{bmatrix} \boldsymbol{L}_E^Q \\ \boldsymbol{L}_E^S \end{bmatrix}^T \tag{105}$$

Where $\boldsymbol{L}_E^Q$ and $\boldsymbol{L}_C^S$ are Boolean localization matrices chosen to ensure a selection of unique coupling DOFs, $\boldsymbol{Z^Q}$ is the dynamic stiffness of the coupled (quarter-car) system, and $\boldsymbol{Z}^S$ is the dynamic stiffness of the residual (suspension) subsystem. The dynamic stiffness is the inverse of the receptance:

$$\boldsymbol{Z} = \boldsymbol{Y^{-1}} \qquad \text{or} \qquad \boldsymbol{Y} = \boldsymbol{Z^{-1}}$$

In Equations (64) and (105), the "+" superscript denotes a "pseudoinverse", sometimes also called a "generalized inverse." The pseudo inverse is an inverse-like operation that behaves like the

inverse in some cases, but can be applied to overdetermined matrices as with Equation (64). In this case, the Moore-Penrose pseudoinverse is used.

For the simplified system of Figure 7-Figure 9 and Equations (102) - (104), the primal formulation can be simplified further. Each Boolean localization matrix simplifies to unit valued scalar and the pseudo inverse can be evaluated as a true inverse since the system is not overdetermined in this case. Equation (106) displays the simplified system with Y^t and Y^s shown again to reinforce to which subsystem each receptance belongs:

$$\boldsymbol{Y^t} = \left(\begin{bmatrix} 1 \\ 1 \end{bmatrix}^T \begin{bmatrix} \boldsymbol{Y^{Q}}^{-1} & 0 \\ 0 & \boldsymbol{Y^{s}}^{-1} \end{bmatrix} \begin{bmatrix} 1 \\ 1 \end{bmatrix} \right)^{-1} \begin{bmatrix} 1 \\ 1 \end{bmatrix}^T \tag{106}$$

Thus we have the receptance of the tire subsystem in terms of the receptance of the suspension subsystem and the receptance of the coupled system. Through matrix multiplication the system reduces to the following form:

$$\boldsymbol{Y^t} = \left(\boldsymbol{Y^{Q}}^{-1} - \boldsymbol{Y^{s}}^{-1} \right)^{-1} \tag{107}$$

Finally we find that:

$$\boldsymbol{Y^Q} = \left(\boldsymbol{Y^{t}}^{-1} + \boldsymbol{Y^{s}}^{-1} \right)^{-1} \qquad \text{or} \qquad \boldsymbol{Y^C} = \left(\boldsymbol{Y^{A}}^{-1} + \boldsymbol{Y^{B}}^{-1} \right)^{-1}$$

Which is the exact form of Equation (15). Thus, for the case of this simplified quarter car system, direct decoupling via the primal formulation yields the exact same results as the method discussed previously. However, it is important to note again, that this primal formulation for direct decoupling is more generalized and allows for the equilibrium condition to be satisfied in only a

least squares sense. These two facts will become more apparent in the following sections when a more complete model of the quarter car system is analyzed.

3.2 Generalized Quarter-Car Model – Multi Degree of Freedom Coupling

After the simplified model used for proof of concept in the previous section, the next step of analytical development is to look at a more realistic model.

3.2.1 Single Coupling Point with Three Coupling DOFs

The goal of this model is to more accurately represent the coupling of the tire and suspension and be applicable to testing. Figure 10 displays the basis for this more realistic model.

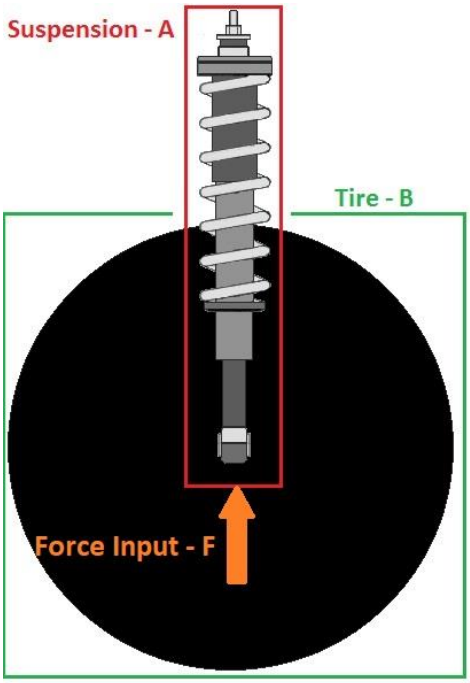

Figure 10: Basis for the improved model of this section. The suspension is considered Subsystem A and the tire is Subsystem B.

The red box outlines the suspension which is denoted Subsystem A and the green box outlines the tire which is Subsystem B. For this model, it is assumed that the tire and suspension are coupled at a single point. In contrast to the model from the previous section, this model in the longitudinal (x), lateral (y), and vertical (z) directions. In place of equations of motion, this model will deal directly with receptances and dynamic stiffnesses for the subsystems at the coupling point.

The dynamics of Figure 10 can be generally expressed by Equations (108) and (109):

$$\boldsymbol{Z^Q}(\omega)\boldsymbol{x^Q}(\omega) = \boldsymbol{f}^Q(\omega) \tag{108}$$

$$\boldsymbol{x^Q}(\omega) = \boldsymbol{Y^Q}(\omega)\boldsymbol{f^Q}(\omega) \tag{109}$$

Where, $\boldsymbol{Z^Q}$ is a matrix of dynamic stiffnesses, $\boldsymbol{Y^Q}$ is a matrix of the receptances, $\boldsymbol{x^Q}$ is a "motion" vector, and $\boldsymbol{f^Q}$ is a "forcing" vector. The superscript "Q" denotes that the values belong to the coupled, or complete system which is the assembled quarter-car system for this case.

For this first stage of the model, the motion and forcing vectors will include only displacements and forces respectively. Moments and rotations at each point will be neglected, but will be included in later work. The displacement vector and force vector will be defined as follows:

$$\boldsymbol{x^Q} = \begin{Bmatrix} d_x^Q \\ d_y^Q \\ d_z^Q \end{Bmatrix} \tag{110}$$

$$\boldsymbol{f^Q} = \begin{Bmatrix} f_x^Q \\ f_y^Q \\ f_z^Q \end{Bmatrix} \tag{111}$$

Where the superscript again denotes the system or subsystem to which the values belong and the subscripts denote the direction. With the forces and displacements as defined above, the receptances for the coupled system are defined as follows:

$$\begin{Bmatrix} d_x^Q \\ d_y^Q \\ d_z^Q \end{Bmatrix} = \begin{bmatrix} Y_{xx}^Q & Y_{xy}^Q & Y_{xz}^Q \\ Y_{yx}^Q & Y_{yy}^Q & Y_{yz}^Q \\ Y_{zx}^Q & Y_{zy}^Q & Y_{zz}^Q \end{bmatrix} \begin{Bmatrix} f_x^Q \\ f_y^Q \\ f_z^Q \end{Bmatrix} \tag{112}$$

3.2.1.1 Decoupling via the Primal Formulation – Coupled at Single Point

With the systems defined as shown in the preceding equations, the generalized primal formulation can be used. Equation (105) has been repeated below to show the size of each matrix in this instance.

$$\underbrace{\boldsymbol{Y}^t}_{3\times3} = \left(\underbrace{\begin{bmatrix} \boldsymbol{L}_E^Q \\ \boldsymbol{L}_E^S \end{bmatrix}^T}_{3\times6} \underbrace{\begin{bmatrix} \boldsymbol{Z}^Q & \boldsymbol{0} \\ \boldsymbol{0} & -\boldsymbol{Z}^S \end{bmatrix}}_{6\times6} \underbrace{\begin{bmatrix} \boldsymbol{L}_C^Q \\ \boldsymbol{L}_C^S \end{bmatrix}}_{6\times3} \right)^+ \underbrace{\begin{bmatrix} \boldsymbol{L}_E^Q \\ \boldsymbol{L}_E^S \end{bmatrix}^T}_{3\times6} \tag{113}$$

Notably, the right side of the expression would have a size of 3×6, while $\boldsymbol{Y}^t$ has a size of 3×3. However, three of the six right side columns are redundant and should thus be omitted. With that in mind, a partial derivation of the relevant quantities will be presented in the following discussion. The dynamic stiffnesses are in the form of Equation (112):

$$\boldsymbol{Z}^Q = \begin{bmatrix} Z_{xx}^Q & Z_{xy}^Q & Z_{xz}^Q \\ Z_{yx}^Q & Z_{yy}^Q & Z_{yz}^Q \\ Z_{zx}^Q & Z_{zy}^Q & Z_{zz}^Q \end{bmatrix} \tag{114}$$

$$\boldsymbol{Z}^{s} = \begin{bmatrix} Z_{xx}^{s} & Z_{xy}^{s} & Z_{xz}^{s} \\ Z_{yx}^{s} & Z_{yy}^{s} & Z_{yz}^{s} \\ Z_{zx}^{s} & Z_{zy}^{s} & Z_{zz}^{s} \end{bmatrix} \tag{115}$$

3.2.1.1.1 Derivation of Boolean Matrices

Central to the application of the primal formulation of direct decoupling is the derivation of the Boolean localization matrices. As a reminder, there are two sets of these localization matrices: one pertaining to the equilibrium condition and one pertaining to the compatibility condition. The following subsections address the derivation of these matrices individually.

3.2.1.1.1.1 Equilibrium Localization Derivation

The matrices $\boldsymbol{L}_{E}^{Q}$ and $\boldsymbol{L}_{E}^{S}$ are Boolean localization matrices pertaining to the equilibrium (force balance) condition. The size of these matrices are dependent upon the selection of DOFs which will treated as "interface DOFs". Among the three options for interface DOFs (standard, extended, or mixed), the standard interface will be used for the present derivation.

To arrive at the complete form of the Boolean matrices for decoupling the tire and suspension via the primal formulation, it is necessary to proceed from an earlier point in the formulation. Equation (54) has been repeated for convenience and displays the starting point of this derivation:

$$\begin{bmatrix} \boldsymbol{Z}^{Q} & \boldsymbol{0} \\ \boldsymbol{0} & -\boldsymbol{Z}^{\boldsymbol{s}} \end{bmatrix} \begin{Bmatrix} \boldsymbol{x}^{\boldsymbol{Q}} \\ \boldsymbol{x}^{\boldsymbol{s}} \end{Bmatrix} = \begin{Bmatrix} \boldsymbol{f}^{Q} \\ \boldsymbol{f}^{\boldsymbol{s}} \end{Bmatrix} + \begin{Bmatrix} \boldsymbol{g}^{Q} \\ \boldsymbol{g}^{\boldsymbol{s}} \end{Bmatrix} \tag{54}$$

Where the $\boldsymbol{Z}$'s are dynamic stiffness matrices, the $\boldsymbol{x}$'s are displacement vectors, the $\boldsymbol{f}$'s are external force vectors, and the $\boldsymbol{g}$'s are internal coupling force vectors.

From Equation (54) the primal formulation proceeds with the assumptions that the coupling forces between the tire and suspension substructures must cancel each other out. Specifically, if the coupling forces are defined as:

$$\boldsymbol{g^Q} = \begin{Bmatrix} g_x^Q \\ g_y^Q \\ g_z^Q \end{Bmatrix} \tag{116}$$

$$\boldsymbol{g^s} = \begin{Bmatrix} g_x^s \\ g_y^s \\ g_z^s \end{Bmatrix} \tag{117}$$

Then the following must be satisfied:

$$g_x^Q + g_x^s = 0 \tag{118}$$

$$g_y^Q + g_y^s = 0 \tag{119}$$

$$g_z^Q + g_z^s = 0 \tag{120}$$

The Boolean localization matrices $\boldsymbol{L_E^C}$ and $\boldsymbol{L_E^B}$ must be formulated in such a way that they satisfy Equations (118)-(120) and are in the form of Equation (56) which has been repeated here for convenience:

$$\begin{bmatrix} \boldsymbol{L_E^Q} \\ \boldsymbol{L_E^s} \end{bmatrix}^T \begin{Bmatrix} \boldsymbol{g^Q} \\ \boldsymbol{g^s} \end{Bmatrix} = \boldsymbol{0} \tag{56}$$

Where:

$$\boldsymbol{L}_E^T = \begin{bmatrix} \boldsymbol{L}_E^Q \\ \boldsymbol{L}_E^s \end{bmatrix}^T$$

Thus, Equation (56) now appears as:

$$\boldsymbol{L}_E^T \begin{Bmatrix} g_x^Q \\ g_y^Q \\ g_z^Q \\ g_x^s \\ g_y^s \\ g_z^s \end{Bmatrix} = \begin{Bmatrix} g_x^Q + g_x^s \\ g_y^Q + g_y^s \\ g_z^Q + g_z^s \end{Bmatrix} = \begin{Bmatrix} 0 \\ 0 \\ 0 \end{Bmatrix} \tag{121}$$

Note that, as mentioned previously, $\boldsymbol{L}_E^T$ would have a size of 3×6 which corresponds to the matrix sizes in Equation (121). Based off of Equation (121), the Boolean localization matrix for the equilibrium condition ($\boldsymbol{L}_E^T$) can be constructed row by row. The result of this row by row construction is shown in Equation (122).

$$\begin{bmatrix} \boldsymbol{L}_E^Q \\ \boldsymbol{L}_E^s \end{bmatrix}^T = \begin{bmatrix} 1 & 0 & 0 & 1 & 0 & 0 \\ 0 & 1 & 0 & 0 & 1 & 0 \\ 0 & 0 & 1 & 0 & 0 & 1 \end{bmatrix} \tag{122}$$

This localization matrix will later be used to obtain the final formulation for decoupling the suspension form the quarter-car system.

3.2.1.1.1.2 Compatibility Localization Derivation

The matrices $\boldsymbol{L}_C^Q$ and $\boldsymbol{L}_C^s$ are Boolean localization matrices pertaining to the compatibility (displacement equivalency) condition. The choice of the compatibility localization matrices relies on the choice of a unique set of DOFs. Since the compatibility condition relies on the displacement of the coupling DOFs, the form of the displacement vectors are shown below:

$$\boldsymbol{x^Q} = \begin{Bmatrix} d_x^Q \\ d_y^Q \\ d_z^Q \end{Bmatrix} \tag{110}$$

$$\boldsymbol{x^s} = \begin{Bmatrix} d_x^s \\ d_y^s \\ d_z^s \end{Bmatrix} \tag{123}$$

As mentioned in the derivation of the equilibrium interface DOFs, for this current model the standard interface DOF selection is being used. Thus the compatibility condition will be satisfied exactly. Mathematically, the compatibility condition for the current system can be expressed as:

$$d_x^Q = d_x^s \tag{124}$$

$$d_y^Q = d_y^s \tag{125}$$

$$d_z^Q = d_z^s \tag{126}$$

Where Equations (124)-(126) qualitatively specify that the assumed coupling point between the tire and the suspension must have the same displacement both for the coupled (quarter-car) system and the residual (suspension) subsystem. With this in mind, the Boolean localization for the compatibility condition need to be constructed such that they satisfy the form of Equation (57)

$$\begin{Bmatrix} \boldsymbol{x}^Q \\ \boldsymbol{x^s} \end{Bmatrix} = \begin{bmatrix} \boldsymbol{L}_C^Q \\ \boldsymbol{L}_C^s \end{bmatrix} \{\boldsymbol{q}\} \tag{57}$$

Where $\boldsymbol{q}$ is the vector of unique DOFs and the compatibility localization matrix is:

$$\boldsymbol{L}_C = \begin{bmatrix} \boldsymbol{L}_C^Q \\ \boldsymbol{L}_C^s \end{bmatrix}$$

Thus, Equations (124)-(126) can be rewritten with the form Equation (57) in mind as:

$$d_x^Q = d_x^s = q_x \tag{127}$$

$$d_y^Q = d_y^s = q_y \tag{128}$$

$$d_z^Q = d_z^s = q_z \tag{129}$$

Thus, according to the form of Equation (57) the compatibility localization matrix must be constructed such that:

$$\begin{Bmatrix} d_x^Q \\ d_y^Q \\ d_z^Q \\ d_x^s \\ d_y^s \\ d_z^s \end{Bmatrix} = \boldsymbol{L}_C \begin{Bmatrix} q_x \\ q_y \\ q_z \end{Bmatrix} \tag{130}$$

As mentioned previously, $\boldsymbol{L}_C$ is a 6×3 matrix which agrees with the dimension of Equation (130). As with the construction of the equilibrium localization matrix, the compatibility localization matrix can be constructed in a row by row manner. The result of this row by row construction is Equation (131) which satisfies the requirements of Equations (127)-(129)

$$\begin{bmatrix} \boldsymbol{L}_C^Q \\ \boldsymbol{L}_C^s \end{bmatrix} = \begin{bmatrix} 1 & 0 & 0 \\ 0 & 1 & 0 \\ 0 & 0 & 1 \\ 1 & 0 & 0 \\ 0 & 1 & 0 \\ 0 & 0 & 1 \end{bmatrix} \tag{131}$$

Equation (131), along with the other necessary equations will be put together in the following subsection to complete the primal formulation for decoupling the suspension from the assembled quarter-car system at a single point.

3.2.1.1.2 Complete Primal Formulation - Single Coupling Point

The full form of the primal formulation for decoupling the suspension from the quarter-car system is obtained by substituting Equations (114), (115), (122), and (131) into Equation (105) which is repeated here for convenience:

$$\boldsymbol{Y}^t = \left(\begin{bmatrix} \boldsymbol{L}_E^Q \\ \boldsymbol{L}_E^S \end{bmatrix}^T \begin{bmatrix} \boldsymbol{Z}^Q & \boldsymbol{0} \\ \boldsymbol{0} & -\boldsymbol{Z}^S \end{bmatrix} \begin{bmatrix} \boldsymbol{L}_C^Q \\ \boldsymbol{L}_C^S \end{bmatrix} \right)^+ \begin{bmatrix} \boldsymbol{L}_E^Q \\ \boldsymbol{L}_E^S \end{bmatrix}^T \tag{105}$$

The result of substituting in the aforementioned equations into Equation (105) is shown in Equation (132)

$$\boldsymbol{Y}^t$$

$$= \left(\begin{bmatrix} 1 & 0 & 0 & 1 & 0 & 0 \\ 0 & 1 & 0 & 0 & 1 & 0 \\ 0 & 0 & 1 & 0 & 0 & 1 \end{bmatrix} \begin{bmatrix} Z_{xx}^Q & Z_{xy}^Q & Z_{xz}^Q & 0 & 0 & 0 \\ Z_{yx}^Q & Z_{yy}^Q & Z_{yz}^Q & 0 & 0 & 0 \\ Z_{zx}^Q & Z_{zy}^Q & Z_{zz}^Q & 0 & 0 & 0 \\ 0 & 0 & 0 & -Z_{xx}^S & -Z_{xy}^S & -Z_{xz}^S \\ 0 & 0 & 0 & -Z_{yx}^S & -Z_{yy}^S & -Z_{yz}^S \\ 0 & 0 & 0 & -Z_{zx}^S & -Z_{zy}^S & -Z_{zz}^S \end{bmatrix} \begin{bmatrix} 1 & 0 & 0 \\ 0 & 1 & 0 \\ 0 & 0 & 1 \\ 1 & 0 & 0 \\ 0 & 1 & 0 \\ 0 & 0 & 1 \end{bmatrix} \right)^+ \tag{132}$$

$$\times\times \begin{bmatrix} 1 & 0 & 0 & 1 & 0 & 0 \\ 0 & 1 & 0 & 0 & 1 & 0 \\ 0 & 0 & 1 & 0 & 0 & 1 \end{bmatrix}$$

When the matrix multiplication within the pseudo inverse is carried out and simplified it results in the following:

$$\boldsymbol{Y}^t = \begin{bmatrix} Z^Q_{xx} - Z^s_{xx} & Z^Q_{xy} - Z^s_{xy} & Z^Q_{xz} - Z^s_{xz} \\ Z^Q_{yx} - Z^s_{yx} & Z^Q_{yy} - Z^s_{yy} & Z^Q_{yz} - Z^s_{yz} \\ Z^Q_{zx} - Z^s_{zx} & Z^Q_{zy} - Z^s_{zy} & Z^Q_{zz} - Z^s_{zz} \end{bmatrix}^+ \begin{bmatrix} 1 & 0 & 0 & 1 & 0 & 0 \\ 0 & 1 & 0 & 0 & 1 & 0 \\ 0 & 0 & 1 & 0 & 0 & 1 \end{bmatrix} \tag{133}$$

In this case, the pseudo inverse is a Moore-Penrose inverse. Due to the lengthy nature of the symbolic solution for $\boldsymbol{Y}^t$, it will not be presented in full. It was mentioned previously that the size of the resulting $\boldsymbol{Y}^t$ was actually 3×6. Since the right most matrix in Equation (133) is simply two identity matrices, it is clear that the resulting $\boldsymbol{Y}^t$ will have three sets of duplicated columns. For practical purposes, the duplicate columns are discarded, finally yielding a 3×3 matrix for $\boldsymbol{Y}^t$.

In summary, Equation (133) gives the receptance of the tire ($\boldsymbol{Y}^t$) in terms of the suspension ($\boldsymbol{Y}^s$) and the assembled quarter-car system ($\boldsymbol{Y}^Q$). However, the assignment of the which subsystem was consider the residual (known) was arbitrary, which means that Equation (133) could also give the receptance of the suspension in terms of the tire and assembled system.

The solution obtained in the previous section is applicable to experimentally obtained data and will be validated once experimental work is complete. Though this solution is sufficient, there are improvements to be made which will increase the quality and reliability of the solution. Namely more realistic locations can be chosen for the interface DOFs (such as the bolts on the wheel hub) and the effects of rotational properties can be accounted for. The following sections presents possibilities for such improvements.

3.2.2 Rotational DOFs

Rotational properties are notoriously difficult to measure when working solely with experimentally obtained FRFs [23]. This difficulty is in part due to the limitations in experimental capabilities for applying pure moments and measuring pure rotations [55]. However, these difficulties apply only

to substructure coupling, not decoupling. Rotational DOFs do not have to be included in decoupling formulations because the rotational constraints are inherent in the interface DOFs measure on the coupled structure. In other words, since the independent substructures experience rotations and moments when they are coupled together, measurements taken on the assembled structure will already include the effects of these rotations [35].

Though rotational DOFs are unnecessary in decoupling, one future application of this work is to couple together FRFs from various tires to the suspension to analyze the combined properties. Thus, it is important to collect data on the coupling interface in such a way that rotational DOFs could be included in subsequent coupling applications. Without accounting for rotational DOFs, the system of the previous section can be thought of as pinned at a single point, but able to pivot about that point. Obviously, the tire cannot pivot freely about the wheel hub in real quarter car system, so rotational DOFs need to be included. One such method for included rotations in the coupling process is the equivalent multi-point connection (EMPC) method.

3.2.2.1 Equivalent Multi-Point Connection (EMPC) Method

In finite element (FE) analysis, subsystems are coupled at discrete DOFs at the interfaces. Rotational information is easily obtained from spacing between and translational information at these discrete DOFs. The EMPC method makes use of similar concepts for frequency based substructuring. The coupling at the interface between structures is performed at multiple points and in multiple directions. Figure 11 displays the concept of coupling at multiple points which is central to the EMPC method.

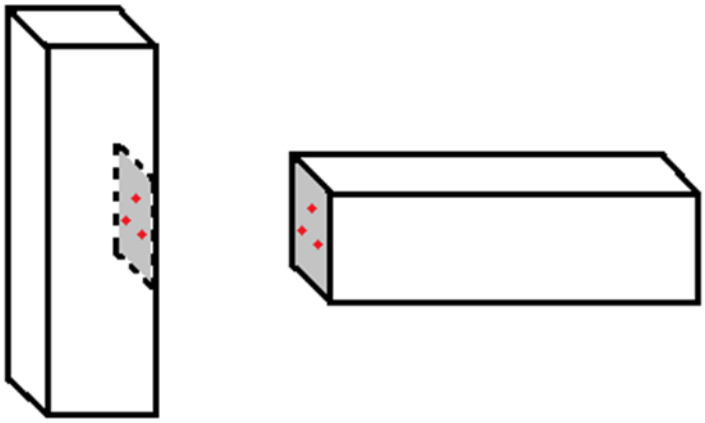

Figure 11: Graphical representation of the EMPC method. The three dots in the shaded regions represent measurement points

If the tire/suspension system was considered to be coupled in the same manner as the system in Figure 11 (3 points), then the system would no longer be able to pivot about the coupling interface. It is important to note that the number of FRFs used in the EMPC method must correspond to at least the number of DOFs which describe the interface. For either the tire/suspension system or the system of Figure 11, the motion of the coupled region can be described by six coupling DOFs (three displacements, three rotations) as long as the interface region can be considered rigid. Thus, at least 6 translational DOFs are needed from the three points of Figure 11 in order to use the EMPC method [17].

It is important to note that the distance between the points used for the EMPC method can determine the overall effectiveness of the method. The EMPC method will deliver good results up to frequencies where the interface starts to deform between the coupling DOFs. This problem can be remedied by the inclusion of DOFs at additional coupling points and comparison with known deformation modes for the coupling interface [17].

3.2.3 Three Coupling Points – Nine Coupling DOFs

The system of Figure 11 in the previous section was considered to be coupled at three DOFs at a single point in the middle of the tire. In reality, the coupling will occur at each of the bolts joining the tire and the wheel hub. The bolting configuration for most passenger cars is in a four, five, or six (or even more in certain cases) bolt configuration with the most common being five bolts. The rest of this section will carry on with the assumption that the tire/suspension system under consideration has a five bolt configuration.

3.2.3.1 Interface DOF Locations and Experimental Considerations

Based on the EMPC method, the most intuitive choice for coupling interface DOFs between the tire and wheel hub is around a circle circumscribing the bolt pattern. This is the case because the circumscribed circle is a generalization of the symmetric nature of the bolt pattern with the assumption that the area between each bolt can be treated as rigid. Figure 12 displays a regular pentagon (the standard pattern for a 5 bolt configuration) with a circumscribed circle.

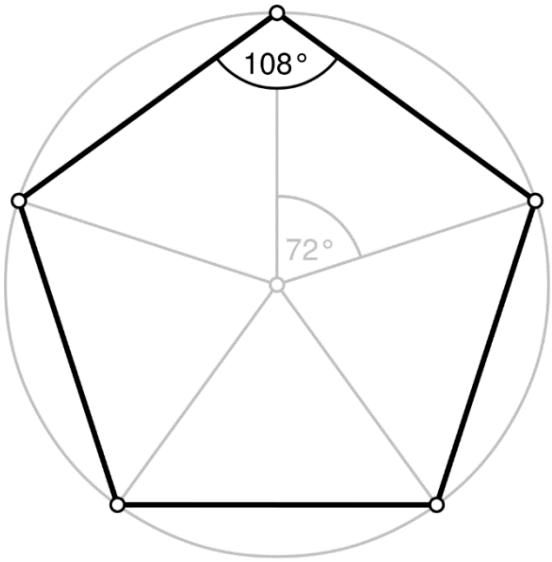

Figure 12: A regular pentagon with a circumscribed circle. This is the standard configuration for a tire with 5 bolts.

Ideally, the points selected for decoupling would be directly on the coupling points which are the bolts in this case. There are a few issues with this choice which would make experimental application difficult. First, though it is easy to measure FRFs (via accelerometers) on the bolts of the coupled system or the wheel hub/suspension subsystem, it is not possible to measure directly on the bolt holes of the tire/wheel assembly. Second, any triangle of measurement points located on the bolts cannot have its geometric center located at the center of the bolting configuration.

Thus, we consider the case of an equilateral triangle of points as the choice for the interface coupling DOFs. Figure 13 displays a potential orientation for this equilateral triangle.

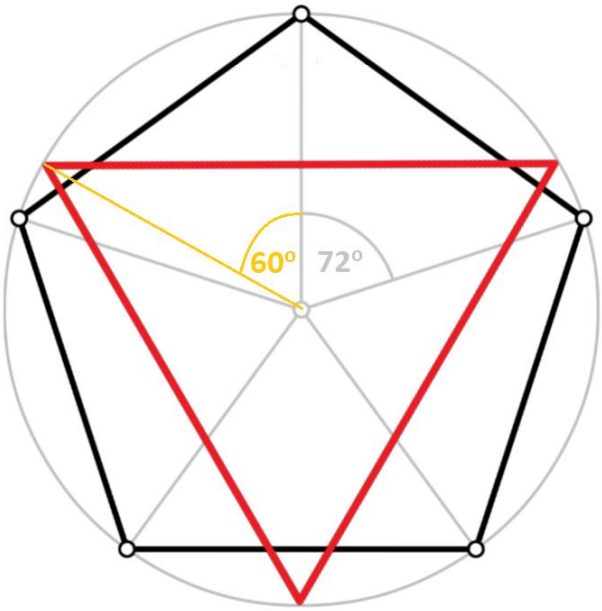

Figure 13: The bolting pattern from Figure 12 with an equilateral triangle superimposed to show the planned choice of interface DOF locations

The interface DOFs would be located at the corners of the triangle in Figure 13. This orientation addresses both of the previously mentioned concerns: no interface DOF is located on a bolt location and the geometric center of the equilateral triangle matches up with that of the bolting configuration. It is important to note that this choice of interface DOFs is based on the assumption

the area between the bolts can be considered rigid and that these points can accurately describe the coupling of the tire and suspension subsystems.

3.2.3.2 Decoupling via the Primal Formulation – Coupled at Three Points

The primal formulation for decoupling the suspension from the assembled quarter-car is conceptually the same for the coupling at three points as it is for the coupling at a single point. However, some generalizations must be made, and will thus be presented here. In the form of Equation (114) we define the dynamic stiffness for the assembled quarter car system at coupling point "k" as:

$$\boldsymbol{Z}_k{}^{Q} = \begin{bmatrix} Z_{xx}^{Q} & Z_{xy}^{Q} & Z_{xz}^{Q} \\ Z_{yx}^{Q} & Z_{yy}^{Q} & Z_{yz}^{Q} \\ Z_{zx}^{Q} & Z_{zy}^{Q} & Z_{zz}^{Q} \end{bmatrix} \tag{134}$$

The dynamic stiffness for the "kth" coupling point is defined similarly for the suspension subsystem and will be denoted with the superscript "s." Thus, the complete dynamics stiffness matrices for the quarter-car system and suspension are defined as follows:

$$\boldsymbol{Z}^{Q} = \begin{bmatrix} \boldsymbol{Z}_1^{Q} & \mathbf{0} & \mathbf{0} \\ \mathbf{0} & \boldsymbol{Z}_2^{Q} & \mathbf{0} \\ \mathbf{0} & \mathbf{0} & \boldsymbol{Z}_3^{Q} \end{bmatrix} \tag{135}$$

$$\boldsymbol{Z}^{s} = \begin{bmatrix} \boldsymbol{Z}_1^{s} & \mathbf{0} & \mathbf{0} \\ \mathbf{0} & \boldsymbol{Z}_2^{s} & \mathbf{0} \\ \mathbf{0} & \mathbf{0} & \boldsymbol{Z}_3^{s} \end{bmatrix} \tag{136}$$

In a similar manner, a corresponding block matrix representation can be developed for both the equilibrium and the compatibility matrices.

$$\boldsymbol{L}_E^T = \begin{bmatrix} \boldsymbol{L}_{E1}^{\boldsymbol{T}} & \mathbf{0} & \mathbf{0} \\ \mathbf{0} & \boldsymbol{L}_{E2}^{\boldsymbol{T}} & \mathbf{0} \\ \mathbf{0} & \mathbf{0} & \boldsymbol{L}_{E3}^{\boldsymbol{T}} \end{bmatrix} \tag{137}$$

$$\boldsymbol{L}_C = \begin{bmatrix} \boldsymbol{L}_{C1} & \mathbf{0} & \mathbf{0} \\ \mathbf{0} & \boldsymbol{L}_{C2} & \mathbf{0} \\ \mathbf{0} & \mathbf{0} & \boldsymbol{L}_{C3} \end{bmatrix} \tag{138}$$

Where the subscript on $\boldsymbol{L}_{E1}$ specifies that the matrix is related to equilibrium at coupling point number 1 and the subscript on $\boldsymbol{L}_{C3}$ specifies that the matrix is related to the compatibility condition at coupling point number 3. Recall from the derivation presented for coupling at a single point that:

$$\boldsymbol{L}_C = \begin{bmatrix} \boldsymbol{L}_C^Q \\ \boldsymbol{L}_C^s \end{bmatrix} \quad \text{and} \quad \boldsymbol{L}_E^T = \begin{bmatrix} \boldsymbol{L}_E^Q \\ \boldsymbol{L}_E^s \end{bmatrix}^T$$

Thus, Equation (137) and (138) contain parts relating to both the quarter-car system and the suspension subsystem. From Equations (135)-(138), the dimensions of Equation (113) can be rewritten to reflect the dimensions corresponding to the coupling at three points.

$$\underbrace{\boldsymbol{Y}^t}_{9\times 9} = \left(\underbrace{\boldsymbol{L}_E^T}_{9\times 18} \underbrace{\begin{bmatrix} \boldsymbol{Z}^Q & \mathbf{0} \\ \mathbf{0} & -\boldsymbol{Z}^s \end{bmatrix}}_{18\times 18} \underbrace{\boldsymbol{L}_C}_{18\times 9} \right)^+ \underbrace{\boldsymbol{L}_E^T}_{9\times 18} \tag{139}$$

Again, recall that the dimensions of the left hand side do not match that of the right hand side due to duplicate entries which will appear.

$$\boldsymbol{Y}^{t} = \left(\begin{bmatrix} \boldsymbol{L}_{E1}^{\boldsymbol{T}} & \boldsymbol{0} & \boldsymbol{0} \\ \boldsymbol{0} & \boldsymbol{L}_{E2}^{\boldsymbol{T}} & \boldsymbol{0} \\ \boldsymbol{0} & \boldsymbol{0} & \boldsymbol{L}_{E3}^{\boldsymbol{T}} \end{bmatrix} \begin{bmatrix} \boldsymbol{Z}_{1}^{Q} & \boldsymbol{0} & \boldsymbol{0} & \boldsymbol{0} & \boldsymbol{0} & \boldsymbol{0} \\ \boldsymbol{0} & \boldsymbol{Z}_{2}^{Q} & \boldsymbol{0} & \boldsymbol{0} & \boldsymbol{0} & \boldsymbol{0} \\ \boldsymbol{0} & \boldsymbol{0} & \boldsymbol{Z}_{3}^{Q} & \boldsymbol{0} & \boldsymbol{0} & \boldsymbol{0} \\ \boldsymbol{0} & \boldsymbol{0} & \boldsymbol{0} & -\boldsymbol{Z}_{1}^{S} & \boldsymbol{0} & \boldsymbol{0} \\ \boldsymbol{0} & \boldsymbol{0} & \boldsymbol{0} & \boldsymbol{0} & -\boldsymbol{Z}_{2}^{S} & \boldsymbol{0} \\ \boldsymbol{0} & \boldsymbol{0} & \boldsymbol{0} & \boldsymbol{0} & \boldsymbol{0} & -\boldsymbol{Z}_{3}^{S} \end{bmatrix} \begin{bmatrix} \boldsymbol{L}_{C1} & \boldsymbol{0} & \boldsymbol{0} \\ \boldsymbol{0} & \boldsymbol{L}_{C2} & \boldsymbol{0} \\ \boldsymbol{0} & \boldsymbol{0} & \boldsymbol{L}_{C3} \end{bmatrix} \right)^{+} \times \\ \times \begin{bmatrix} \boldsymbol{L}_{E1}^{\boldsymbol{T}} & \boldsymbol{0} & \boldsymbol{0} \\ \boldsymbol{0} & \boldsymbol{L}_{E2}^{\boldsymbol{T}} & \boldsymbol{0} \\ \boldsymbol{0} & \boldsymbol{0} & \boldsymbol{L}_{E3}^{\boldsymbol{T}} \end{bmatrix} \tag{140}$$

The duplicate entries from Equation (140) should be discarded as mentioned previously in this chapter. In its current form, Equation (140) can be directly applied to experimental data, given that the sub-matrices are organized as discussed earlier in this section. It is important to note that the translational information at these three points can be used to extract rotational information using the EMPC method which was also discussed in this chapter. Though accounting for rotations is not strictly necessary for the decoupling process [35], the final formulation of Equation (140) supports the ability to do so and improves the potential for later coupling other tire or suspension data together.

The work presented in this chapter will be expanded upon in the follow chapters. Specifically, the formulations developed here will be validated in **Chapter 5** with several levels of models and, finally, with experimental data. First, the following chapter, **Chapter 4**, will detail the design and construction of the various test setups.

Chapter 4 – Experimental Design and Setup

In order to put the analytical developments of **Chapter 3** into practice, frequency response functions must be obtained for the quarter car system and one of its subsystems. While this can be done analytically or for simulated models, the ultimate goal of the present work is to apply these developments to experimental data. To that end, it was necessary to develop a quarter car test rig which was capable of the required testing. Currently, only a small-scale system will be used for experimental testing. However, much time and effort was put into preparing a full scale test rig so a brief overview of that work will also be presented in this chapter.

4.1 Full Scale Quarter Car Test Rig

The Center for Tire Research (CenTiRe) possess a quarter-car test rig which was partially developed as part of a senior design project and was completed during this research. Though the rig itself was fully functional, there were several issues which prevented it from being of immediate use. Specifically, the setup of the hydraulic actuation system was incomplete and the vibration of the test fixture overlapped too much with the frequency range of interest. The following subsections will provide an overview of the existing test setup as well as a brief description of the design work which was done to make the system fully functional.

4.1.1 Test Rig Overview

As an overall view, the rig can be described as four support beams which are fixed to the ground and hold the guide rails along which the test fixture can translate in the vertical direction. A more

complete description of each component will be given in turn. To facilitate the description, the test rig can be broken down conceptually into its two primary components: the “inner cage” and the support beams.

The inner cage is an assembly of 80/20 aluminum extrusions which are composed of 6105-T5 aluminum alloy. The specific extrusions used in the test setup are either 1515 or 1530 which indicates rectangular cross section dimensions of 1.5 x 1.5 inches or 1.5 x 3.0 inches, respectively. Figure 14 displays the completed, assembled test rig.

Figure 14: Completed CenTiRe Quarter-Car test rig

In Figure 14, the four support beams are the steel beams which are bolted to the ground and the inner cage is the silver assembly between the supports. The top of the inner cage is a wide, flat area where weights can be fastened to increase the sprung mass of the system or to apply a static load to the quarter-car system. Directly below that area is the mounting point for the suspension strut. In the interest of brevity, the finer details of the inner cage design will be omitted here.

As mentioned previously, the four support beams are used to hold the inner cage and are fixed to the ground. These support beams are 10 feet long 3/8-inch-thick square tube steel beams which hold the steel rails of the bearing system mentioned in the previous section. Figure 15 shows a single support beam with the guide rail being prepared to be attached.

Figure 15: Single support beam with guide rail attached

As shown in Figure 15, each guiderail mount is connected to the support beam on a steel plate with slotted holes. This connection method is important for the alignment of the guiderails in order to reduce friction. The connection between the supports and the ground is shown in Figure 16.

Figure 16: Connection between support beam and ground

Figure 16 shows the steel baseplate which was welded to the bottom of the support beam in order to provide a more stable and rigid connection between the support and the ground. Four bolts, each 5 inches long and 5/8 inches in diameter are used to fix the baseplate to the concrete floor.

The precision of the guiderail alignment and the support beam distancing is vital to ensure that there is minimal vertical friction exerted on the bearings by the guide rails. Thus, these parameters were a central part of the design changes which were planned for the test rig. These changes will be discussed in detail later in the current chapter.

Just as important as the mechanical issues related to bearing friction, the vibration of the test structure must be kept out of the range of interest (up to ≈70 Hz for the full scale system). The senior design group responsible for the test rig carried out some finite element modal analysis during the design process. However, the analysis was on each component individually (i.e. on a

single support beam and on the inner cage by itself). While a good starting place, that modal analysis did not accurately represent the assembled rig. Preliminary hammer tests on the rig revealed modes between 10 and 15 Hz. Thus, much of the additional design work for the test rig centered on stiffening the entire structure to increase the first natural frequency above 70 Hz. The design improvements to the test rig, along with the design of accompanying test setup components is discussed in greater detail in the following section.

4.1.2 Redesign and Continued Development of Full Scale Test Rig

Though the quarter car test rig had been completed and installed, the design problems raised in the previous section needed to be addressed. Aside from design improvements, several other components needed to be developed or assembled, such as the actuator mount table and the hydraulic system. These designs and developments will be discussed in greater detail in the present section.

Design changes relating to vibrations were addressed first, because the addition of new stiffening members may cause beam alignment changes. A full 3D finite element (FE) model of the test rig was created in ABAQUS along with some necessary simplifications. Since this test rig was not put into use for this research, a full account of the FE model will not be discussed in this dissertation in the interest of brevity. Modal analysis was performed on the model which showed swaying of the support beams similar to that seen in the preliminary testing, approximately 10-15 Hz. When the rig was designed, only vibration of each component individually was considered. However, when the inner cage is attached to the support beam, it can be viewed conceptually as a lumped mass being added to the end of a cantilevered beam. Thus, though the support beams did

not exhibit unwanted frequencies by themselves, the resulting frequencies for the assembled system were directly in the range of interest, 0 – 70 Hz.

In order to validate the FE model, a full modal test was planned and set up for the test rig. However, only preliminary modal tests were conducted before work on the test rig was halted (the reason for which will be discussed later in this section). Though the FE model was not fully validated, the preliminary results showed that the model could give at least a general idea of the frequency response characteristics. Thus, additions were made to the model in order to stiffen the support posts and increase the first natural frequency. Several different iterations of stiffening support structures were considered, such as members connecting to the adjacent walls or alternatively as members connected to the ground. One such model is shown below in Figure 17.

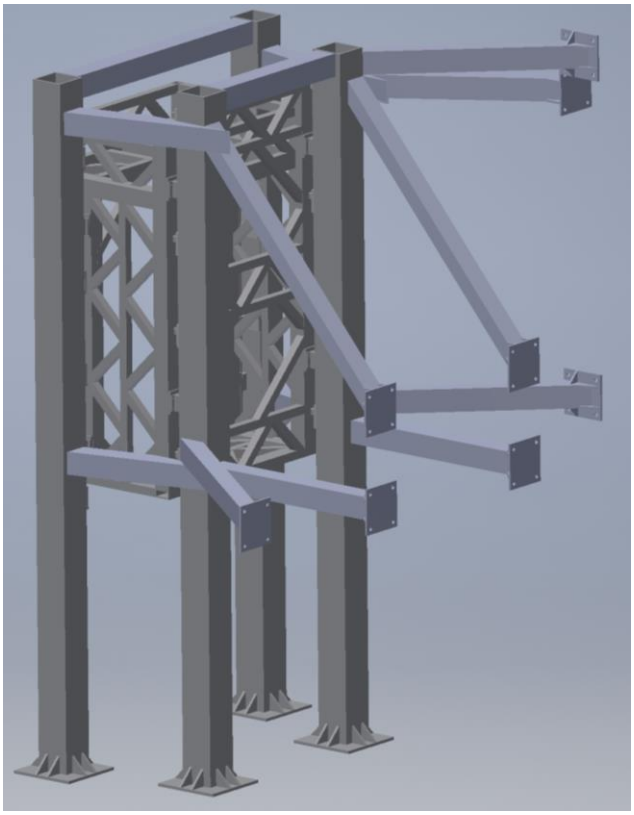

Figure 17: CAD model of quarter car test rig with additional stiffening members

Figure 17 shows a back view of the test rig where supports were connected to adjacent walls. Some aspects of the design were influenced by the structure of the walls to which the support members were to be connected. Both new designs (supports to the wall or to the ground), pushed the first natural frequency of the test rig just above 70 Hz. Final design selection and approval from Facilities managers were in progress when work on the test rig was halted.

One challenge that had to be addressed for the actuation of the system was the design of mounting table for the hydraulic actuator. The actuator mount needed to be able to support any forces imposed on it during tests, while also being adjustable for testing of other tire/suspension systems. A final design was decided on which consisted of permanent bolts into the concrete floor with an adjustable upper portion. A drawing of this design is shown in Figure 18

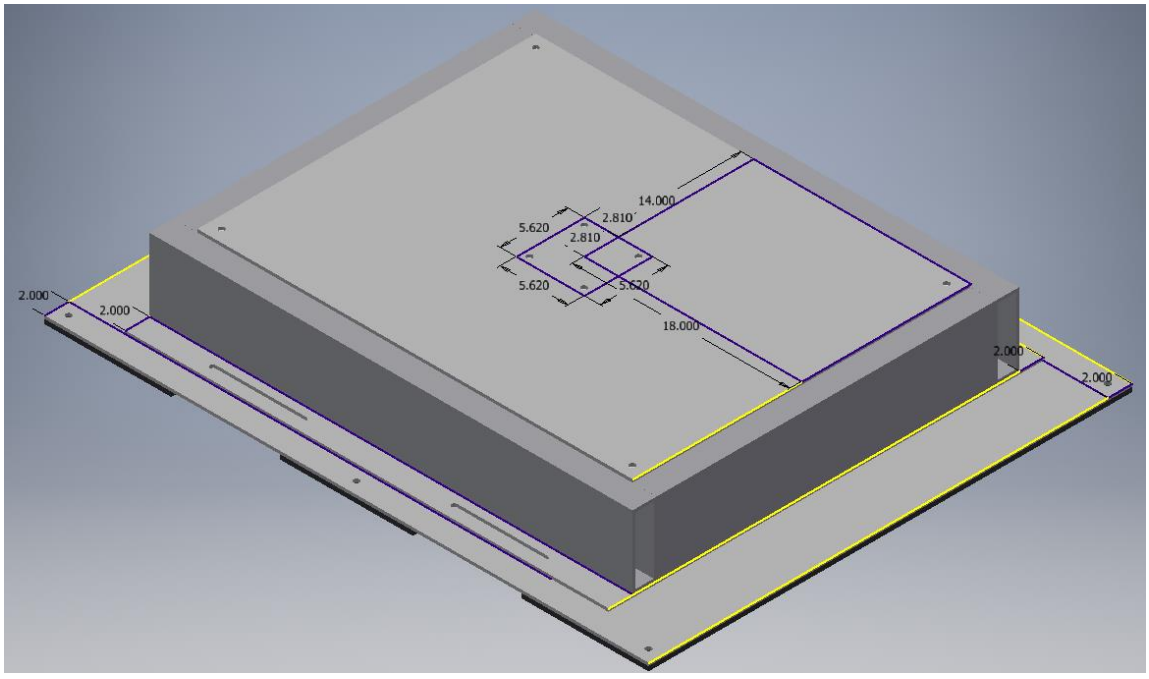

Figure 18: Hydraulic actuator mounting table

The upper portion of the assembly is square steel tubing which surrounds a poured concrete base with a steel plate on top. Four holes in the center of the steel plate mark where the actuator would be mounted.

Before any of the design changes from this section could be put into place, the hydraulic actuation system needed to be assembled and calibrated. Many design considerations went into the selection and assembly of the hydraulic system, such as hose size, servo valves, load cell, and control method to name a few. As with the other developments described in this section, further detail will not be given in order to keep descriptions concise. Once all design decisions were made, technicians from MTS (the manufacturer of our system) were brought in to finish the assembly and calibrate the system.

During the final stage of setup, when the system was being run for calibration, one of the technicians discovered an issue with the hydraulic supply unit. The heater exchanger was leaking water into the oil reservoir of the supply unit. Unfortunately, replacement of the heat exchanger and hydraulic oil was cost prohibitive for this project. Thus, all of the aforementioned designs and developments were halted immediately. The work presented in the preceding section was included here due to the time and effort which went into the process. However, as soon as work on the full scale test rig stopped, development began on a small-scale system which could be fabricated and tested within the budgetary confines of this project.

4.2 Motivation for small-scale quarter car system

The original test plan was to validate the work in previous sections by carrying out the corresponding experimental application for coupling/decoupling on a full scale quarter car setup

as discussed above. Due to unforeseen issues with the hydraulic actuation system, the process will instead be validated using a new small scale quarter car setup.

Scale models have been used extensively throughout the history of engineering. Furthermore, there is ample precedent specifically in the field of vehicle dynamics for using scaled vehicle systems to test or validate concepts. With respect to vehicle dynamics, these systems are typically used in the case that full scale testing is not possible for capability or safety reasons. For instance, scaled vehicles have been used for anti-lock braking system (ABS) control development [110-112], development of vehicle automation [113], or simply as a cheaper and more controllable method to test vehicle dynamics [114-118].

One of the most important factors in any scaled model is the ability to accurately represent the full scale system. In many applications, Pi's theorem of dimensionless parameters is often used for this purpose. However, as the present application is only concerned with vertical vibration of the tire and suspension, the scaling down of the system is greatly simplified from other applications. In any application that relates to on road handling or vehicle dynamics, dimensionless parameters which relate to a number of handling factors must be established. For example, even for the bicycle model in [114], dimensionless parameters must be established for factors relating to: center of gravity location, cornering forces and yaw moment of inertia.

As mentioned, scaling for the current application is much more direct since it pertains specifically to vertical vibrations of the quarter car system. In terms of vibrations, frequency (in radians) and viscous damping ratio are already effectively dimensionless parameters. Thus, a "similar" quarter car system could be constructed which has approximately the same natural frequencies and damping ratios as the full scale model. However, for the present purpose, not even those values

necessarily need to be the same in order to demonstrate application of the coupling/decoupling process to a quarter car system. A major contribution of this work is the experimental test setup suitable for applying decoupling processes. Even though all accompanying equipment would also need to be scaled up, the test setup developed for the small scale system will be conceptually applicable to full scale.

Though unnecessary, an attempt was made to preserve natural frequencies of the full scale system. However, not all properties of the system could actually be scaled. One such property is the nonlinearity in the tire. The nonlinearity in a typical radial passenger car tire is caused by a combination of complex factors. Among these factors are the pressure-deflection relationship and the composite construction of the tire body from a combination of steel and rubber components. Even commercially available small pressurized tires do not mimic the nonlinearities of the full scale radial tires.

Though the type of nonlinearity will be different, it is crucial for the present application to have some nonlinearity present. One of the challenges of applying FBS decoupling techniques to a quarter car system is the nonlinearity of the tire. Thus, it is of primary interest if the tire of the small scale system demonstrates nonlinearity, and if so, how can it be described. This and other experimental considerations will be discussed in the following sections.

4.2.1 Development of small-scale quarter car system

The scaled vehicle chosen for this experiment was the 1/5 scale Traxxas X-maxx 6s model, hereafter referred to as the “test vehicle.” The test vehicle is a large off-road model which has an independent suspension for each wheel. Among the most important factors in the selection of this vehicle were the relatively large scale and the ability to completely remove a suspension system

from one corner without destroying any components. To give a better idea of the vehicle used for the present research, a picture of the test vehicle is shown in Figure 19.

Figure 19: The Traxxas X-maxx 6s used for the present research is a 1/5 scale vehicle

It is important to note that the "1/5 scale" of the vehicle refers to the vehicle size. Thus, this vehicle is clearly designed after a large scale, off road sort of vehicle. The 1/5 scale does not apply to the vehicle weight, as the test vehicle weighs only about 20 pounds.

Previous sections in this chapter focused on full scale passenger car tires and suspension. However, the decoupling techniques discussed in those and in the present section can readily be applied to any size or type of wheeled vehicle. The remainder of this work will reinforce these assertions and show that experimental application, even to a small scale vehicle, can validate the process for a range of wheeled vehicles.

The following subsections will present greater detail on the test vehicle components, describe the general design of the small scale setup, and will discuss experimental considerations.

4.2.1.1 Scale vehicle component details

As the tire and suspension systems are of particular relevance to the current research, this section will focus primarily on their properties.

Previous work has focused on pressurized, full scale passenger tires. In contrast, standard tires for this test vehicle are not pressurized, but are constructed of an outer rubber layer on top of a foam support structure. There were two different tires available for the 1/5 scale vehicle. Both tires have the same construction, but different stiffnesses. Figure 20 shows the basic construction for one of these tires.

Figure 20: Construction of a typical tire for the test vehicle

Another benefit of using this 1/5 scale model (as opposed to something smaller, like a 1/10 scale) is the possibility to replace the foam tire with a small pressurized tire for future work. Though the wheel hub of the test vehicle is not designed to attach to common bolting configurations for small

pressurized tires, it is well suited to connect to an adapter which could easily then connect to the pressurized tire.

It is well known that the stiffness of typical pressurized passenger car tires varies nonlinearly with loading and deflection. As noted previously, this foam based tire will not display the same sort of nonlinearity as a pressurized, full scale tire. However, this foam based tire does still displays nonlinearity suitable for the application of this experiment.

Stiffness data was not available for either of the test vehicle tires, so approximate stiffness calculations were carried out in house. Figure 21 shows a diagram of the test setup used to measure the force-displacement relationship for these tires.

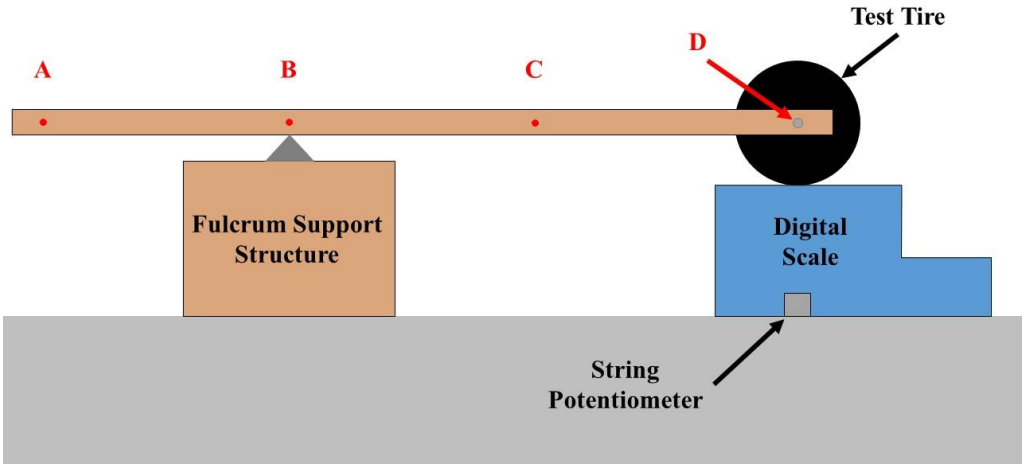

Figure 21: Stiffness test setup. I might need to include more than 1 picture here

Points A through D lie along a wooden plank to which the tire was mounted. This plank served both as the mounting structure for the tire and as the loading surface. A “plain steel angle” was used as the fulcrum of the system and contacted the wooden plank at Point B. The fulcrum was made wider than the plank to ensure an even loading distribution during testing. Point D marks the

bolting location for the test tire, which could rotate freely when attached to the plank. The bolt at Point D was centered over the weighing surface of the digital scale and string potentiometer. Furthermore, the bolt extended far enough from the wooden plank for the potentiometer to connect with only vertical extension. The string potentiometer was connected to a NI-DAQ from which displacement data was monitored and recorded on a PC.

The tension from the string potentiometer caused some additional, asymmetric loading to the tire. Since a single potentiometer was used on one side of the tire mounting bolt, we decided that this loading, however slight, must be balanced in order to produce the most reliable results. Thus, incremental weights were added to the opposite side of the bolt until the loading was even. It is important to note that force readings were relative to zero, not relative to the base weight of the tire and support structure.

Once the loading from the potentiometer was balanced, weights were added to Point A until the scale barely registered zero pounds ("barely" meaning fluctuation between readings of 0.000 lbf and 0.002 lbf) and data was collected from the potentiometer. At present, values for force will be displayed in pounds and displacement in inches since these were the units in which readings were taken from the equipment. Later, these values will be reported in newtons and meters, respectively. A reference point had to be established so that all deflection readings could be made relative to the un-deformed length. In other words, it was necessary to establish a reliable "zero point" to which all tire deflections values were relative. Ideally, the data collected for readings between 0.000-0.002 lbf would provide this point. However, due to the nature of the tire contact surface, where it is possible that only a single tread element was in contact, we deemed it necessary to record several alternate "zero points." In that interest, weight was increased in small increments (between 0.03

lbf and 0.1 lbf) up to half of a pound. Table 1 shows the force and displacement readings for these small increments.

Table 1: Potential "zero points" for the displacement

Measurement Point #	Weight Reading (lbf)	Calculated Displacement (in.)
1	0.002	5.8131
2	0.035	5.8128
3	0.065	5.8097
4	0.1	5.8097
5	0.195	5.804
6	0.295	5.8004
7	0.41	5.7972
8	0.505	5.7931

From the data in Table 1, it was determined that Point 2 gave the best zero point. This decision was based on the fact that the change in displacement between Points 1 and 2 was roughly one tenth of that for a similar weight change between Points 2 and 3. The decision was further supported through observations of the tire contact during experimentation. Specifically, the tire was only contacting the scale by the tips of several tread elements for Point 1, whereas the tire was more fully in contact at Point 2. It is worth noting that the displacement reading was the same for Points 3 and 4. However, through observation during the experiment and an analysis of the

complete data set, it was determined the issue between Points 3 and 4 was caused by random error as opposed to being caused by a lack of tire contact.

Once the zero point was chosen, weight on the tire was then gradually increased in 0.5 pound increments starting from Point 8, and then in 1.0 pound increments at higher loading. The full set of data for these tests on one of the test vehicle tires is shown in Figure 22. As mentioned previously, values will be specified in SI units going forward.

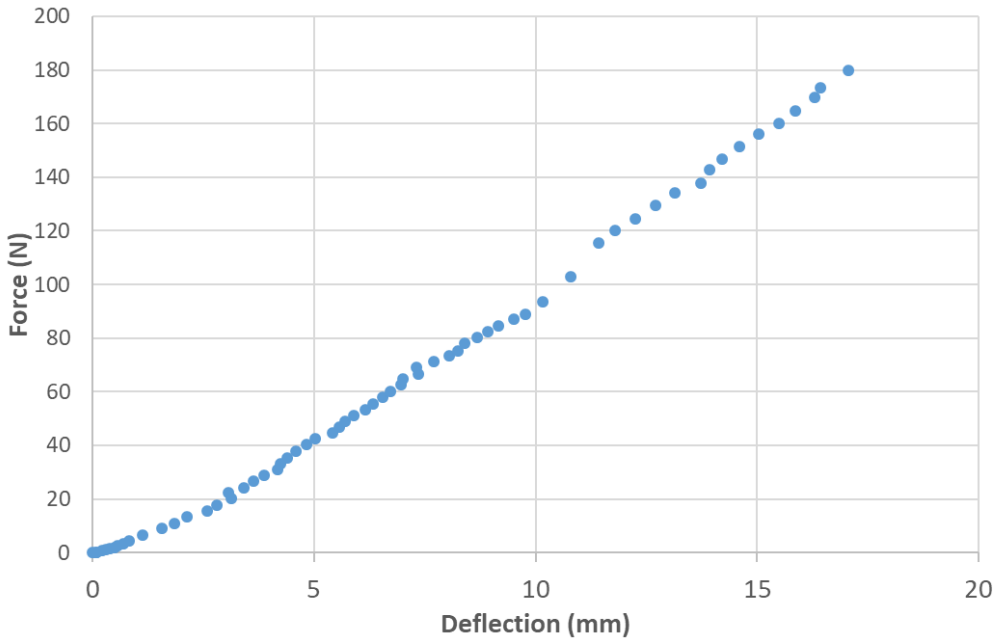

Figure 22: Deflection for the 8s tire was measured over a wide range of loads. Typical loading on tire is ~22-31 N (5-7lbs)

As can be seen in Figure 22, there is some nonlinearity in the force-deflection relationship, primarily for low loading and deflection values. Deflection is now used in place of displacement since we are measuring the size of the tire relative to its un-deformed shape. Though the nonlinearity demonstrated in the foam tire differs from that of a pressurized tire, the very presence of nonlinear behavior will help to validate the decoupling techniques for this quarter car system. A new model containing the foam tire and its nonlinear stiffness will be simulated in the

Matlab/Simulink environment, similar to that of previous work. This simulated data will then later be compared to the experimental results.

In the interest of developing this nonlinear model, it is necessary to first describe the nonlinear relationship between the force and the deflection of the tire. Given that the total weight of the test vehicle is approximately 89 N (20 lbf), the force on an individual tire should typically be around 22.2 N (5 lbf). In order to ensure that the nonlinear tire stiffness is described for the entire range of normal operation, it was assumed that the tire may experience normal force up to 250% of its static load. To provide some additional buffer to the 250% assumption, Figure 23 includes data up to 62 N (14 lbf).

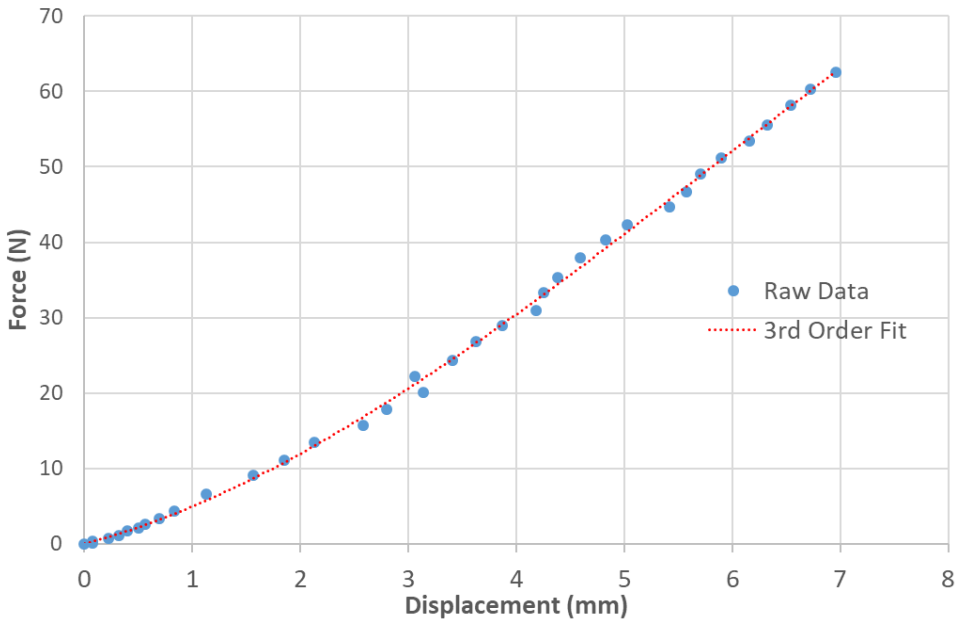

Figure 23: Data from Figure 22 up to 62 N along with a 3rd order trendline.

Figure 23 shows the nonlinearity of the stiffness even more clearly than Figure 22, more specifically for lower loading and deflection values. As displayed in the legend of the plot, a 3rd order trendline was selected. The choice of a 3rd order polynomial was motivated by the

nonlinearity relationship in the rigid ring model and also by applicability over the entire range of loading from Figure 22 [119, 120]. Again, in the present application, the nature of the nonlinearity is not as important as the fact that it present at all. The equation for the trendline is shown in Equation (141):

$$F = -0.0697d^3 + 1.2336d^2 + 3.7936d \quad (141)$$

Where F is the force in newtons and d is the deflection of the tire of the tire in millimeters. The coefficient of determination for the trendline in Equation (141) is 0.9989. This value supports the closeness of fit observed in Figure 23. Equation (141) is the nonlinear stiffness relationship which will be used in the simulations for the small scale system.

One important consideration for comparing simulated results with experimental results will be the apparent tire stiffness. Aside from nonlinearities in stiffness which may not be modeled exactly, it is also a known property of tires to exhibit varying stiffness values depending upon loading and operating conditions. Specifically, it has been shown that static tire stiffness tests display different stiffness values compared to vibrational stiffness tests, which in turn produce different results than rolling stiffness tests [120-122].

Considering these variations for full scale tires, it is reasonable to expect that there may be some discrepancies for the foam tire as well. Since the stiffness test was carried out for a static system, there may be discrepancies compared to the experimental system as it is excited in the vertical direction. Based on the results of the present research, future work may involve attempting additional testing for a rolling tire.

The other main component of the scale vehicle we are interested in is the suspension system. As discussed earlier in this chapter, part of the motivation for choosing the test vehicle was that it had

independent suspension systems. A close up view of one of these suspension systems is shown in Figure 24.

Figure 24: Independent suspension system on the scaled test vehicle

Figure 24 displays the independent, MacPherson strut type suspensions that were important in the selection of the test vehicle. The shock is connected from the lower control arm to a mounting point on the body of the vehicle. Essentially, this suspension is a scale version of a typical double a-arm or double wishbone suspension system. Given that the double wishbone is commonly used on many passenger vehicles, the general kinematic behavior of the 1/5 scale system should be comparable to that of a full sized vehicle. Thus, we also expect the vibrational behavior of the scaled system to conceptually mimic that of the full sized quarter car system. This similarity between the systems is important for the present application to vertical vibration, but will become

even more crucial in future work when decoupling is extended to lateral and rotational degrees of freedom as well.

The parameters of the shock are important for the modelling and experimental testing as well. Spring rate information for the suspension system is readily available online. The stock spring presently in the system is 1199 N/m. Additionally, stiffer or softer springs can be purchased for the system which is conducive to further testing of the system. Specific data for the damper, however, is not available online or even from the manufacturer. Thus, for the present, the viscous damping ratio for the scaled system will be assumed to be similar to that for a full sized vehicle. This assumption will be checked later against the experimental data and the model will be updated accordingly. More specific data on this damping ratio will be discussed later in the section on the small scale simulations.

The final property of the quarter car system which will be discussed in this section are the masses associated with each part of the system. It was mentioned earlier in the present chapter that the 1/5 scale of the vehicle refers to the overall dimensioning of the vehicle: height, wheelbase, track, etc. The weight, on the other hand is not 1/5 scale. Overall weight for the test vehicle used in this study was approximately 20 pounds. One of the independent suspensions was deconstructed to obtain the parts necessary to build the quarter car test system. During deconstruction, each component of the unsprung mass was weighed. Furthermore, the weight of connecting components was assumed to be split evenly between the sprung and unsprung masses. For example, half of the mass of the shock was assumed to belong to the sprung mass and half to the unsprung mass. The total unsprung mass for the quarter car system was determined to be 1.87 pounds (or 0.848 kg) from which the sprung mass was estimated as 3.13 pounds (1.42 kg).

Values for the sprung and unsprung masses will be especially significant in the approximation of the damping ratio and in the simulation/experimental testing of the small scale quarter car system. All parameters and values presented in this section will be used in the simulations for the small scale system, which will be described in a later section.

4.3 Development of small scale test rig

Design of the test support structure was heavily influenced by existing vibrational testing setups and by the unique requirements for this research. The experiment was conducted in the Vibrations, Adaptive Structures, and Testing (VAST) Laboratory where a flexible test table was already available on site. This test table was used as the basis for the support structure and experimental setup for the present work. Figure 25 shows this test table.

Figure 25: Test stand in VAST laboratory with small-scale quarter car rig attached

There are steel plates with pre-tapped holes on each surface on the stand which allow test fixtures to be secured. As Figure 25 shows, the test stand is particularly well suited to mount 80/20 aluminum extrusions, which are a versatile structural component in and of themselves.

Given the pre-existing compatibility with the test stand, the test structure for this experiment was also constructed out of 80/20 extrusions. The support structure for the small scale quarter car system is shown in Figure 26.

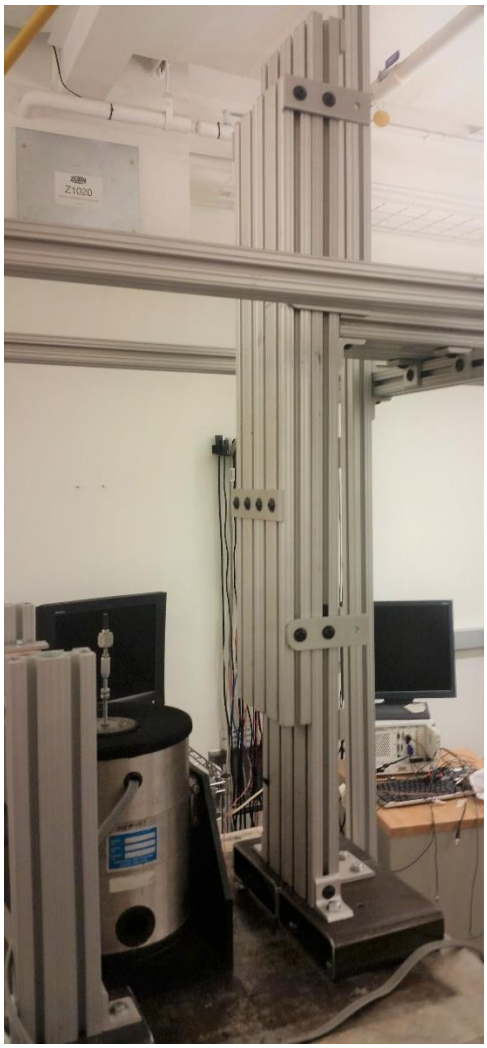

Figure 26: Small-scale test stand of 80/20 extrusions

Aside from compatibility with the test table, this support structure was designed with several important experimental considerations in mind. First among these considerations is effect of the support structure on the measured data. In particular, the structure had to be designed such that the flexing vibration of the main support beams (the ones that hold the guide rails) is not at a frequency such that it would pollute and interfere with the frequency range of interest for the small scale quarter car system. Again, the frequencies of interest at present are approximately 0 – 30 Hz.

A direct vibrational analysis of one of the main support beams was conducted to ensure that its natural frequencies were considerably separated from the range of interest. All decisions in this analysis were made such that a conservative estimate for the natural frequencies was obtained. First, it was necessary to determine if Euler-Bernoulli equations could be used for the beam. In that interest, a cross section of the beam is shown in Figure 27.

Figure 27: Cross section of a 1530 - Lite aluminum 80/20 extrusion

The beam is "1530 – Lite" aluminum 80/20 extrusion (hereafter referred to only as 1530 for brevity) which indicates that the length of one side is 1.5 inches and the other is 3.0 inches. The assumption necessary to use the Euler-Bernoulli equations is that beam deflection is large

compared to shear deformation. Effectively, we can determine if the beam is "long" by the ratio of length to the cross sectional height across which it is bending. Specifically, as long as:

$$\frac{l}{h_{cs}} \geq 10$$

then the assumptions necessary to use Euler-Bernoulli equations hold [97]. Though the main support of the structure shown in Figure 26 is comprised of multiple 1530 beams, the first conservative assumption in the calculation of frequency is that the support is actually only made of a single beam. Given that beam is 35 inches long, the assumption is met for either axis.

Properties for the 80/20 extrusions are available on the 80/20 Inc. website. Using these available properties along with Euler-Bernoulli beam theory for a simply supported beam (pinned-pinned boundary conditions), the first flexible bending mode was found to be at approximately 230 Hz. Though this number is already considerably outside of range of interest, the beam calculation was for a single 1530 extrusion, whereas there are actually two such beams fixed together. With the conservative estimate of 230 Hz, the vibration of the support structure will not significantly affect the measurements for the present experiment. As the axis over which bending was considered was the most flexible axis of the beams, it was deemed unnecessary to perform calculations across the other axis.

In a similar manner, Euler-Bernoulli calculations were also performed for the guide rails and for the road surface support beams. The first natural frequency of the 15-inch-long steel guide rails was found to be approximately 390 Hz, while that of the 16-inch-long 80/20 road surface support beams was found to be approximately 395 Hz. Though these calculations were for simplified scenarios, the conservative assumptions along with the large separation from the frequencies of

interest indicate that the components of the test setup should not interfere with those of the quarter car system during testing.

Another important experimental consideration for the design of the test setup was the ability to accommodate variations in test setup height and horizontal position. As will be described in more detail in the section on experimental application, it was necessary to have several different drive points on the structure. Thus, the setup had to allow for such adjustments without extreme variation of components.

In an effort to work off of the existing test table, rectangular steel tubes were used to allow for horizontal adjustability. Slots in the bottom of each tube were used to bolt the tubes directly to the test table. This mounting method is shown in Figure 28.

Figure 28: Tubes were bolted to table to allow flexibility for mounting method in this particular experiment

Once secured to the table, the top of the rectangular tubes become the new mounting surface which can be machined as desired. A slot was made lengthwise on the top surface to allow horizontal adjustability of the "road surface" support beams. As will be described in the section on experimental procedure, the assembled system will be tested with excitation to the unsprung mass directly. Thus, the effective road surface (support platform) can be held stationary, which allows for a normally loaded tire to be tested. The use of the 1530 extrusions to hold the support platform provided a wide and stiff base on which to mount the support surface. This setup configuration is shown below in Figure 29.

Figure 29: 1530 sized extrusions supply a stiff base along with adjustability

The use of the 1530 extrusions will keep any bending vibration modes of the support structure well outside the range of interest, 0-30 Hz. Additionally, the standard connecting pieces allow for easy

adjustability, which will be crucial while leveling the support surface. The support surface is made of oak plywood due to the relative stiffness and light weight. A thin steel plate is fastened to the top of the plywood to provide a hard surface on which to rest the tire.

The height adjustability of the test structure as a whole is also accomplished through the use of the 80/20 extrusions and the way in which the guide rails are mounted. Figure 30 shows a single guide rail mount attached to the main support beam.

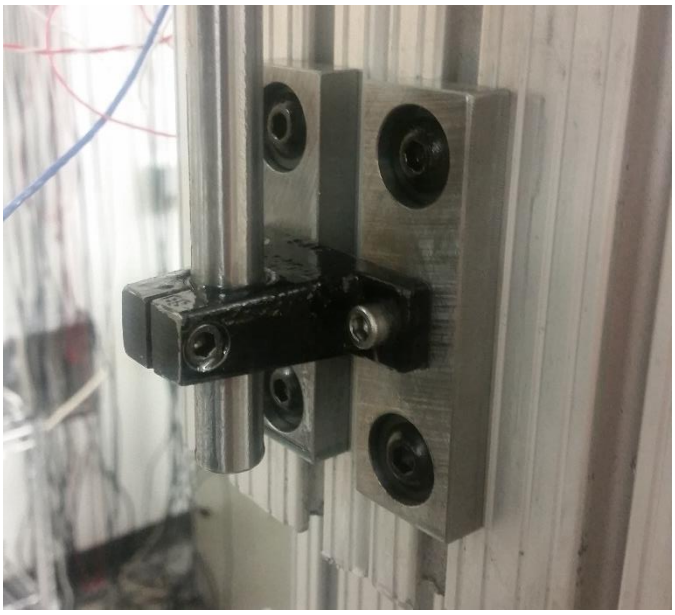

Figure 30: 80/20 extrusions allow for simple height adjustability in the test setup

This height adjustability is important for the switch between testing the assembled system and the suspension subsystem. It will also be important during later use of the test rig for other projects when tire or suspension systems of different sizes will be tested.

The final and most important facet of the setup which can be adjusted is the alignment of the guide rails. As shown in Figure 30, each guide rail stop is mounted on two steel plates which can be moved independently along the slot in the 80/20 extrusion. Through the mounting method, slight

corrections can be made to ensure that the rails are as close as possible to parallel. In turn, this helps to prevent additional and unnecessary friction to be introduced into the test system through the bearings. Since the alignment of the guide rails will affect every test performed on the system, great care was taken to adjust the system before testing in order to achieve the lowest possible friction.

The level of friction is also determined by the choice of bearing. For the current experimental setup, Thomson TWN8 linear ball bearings were used. For a single bearing the coefficient of friction is designed to be between 0.001 and 0.004. Even with the great care taken to ensure alignment, the actual level of friction in the test setup will be higher for the system when two bearings are used. In an effort to minimize this increase of friction, mounting holes for the bearings were made slightly larger than the bolt size. With a small amount of play at each bolt, small variations of horizontal positioning and angular orientation could be achieved. However, as will be discussed in the section on experimental application, the methods presented in this work should allow us to obtain frequency response data for the tire without the additional damping effects of the bearings.

In order to have an idea of the effect of static friction for the two-bearing setup, a simple test was performed on the system when only the main mounting plate was attached to the bearings. The 80/20 structure which supports the guide rails was slowly lowered until the bearings and mounting plate just began to move. A side profile diagram of this setup is shown in Figure 31.

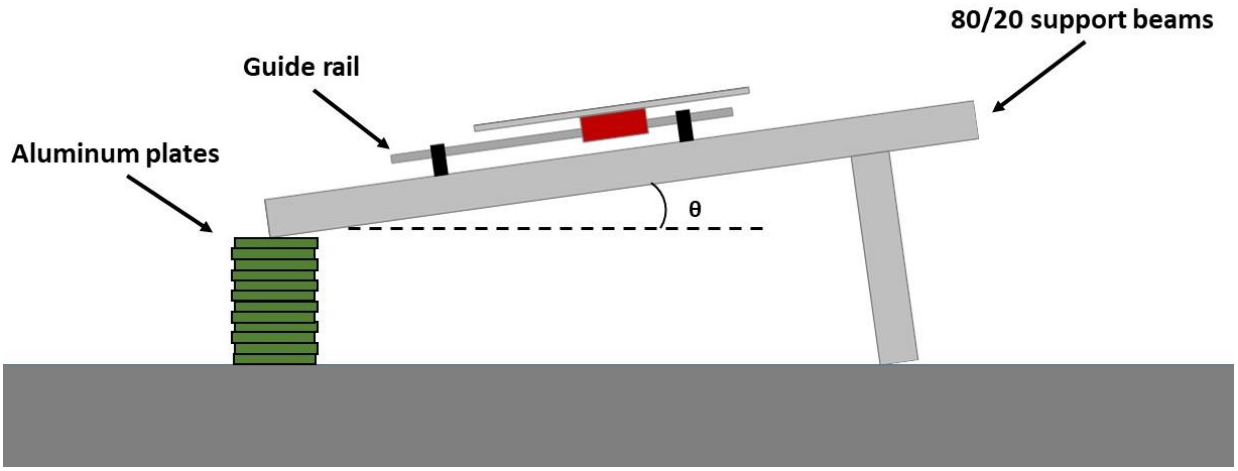

Figure 31: Bearing friction test setup

In Figure 31, the bearing is shown in red and the aluminum plates are shown in green for visibility. The thin aluminum plates (0.1" thickness) were removed one at a time until the system reached an angle at which the bearings and plate just began to move. The slope of the main support beam was measured to obtain the angle, θ. Then, that angle was used to estimate the coefficient of static friction.

For the mounting plate with the two bearings, the coefficient of static friction was determined to be 0.057, while for the single bearing it was 0.013. According to specifications from the manufacturer, the coefficient of friction in a single bearing should be between 0.001 and 0.004. Even on the high end of that estimation, the friction in the test setup with two bearings is still an order of magnitude higher. Given that the guide rails are oriented so that the bearings translate vertically (Figure 26) and the bearings are not supporting the weight of the system, the normal force between the bearings and guiderails will be reduced. In turn, the reduction in normal force will reduce the effective Coulombic damping, though there is still some inherent friction in the system due to the fit of the bearings/rails.

To summarize the design and construction of the test structure, adjustability is paramount. Whether the considerations are spatially to accommodate for variations in test setup, or alignment to ensure optimal bearing operation, most components of the test setup were designed to allow for some level of adjustment. The importance of many of the factors has been mentioned in this section, but will become more apparent in the discussion of the experimental procedure.

4.4 Testing considerations and procedures

Since the focus of the present work has shifted to the small-scale system, this section will primarily address testing considerations and procedures as they relate to that particular system. However, there will be some discussion of testing considerations for the full-scale system as well.

The most important aspect of the testing for the current decoupling process is the input force. More specifically, the location, method of attachment, and orientation of the input will determine the efficacy of the process as a whole. The input must be directly to the unsprung mass in order to obtain the data necessary for decoupling both the full-scale and the small-scale quarter car systems.

For the small-scale system, excitation directly to the unsprung mass is accomplished through two methods: 1) a steel stinger attachment to the "axle bolt" which holds the tire to the wheel hub (shown previously in Figure 25 and more clearly in **Chapter 5** in Figure 75); or 2) a wire attachment to the axle bolt directly in the center of the tire (shown in **Chapter 5** in Figure 83). These two methods also demonstrate the importance of the "method of attachment" which was mentioned in the previous paragraph. It is vital for the decoupling process that the method of force input not significantly alter the dynamics of the quarter car system. Thus, in the following chapter a series of tests are detailed which were performed to ensure that neither of the attachment methods listed cause any significant change to the dynamics of the system.

The final aspect of the input force which is important to the present work is the orientation of the input. Current experimental work is focused on only the vertical vibrations of the quarter car system due to vertical input. Thus, the orientation of the force input is greatly simplified. However, future extensions of this work could involve system response in x, y, and z-directions due to input in each direction. For example, vibrations in the y-direction would be measured for input in the z-direction. Depending on time constraints and equipment availability, this testing could be accomplished through different setups.

Orientation of the force input can be simplified by conducting three separate tests, one for force input solely in the x, y, and z-directions. For each of these individual tests, response would also be measured in all three directions. By limiting the force input to application along each coordinate axis, errors due to orientation measurement can be reduced. However, these tests would require more time to conduct and may not be possible depending on the capabilities (such as placement flexibility) of the actuation system. These difficulties can be avoided by orienting the actuation system such that there is force input in all three directions at once. The orientation of such a configuration would be more difficult ensure or measure, but requirements for time and actuation flexibility are less limiting. Which option is more feasible or would produce better results will depend on the physical setup, equipment availability, and time constraints for the given testing.

The last part of testing considerations which is directly applicable to both the full-scale and small-scale quarter car systems is the necessity of being able to test at least one subsystem independently. Results in **Chapter 5** will highlight the need for well-designed mounts for the suspension subsystem. Specifically, to test the suspension subsystem individually, the tire needs to be replaced by a rigid mount which will itself have frequencies outside the range of interest, but will allow the suspension to move in the same way as when the tire is attached. Alternatively, the tire could be

tested independently as the “known” subsystem, but several difficulties arise when considering the full-scale tire. Nonlinearities in the tire prevent the testing of a free standing tire from being a possibility. For the small-scale system, this is addressed by preloading the tire using the wire attachment and the actuator. However, for the full scale system a wire would have to be replaced by cables, and an assembly would have to be constructed around the tire to allow the cables to attach at a single point to the actuator. Furthermore, the actuator would have to be capable of sustaining such a preload and the strength required of the cables may be such that their weight significantly alters the unsprung mass associated with the tire subsystem. Overall, the choice of either tire or suspension as the known subsystem represents significant design requirements, especially for the full-scale system.

With the most important testing considerations having been discussed in the preceding paragraphs, a framework for the testing process can be established. This framework will be presented in list/step format and is based on the assumptions that: 1) all relevant modelling has been completed; and 2) the general test setup (quarter car rig, actuation system, etc.) is completed and working. The following steps are generalized for conducting the testing necessary for decoupling any quarter car system.

General procedures for the testing in the present work are as follows:

1. Selection and setup of actuation point on unsprung mass
    a. Design of necessary components/attachments to actuate at said point without altering system dynamics
2. Design of components to test individual subsystems (ex. rigid support for suspension)
3. Preliminary testing of setup to ensure no interference with quarter car dynamics

a. Testing of the rig without quarter car system attached
b. Testing with various stingers
c. Testing with multiple actuation attachments

4. Testing on assembled quarter car system
    a. These tests will be carried out differently depending on the choice of orientation for the actuation
    b. Repeated tests performed for original quarter car system as well as a "new" system for comparison of decoupling/recoupling
        i. "New" refers to a quarter car system with either the original tire or suspension replaced
5. Testing on the "known" subsystem which could be either the tire or suspension
    a. The suspension as the known subsystem requires a mount which rigidly supports the weight of the suspension, but allows the control arms to move as if connected to the tire
    b. The tire as the known subsystem requires some method for force loading the tire without adding significant inertial loading (ex. the cable/wire system described in preceding paragraphs), if possible
    c. Repeated tests on the original subsystem and the "new" subsystem, where either the tire or suspension has been replaced

Once results have been obtained for both the assembled quarter car system and one of the individual subsystems, the next step is to actually decouple the data. Depending on the level of success of the decoupling process, changes may need to be made to the system/test rig and the entire process repeated. Assuming that all components have been designed such that they do not

alter the dynamics of either system, the decoupling will provide frequency response data for whichever subsystem was not tested independently (i.e. if suspension was the known subsystem, decoupling will provide information for the tire). Furthermore, the procedures given in the preceding list are generalized and could be applied to either the small-scale or the full-scale quarter car systems.

Before this experimental setup and testing procedure can be put to use, it is important to first simulate the small-scale system in order to have an estimate of the frequencies which should be present during testing. These simulations, along with the experimental results, are discussed in detail in **Chapter 5**.

Chapter 5 – Results and Validation

The analytical model development of the present work, which were discussed in **Chapter 3**, must be validated before any strong conclusions can be made. In order to validate these models, the coupling/decoupling processes described in **Chapter 3** will be applied to three different levels of systems. First, purely analytical, numerically populated system models will be used to demonstrate applicability from a high level perspective. Next, simulations with a rigid ring tire model will be used to show the effect of errors and the treatment of nonlinearity. Finally, the small-scale quarter car rig discussed in **Chapter 4** will be used to demonstrate the necessary testing procedures and the application of the analytical developments to experimental data. Each of the systems and the accompanying results will be addressed in the following sections

5.1 Analytical, numeric quarter car system

In order to further demonstrate the use of FBS coupling/decoupling with the quarter car system, the preceding application was next taken and applied to numerically populated analytical FRFs. There are two primary differences between the current section and the preceding section. First, FBS techniques will now be used to **decouple** FRFs in addition to coupling them. Second, rather than the oversimplified system of Equations 10 – 12, the numeric FRFs in this section include damping for both the suspension and tire. Base values of parameters used for the models are shown in Table 2. In the interest of brevity, the equations for the analytical quarter car model with damping will not be included here.

Table 2: Parameters and values used for both analytical models and simulations

Parameter	Designation		Value
	Simple Model	Rigid Ring Model	
Sprung Mass	m_s	m_s	300 kg
Unsprung Mass	m_{us}	m_{us}	35 kg
Belt Mass	---	m_b	7.25 kg
Suspension Stiffness	k_s	k_{sz}	20 kN/m
Sidewall Stiffness	k_t	k_{bz}	170 kN/m
Residual Stiffness	---	k_{rz}	---
Suspension Damping	c_s	c_{sz}	750 Ns/m
Sidewall Damping	c_t	c_{bz}	392 Ns/m

The parameters in Table 2 were taken from measured data for a 205/60R15 radial ply tire. This is the same tire as what is used for the simulated model discussed in the next section. One item of note from Table 2 is the sidewall damping, which appears relatively high as compared to a typical quarter car system. The high value arises from the structure of the rigid ring model and the method by which the parameters were extracted for the tire. Later in the present chapter, once results are displayed for the rigid ring model, the effect of this damping value will be addressed in more detail.

From the table, one can see that there is no belt mass or residual stiffness included in the analytical model of this section. However, these parameters are included in the simulation model of the following section. A number of other parameters such as longitudinal stiffness, rotational stiffness and moments of inertia, to name a few, are also included in the simulations, but are not included in Table 2 due to the proprietary nature of the data. Furthermore, it is important to note that both the residual stiffness and sidewall stiffness do not have set values for the simulation model because they are treated as nonlinear parameters.

With the parameters from Table 2 for the analytical "simple model" of this section, the FRF for the unsprung mass of the assembled quarter car appears as shown in Figure 32.

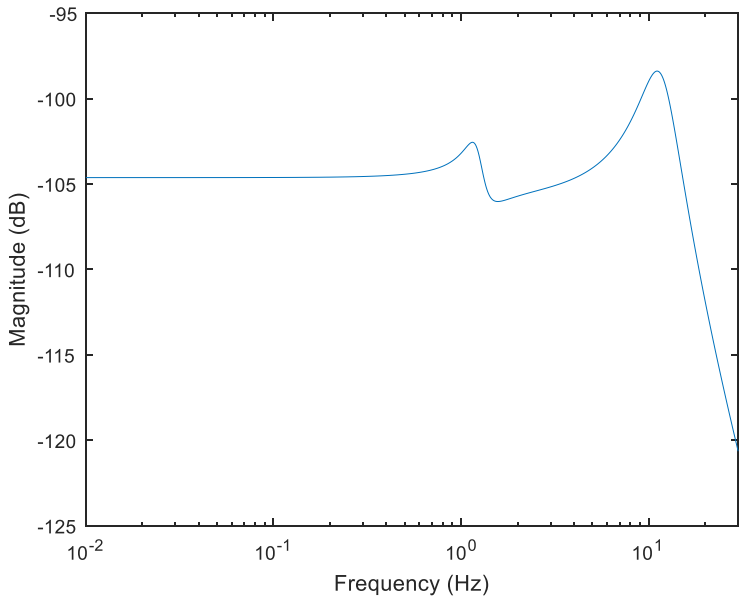

Figure 32: Analytical FRF for unsprung mass of 2 DOF spring-mass-damper quarter car system

For reference, the FRF of Figure 32 is based on the damped equivalent of Equation 10. The natural frequencies appear at 1.16 Hz and 11.1 Hz which are typical for a quarter car system [123-125].

Decoupling the FRFs requires knowledge of at least one of the subsystem FRFs. Since everything in this section has been analytically derived, we could treat either the tire or the suspension as the

known (or “residual”) subsystem. However, since the tire is in direct contact with the road and serves as the receiving end for the assembled system, it makes more sense conceptually to maintain the same road input for the tire subsystem. In other words, by treating the tire as the known subsystem, the input remains the same for the assembled system and the tire subsystem. The following section will show that treating the suspension as the known system is the superior choice, but it is instructional to continue with the tire for the present section.

For simplicity, it was assumed that exactly half of the unsprung mass belongs to the tire (m_{usA}) and half belongs to the suspension (m_{usB}). Conceptually, it does not matter for the present application what the proportion of unsprung mass is for each subsystem. As long as these proportions remain constant, the coupling and decoupling techniques will still work. Figure 33 shows the FRF for the tire subsystem.

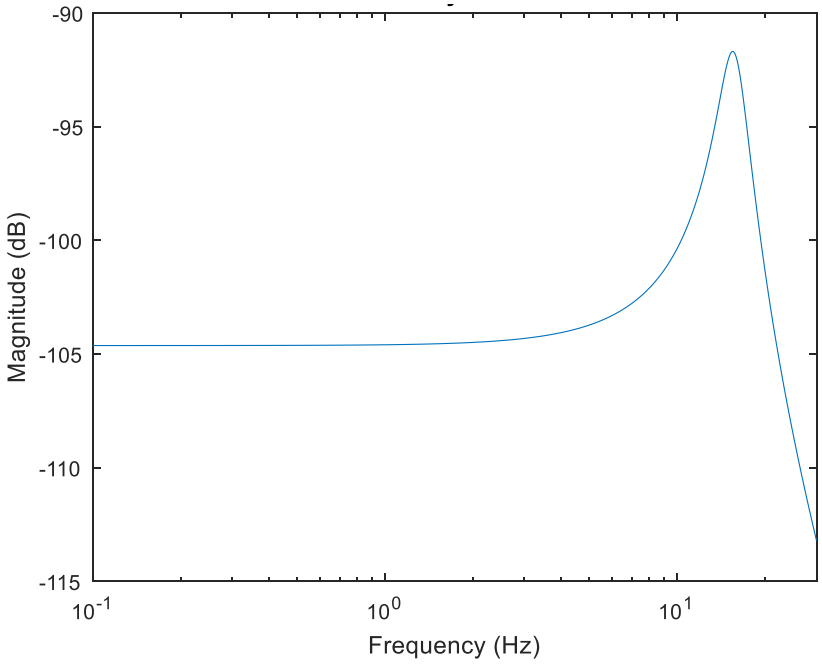

Figure 33: Analytical FRF for tire subsystem

In the current model, the tire subsystem is simply a single DOF spring-mass-damper system (recall Figure 8 with the addition of a damper). The FRF of Figure 33 appears to have too high of damping for a typical tire. Many quarter car models neglect tire damping entirely or specify a damping ratio of usually less than approximately 6% [126-129]. This high damping occurs here because of the simplification of the current model from that used for the simulation shown in the following section. The following section will provide more details on these differences and show a more realistic tire FRF. However, despite the difference from a typical tire FRF, the FRF of Figure 33 provides a suitable base to demonstrate decoupling for the current application. With numeric FRFs in hand, the tire subsystem can be decoupled from the assembled system by rearranging Equation 9 as follows:

$$Y^S = \left(Y^{Q^{-1}} - Y^{t^{-1}}\right)^{-1}$$

This simple formulation clearly shows that the tire subsystem is being "subtracted" from the assembled system in the decoupling process. The resulting decoupled FRF for the unsprung mass of the suspension subsystem is shown in Figure 34.

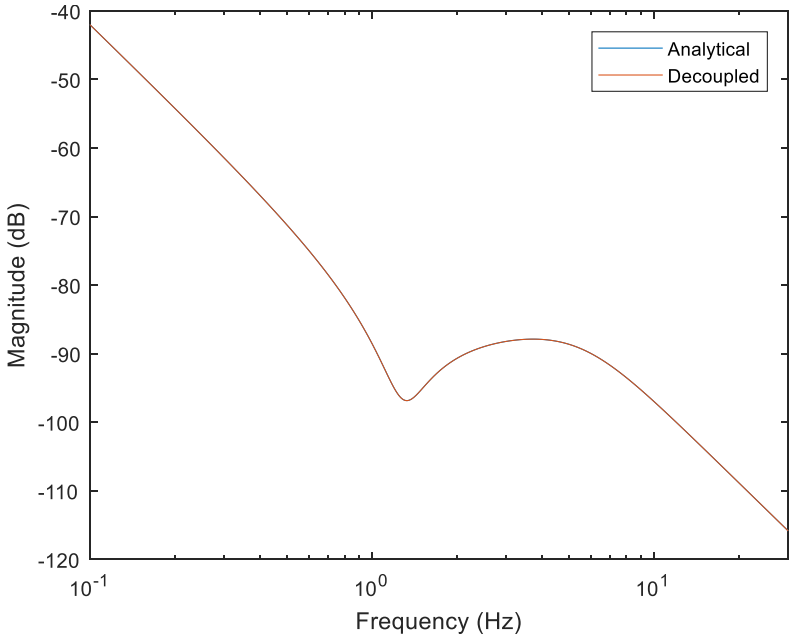

Figure 34: Comparison of analytical and decoupled FRFs for the suspension subsystem

The FRF generated via the damped equivalent of Equation 12 matches exactly with that obtained through decoupling. This is as expected, since the data was based on analytical equations with no noise, nonlinearities, or errors of any kind. Results in the following section will demonstrate what happens when errors are present in the FRFs involved in the decoupling process.

In its general shape, the FRF of Figure 34 may appear strange at first, but it can be easily explained. The shape of this particular FRF is caused by the large discrepancy between the two masses along with the relative stiffness of the suspension spring. The first peak of the FRF has been pushed below 0.1 Hz, which has caused it to not appear on the plot. If the axes were to be expanded, we would be able to see the entirety of the first peak. However, for the coupling or decoupling process, it is not necessarily required to have data for the entire FRF. Instead, it is only necessary over the range of interest for coupling. In the present case, our desired range is found from Figure 32 and is approximately 0.1 – 30 Hz. Thus, going forward, the range of the suspension FRF shown in Figure 34 is suitable for subsequent application.

The next step is to “recouple” the suspension FRF with a new tire. Data was only available for the one 205/60R15 tire, so slight changes were made to system parameters to approximate a “new” tire. Specifically, stiffness was increased and the unsprung mass associated with the tire was decreased. A comparison of the original tire and the lighter, stiffer tire is shown in Figure 35.

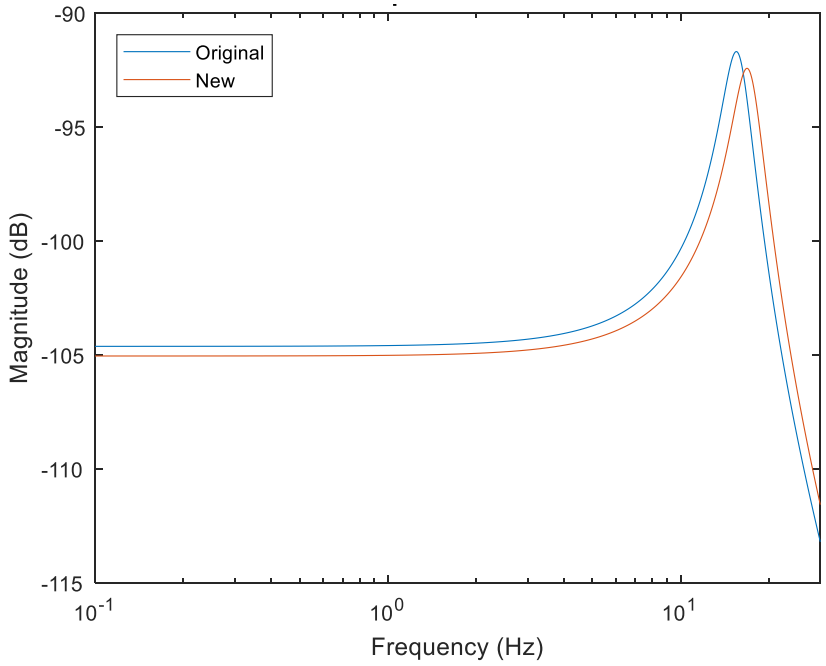

Figure 35: Comparison of original tire and lighter, stiffer tire FRFs

Notably, the frequency has shifted from 15.5 Hz up to 16.8 Hz. This change is desirable for the present demonstration, as it should produce a noticeably different FRF for the assembled quarter car system. Since the response for the “new” quarter car system should be clearly different compared to the original, it should be easy to determine whether the recoupling was successful.

Figure 36 shows a comparison of the recoupled, new analytical, and original analytical FRFs for the assembled quarter car system.

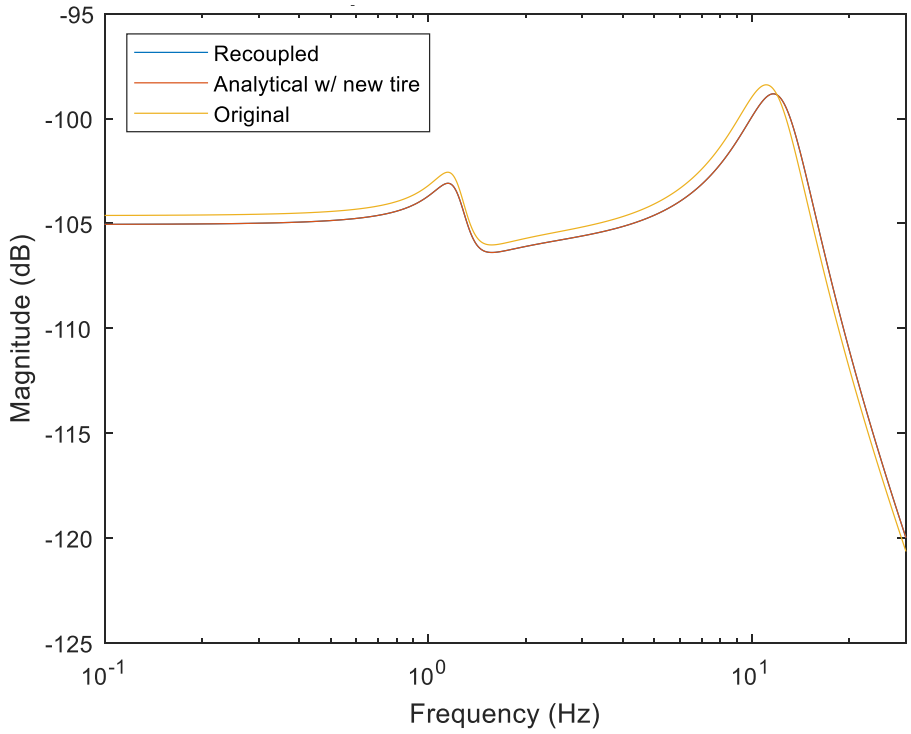

Figure 36: Comparison of FRFs for the quarter car system with the new and original tire

The results of coupling the new tire with the decoupled suspension match exactly with those obtained for the new system analytically. Furthermore, the plot shows that the second natural frequency has been increased from that of the original system, from 11.1 Hz, to 11.7 Hz. This observed change in natural frequency demonstrates one of the potential benefits of applying FBS techniques to the tire-vehicle system: it is possible to observe the change in the assembled system without having to experimentally measure, or even simulate the entire assembled system.

Since all FRFs were obtained analytically in this section, the full benefit of this technique may not be immediately clear. The process described in this section allows data for the tire and suspension to be combined from any sources. For example, FRFs for an analytical suspension model could be coupled with experimental FRFs for a tire, or FRFs from a multi-body dynamic model for a suspension could be coupled with those from a finite element tire model. This flexibility of

coupling and decoupling provides a powerful tool for modelling the vibrations of the tire-vehicle system.

5.1.1 Extension to 3 DOF analytical model with belt mass included

The preceding discussion was for a 2 DOF quarter model coupled at a single SDOF. However, as mentioned in that discussion, the damping for the tire appeared too great due to oversimplification of the model along with the parameters obtained for the quarter car model with the rigid ring tire. While the preceding section was intentionally kept simple for demonstration purposes, it is also useful to look at an analytical model more similar to that which will be seen when the rigid ring tire is incorporated. In that interest, the discussion will now be extended to a 3 DOF analytical quarter car model, where the masses are the sprung, unsprung, and tire belt mass. This system is shown below in Figure 37. Again, there is assumed to be a force input directly to the unsprung mass.

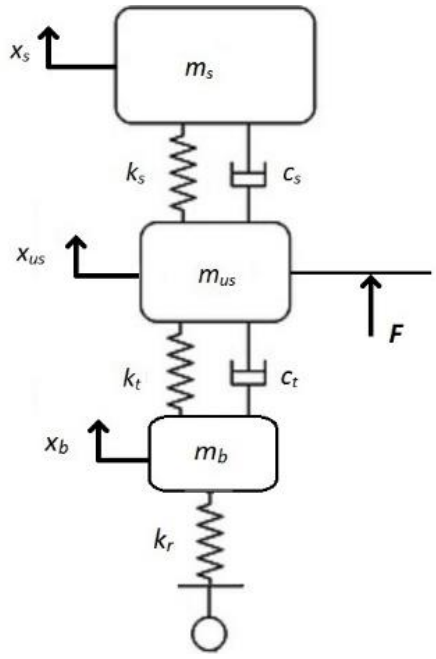

Figure 37: Quarter car model with 3 DOFs where the belt mass is now included

Even though the system of Figure 37 has three DOFs, it is still assumed to be coupled at only a single DOF, at the displacement of the unsprung mass. Based on that assumption, the suspension subsystem remains the same as for the two DOF system of the previous discussion and is still described by Figure 9, with the addition of a damper. However, the tire subsystem is now described as shown in Figure 38.

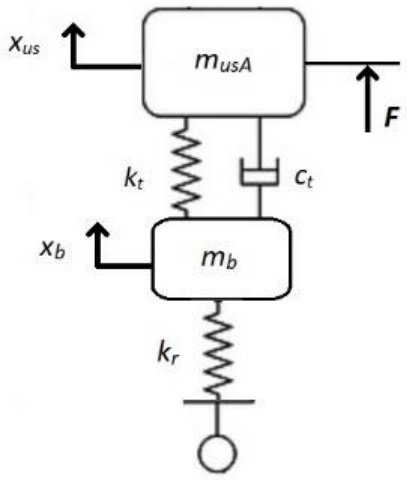

Figure 38: New tire subsystem with belt mass included

Derivation of the equations of motion, and subsequently, the analytical FRFs closely follows that for the two DOF system. Since the process for the two DOF system was described in detail, an abbreviated discussion will be provided here. With the parameters listed in Table 2, the receptance FRF for the unsprung mass of Figure 37 is shown in Figure 39.

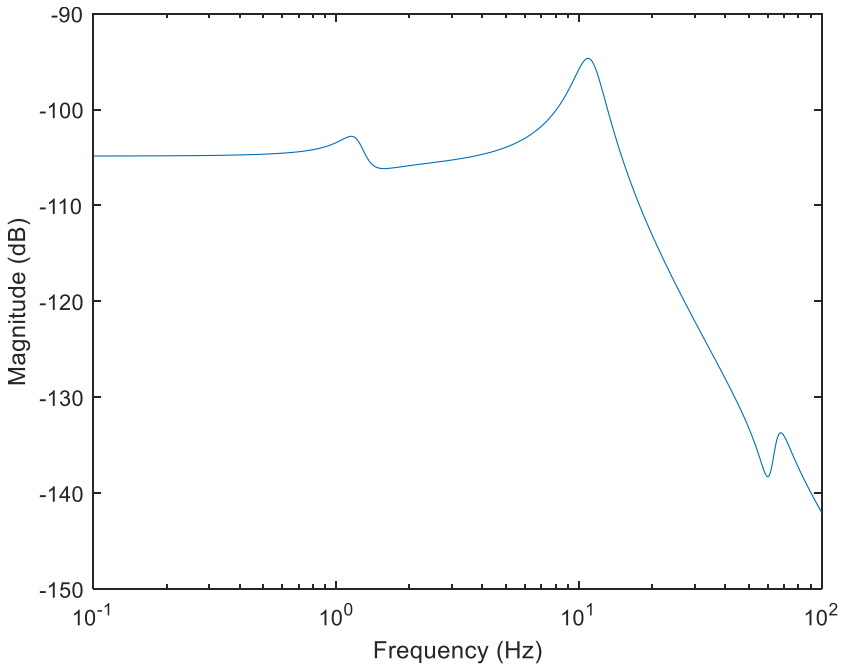

Figure 39: Receptance FRF for unsprung mass of 3 DOF quarter car model

The three natural frequencies in Figure 39 occur at 1.17 Hz, 10.9 Hz, and 68.33 Hz respectively. Compared with Figure 32 for the two DOF system, the first two frequencies of Figure 39 match closely (1.16 Hz and 11.1 Hz). The main differences will arise in the FRF for the tire subsystem and in the fact that there is now a third peak, corresponding to the belt mass.

Following the process described in the previous section, we will next examine an FRF for the tire subsystem. The system of Figure 38, again with the parameters of Table 2 results in an FRF for the unsprung mass as shown in Figure.

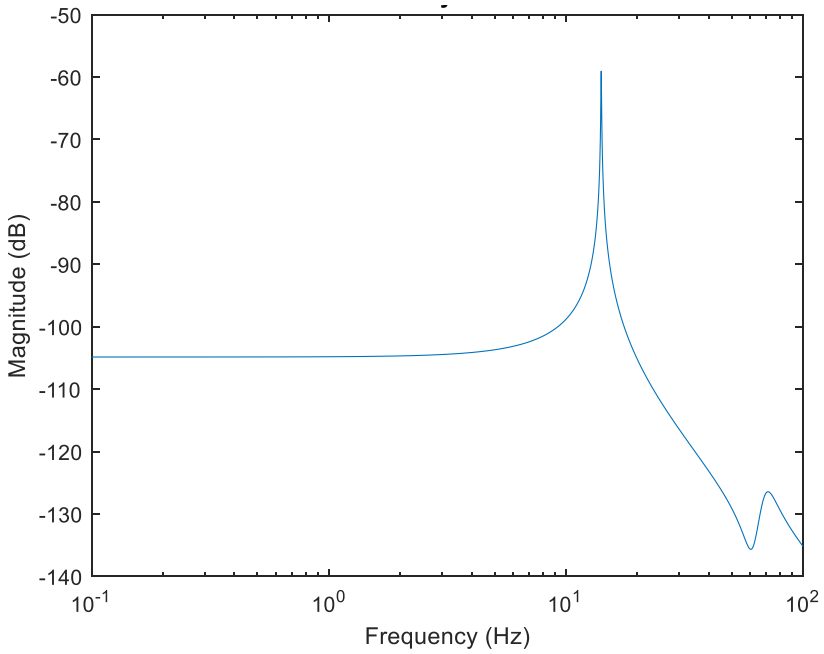

Figure 40: FRF for unsprung mass of tire subsystem

Natural frequencies for the tire subsystem appear at 14.09 Hz and 71.17 Hz. The most notable aspect of Figure 40 is the apparent change in damping on the first peak compared to its two DOF counterpart in Figure 33. As mentioned previously, the parameters in Table 2 were for a more complex model, and thus, were not suitable for the simplified two DOF model. With the inclusion of the belt mass DOF, the damping on the tire appears as normally expected. Though the rigid ring model and the associated parameters were validated in previous work, this new apparent damping in the analytical model gives more confidence that the simulations of the following section will provide meaningful results.

Continuing with the procedure of the previous section, the FRF of the tire subsystem (Figure 40) was then decoupled from that of the assembled quarter car system (Figure 39). The resulting FRF for the suspension system is shown alongside the analytically derived FRF below in Figure.

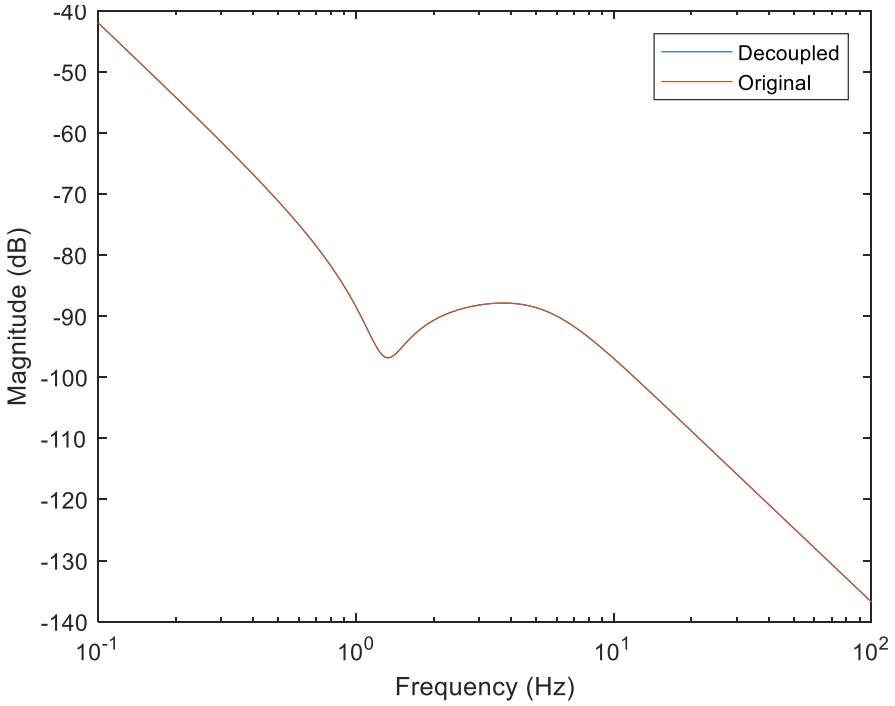

Figure 41: Comparison of decoupled suspension FRF with analytical

Figure 41 shows that, as was the case in the two DOF model, the FRF for the suspension obtained through decoupling matches exactly with the analytical model. Furthermore, these FRFs match exactly with those of the two DOF model as well, which was expected due to the fact that the suspension subsystem was defined in the same way. These results reinforce the applicability of the FBS decoupling process to the quarter car system, even in presence of additional DOFs.

To complete the process outlined in the previous section, a "new" tire will again be coupled to the suspension system. This new tire was made slightly lighter and stiffer in order to produce a noticeably different FRF. For the case of this three DOF model, both the sidewall stiffness and the residual stiffness were proportionately increased, while both the unsprung mass and belt mass were proportionately decreased. The resulting FRF is shown in Figure 42.

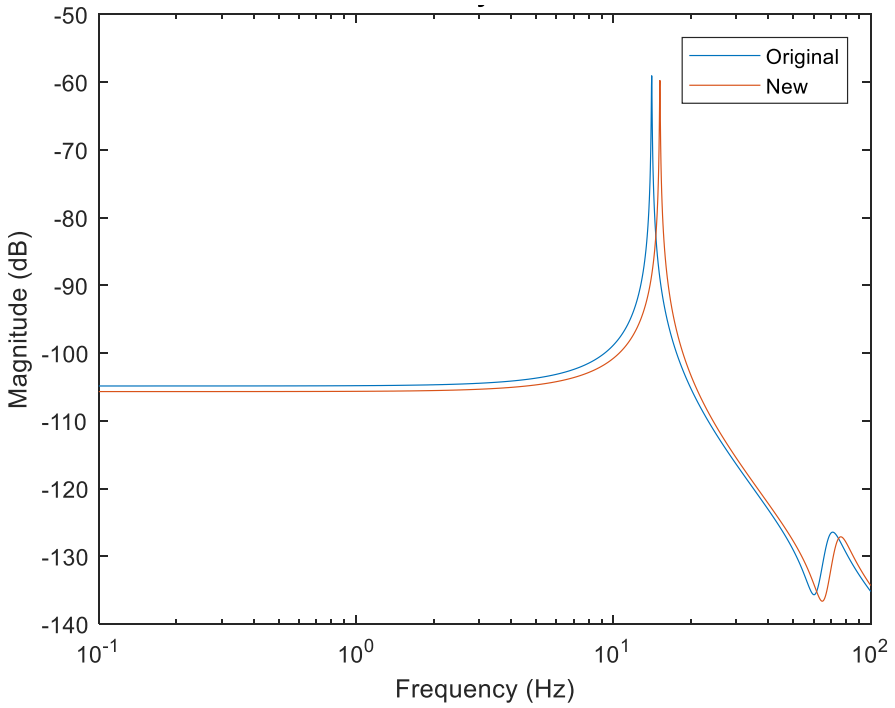

Figure 42: FRF for the "new" tire compared with the original

In comparison to the original tire, the natural frequencies have risen to 15.16 Hz and 76.51 Hz. This new tire should also produce an FRF for the assembled system that is different enough from the original to show that the full decoupling-recoupling process is still applicable. The FRFs for the assembled quarter car system with new and original tires are shown in Figure 43.

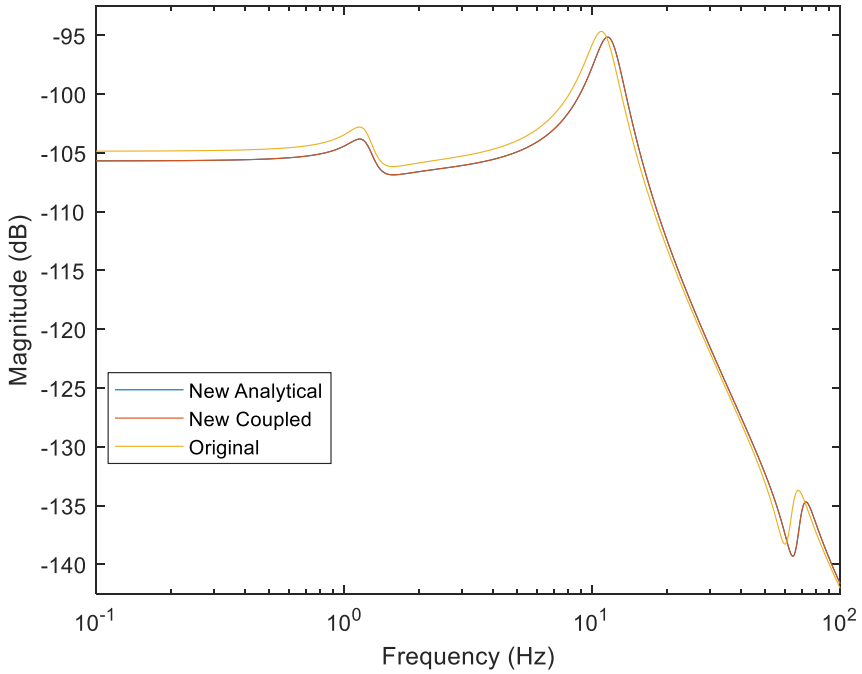

Figure 43: FRFs for the "new" quarter car system compared to the original

An analytically derived FRF for the new quarter car system is shown in Figure 43 alongside the FRF obtained through recoupling the tire and suspension systems (Figure 42 and Figure 41, respectively). These FRFs match exactly, which shows that the recoupling process works and was carried out successfully. Additionally, the FRF from the original quarter car system is included to show the change in frequency response that was correctly predicted through the recoupling process. The application of the FBS coupling and decoupling techniques presented in this section will be paralleled by the application to a simulated quarter car system in a later chapter.

As mentioned previously, all results in this section for coupling and decoupling were exact due to the use of analytically derived FRFs. However, when noise or errors are present, the techniques of this section do not provide exact results and can sometimes break down. Before applying these techniques to experimental data, the next logical step is to first perform them on data from a more

complex simulated system. The following section introduces the model which was used for simulations and then presents an application similar to that of the current section.

5.2 Simulated quarter car system with rigid ring tire

The next step towards applying FBS to a physical quarter car system is to first apply the techniques to a simulated system. For the simulations of the present section, the level of complexity of the quarter car model was increased from that of the previous section. A rigid ring tire model developed at the Center for Tire Research (CenTiRe) was used in place of the spring-mass-damper model. This model has been tested and validated in previous work [130].

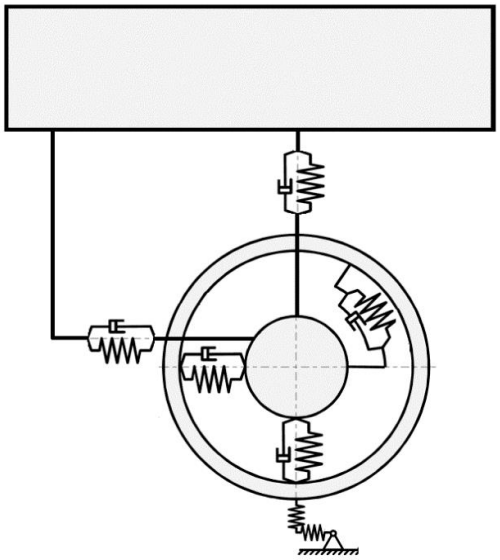

Figure 44: Rigid ring model used for simulations

Figure 44 shows how the rigid ring model is incorporated into the overall quarter car model. However, the present application only involves dynamics in the vertical direction for a static tire. Thus, the model can be simplified conceptually to include only vertical elements.

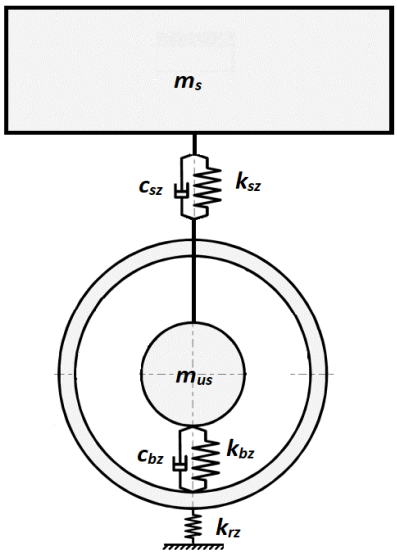

Figure 45: Rigid ring model conceptually simplified for vertical displacement only

Though Figure 45 only shows the vertical components which are relevant in the current simulation, the full model of Figure 44 was used for simulations. Essentially, we are left with a three DOF system where coupling still occurs conceptually at the unsprung mass. Furthermore, in this tire model, the sidewall stiffness (k_{bz}) and the residual stiffness (k_{rz}) are not strictly linear elements. As will be demonstrated later in this section, these nonlinearities will heavily influence the decoupling process.

As mentioned previously, simulations were carried out for a static (non-rolling) tire, subject to a force input in the vertical direction. The simulations were carried out in the Matlab/Simulink environment. Parameters for the rigid ring model are for the same tire which was used in the previous section (a 205/60R15 radial ply tire) and so are listed there in Table 2. Simulations were carried out with both band limited noise and sine sweep force inputs. The best FRF results were used for each system.

Once the necessary FRFs were obtained from the simulated data, the same process as in the previous section was applied. Figure 46 shows the FRF of the unsprung mass from the assembled quarter car system.

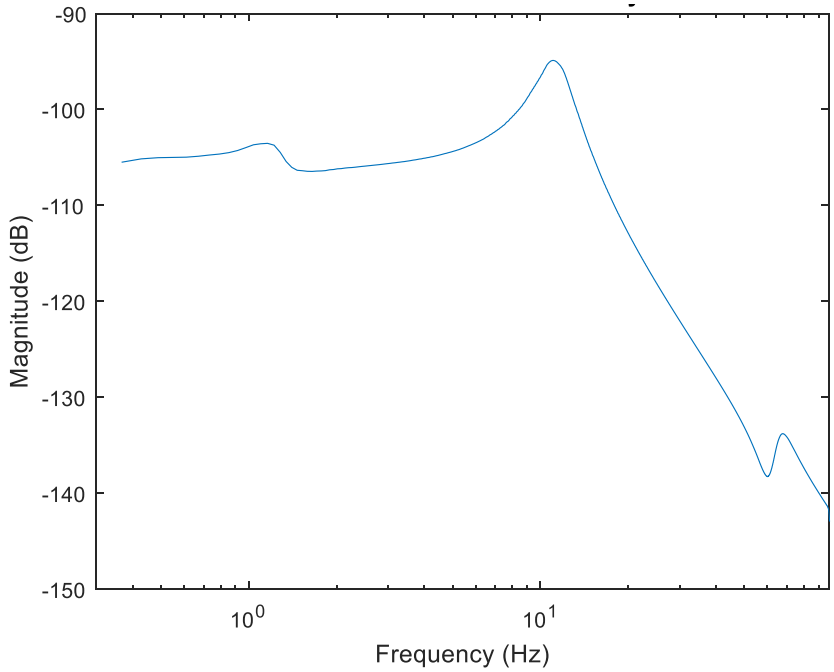

Figure 46: FRF from simulated data for unsprung mass of assembled quarter car

The most noticeable difference between the simulated system of Figure 46 and the analytical system of Figure 32 is the inclusion of the tire belt mass. Natural frequencies for the first two peaks remain the same, with just a slight shift in magnitude. The belt mass is low relative to the other masses and the stiffness is high. Thus, Figure 46 shows that vibration of the belt is separated by about 57 Hz and the magnitude is approximately 40 dB lower. This frequency separation is typical for rigid ring tire models, where the dominant frequency for the belt is generally in the neighborhood of 70 Hz [120, 130, 131]. Due to the frequency and magnitude separation, the relative similarity to Figure 32 is expected.

Based upon the construction of the simulation, the tire was first treated as the known subsystem. Since the simulation was already configured for input to the tire from the road, it was more direct to remove the suspension system from the model and maintain the same input method to the tire. Again, exactly half of the unsprung mass was assumed to belong to the tire. Simulations were then carried out for the tire Subsystem by itself. Figure 47 shows the resulting FRF for the unsprung mass of the tire.

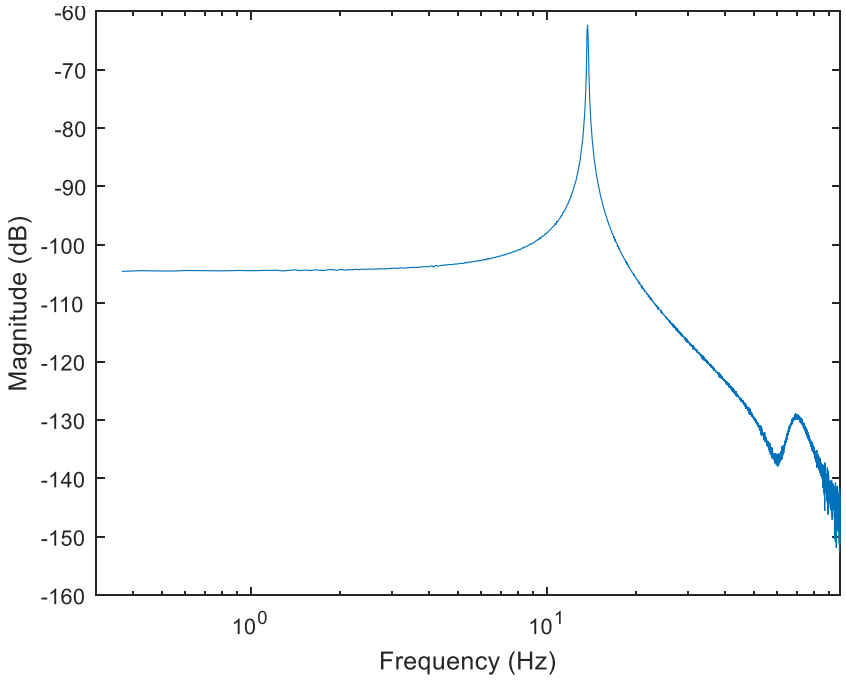

Figure 47: FRF for unsprung mass of the tire Subsystem

The natural frequency is only 13.7 Hz, which is significantly lower than expected based on results from the previous section. However, the inclusion of the belt mass and nonlinear stiffness elements were thought to be potential sources of difference. In the interest of fully investigating the changes, this tire FRF was decoupled from that of the assembled system in order to obtain the suspension FRF. The results of the decoupling are displayed in Figure 48.

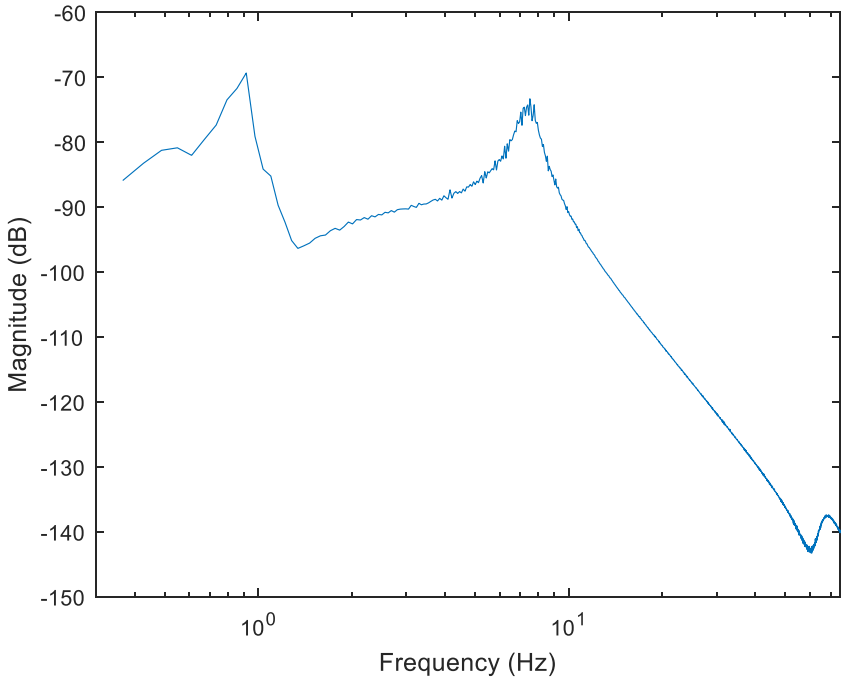

Figure 48: Result of decoupling FRF of Figure 47 from that of Figure 46

The plot in Figure 48 is clearly different than expected. Based on the model of Figure 44 and Figure 45, the suspension subsystem is still represented as before with the sprung mass connected to a portion of the unsprung mass by a spring and damper. Thus, Figure 48 should appear the same as Figure 34.

The most obvious possibility for the error is the nonlinearity in the residual and sidewall stiffnesses of the tire model. In an effort to support this idea, the effective residual stiffness was calculated for the tire both as a part of the assembled quarter car system and for the tire subsystem.

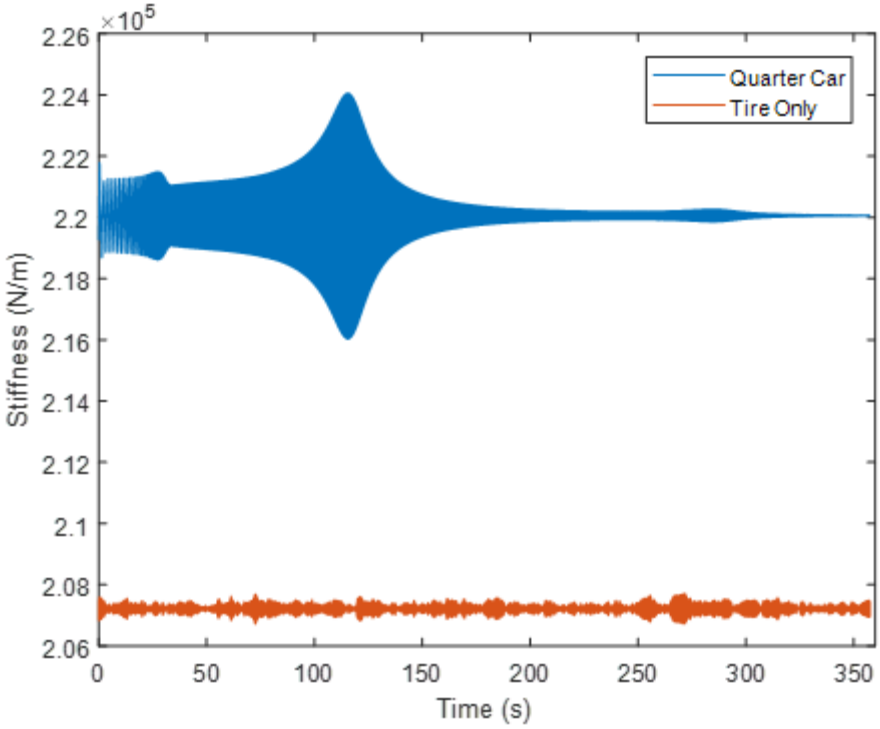

Figure 49: Residual stiffness for the assembled quarter car system and tire subsystem measured over 360 seconds

At first glance, it appears that Figure 49 shows high frequency vibration over the entire range. However, this is simply a result of the extended time period over which the data is shown. Figure 50 shows the same data for a 10 second section.

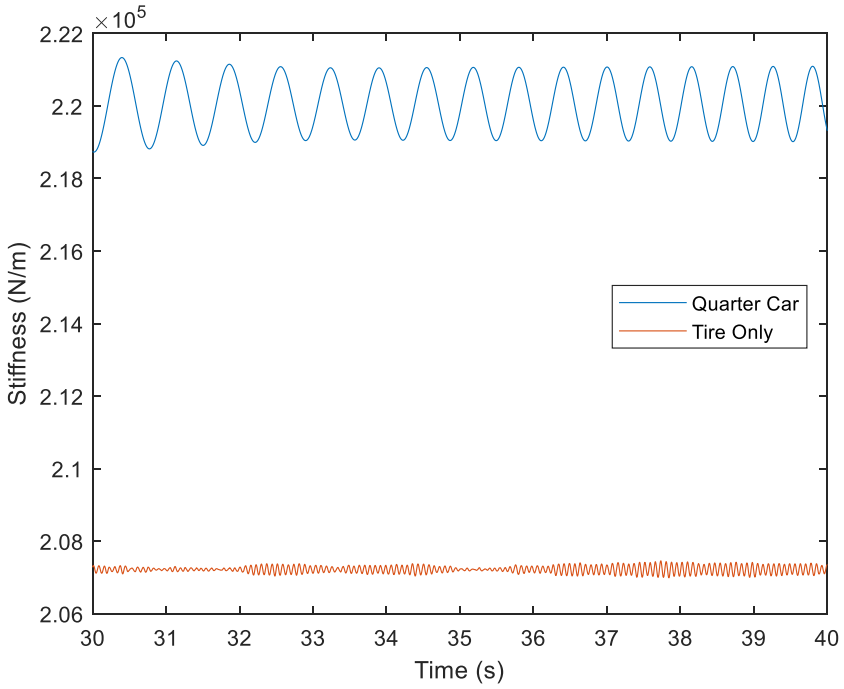

Figure 50: Data of Figure 49 shown from the 30 to 40 second marks

Figure 50 shows the response of the quarter car system, which was subject to a sine sweep excitation, has an average frequency of 1.6 Hz over the 10 second range. In contrast, the tire subsystem was subjected to band limited noise input. The sine input was simulated over an extended period of time (approximately 6 minutes) in order to more clearly see the dominant frequencies in the system, as well as to cause more extreme changes in the residual and sidewall stiffness. More significant changes in stiffness were desired in order to show the effects of the nonlinearity on the decoupling process.

In Figure 49, we see that the stiffness experiences variation of +/- 1.8% in the vicinity of the largest peak of the assembled system. For the tire with the band limited noise input, the stiffness remains even more linear with a maximum variation of approximately 0.25%. The most important takeaway of the figure comes from the difference between the average values of the two stiffnesses.

On average, the residual stiffness of the tire as part of the assembled system is 6.2% higher than that of the tire by itself. In addition to the residual stiffness shown in Figure 49, there is also nonlinearity in the sidewall stiffness, which could contribute to the error. These nonlinearities in stiffness effectively cause the tire to be a different subsystem when tested by itself compared to as part of the assembled system.

To overcome these challenges posed by the nonlinear tire model, it is important to first determine if the decoupling and recoupling procedures can handle the tire nonlinearity for a given system load. There are two possible solutions to determine if the same techniques can still be used to decouple the two systems: 1) a simulated load can be added to the tire subsystem without altering inertial properties, or 2) the suspension subsystem can instead be treated as the known subsystem since it is considered linear over the range of operation.

The ultimate goal of the current work is to validate this coupling and decoupling process by applying it to experimental data. While adding a load to the tire subsystem would be simple to do in simulation, the testing equipment needed to apply the load experimentally is not currently available in the CenTiRe lab. Thus, the procedure going forward will be to treat the suspension as the known subsystem instead of the tire.

The choice to use the suspension as the known subsystem opens up an intriguing possibility which demonstrates the power of frequency based substructuring and why it is particularly applicable to the quarter car system. This possibility is to use the analytical FRF for the suspension subsystem in place of a FRF from the simulated system. However, it is instructional to first compare the analytical and simulated FRFs to ensure that the simulated system behaves as expected. The comparison of these FRFs is shown in Figure 51.

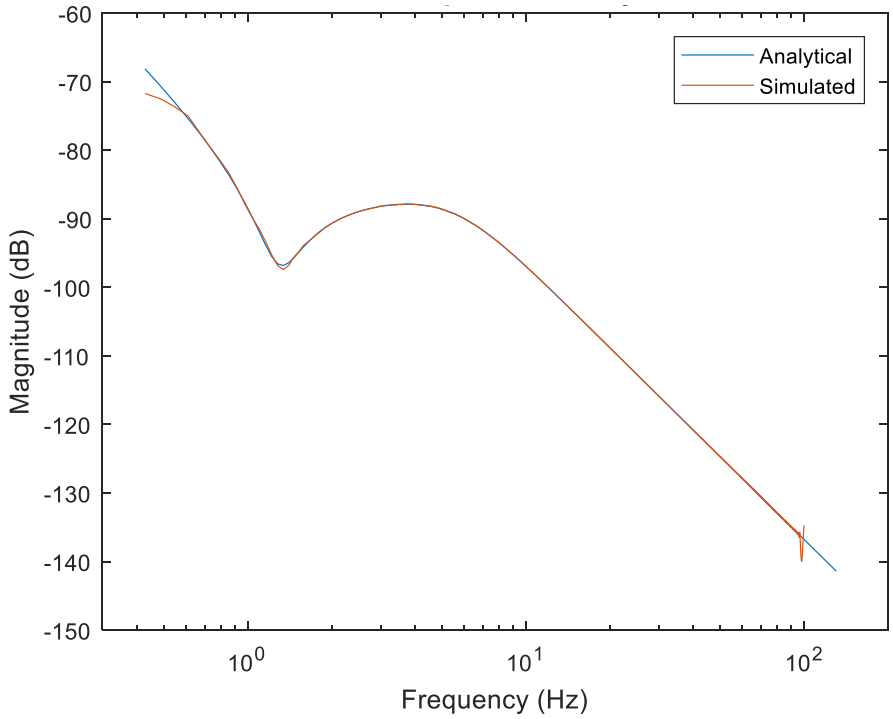

Figure 51:The simulated FRF matches well with the analytical

The agreement between the FRFs suggests that the suspension system in the simulation matches with the analytical model, as expected. It is, then, possible to use the analytical FRF in the decoupling process. The results of the decoupling should be improved by using the analytical model in place of the simulated, since the analytical model produces exact results with no noise or errors.

Decoupling the analytical suspension FRF (Figure 51) from the simulated FRF for the assembled system (Figure 46) results in an FRF for the tire subsystem under loaded conditions (Figure 52).

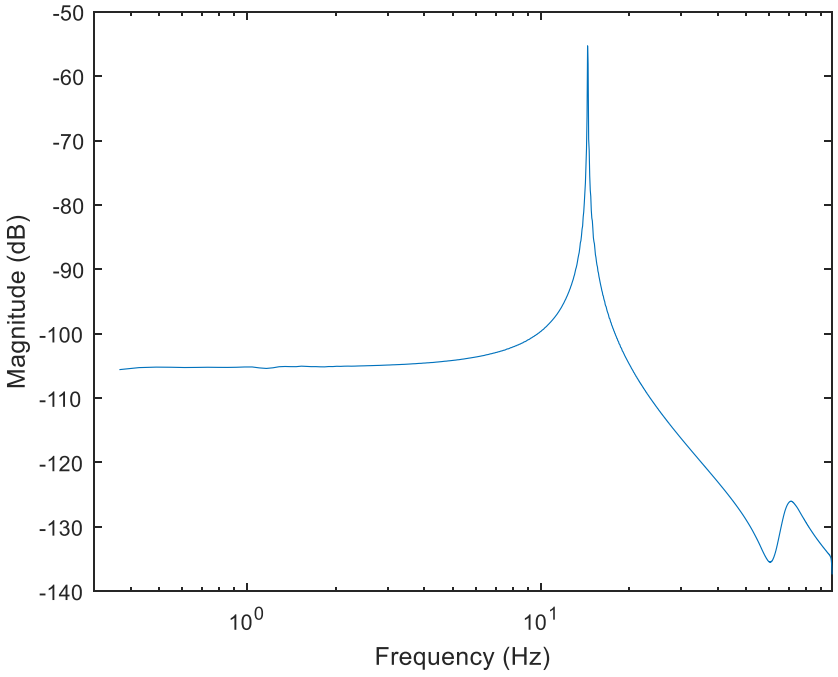

Figure 52: FRF for tire subsystem, obtained through decoupling

The results in Figure 52 match closely with what was expected for the tire. Compared to Figure 47, the first natural frequency has risen from 13.7 to 14.4 Hz. This rise in frequency corresponds to the increase in stiffness shown in Figure 49. We now have the FRF for the loaded tire without having to simulate the tire under loaded conditions. As mentioned earlier, the ability to avoid testing a loaded tire will be important during experimental validation.

Earlier in the present chapter, it was mentioned that the damping constant shown in Table 2 appears high compared to what may normally be expected from a tire overall. However, Figure 52 shows a peak for the tire which is clearly lightly damped. This discrepancy comes from the construction of the rigid ring model and the particular specification of the damping constant. First, the inclusion of belt mass and residual stiffness makes it so that the damping ratio cannot be calculated directly using the sidewall stiffness and damping as listed in Table 2. Instead, the interaction between the belt mass/residual stiffness and the unsprung mass/sidewall stiffness is a more complex

relationship which must be considered as a whole in order to have an accurate view of the overall tire damping. This relationship brings up a second point which merits clarification: the damping value from Table 2 is the sidewall damping. In other words, the value from the table is specifying damping for only part of the tire, not for the tire as a whole. Thus, as mentioned in the preceding paragraph, the interaction of the unsprung mass and belt mass must be considered together to give an accurate view of the overall tire damping. Figure 52 shows a lightly damped tire, with a damping ratio in the neighborhood of 1% (as determined through the circle fit method [20]).

With decoupling having been applied successfully, we turn again to the general framework of the previous section. Therefore, the next step is to couple this tire to a "new" suspension and compare the results to those simulated for the new assembled system. This comparison is shown in Figure 53 and Figure 54.

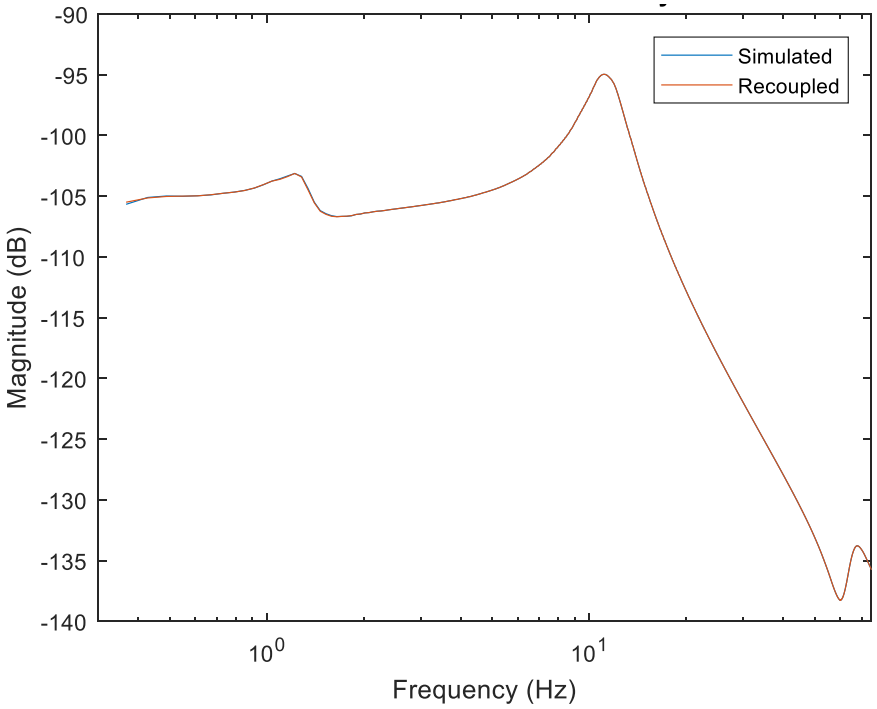

Figure 53: Data from the simulated system matches closely with data for the coupled system

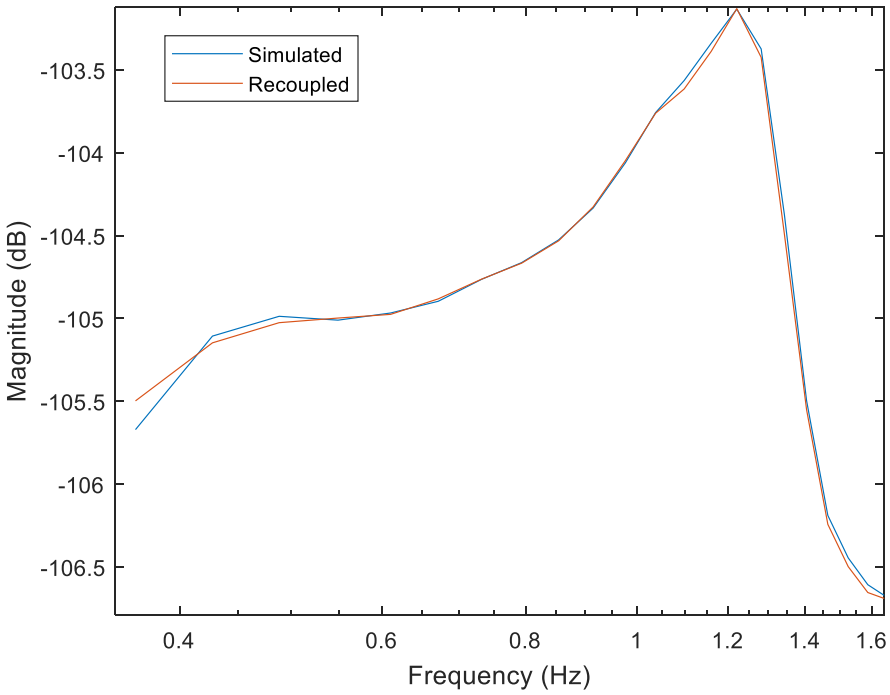

Figure 54: Minor discrepancies between FRFs of Figure 53 below 2 Hz

Aside from minor discrepancies at frequencies less than 2 Hz (Figure 54), the recoupled FRF matches closely with the simulated quarter car system. The close agreement suggests that the FRF obtained for the tire subsystem through decoupling accurately represents the tire dynamics within the quarter car system. Furthermore, though the FRF for the tire is only applicable for the given loading, the successful decoupling and recoupling shows that the process can handle the nonlinearities which occur during normal operation.

5.2.1 Applicability to different sprung and unsprung mass values

As mentioned previously in this section, the decoupled FRF for the tire subsystem is only applicable for the current sprung and unsprung mass values. If either of these values were to change, the static deflection of the tire would change, and thus the nonlinear nature of the tire stiffness elements would cause the dynamics of the tire subsystem to change. However, Figure 49 showed that the residual stiffness only changed by 6.2% for mass change of over 300 kg. It is,

therefore, reasonable to assume that small changes in the sprung or unsprung masses may not significantly change the apparent stiffness of the tire.

In order to investigate whether or not these changes in stiffness may be negligible, simulations for the assembled quarter car system were first carried out for two "new" suspensions: one with a 10% increase in sprung mass and one with a 10% decrease in sprung mass. It should be noted that the following section contains many figures which are very similar to each other and to those seen in previous sections. This similarity is expected due repetition of the decoupling process for systems with percentage variations mass. The residual stiffnesses for the systems with 10% variations in sprung mass are shown in Figure 55.

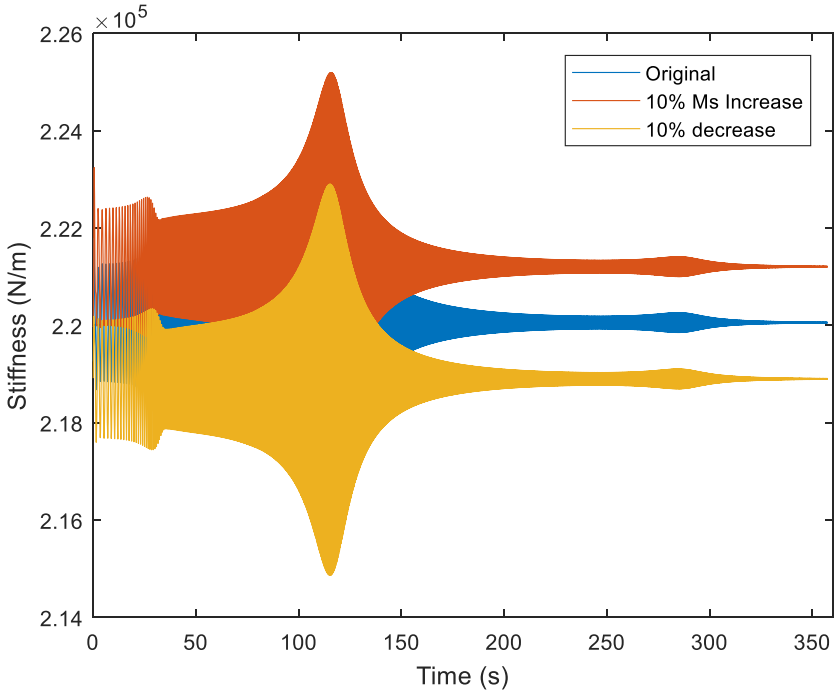

Figure 55: Residual stiffnesses for the tire for three different sprung mass values

Though the full response for the original system is not visible in the plot, it follows a similar trend as the other two systems. Again, the average value for each system is of more interest than the

time response. The same analysis was performed with the unsprung mass, where two “new” systems were simulated with a 10% increase and decrease from the original unsprung mass. Table 3 shows the average values for each system and the percent change in residual stiffness.

Table 3: Changes in residual stiffness are shown for a 10% increase and 10% decrease for both the sprung and unsprung masses

System	Average Stiffness (N/m)	Change from Original (N/m)	Percent Change (%)
Original	2.200×10^5	---	---
10% Increase in Sprung Mass	2.212×10^5	1.15×10^3	$+ 0.5\%$
10% Decrease in Sprung Mass	2.189×10^5	-1.16×10^3	$- 0.5\%$
10% Increase in Unsprung Mass	2.202×10^5	1.34×10^2	$+ 0.06\%$
10% Decrease in Unsprung Mass	2.199×10^5	-1.35×10^2	$- 0.06\%$

Since Table 3 shows that the variations in stiffness are negligible for the systems with altered unsprung masses, time responses will not be displayed for these systems. On the other hand, the percent change in stiffness for the systems with altered sprung mass is not negligible at approximately 0.5%.

As demonstrated earlier in this section, a 6.2% change in residual stiffness was enough to cause the decoupling process to not work. Thus, question now is whether or not the small change in stiffness caused by change in either mass is enough to similarly render the decoupling and recoupling process ineffective.

Figure 56 shows the analytical FRFs for both suspension subsystems with new sprung masses compared to the original subsystem.

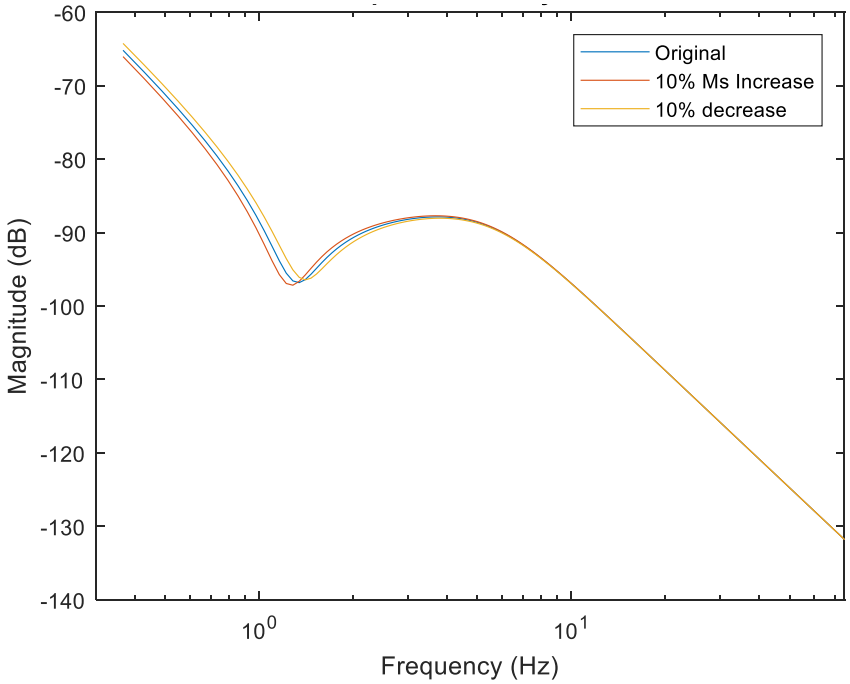

Figure 56: FRFs for suspension subsystems with new sprung masses compared to the original

These new suspension FRFs were each then recoupled with the tire subsystem FRF of Figure 52. Note that the FRF for the tire was obtained by decoupling the original suspension FRF from the original assembled quarter car system. The results of the recoupling for the suspension with increased sprung mass are shown in Figure 57.

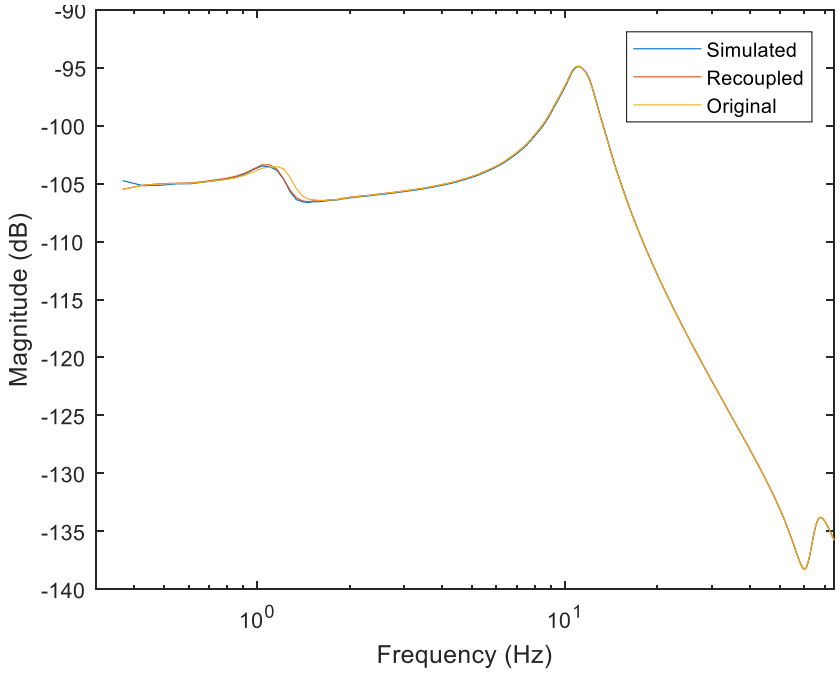

Figure 57:The simulated and recoupled FRFs for increased sprung match well. They are shown with the original for comparison.

Though it appears that the simulated and recoupled systems match almost perfectly, it is worth noting that there are small discrepancies below 2 Hz (Figure 58).

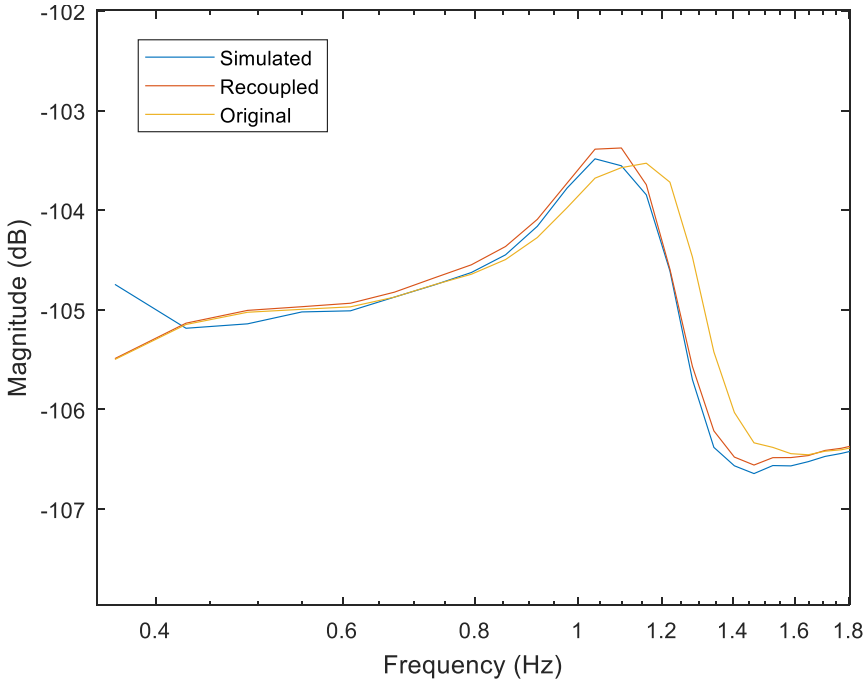

Figure 58: A zoomed view of Figure 57 below 2 Hz. There are small discrepancies between the simulated and recoupled FRFs

Despite the small error between the simulated and recoupled systems, a comparison to the original system (from which the tire FRF was obtained), shows that the recoupling effectively describes the change in dynamics.

The coupling of the tire with the suspension with reduced sprung mass produced similar results. Figure 59 and Figure 60 again show the comparison of the simulated and recoupled systems along with the original.

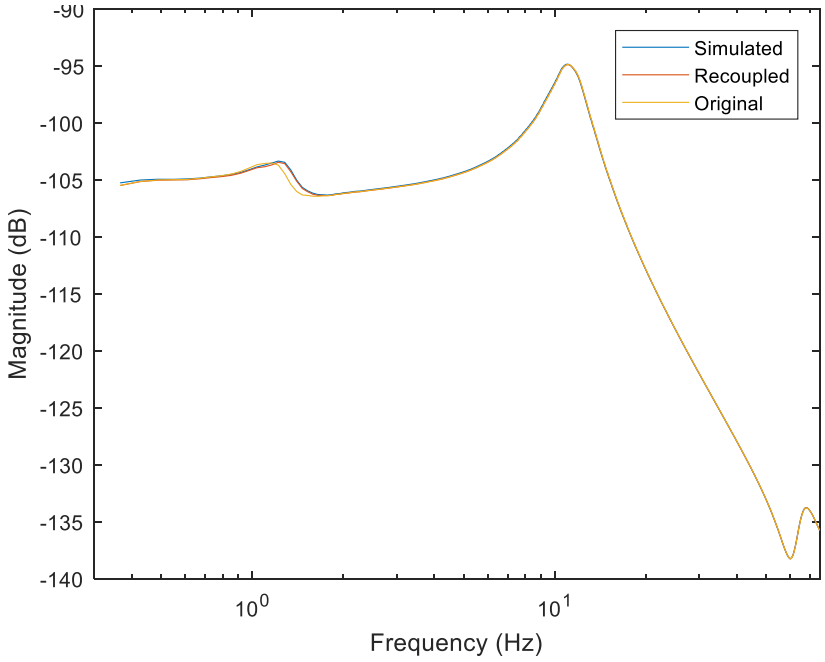

Figure 59: The simulated and recoupled FRFs for decreased sprung match well. They are shown with the original for comparison

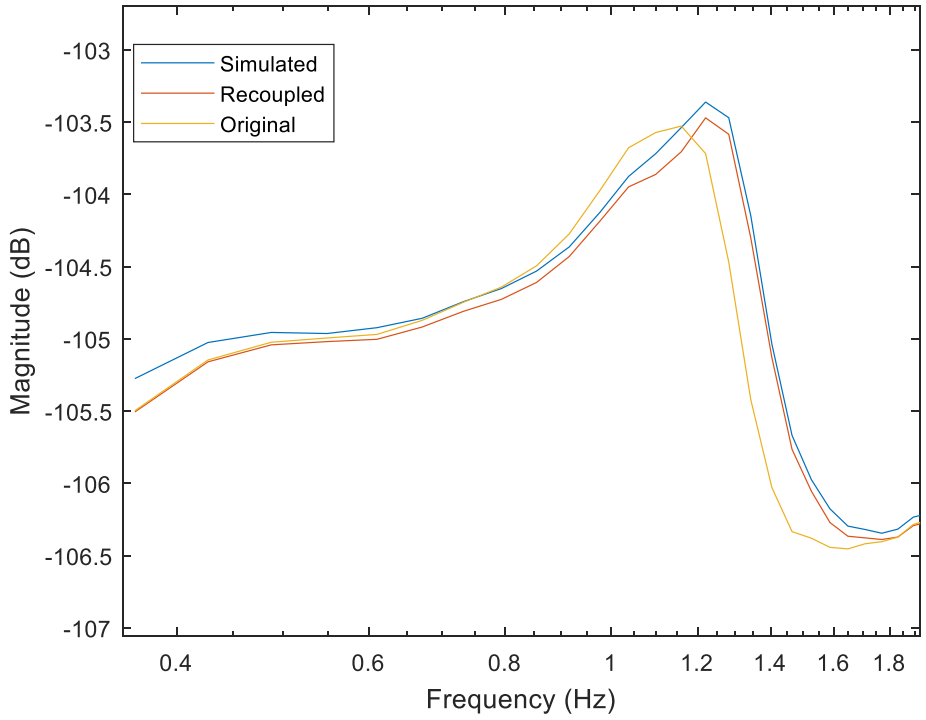

Figure 60: A zoomed view of Figure 59 below 2 Hz. There are small discrepancies between the simulated and recoupled FRFs

As with Figure 58, we see minor discrepancies between the recoupled and simulated system receptance FRFs in Figure 60. Again, these errors are relatively small and the recoupled FRF is able to show the shift in natural frequency away from the original system. The fact that the process still works for both the 10% increase and 10% decrease on sprung suggests that using the analytical suspension model and treating it as the known subsystem is a suitable work around for an FBS process which is known to not work well with nonlinearities. Before a strong statement can be made about the efficacy of this process for the quarter car system, we must first determine whether the findings for changes in sprung mass hold true for unsprung mass as well.

As shown in Table 3, similar to the new sprung mass systems, two new systems were simulated with a 10% increase and 10% decrease of sprung mass. Since the unsprung is considerably smaller than the sprung mass, a 10% change corresponds to a much smaller change in tire loading. That smaller change in loading corresponds, in turn, to a less significant change in tire stiffness. With a change of less than a tenth of a percent in either direction, along with the insensitivity shown to a 0.5% change caused by the sprung mass variation, it may seem at first glance that the nonlinearity can be considered negligible.

However, the nature of changing the sprung mass of this quarter car system is not the same as changing the unsprung mass. Particularly, the sprung mass itself has no bearing on the tire subsystem. In other words, since the tire and suspension are assumed to be coupled at the unsprung mass, the sprung mass is not directly connected to the tire subsystem. On the other hand, the unsprung mass is a coupled degree of freedom and is thus present in both subsystems. As addressed in [34] uncertainty propagation is more prominent between coupled degrees of freedom. Thus, it is important to make sure that the small error from the tire non-linearity does not cause issues during the coupling process.

It is important to note the way in which the unsprung mass of the system has been changed. In the simulations of the full quarter car system, the unsprung mass was increased or decreased by 10 percent of its total value. However, when translating this change to the individual subsystems, the entire change must be accounted for by the suspension subsystem. In the interest of clarity, recall that:

$$m_{us} = m_{usA} + m_{usB}$$

Where the tire is subsystem A and the suspension is subsystem B. Since we are currently working with a simulated FRF for the tire subsystem which was obtained via decoupling, m_{usA} is conceptually fixed at its current value. Thus, when the unsprung mass is being increased by 10 percent, the suspension subsystem sees this increase as:

$$m_{usA-new} = m_{usA} + 0.1 \times m_{us}$$

With that changed in mind, the FRFs for the new suspension subsystems with altered unsprung masses are shown in Figure 61.

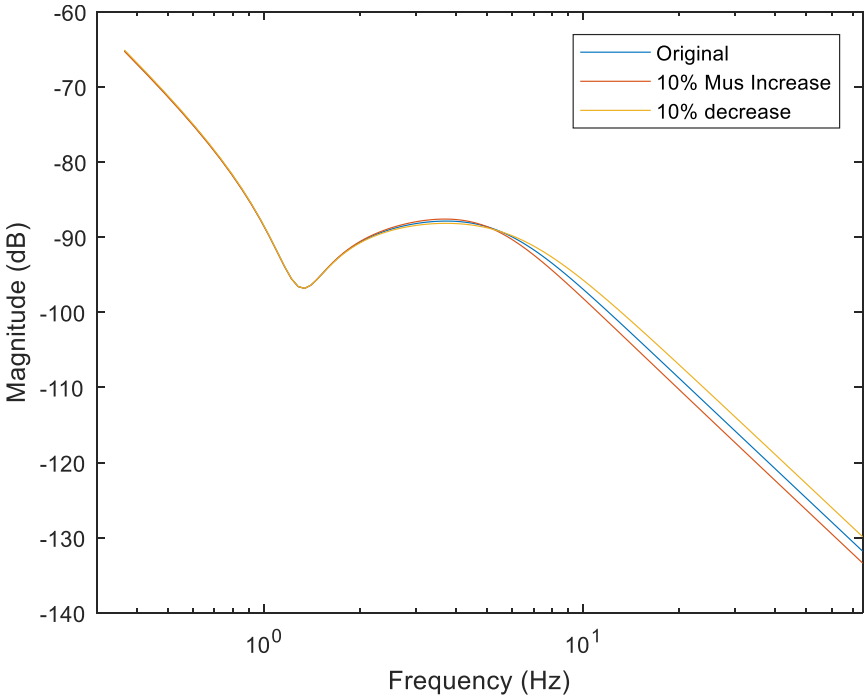

Figure 61: FRFs for suspension subsystems with new unsprung masses compared to the original

Following the same process as for the new sprung mass systems, the FRFs of Figure 61 were then recoupled with the tire subsystem FRF of Figure 52. The coupling results for the system with increased unsprung mass are shown in Figure 62.

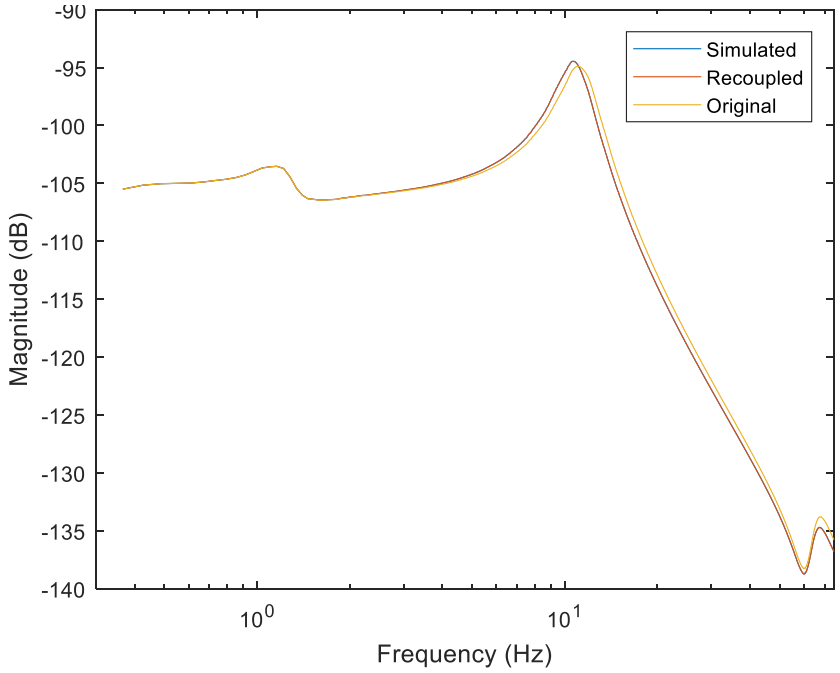

Figure 62:Simulated and recoupled FRFs for the system with a 10% increase on sprung mass

Again it appears that the simulated and recoupled results match well. Unlike the previous cases, it appears that the simulated and recoupled systems match almost exactly at low frequencies. Instead, there is some slight variation in the neighborhood of the second natural frequency, shown in Figure 63.

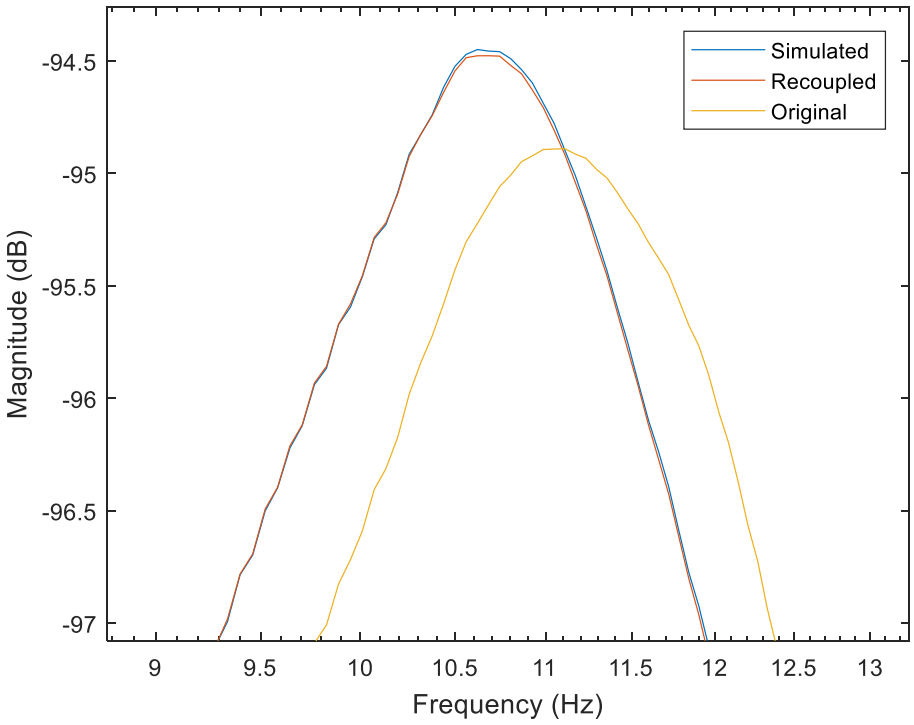

Figure 63: Zoomed view of second peak from Figure 62

Compared to the slight variations shown in Figure 58 and Figure 60, those in Figure 63 are even less significant. The recoupling process has again reproduced the frequency and magnitude shift from the original system in spite of the non-linearity error.

The recoupling of the suspension with reduced unsprung mass behaved similarly and is displayed in Figure 64.

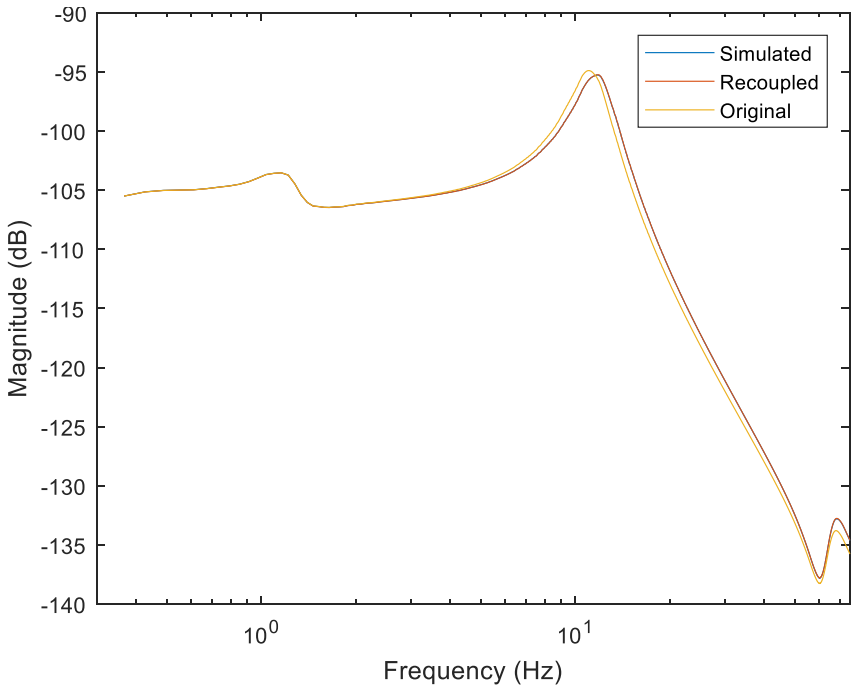

Figure 64: Simulated and recoupled FRFs for the system with a 10% decrease on sprung mass

Results similar to those in Figure 62 can be seen in Figure 64. Closer inspection of each peak confirms observation with the recoupled FRF matching the simulated one almost exactly at the first and third peaks. While there are, again, very slight discrepancies in the neighborhood of the second peak, comparable to those shown in Figure 63.

Up to this point, it has been shown that, once a tire FRF has been obtained through decoupling, an arbitrary new suspension subsystem can be coupled to the tire to produce reliable FRFs for the "new" quarter car system. These results were found to be reliable in spite of tire non-linearity which is known to cause many issues with FBS. Specifically, it was found that the suspension stiffness and damping could be altered as desired, while both sprung and unsprung mass could be altered by +/- 10% without causing issues with the recoupling. In the future, further testing could be done to determine a more exact neighborhood for mass variation where the process begins to

break down. However, we determined that it was first necessary to validate the preceding process and given mass variation range experimentally.

5.2.2 Small-scale simulation

Prior to experimental testing, the decoupling process was applied again to simulated systems in order to determine the approximate range needed for testing. Many aspects of these small-scale simulation were similar to those done for the full scale system with the rigid ring model. A more comprehensive description of the full scale simulations can be found in the preceding sections. Due to the similarities in application to the full scale model and to the small-scale model, a briefer discussion will be presented in this section.

The two most important factors that had to be designed for in the small-scale simulations were the damping ratios and the nonlinear stiffness of the tire. Since no data was available for these parameters, values had to be established for the simulations.

Tire stiffness was the only one of these values which was possible to estimate outside of the vibrational testing. Though it is expected that vibrational tests will reveal a somewhat different stiffness value, static tests can provide a good starting point. The specific procedure which was applied to estimate the tire stiffness is detailed in the section on the development of the small-scale test setup.

Though there is a shock dynamometer available in the CenTiRe lab, the damper from the test vehicle is too small to test. Thus, there is no direct way to obtain viscous damping values for the tire or suspension. Instead, it was assumed that the damping ratios for the small-scale system would be similar to those for a full scale system. Namely, it was assumed:

$$\zeta_{susp} = 0.2$$

$$\zeta_{tire} = 0.02$$

Where ζ_{susp} is the damping ratio for the suspension, and ζ_{tire} is the damping ratio for the tire. These values were assumed to be typical for tires and suspensions based on several vehicle dynamics sources [2, 124, 132]. From these ratios, mass and approximate stiffness values for each system were used to back calculate for the viscous damping coefficients. All values used for the simulations of the small-scale system are displayed in Table 4.

Table 4: Parameters for small-scale model

Parameter	Designation	Value
Sprung Mass	m_s	1.257 kg
Unsprung Mass	m_{us}	0.848 kg
Suspension Stiffness	k_s	1119 N/m
Tire Stiffness (linearized)	k_t	9121 N/m
Tire Stiffness (non-linear)	k_t	See Equation (141)
Suspension Damping	c_s	17.6 Ns/m
Tire Damping	c_t	3.51 Ns/m

Following the same structure as for the full scale simulations, the decoupling process was first applied to analytical, linearized models with parameters from Table 4. The receptance FRF for the unsprung mass of the assembled system is shown in Figure 65.

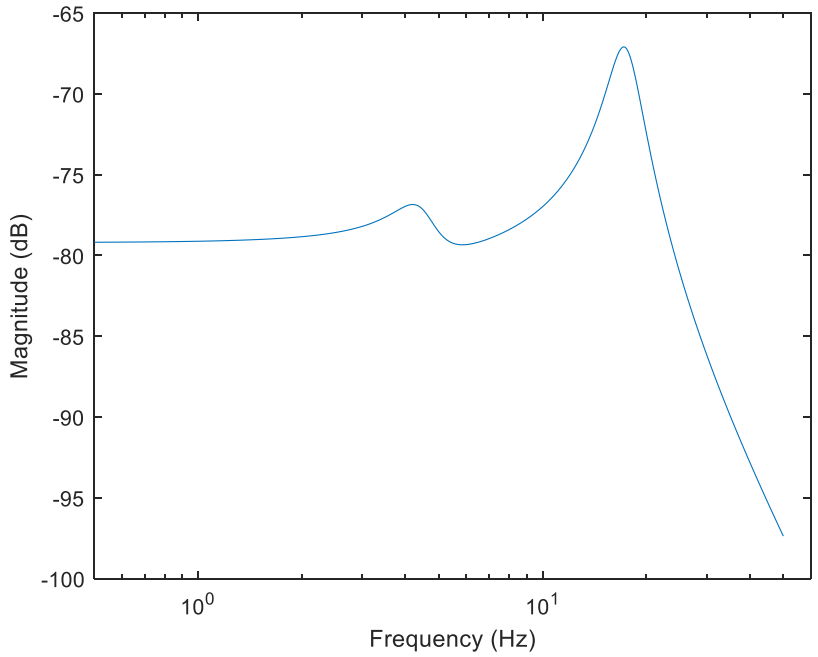

Figure 65: Analytical FRF for unsprung mass of assembled small-scale quarter car system

There are several differences in Figure 65 compared to the FRF of the full scale system in Figure 32. The general shape has been preserved, as expected, but both peaks have increased (to 4.5 Hz and 17.25 Hz, respectively) and the overall magnitude has increased.

Again, the suspension system was considered the known, or residual, subsystem. The analytical FRF for the unsprung mass of the small-scale system is shown in Figure 66.

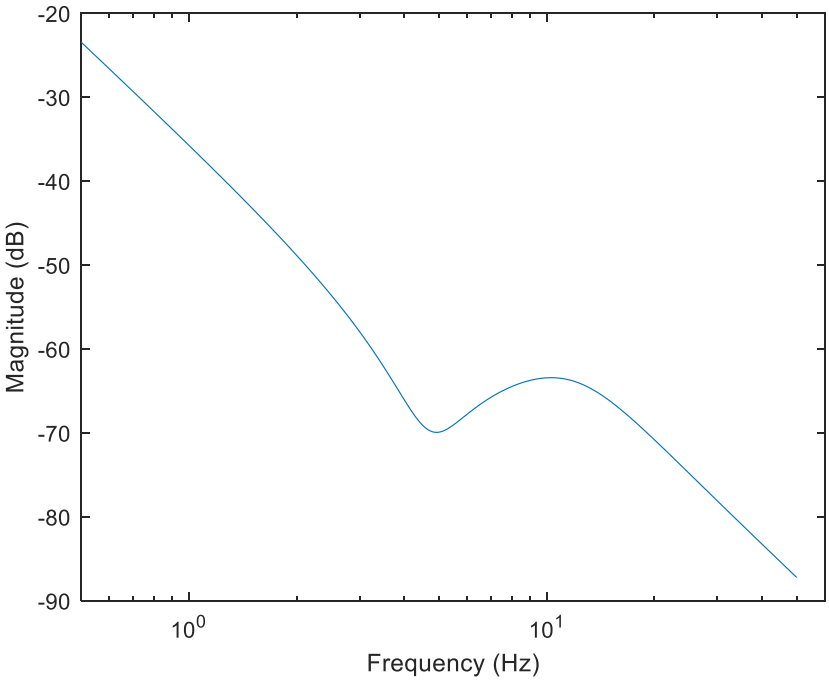

Figure 66: FRF for unsprung mass of small-scale suspension subsystem

As with the assembled system, the FRF for the suspension matches closely in shape with that of the full scale system. Then, the FRF of Figure 66 was decoupled from that of Figure 65 to give the response of the linearized tire, shown in Figure 67.

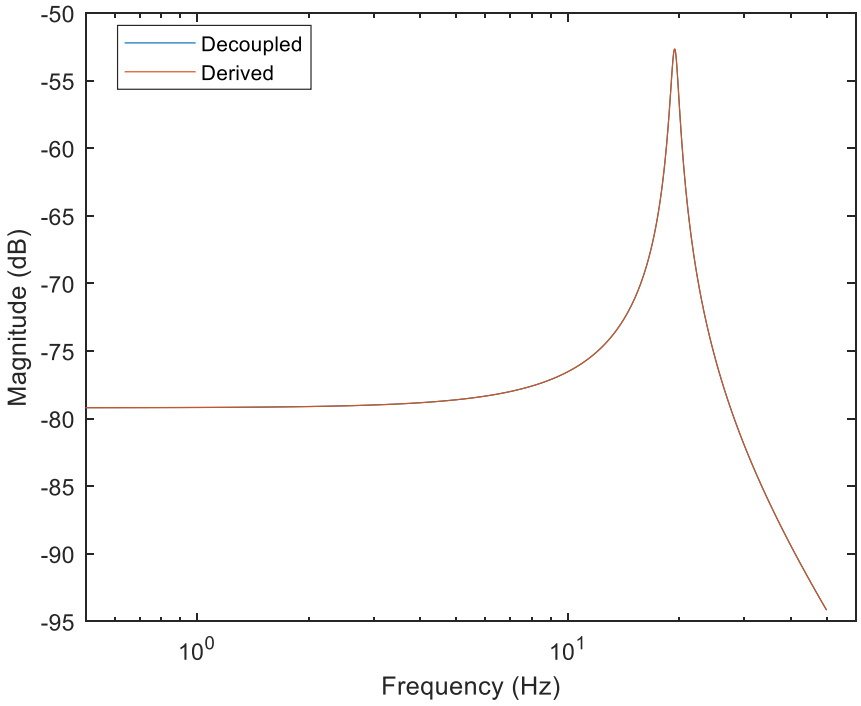

Figure 67: Comparison of decoupled and analytically derived FRFs for the linearized tire

Results from the decoupling match exactly with the analytically derived FRF for the linearized tire. Instead of demonstrating recoupling with a new tire or suspension again for the small-scale linearized model, the process will only be conducted on the nonlinear simulated system.

The small-scale model was created in Simulink and had all of the same parameter values as the analytical model, with the exception of the tire stiffness. Where linearized stiffness shown in Table 4 was used by the analytical model, the nonlinear tire stiffness is described by Equation (141). Similar to the simulations with the rigid ring tire, the small-scale system was simulated with a sine sweep force input directly to the unsprung mass. The time response for each mass is shown in Figure 68.

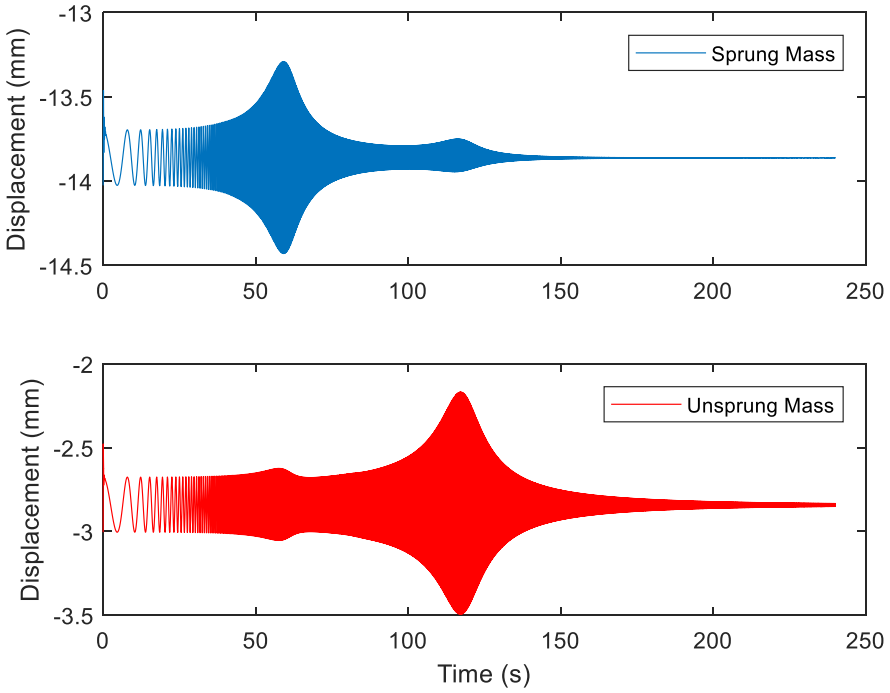

Figure 68: Time response for simulation of small-scale quarter car model with nonlinear tire stiffness

The plots in Figure 68 show the displacements of each mass relative to an initial zero point which corresponds to an un-deflected point of the spring and tire. This behavior ensures that the tire is being deflected to according to the nonlinear stiffness of the system, and will thus operate about the static deflection point. These displacement time responses were then used to obtain the corresponding FRFs. The FRF for the unsprung mass is shown in Figure 69 along with that of the analytical, linearized system.

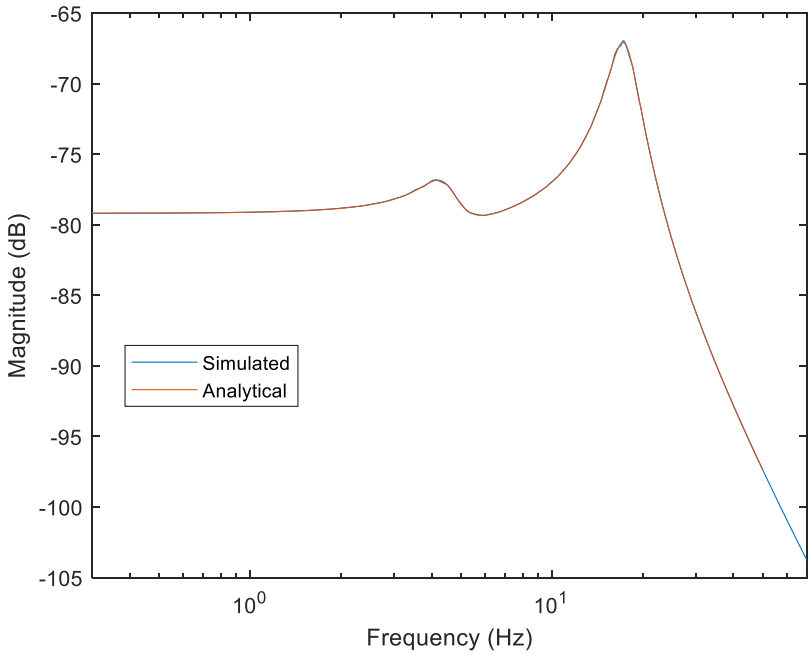

Figure 69: Comparison of FRFs for the unsprung mass of the simulated and analytically derived systems

The FRFs in Figure 69 match very closely with just small discrepancies in the neighborhood of each peak. Conceptually, this result is as expected. Though the nonlinearity in the tire does cause some differences, the tire operates about some static deflection point. From Figure 68, the minimum and maximum deflections of the tire throughout the simulation are 2.17 mm and 3.50 mm which correspond to tire stiffnesses of 8162 N/m and 9867 N/m, respectively. The average of these two stiffnesses is 9014 N/m which is close to the estimated linearized stiffness of 9121 N/m (about 1.2% difference).

Instead of simulating the small-scale suspension subsystem by itself, the process for the full scale system was repeated and an analytical FRF for the suspension was used. Thus, the FRF of Figure 66 was decoupled from the simulated system of Figure 69. The resulting FRF for the tire with nonlinear stiffness is shown in Figure.

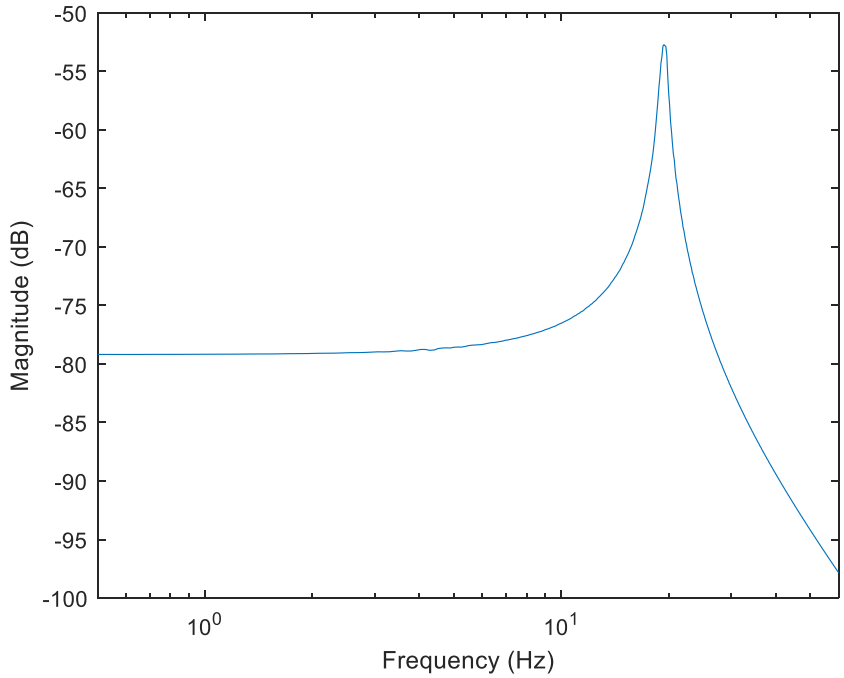

Figure 70: Decoupled FRF for small-scale tire with nonlinear stiffness

Again, the result of Figure 70 matches well with the linearized counterpart in Figure 67. At this point, the analysis for the small-scale system will deviate somewhat from that of the full scale system. Namely, where the full scale system was recoupled with a separate tire, the small-scale system will be the original tire recoupled with a new suspension. The motivation for this change was the availability and ease of changing the stiffness properties of the suspension.

The manufacturers of the test vehicle sell a range of suspension springs ranging from 824 N/m to 1538 N/m. Furthermore, only two connections must be removed to replace the spring, making it more feasible to test a range of springs. For the present work, only the stock spring and the stiffest spring (1199 N/m and 1538 N/m, respectively) were used for testing, and thus, for the simulations. In that interest, the analytical model for the suspension was updated with the new stiffness, and is shown in Figure 70.

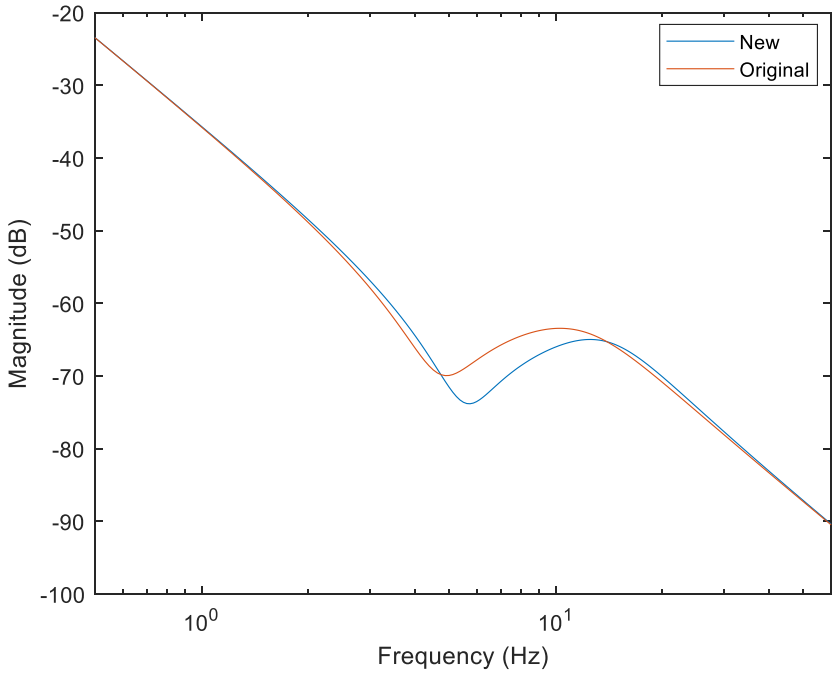

Figure 71: Comparison of FRF for new, stiffer suspension subsystem with the original

One item of note for this new analytical suspension system is how the damping was handled. Recall that it was assumed the damping constant was such that the damping ratio was 0.2 for the original system. However, it is desired to model this new, stiffer suspension system in a way that is conceptually similar to how the experimental system will be updated. Thus, instead of also updating the damping constant to maintain the 0.2 ratio, the constant will be kept the same as for the original system and as shown in Table 4, at a value of 17.6 Ns/m. This modelling decision is reflected in the "New" FRF of Figure 71.

Next, the FRF for the new suspension from Figure 71 was coupled with the FRF for the nonlinear tire from Figure 70. Additionally, the simulations were run again for the assembled small-scale quarter car system with the new suspension stiffness. Results from the coupling and from the simulation of the new system are shown together in Figure 72.

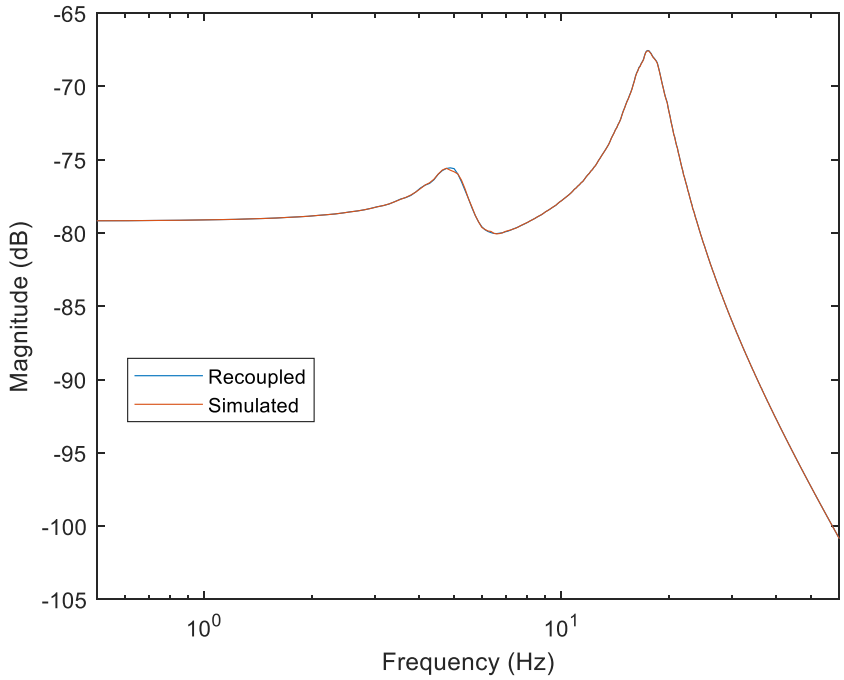

Figure 72: Recoupled and simulated FRFs for the unsprung mass of the system with the new suspension

The recoupled FRF for the system with new suspension matches well with the FRF obtained from a repeated simulation. Given that only the stiffness of the suspension was changed, there was little change in the loading of the tire during testing. Thus, the closeness of results is as expected.

Results from Figure 69 to Figure 72 will serve as a basis for the testing plan for the experimental system. In particular, the initial range for testing will be 0-30 Hz and the peaks of the system are expected to be around 4.5 Hz and 17.25 Hz. Though these values provide useful initial estimates, they are for a highly idealized model and test, and as such, it is expected that there may be some significant variations in the actual experimental system. Details of the experimental setup were given in **Chapter 4 – Experimental Design and Setup** and results are displayed later in this chapter.

5.3 Experimental results

Prior to collecting the data to be used for application and validation of the decoupling techniques, general tests were performed to validate the small scale experimental system and compare it to the analytical model. These tests, and all subsequent tests in the experiment were carried out using the following equipment:

- LMS Test.Lab software
- LMS DAQ/Signal Conditioner
- Vibration Test Systems (VTS) VG-100 electronic shaker
- APS 125 Power Amplifier
- PCB 208A02 Load Cell
- PCB U352C67 Accelerometers

5.3.1 Preliminary Testing and Validation of Test Rig

During setup, it was determined that the bearings were causing significant damping to the system. Thus, several preemptive actions were taken before the first test. The system was augmented to mount to a single bearing and the damper of the shock assembly was emptied so that most of the damping would be due to the bearing. The damper had to be emptied instead of removed due to the structural support it provides to the shock assembly. Furthermore, it was decided that a step sine input would be used in order to ensure that the highly damped modes had time to develop. Step size and frequency range varied depending on the test and will be specified as applicable. A summary of results from all of the following tests will be given at the end of the present section.

The first preliminary test was to directly excite the sprung mass with the suspension and tire removed from the test setup. For this test, the system being excited is essentially just a mass-damper system because the sprung mass consists of the mounting plate and the bearing. An image of the setup is shown in Figure 73.

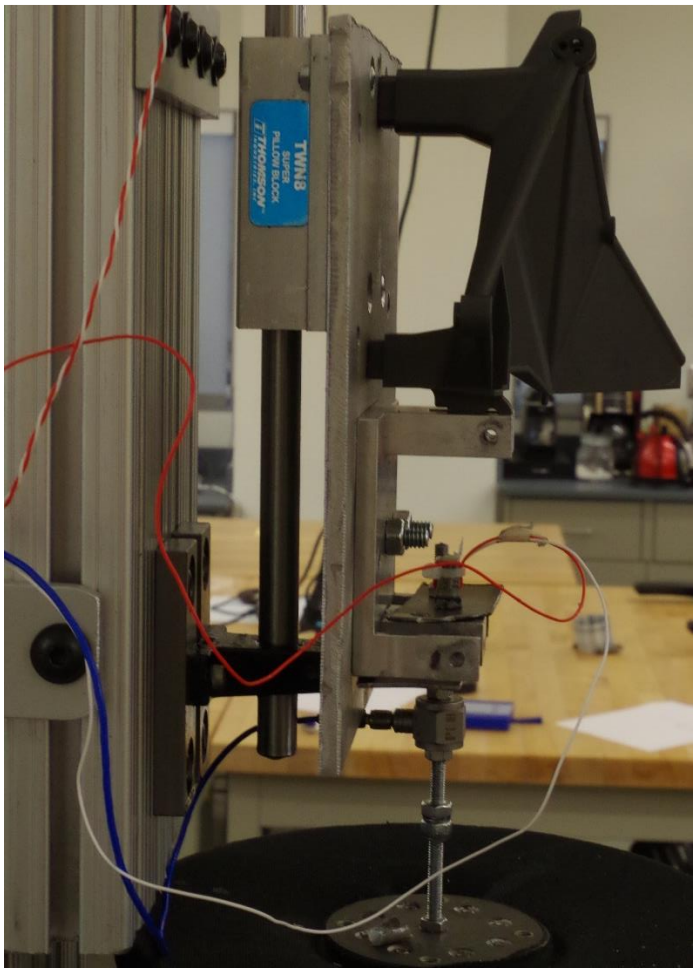

Figure 73:Setup for preliminary test with no tire or suspension attached to test rig

Some stiffness may be provided by the stinger, but the stiffness in the vertical direction should be high enough that no peak appears for the range of interest. Thus, it is expected that the response of the system should be relatively flat. Figure 74 shows the measured response.

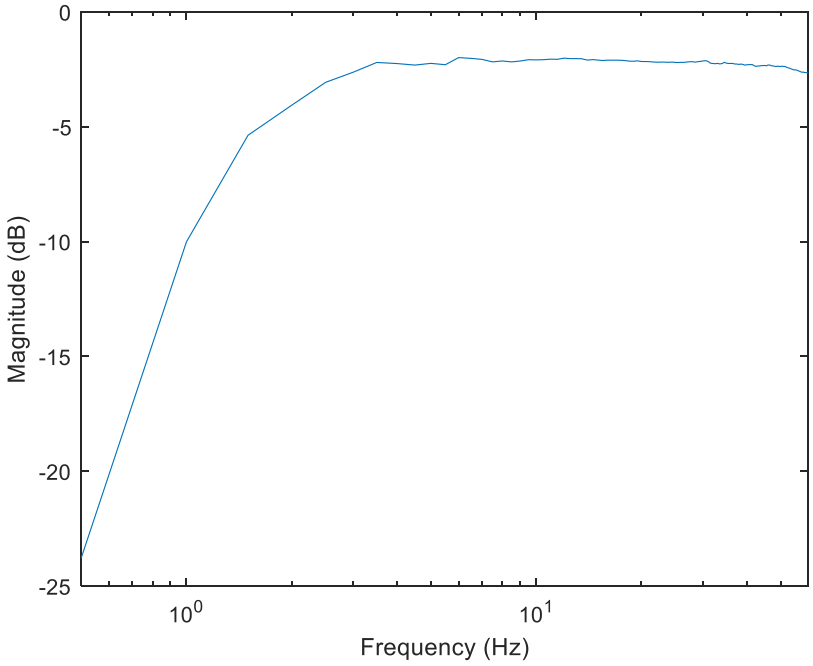

Figure 74: Response of sprung mass for the setup of Figure 73

Figure 74 shows the expected, flat response of the system. This result is important because it shows that the construction of the test rig should not interfere with the vertical dynamics of the quarter car system over the range of interest.

The second preliminary test was to actuate the experimental system in the same way as for its simulation counterpart as discussed earlier in this chapter (recall that the decoupling process requires excitation directly at the unsprung mass). In order to achieve this excitation, the stinger was attached directly to the steel bolt which connects the tire to the wheel hub. The tire, meanwhile, was resting on a rigid surface and supporting the entire weight of the quarter car system. This setup is shown in Figure 75.

Figure 75:Test setup for excitation directly to unsprung mass

One concern for the setup of Figure 75 was that the distance from the force input to the center of the tire would cause an input moment in addition to the force. This distance does not turn out to have a significant impact on the vertical motion as will be shown in later tests.

For the setup of Figure 75, it was necessary to ensure that the tire was not moved from its equilibrium point during the attachment of the stinger. By exciting the tire about the static equilibrium point, the test will more closely mimic the loading seen for a typical “road input.” Additionally, the shaker input was decreased as much as possible without sacrificing the quality of the data. In an effort to ensure that all dynamics of the system were fully captured, the test was run from 0.5 Hz to 60 Hz. The resulting FRF is shown in Figure 76.

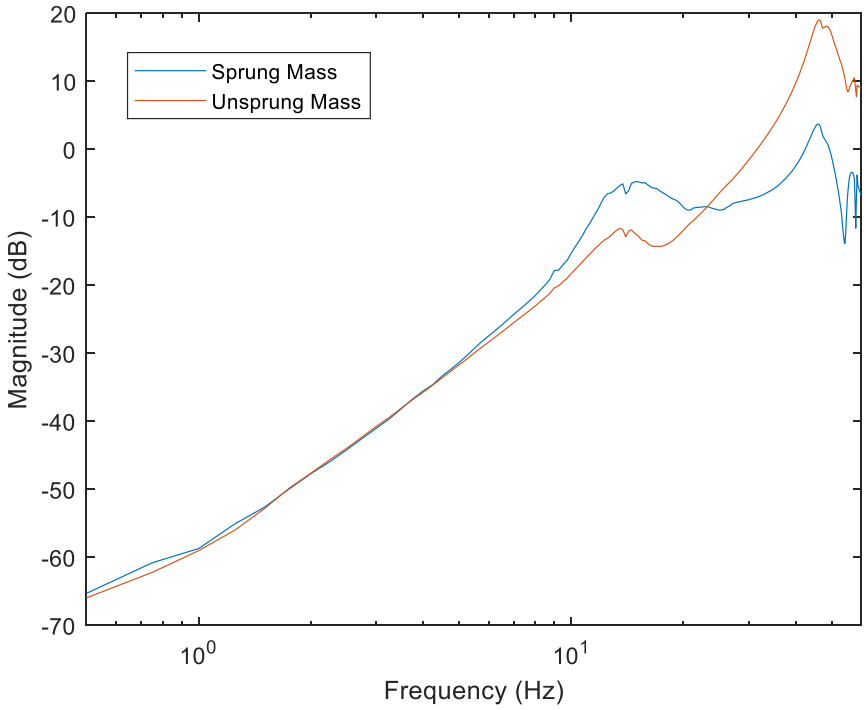

Figure 76: Accelerance FRF for the test setup shown in Figure 75

At first glance, Figure 76 appears mostly as expected, with a more damped first peak and considerably less damped second peak. However, closer inspection reveals that these peaks do not occur at the expected frequencies and that there are, in fact, at least two independent peaks between 10 and 20 Hz. Based on physical observation, it appears that at least part of the double peak between 10 and 20 Hz is caused by rotation of the tire and control arms, while the peak near 45 Hz could be the vibration of the tire. These physical observations will be investigated and discussed further later in the present section. Before investigating these unexpected dynamics, the first vertical mode of the system will be identified and explored.

A more in depth inspection of Figure 76 reveals a peak for both masses at 9 Hz. Though the frequency is considerably higher than predicted by the model, the presence of such prevalent

dynamics which were not modeled raises the possibility that the peak at 9 Hz is indeed the first vertical mode of the system. A zoomed view of Figure 76 is shown in Figure 77.

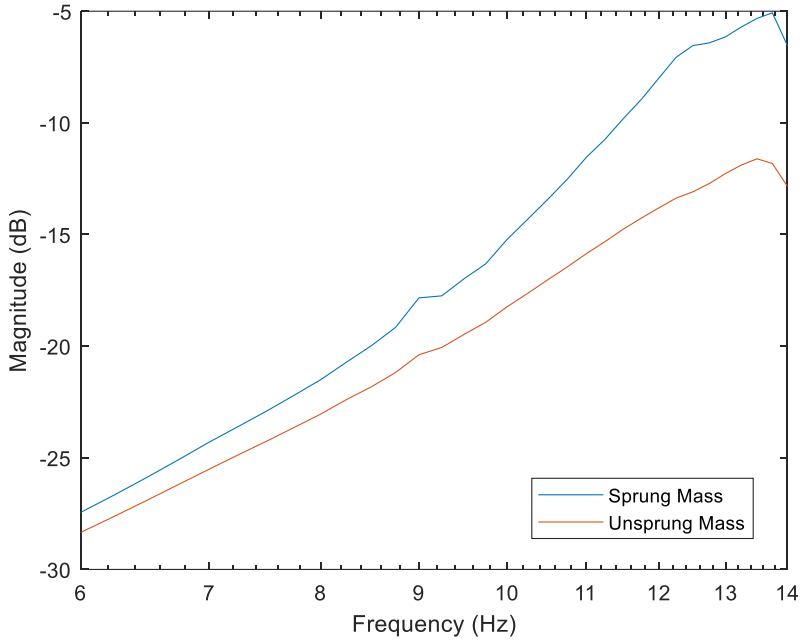

Figure 77: Zoomed view of Figure 76 to show first vertical mode at 9 Hz

This peak at 9 Hz is thought to be the first vertical mode of the system due to it being the first noticeable peak from Figure 76 and the fact that it has a higher magnitude for the sprung mass, as predicted by the model. The increase over the frequency predicted by the model could be caused by friction of the bearing or by the general construction of the system causing the full sprung mass to not be supported by the suspension. Alternatively, the increase could have caused by a deviation in expected spring stiffness, but static tests of the springs confirmed the manufacturer specified values.

The view of Figure 77 and the aforementioned reasoning are not sufficient evidence alone to support the claim that the peak at 9 Hz is indeed the first vertical mode of the system. In the interest

of further proving this assertion, the phase diagram for the FRF of Figure 77 is shown in Figure 78.

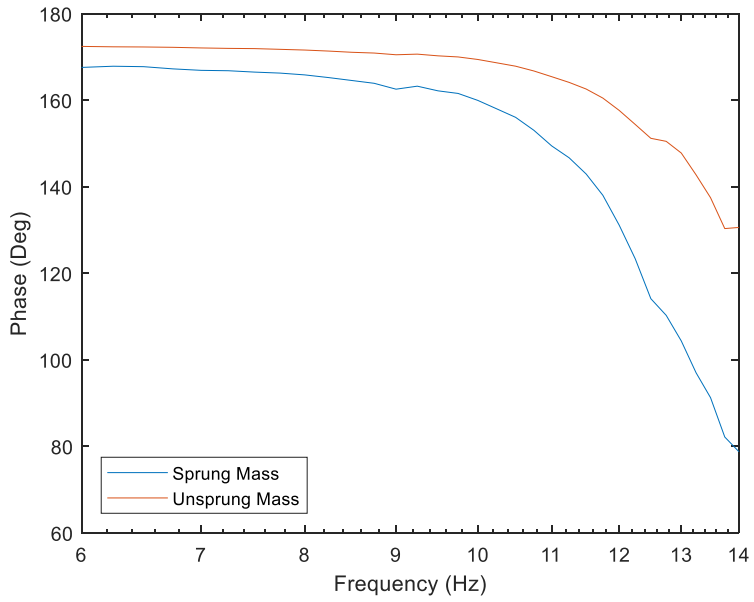

Figure 78: Phase diagram for Figure 77, showing a slight phase shift around 9 Hz

Figure 78 shows a slight shift in phase around 9 Hz. Though the shift is slight, the peak appears to be severely damped in Figure 77 so a more gradual shift is expected. Moreover, the relative prominence of the peaks between 10 and 20 Hz appear to be dominating the effects of the mode at 9 Hz. A close watch will be kept on this first peak during later tests, but regardless of the discrepancy with the model, as long as all tests for similar excitation produce the same results then the data accurately describes the system for the given loading condition, and should thus be accounted for during the decoupling.

The emergence of the peaks between 10 and 20 Hz was still cause for some initial concern due to the significant deviation from the models. However, the second vertical mode of the system was expected near 17 Hz so it is possible that some of these dynamics are due to that mode. Still, this

deviation from the analytical and simulated models suggests that there were significant dynamics in the test setup which were not included in the model. If these dynamics are due to the quarter car system itself, whether tire or suspension, the decoupling process will encompass these effects and still provide meaningful results. Even in the case of the dynamics being due to the test setup, as long as they are present in the respective subsystems, the decoupled FRFs will still prove accurate.

In either case, it is necessary to first determine the cause of the unexpected peaks in the 10-20 Hz range and to determine if one of these was due to the second (expected) vertical mode of the system. The first indication of the cause of the unexpected peaks came from visual observation during several test runs. During testing, it appeared that the tire was rotating slightly for frequencies around 14 Hz. In the interest of showing that this behavior is not due to the specific tire used in these tests, the system was augmented to attach a pressurized tire, 8 inches in diameter, shown in Figure 79.

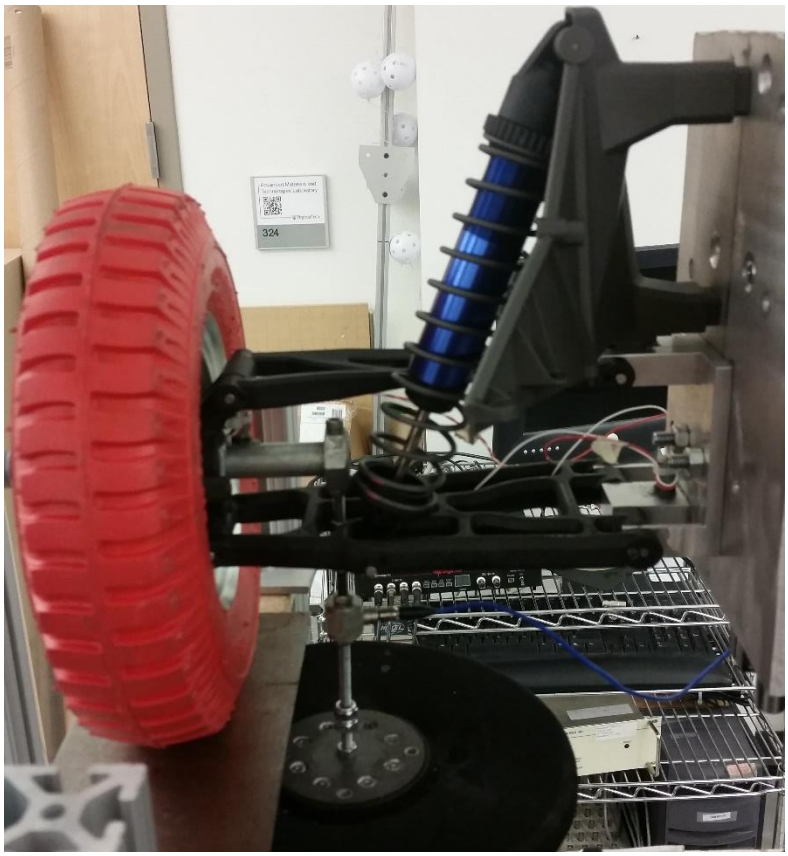

Figure 79: 8-inch pressurized tire mounted to small-scale suspension system

This tire is for a hand truck and, though pressurized, will still not display behavior similar to that of a passenger car tire. However, since the purpose of the tire at this stage of the testing was to investigate the unexpected peak in frequency response, the tire was deemed acceptable. From this point forward, the 8-inch tire of Figure 79 will simply be referred to as the "red tire" for simplicity. Results from the test on the red tire are shown in Figure 80.

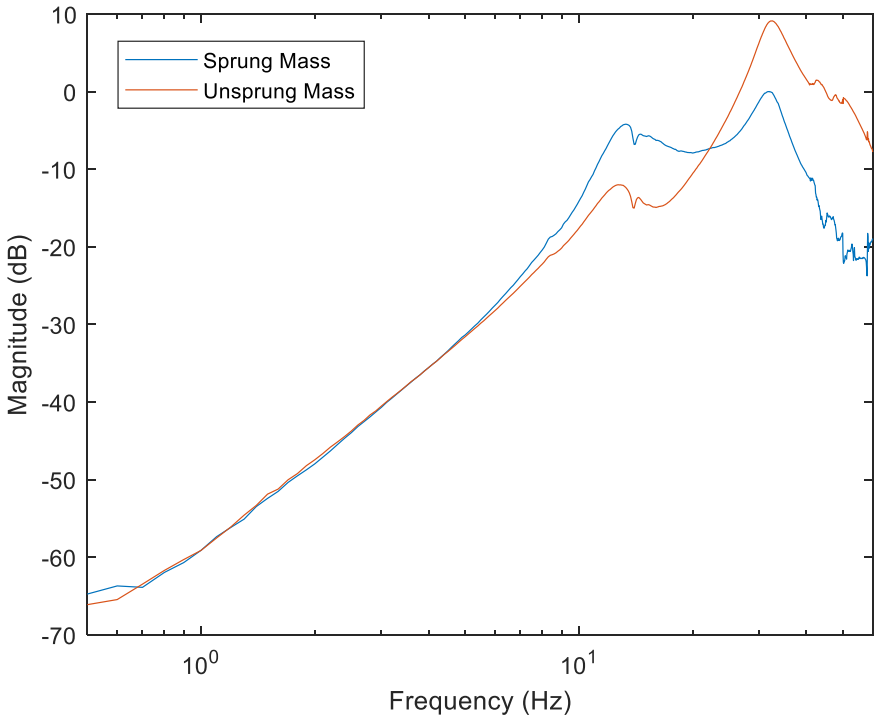

Figure 80: Accelerance FRF for the system with the red tire

Again, the first peak of the system is appearing right around 9 Hz while the second peak has decreased to 33 Hz. Considering that the only change to the system was the tire, this result supports the earlier assertion that the 9 Hz peak is the first vertical mode of the system. Additionally, some peaks are visible around 14 Hz, which implies that those modes are not specific to the original RC tire. Since the tire was not the source of the mode, the original system was restored in order to further investigate the system by methodically changing aspects of the test setup.

The first change was the replacement of the original, steel stinger. The reasoning behind the stinger replacement was to ensure that the unexpected dynamics were not, in fact, stinger dynamics. Thus, two new options were used in place of the original stinger. One of these new stingers was a shorter version of the original, while the other was of comparable length, but made from plastic. Figure 81 shows the FRFs which resulted from these new stingers alongside the original FRF.

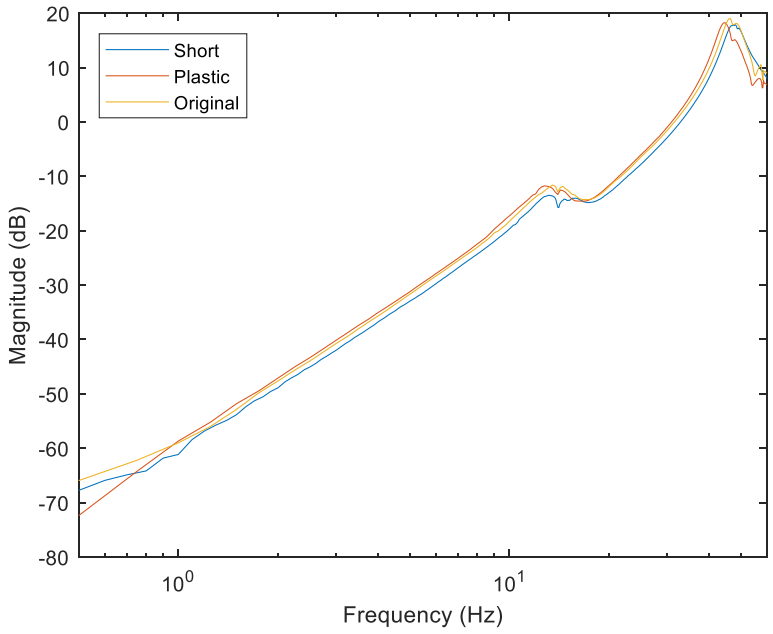

Figure 81: Unsprung mass FRFs resulting from shorter stinger and plastic stinger

FRFs for only the unsprung mass are shown in Figure 81 in the interest of clarity, but similar trends were seen for the sprung mass. There are some differences compared to the system with the original stinger, but the modes near 14 Hz appear relatively unchanged. These results show that the vibration near 14 Hz is not being caused by the stinger dynamics. A zoomed view of Figure 81 is shown below in Figure 82.

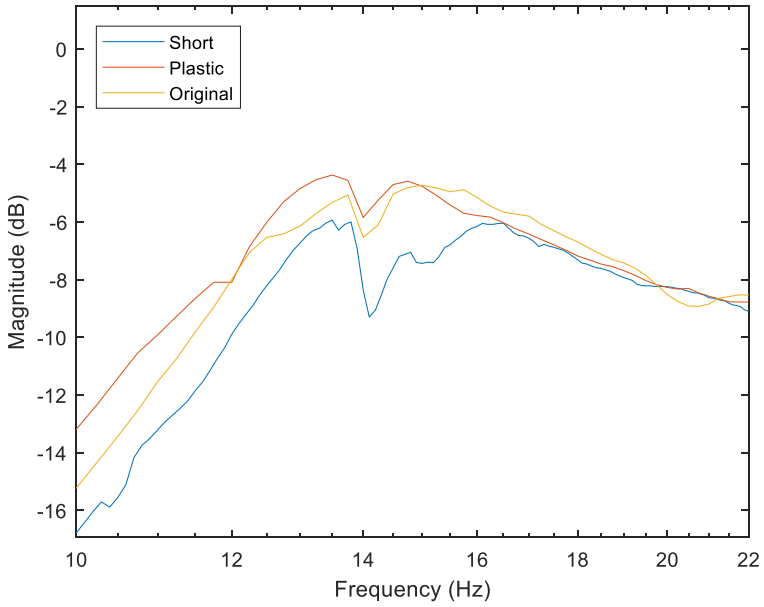

Figure 82: A zoomed view of Figure 81 between 10 and 22 Hz

This closer inspection reveals that there are actually three peaks between 10 and 20 Hz, though the third peak is barely visible for some tests. The test with the short stinger most clearly shows this peak around 16.5 Hz which could possibly be the second vertical mode of the system, but is being obscured by non-vertical dynamics. As analysis of the modes between 10-20 Hz continues, this possibility will be investigated further.

While variations were being made to the stinger, another configuration was tested in which the point of excitation was also altered. Instead of attaching the stinger to the unsprung mass at some point along the bolt outside of the tire, a steel wire was attached directly to the center of the wheel hub. Then, utilizing the through hole in the tire from the road input tests, the wire was taken down through a small hole in the support surface and attached to the load cell. This configuration is shown in Figure 83.

Figure 83: A steel wire is attached directly to the wheel hub and down to the load cell through a small hole in the tire and support surface.

The small hole in the support surface should have little-to-no impact on the force/deflection of the tire due to the location of the hole, between tread elements. The resulting FRF is shown in Figure 84.

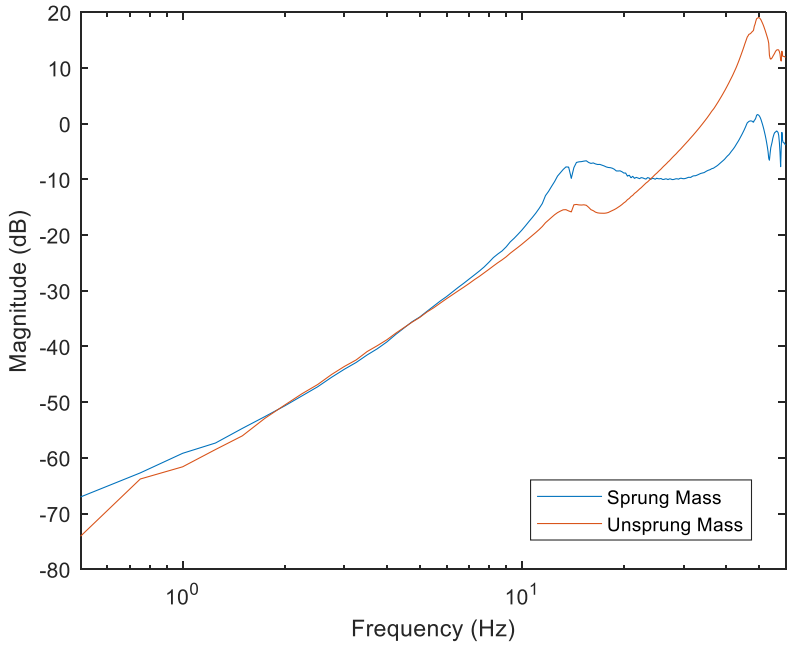

Figure 84: FRF for the wire attachment configuration of Figure 83 along with that of the original system

Again, there are some variations, but the modes near 14 Hz have not disappeared. Thus, it is concluded that the point of excitation was not causing the additional dynamics. One item of note in Figure 84 is that the second peak between 10 and 20 Hz appears to be spread across a wider frequency range. After repeated tests for the wire excitation, it was determined that this behavior was not a random occurrence. Close inspection of previous tests (most notably the test for the short stinger from Figure 82) revealed 3 separate peaks between 10 and 20 Hz: one near 13.5 Hz, a second around 14.7 Hz, and a third around 16.5 Hz. In Figure 84 it appears that the 16.5 Hz peak decreased slightly and is now overlapping somewhat with the 14.7 Hz peak, causing a single, broader peak in between.

Having found that the unexpected dynamics were not due to the stinger or excitation point, the original configuration of Figure 75 was restored, though some later tests will use the wire attachment yet again. It was thought that the system might have been able to rotate about the z-

axis (vertical) with the single bearing, so the second bearing was then added back to the system. A picture of this configuration is shown below in Figure 85.

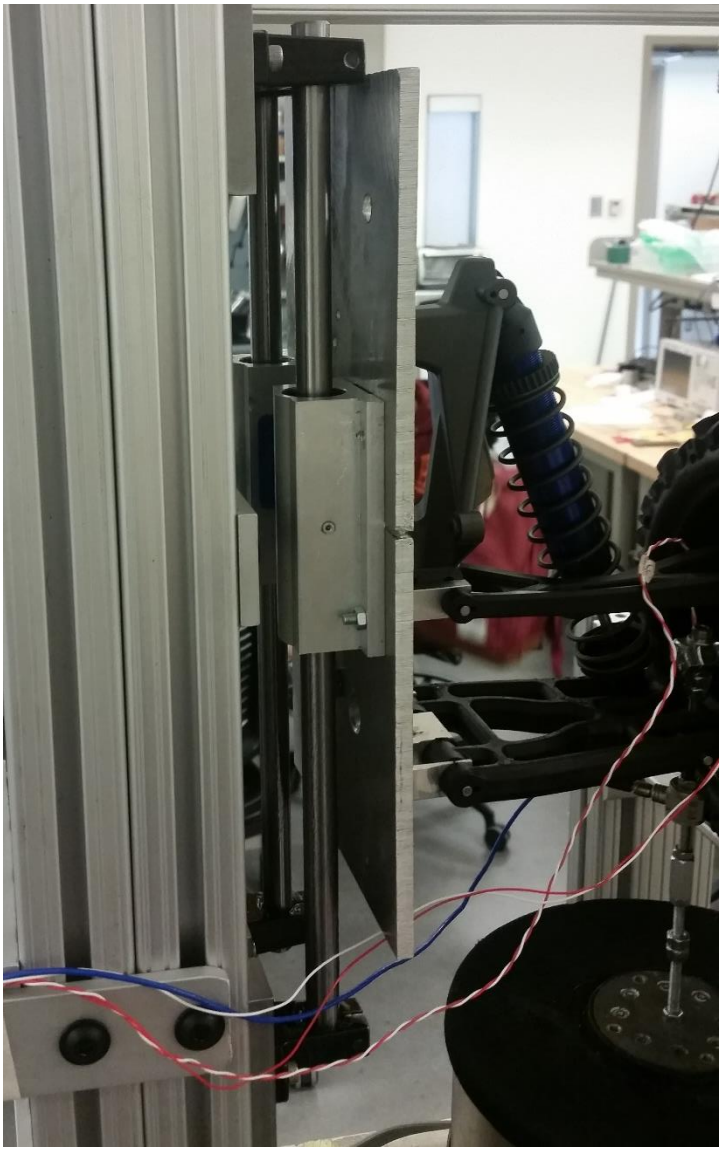

Figure 85: Test setup with second bearing reattached

The original test for excitation to the unsprung mass was then repeated for the setup with 2 bearings. Results from this test are shown in Figure 86.

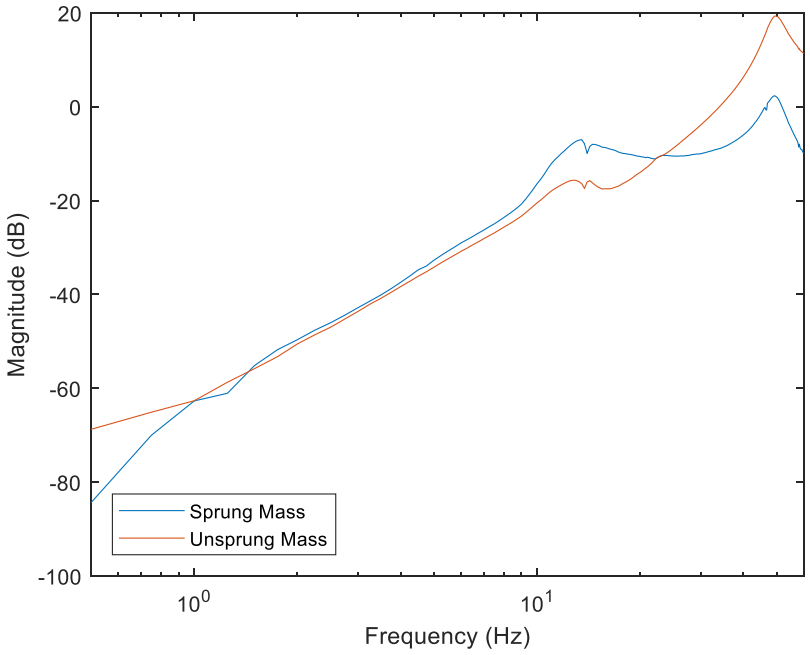

Figure 86: Accelerance FRF for test setup of Figure 85

Though the replacement of the second bearing did have some effect, the modes still appear around 14 Hz. This result suggests that the mode is not caused by rotation of the mounting plate around the vertical axis. Also, as a result of the increased damping, the first peak of the system that was seen around 9 Hz previously is no longer visible, which justifies the original switch to a 1-bearing system.

The guide rails and the (road surface) tire support platform are the only remaining components of the test setup which are not also a part of the quarter car system. Both of those components are very stiff and have a first natural frequency well over that of the measured data (270 Hz or greater as a conservative estimate from Euler Bernouli beam theory), which is supported by the results displayed earlier in Figure 74. Thus, the vibration must be due to some un-modeled dynamics of the quarter car system.

Given that the system was only modeled in the vertical direction, the primary suspect for the vibration around 14 Hz is the control arm assembly. As mentioned earlier, since this vibration is due to some component of the quarter car system, the FRF obtained for the original system with one bearing (Figure 75) does indeed describe the dynamics for this quarter car system. However, before returning to the original system with a single bearing, further tests were conducted on the two-bearing system in order to better understand the dynamics which are causing these extra modes.

The following analysis focuses primarily on motion of the control arms of the suspension in an effort to verify that the mode in question originates there. The first such test was for both accelerometers on the sprung mass side of the lower control arm. Accelerometers were oriented to collect data in the z-direction (vertical) from the left and right sides of the control arm mount. This accelerometer placement is shown in Figure 87.

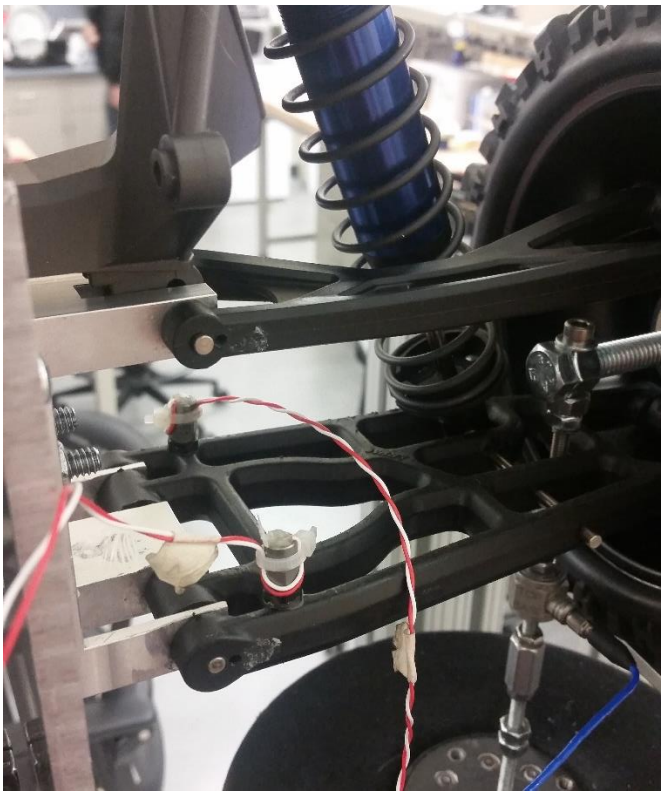

Figure 87: Accelerometer placement on the lower control arm in the vertical direction

The motivation behind the accelerometer placement in Figure 87 is to determine whether there is any sort of flexing or rotation of the control arms near 14 Hz. If there is flexing or rotation about the y-axis (lateral), then the accelerometers in the above orientation should have some significant deviation in phase. This plot is shown in Figure 88.

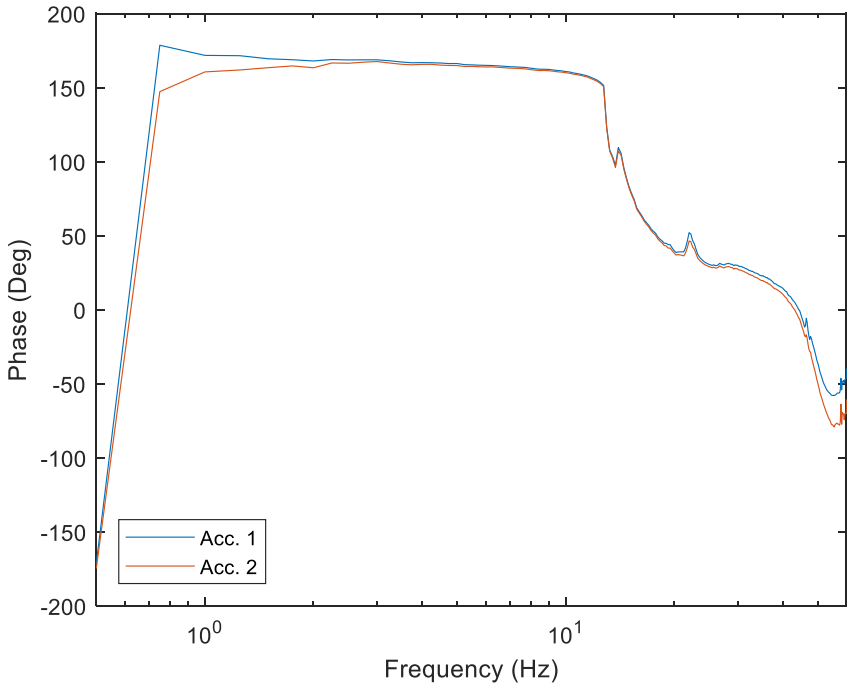

Figure 88: Phase plot for accelerometers in Figure 87

Both accelerometers, and thus both sides of the lower control arm near the suspension are in phase with each other for almost the entire frequency range. Similar behavior was demonstrated for the upper control arm and, furthermore, the phases for the upper control match as well with those of the lower. Therefore, it can be assumed that there is no rotation or flexing of the control arms about the y-axis, near the sprung mass, around 14 Hz. The test in the z-direction was repeated for each control arm, except with accelerometers near to the wheel hub. The phase of the accelerometers on the lower control arm is shown in Figure 89.

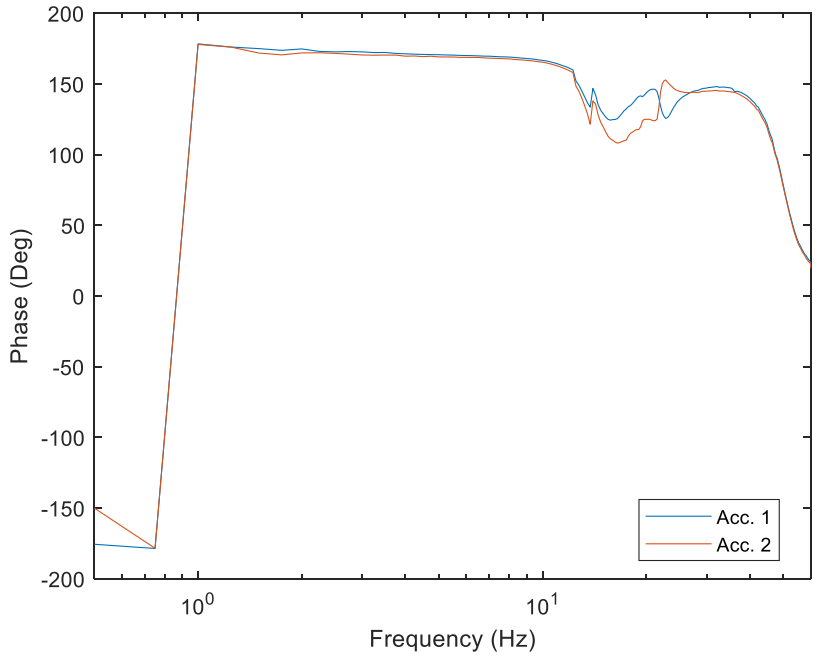

Figure 89: Phase plot for accelerometers on lower control arm, located near the wheel, and oriented in the z-direction

Again, the two sides of the control arm are in phase for most of the frequency range and the same behavior is seen for the upper control arm. After 14 Hz, there is some slight deviation in phase, which could indicate some flexing of the control arms or wheel hub assembly between 10 and 20 Hz. This separation, though slight, partially explains the behavior of the system. Since the suspension cannot translate longitudinally (along the x-direction), if the tire rolls at all, there will be some slight rotation of the wheel hub and an accompanying flexing of the control arms.

Furthermore, this behavior could be caused by the construction of the lower control arm. As can be seen in a number of the images included of the test setup, the shock assembly connects to the lower control arm at an off-center point. Thus, as the system vibrates there is off-center loading by the suspension which, in turn, could be causing the rotational behavior between 10 and 20 Hz. Another point of Figure 88 and Figure 89 which could be caused by this off-center connection is the behavior near 45 Hz. For locations close to the sprung mass, there is some phase deviation

between the two sides of the control arm. In contrast, for locations near the wheel hub, the two sides are perfectly in phase. This discrepancy indicates that there is some flexing occurring in the control arms near 45 Hz, which will be investigated later in the present section.

The next setup consisted of one accelerometer on the lower control arm and one on the upper, both oriented in the x-direction. Figure 90 shows this configuration.

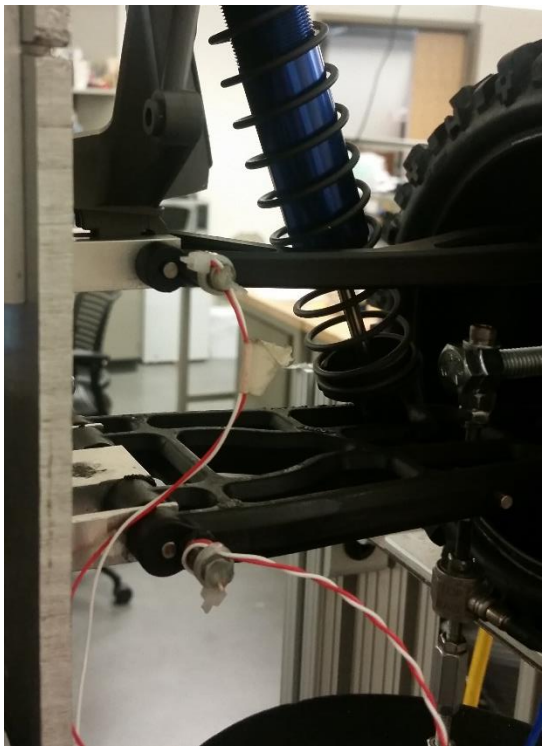

Figure 90: Testing configuration for one accelerometer on each control arm in the x-direction

Tests for the configuration of Figure 90 will show if the system is rotating about the y-axis, or if the control arms are flexing in the x-direction at points near the sprung mass. The phase plot for Figure 90 is shown in Figure 91.

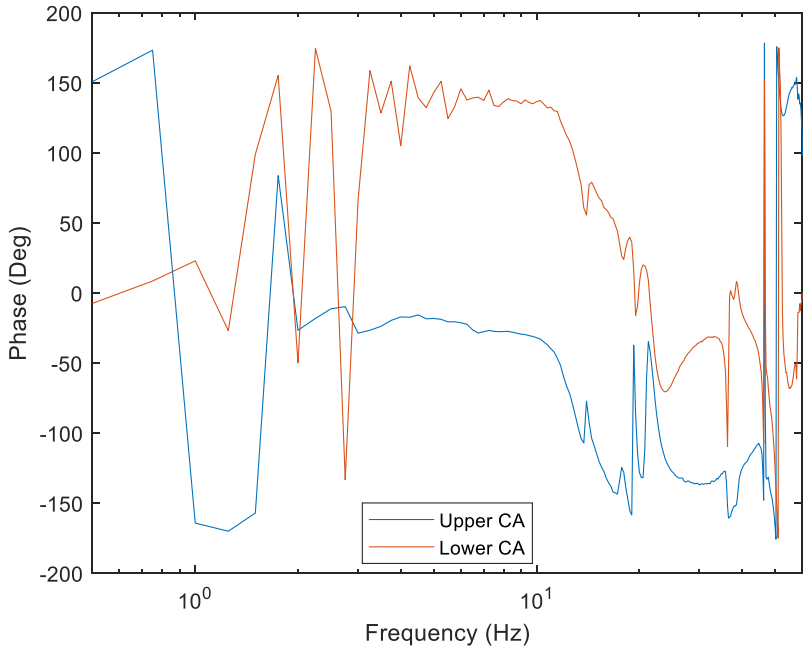

Figure 91:Phase plot for the accelerometer placement of Figure 90

Due to the messy nature of Figure 91, repeated tests were conducted to ensure that the results were not due to random error. The plot shows that the control arms are moving out of phase with each other in the x-direction over most of the frequency range of interest. Accelerometers were kept in the same configuration, but moved to location directly beside the wheel hub. Figure 92 shows the corresponding phase plot.

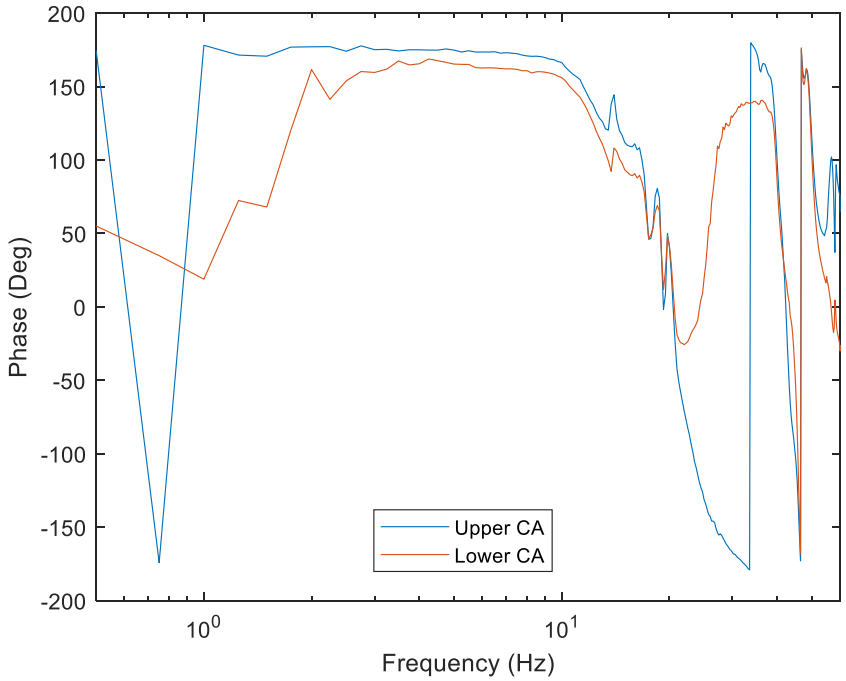

Figure 92: Phase plot for one accelerometer on each control arm, near the wheel hub, in the x-direction

In contrast to Figure 91, the upper and lower control arms are in phase with each other over most of the range of Figure 92, with the exception of 20-30 Hz. Again, this discrepancy between locations near the sprung mass and locations near the wheel hub suggests that there is some flexing of the control arms occurring.

Together, Figure 88 through Figure 92 give a good indication of the overall behavior of the system, particularly in the neighborhood of 14 Hz. Through the preceding analysis, it is concluded that the dynamics which cause the peaks around 14 Hz arise from the properties of the control arms. Future work may include design and fabrication of new, metal control arms which are less flexible. For the present work, since the dynamics arise from the quarter car system, the FRFs presented thus far should accurately represent the experimental setup and will be present in the suspension subsystem. Therefore, whether the suspension subsystem is tested experimentally, or FRFs are

obtained for it through decoupling, it is expected that these dynamics between 10 and 20 Hz will be present.

The final aspect of the test system which must be investigated before discussion turns to decoupling, is the peak around 45 Hz. As mentioned previously, this peak is assumed to be the second (expected) vertical mode of the system, the one caused by the stiffness of the tire. However, 45 Hz is considerably higher than predicted by the model based on the static stiffness of the tire. Moreover, Figure 81 and Figure 84 suggest that there may be more than one mode present in the system around 45 Hz.

As mentioned previously, the first vertical mode was also observed to be higher than expected, which raised the possibility that the full sprung mass is not being supported on the system. In turn, the tire would also be less loaded than expected, but this change in loading would not cause the frequency to shift so dramatically (from 17 Hz to 45 Hz). Instead, it appears that the 17 Hz frequency is either being damped out completely or dominated by the other modes around 14 Hz, while the 45 Hz frequency is arising from a different stiffness element in the tire, namely the plastic rim. An attempt to validate this assumption could be made by deconstructing a tire and testing the stiffness of the rim, which may be done as a part of future work. However, for the present work, a test will be performed on the tire alone to confirm that the dynamics are not arising from some other behavior of the suspension control arms.

Recall from the section about the full scale simulations earlier in the current chapter, that the decision to treat the suspension as the known subsystem was based on the nonlinearity in the tire. On the other hand, the nonlinearity in the small-scale tire is much less severe. Thus, testing the small-scale tire by itself should still yield meaningful results, the significance of which will

become more apparent during the following section on decoupling of experimental data. For the present discussion, the testing of the tire by itself should confirm the expected behavior around 45-50 Hz.

In order to test the tire by itself, the wire excitation shown earlier in Figure 83 was utilized again. Figure 93 shows the setup for testing the tire by itself with the wire attachment.

Figure 93: Tire subsystem being excited using the wire setup

As with the previous tests using the wire setup, the wire was connected from the load cell to the axle bolt by passing through the hole in the support surface and the hole between tread elements of the tire. After connecting the wire to the bolt, the support surface was raised until there was tension in the wire. The resulting FRF is shown in Figure 94.

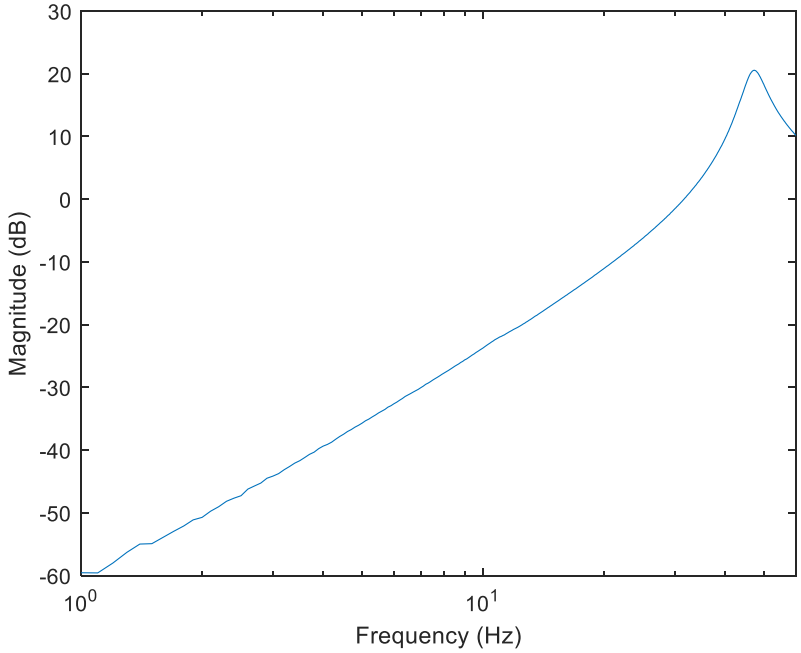

Figure 94: FRF resulting from the test on the setup of Figure 93

Figure 94 clearly shows the peak for the tire at 47.3 Hz which confirms the assertion that at least some of the dynamics around 45 Hz for the assembled system are being caused by the tire. Another important aspect of Figure 94 is the complete absence of any peak around 17 Hz. The tire is effectively functioning as a single DOF, spring-mass-damper system as expected, with the exception that the effective stiffness during vibration is considerably higher than that predicted by the static tests described in **Chapter 4 – Experimental Design and Setup**.

In an effort to more fully describe the behavior of the assembled quarter car system around 45 Hz, the tire was removed and the suspension was tested by itself. A picture of this setup is shown in Figure 95.

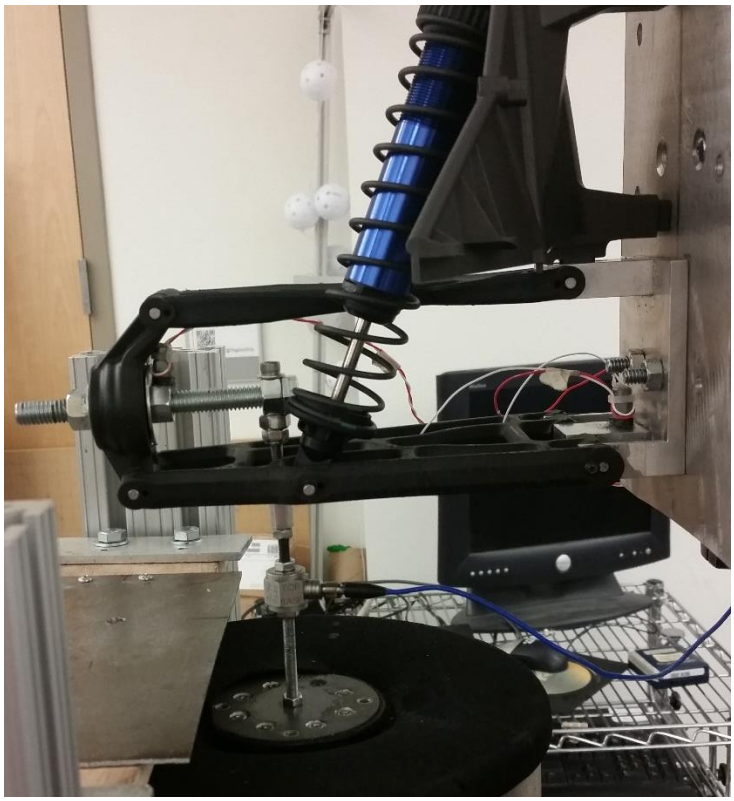

Figure 95: Test configuration for the suspension subsystem by itself

As shown in Figure 95, the actuation point and excitement method were kept the same. The resulting FRFs are shown in Figure 96.

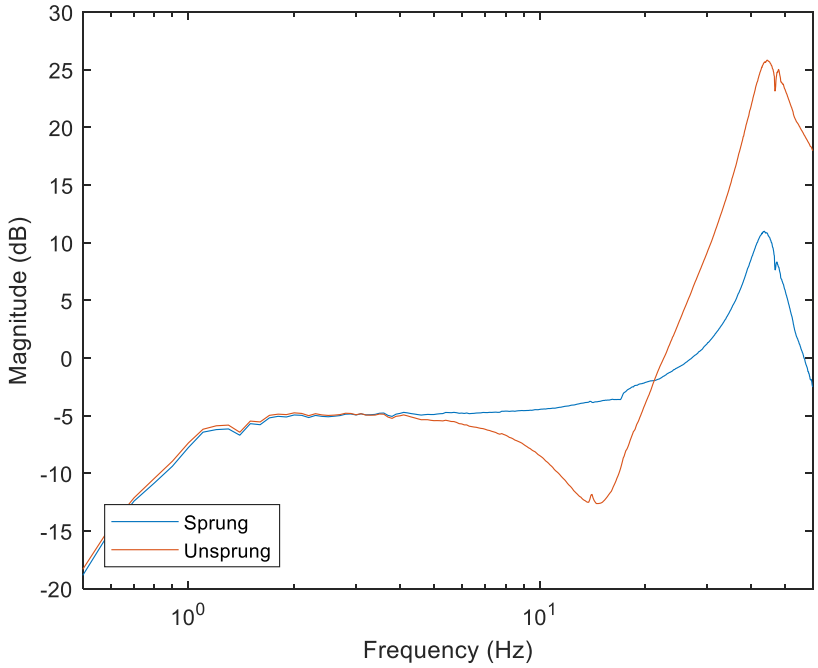

Figure 96: FRFs for the sprung and unsprung masses of Figure 95

As anticipated, there are some dynamics of the system still causing peaks right around 45 Hz. Based upon physical observation during testing of the setup of Figure 95, it appeared that the vibration around 45 Hz was caused by flexing of the lower control arm about the point at which the shock assembly connects. Since this behavior could not be captured on camera, a diagram of the observed behavior is shown in Figure 97.

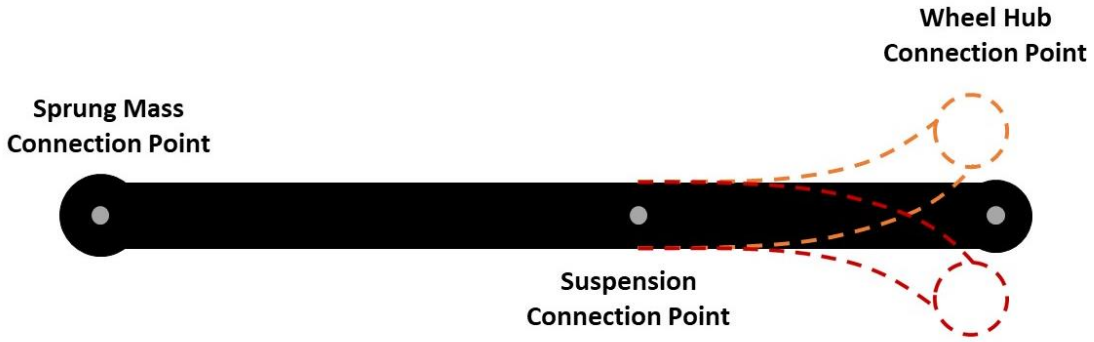

Figure 97: Diagram of observed behavior during the test for the setup of Figure 95

In an effort to validate the behavior seen in Figure 97, a test of the configuration of Figure 95 was repeated with accelerometers placed at the suspension connection point and the wheel hub connection point, oriented in the z-direction. As the range of interest was around 45 Hz, the test was only conducted from 20-60 Hz instead of the full 0.5-60 Hz range of previous tests. The resulting FRFs are shown in Figure 98.

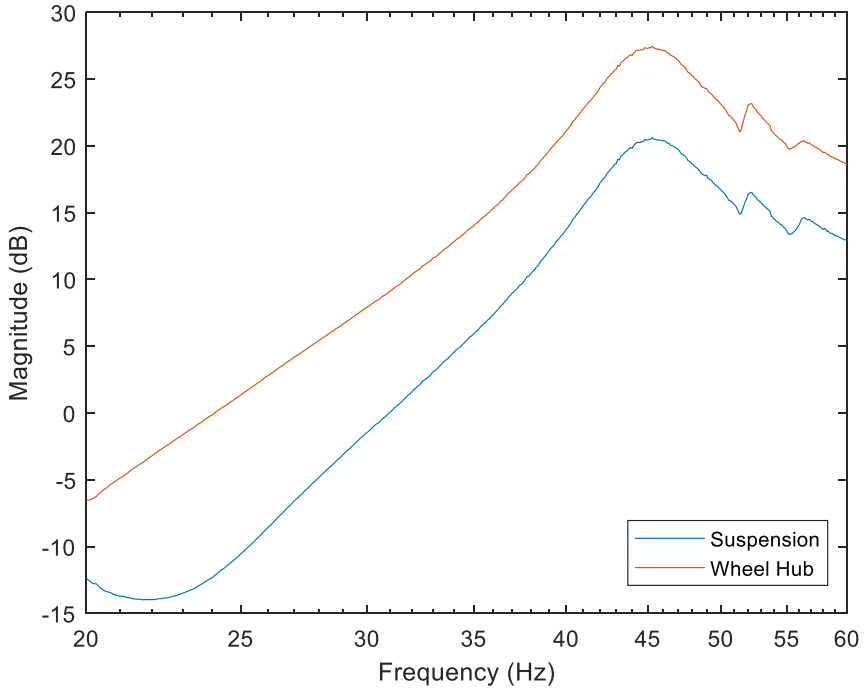

Figure 98: FRFs for the suspension connection point and wheel hub connection point of Figure 97

Based on the observed behavior demonstrated in Figure 97, it is expected that the two points should have very similar FRFs with the wheel hub connection point demonstrating a higher magnitude. Figure 98 confirms the expected behavior and also clearly shows other peaks at 52 Hz and 57 Hz. Together, Figure 94 and Figure 98 show that the behavior of the assembled quarter car system around 45 Hz is due to a combination of tire and control arm dynamics.

5.3.1.1 Summary of Preliminary Tests

All tests in the preceding section were conducted in order to describe and validate the behavior of the small-scale quarter car rig. First, the mounting plate of the test rig was excited directly, without the control arms or tire attached. The results of this first test (Figure 74) show a relatively flat response of the system, which indicates that natural frequencies of the test rig itself will not interfere with the data collected during other tests.

When the results of initial tests (Figure 76) showed significantly different FRFs than expected for the small-scale system, further tests were conducted to investigate and describe these unexpected dynamics. Through a series of tests, it was found that the unexpected vibration between 10 and 20 Hz was not caused by the specific tire (Figure 80), by the stinger (Figure 81), or by the location of the point of excitation (Figure 84). Furthermore, the dynamics between 10 and 20 Hz were still present when a second bearing was added back to the system (Figure 86), which shows that the behavior was not caused by rotation about the guide rail of the single-bearing system. More exhaustive tests on the system, Figure 87 through Figure 92, showed that this unexpected behavior was due to flexing and rotating of the control arms.

The initial tests of Figure 76 also showed a significantly higher frequency than expected for the second vertical mode of the system. A test of the tire by itself (Figure 94) confirmed that at least part of behavior around 45 Hz was due to the tire stiffness, which implies a significantly higher stiffness for the tire than was predicted by the static tests in **Chapter 4**. In contrast to the behavior during static tests, the primary stiffness of the element of the tire during vibrational testing is the plastic rim, thus yielding higher than expected natural frequencies. Independent testing of the suspension subsystem showed that some of the dynamics around 45 Hz were also due to flexing of the control arms (Figure 95 – Figure 98).

Though there are dynamics present in the test rig which were not modeled, the decoupling procedure will still work and will, in fact, encompass this unexpected behavior. The preceding discussion has been focused on describing or confirming the observed behavior of the quarter car system. Now that the behavior has been fully investigated, the focus will be shifted to application of coupling/decoupling techniques to the experimental data.

5.3.2 Experimental Application of Decoupling

With the behavior of the small-scale quarter car system having been fully investigated in the preceding section, decoupling techniques can now be applied to the acquired data. Results from simulations showed that, for a full-scale system at least, it would be better to treat the suspension as the known subsystem due to testing limitations and significant nonlinearity in the tire. However, it was found that the small-scale tire did not exhibit the same degree of nonlinearity and, in fact, was just as easy to measure independently as the suspension. Given these discoveries, the coupling/decoupling in this section will be applied two distinct scenarios: 1) decoupling the suspension subsystem from the assembled system, and 2) decoupling the tire subsystem from the assembled system.

By applying the technique from both directions, a comparison can be made to determine if the results match with each other and which, if either, was a more effective choice.

5.3.2.1 Suspension as Known Subsystem

Since the original plan, based off of simulation results, was to treat the suspension as the known subsystem, those results will be discussed first. The test setup of Figure 75 was restored, where the system was mounted to one bearing and the stinger was connected directly to the axle bolt. The "shorter" steel stinger discussed in the previous section was used in place of the original and the suspension stiffness was kept at the stock value of 1199 N/m. Additionally, these tests were run with a step sine input from 0.5-60 Hz with a 0.1 Hz step. Resulting FRFs are shown in Figure 99.

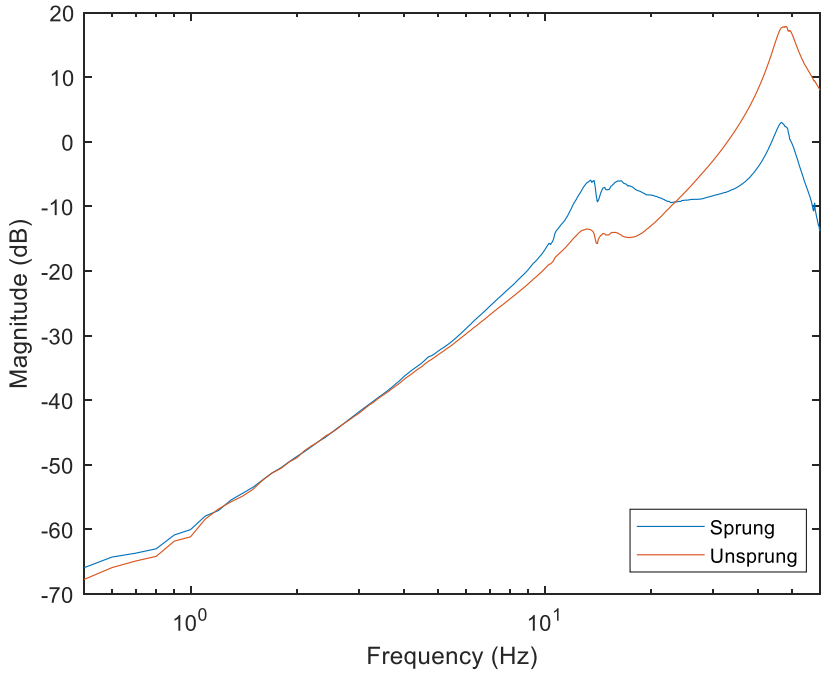

Figure 99: FRFs for small-scale quarter car system with stock spring

FRFs in Figure 99 appear as typical for the system based upon the results of the previous section. Maintaining everything else in the test setup, the suspension spring was replaced with one of higher stiffness, 1538 N/m. Tests were repeated and resulting FRFs are shown in Figure 100.

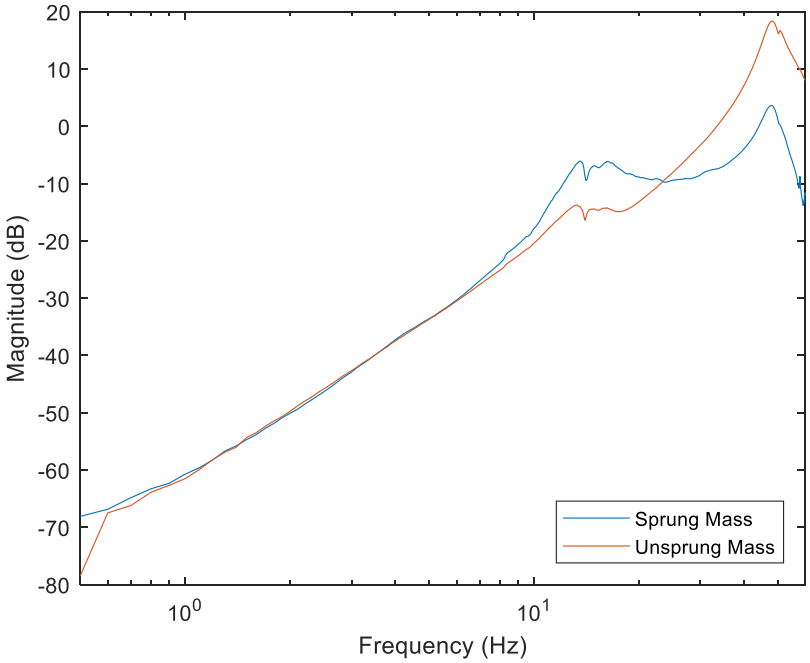

Figure 100: FRFs for small-scale quarter car system with suspension stiffness increased

In both Figure 99 and Figure 100, the first vertical peak is not very visible so a direct comparison of the unsprung mass of each system is shown in Figure 101 to highlight the differences.

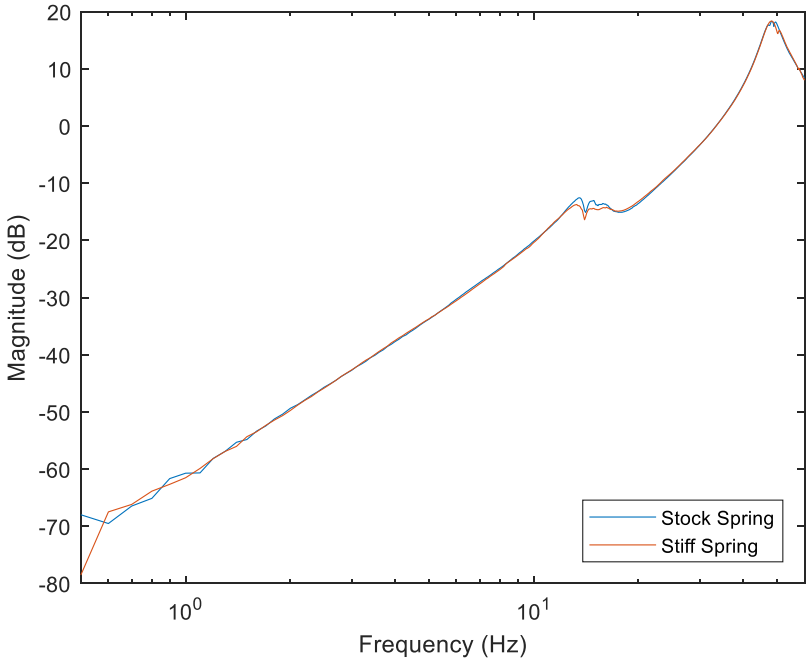

Figure 101: Comparison of unsprung masses for suspension with stock spring and with a stiffer spring

Over most of the range of Figure 101, the two systems match very closely, with the exception of the 10-20 Hz range. A closer view of this range is shown in Figure 102.

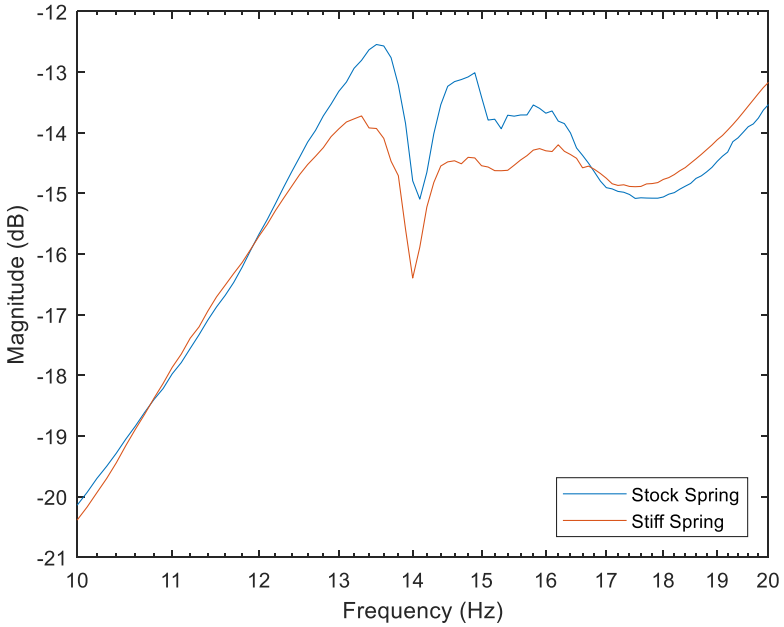

Figure 102: Zoomed view of Figure 101 in the neighborhood of 10-20 Hz

Since it was determined in the previous section that the peaks between 10 and 20 Hz were due to interaction between the suspension and control arms, the change in this range was expected. However, Figure 101 and Figure 102 offer some initial motivation for treating the tire as the known subsystem and testing with two different tires. Though the FRFs for the two systems do differ between 10 and 20 Hz, the change in frequency of the peaks is not as significant as could be desired for demonstrating change within the systems. This subject will be addressed later in the present section when the suspension FRFs are being decoupled from the assembled system FRFs of Figure 101.

Next, the tire was removed and the suspension was tested by itself. This setup was already used in the previous section to demonstrate the flexing of the control arms around 45 Hz. The configuration from this stage of testing was identical to that used previously and is thus still described by Figure 95. For decoupling, the datasets for the assembled system and the suspension subsystem must be

the same size. In that interest the same test parameters were used: step sine, 0.5-60 Hz range, 0.1 Hz step size. The resulting FRFs for the suspension subsystem are shown in Figure 103.

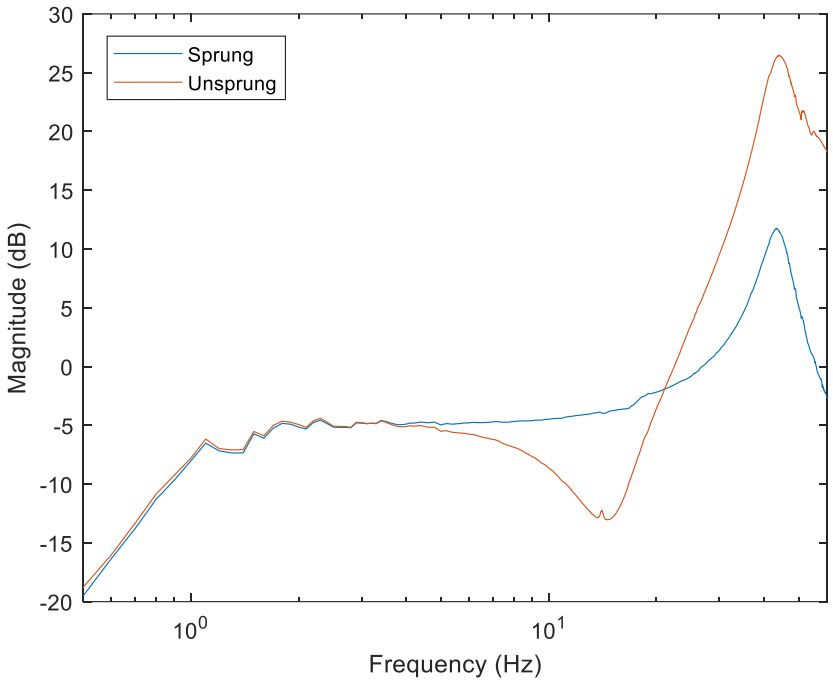

Figure 103: Sprung and unsprung mass responses for the suspension subsystem

As seen in the previous section, the peak caused by the flexing of the lower control arm is again present in Figure 103. One important aspect of the FRF for the unsprung mass is the response between 10 and 20 Hz. There appears to be a section of anti-resonances in the suspension subsystem, corresponding with the peaks in the assembled system. Though the data for the simulated systems appeared very different than what is shown in Figure 103, a similar trend between the assembled system and suspension subsystem was observed. If these dynamics have been fully captured, then the peaks between 10 and 20 Hz should be completely removed from the assembled system during decoupling, leaving only the single, higher peak we expect for the tire.

Following the same procedure as for the simulated data, the FRF for the unsprung mass of the suspension subsystem (Figure 103) was decoupled from that of the assembled system (Figure 99). The process was first performed for the suspension system with the stock spring and the resulting tire FRF is shown in Figure 104.

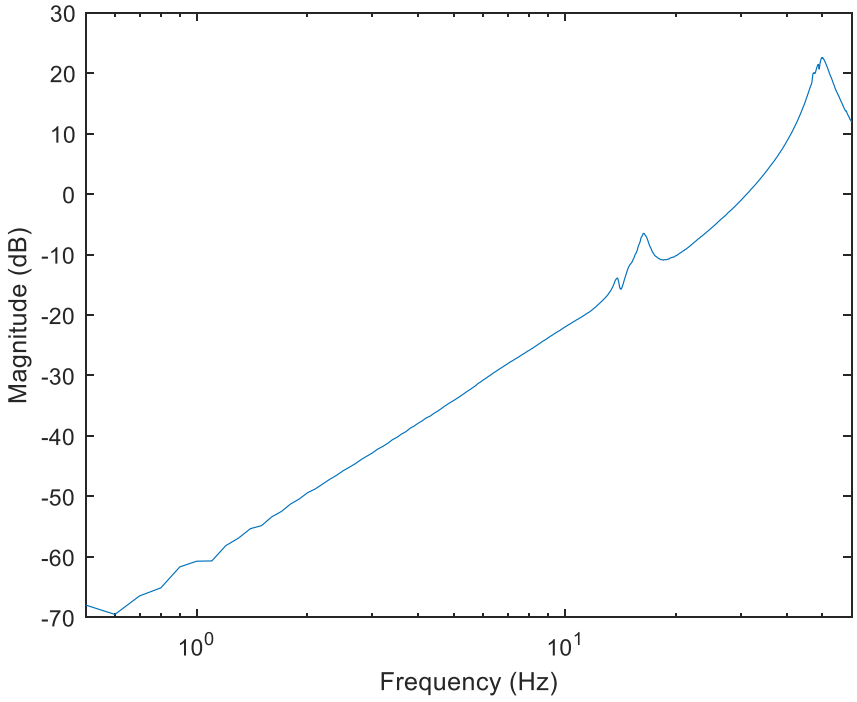

Figure 104: Tire FRF obtained through decoupling

Two aspects of Figure 104 stand out: 1) there are still peaks present between 10 and 20 Hz when they were not expected, and 2) the expected peak for the tire is present near 50 Hz. Before discussing these two points, the decoupling process will be repeated for the suspension with the stiffer spring. The results of that decoupling are shown in Figure 105, along with the FRF of Figure 104 and the FRF for the tire when it was tested by itself (Figure 94)

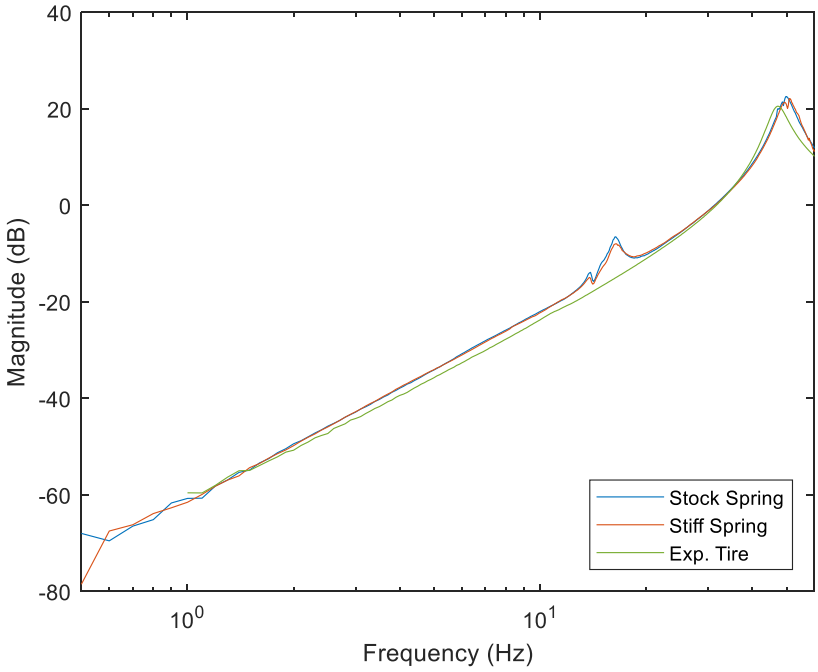

Figure 105: "Stock Spring" and "Stiff Spring" refer to the suspension system which was used to obtain the tire FRF through decoupling. "Exp. Tire" refers to FRF which was obtained for the tire directly through testing

The tire subsystem FRFs obtained through decoupling with the stock suspension and the stiff suspension match well across the entire range of Figure 105. Furthermore, these decoupled FRFs predict the frequency of the tire to within 4.1% of the experimentally obtained tire FRF (49.3 Hz compared to 47.3 Hz respectively. Nonetheless, both decoupled FRFs still contain peaks between 10 and 20 Hz.

As discussed in the previous sections, these peaks between 10 and 20 Hz are cause by the dynamics of the suspension control arms. Conceptually, these should have been decoupled completely from the FRF for the assembled line and the two decoupled FRFs should have a constant slope for that frequency range, similar to that of the experimental tire. The fact that these dynamics are still present in the decoupled FRF for the tire subsystem indicates that the suspension subsystem dynamics were not perfectly captured during testing.

The primary cause for the discrepancy between the expected suspension behavior and the observed behavior during experimentation lies in how the system was supported. As part of the assembled system, the entire weight of the suspension was supported by the tire, while the stinger was connected in such a way as to not bear any weight of the system (see previous sections for more complete details). In contrast, when the suspension subsystem was tested by itself, as seen in Figure 95, the entire weight of the suspension system was supported on the stinger. In turn, it appears that the stinger introduced some additional stiffness into the system and reduced some of the rotating or flexing behavior which was seen for the assembled system.

Since the additional stiffness of the stinger prevented some amount of the rotation and flexing, these dynamics were not completely removed when the suspension was decoupled from the assembled system. Thus, both decoupled FRFs for the tire in Figure 105 still contain some effects of the suspension dynamics. An ideal solution to this testing difficulty would be to fix the shaker overtop of the test system and have a wire connection come down from the shaker to the mounting point on the suspension subsystem. With the wire connection, the additional stiffness against rotation or flexing would be minimized and the suspension subsystem would be allowed to more truly act as the completely independent subsystem should. Unfortunately, the capabilities of the current test setup do not allow for such a configuration, though, this option will be considered for future work.

In the meantime, it is possible to approximate this free behavior of the suspension through other means. One such configuration is to support the weight of the sprung mass on a compression spring and excite the system with the wire. The motivation behind said configuration is to allow the system more freedom to flex and rotate, while simultaneously keeping the addition to system

relatively simple. If the compression spring does not add too significant out-of-plane dynamics, modelling of the addition to the system is straightforward.

The spring does, in fact, introduce significant out of plane dynamics which render the simple model useless, as the following analysis will demonstrate. A setup was constructed as described in the preceding paragraph and the results for the unsprung mass are shown in Figure 106.

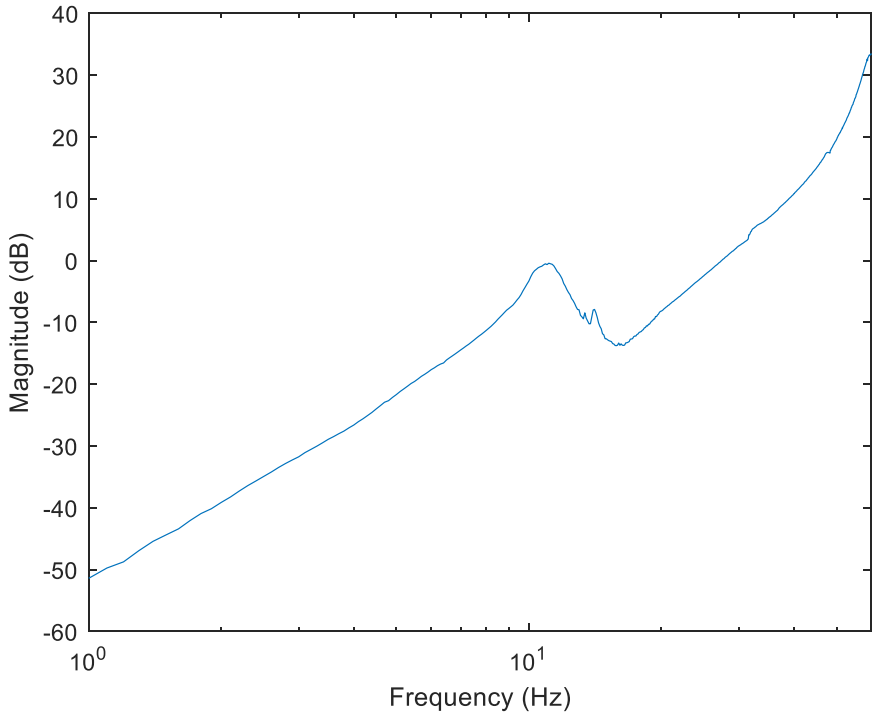

Figure 106: FRF for unsprung mass of suspension subsystem excited by wire attachment and supported by a single compression spring

Compared to Figure 103, the FRF of Figure 106 has at least two new peaks around 10 Hz in addition to the 45 Hz peak being pushed outside the range of the test (greater than 60 Hz). The next step in the current process is to decouple an analytical model for the compression spring from the FRF of Figure 106. If the spring were to only significantly affect the system in the vertical direction, as assumed previously, then the analytical model for the compression spring is simply a

spring-mass model. In the interest of brevity, the FRF for the spring-mass model will not be shown here.

Temporarily continuing with the assumption that the spring-mass model for vibration in the vertical direction is correct, the FRF for the model was decoupled from the experimental data of Figure 106. The resulting FRF for the suspension subsystem is shown in Figure 107.

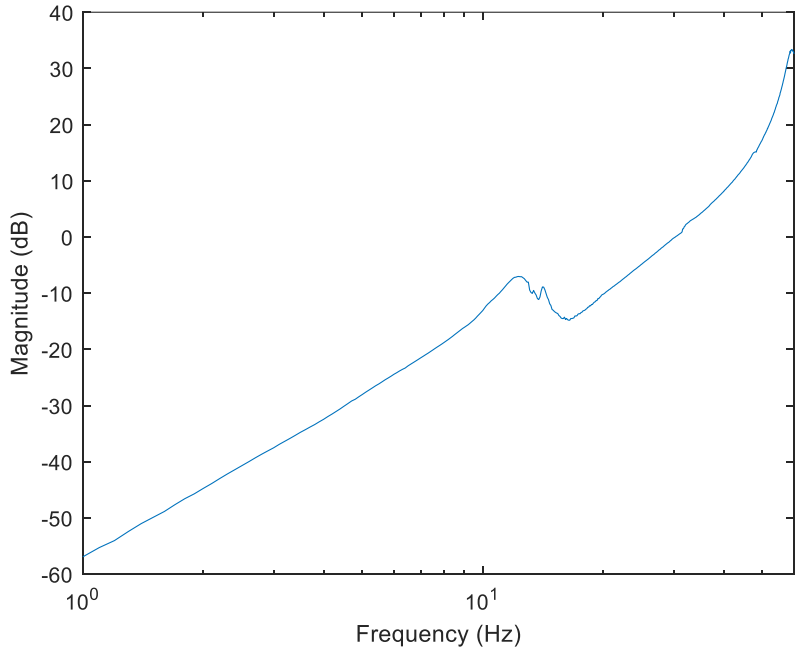

Figure 107: FRF for suspension subsystem after decoupling spring-mass model for compression spring. Further results will show that this FRF does not accurately describe the suspension subsystem.

Though the prominence of the first peak is reduced, the FRF for the suspension subsystem still does not appear as expected. However, the true test will be in the form of the tire FRF once that of Figure 107 is decoupled from that of the assembled system. This tire subsystem FRF is shown in Figure 108 in comparison with the decoupled FRF from Figure 104 and the one obtained through testing of the tire alone.

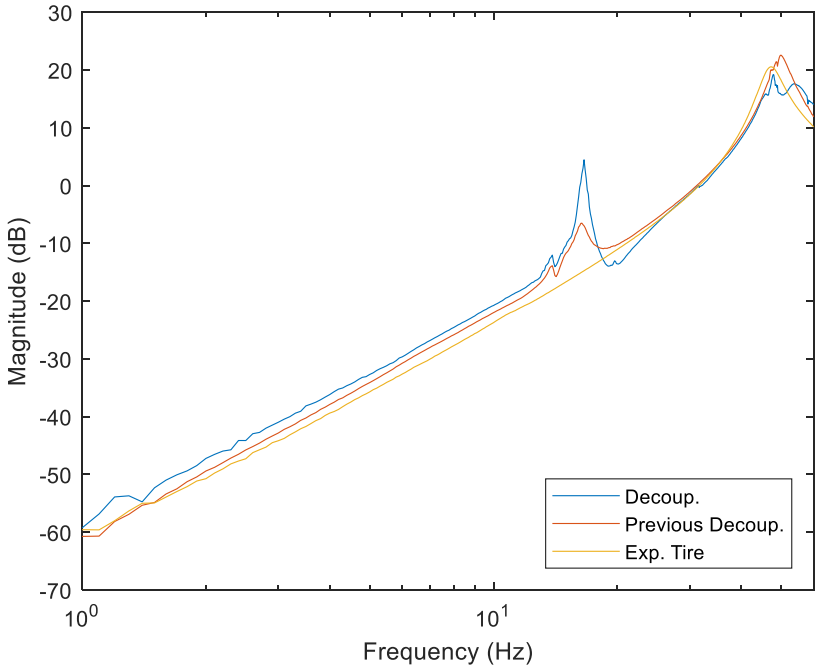

Figure 108: Result of decoupling Figure 107 from the assembled system, compared to results from Figure 104 and for the tire by itself (Figure 95)

A comparison of the various results in Figure 108 shows that the decoupling with the FRF of Figure 107 provides even worse results than when the suspension was supported directly on the stinger. Thus, it is concluded that the compression spring does induce significant non-vertical dynamics into the system when it is used to support the suspension system. In turn, these dynamics would need to be modeled analytically or obtained experimentally in order to fully decouple from test data.

The preceding discussion highlights the difficulty of using the suspension as the known subsystem for the current small-scale quarter car rig. Due to the dynamics introduced into the system through the rotating/flexing of the control arms, great care would need to be taken in the design of the support structure for the suspension subsystem. The support structure must be such that it either: A) does not interfere significantly with the suspension dynamics over the range of interest, or B)

can be modelled well enough to fully decouple the dynamics of the support structure from those of the suspension.

For the small-scale system, it has already been shown that the tire subsystem can be tested by itself. Furthermore, testing the tire subsystem alone does not require any additional support elements to be added to the system. Thus, the following section will repeat the decoupling process in a similar manner to the present section, with the exception of the tire being treated as the known subsystem.

5.3.2.2 Tire as Known Subsystem

As mentioned previously, for this small-scale quarter car system, testing the tire by itself does not require the use of any additional support elements. The preceding section showed the difficulties which quickly arise when support elements must be accounted for, either analytically or experimentally, in the decoupling process. By choosing the small-scale tire as the known subsystem, any added dynamics caused by support elements are avoided and, as a result, an additional level of uncertainty is removed from the process.

In order to remove any discrepancies that could be caused by the choice of stinger, the configuration of Figure 83 was restored, wherein the steel wire which was used to excite the tire subsystem was again used to excite the entire quarter car system. Instead of testing the small-scale system with the same tire and varying suspension stiffness, the stock suspension was maintained and a second, softer tire was tested. Results for the unsprung mass of each system are shown in Figure 109.

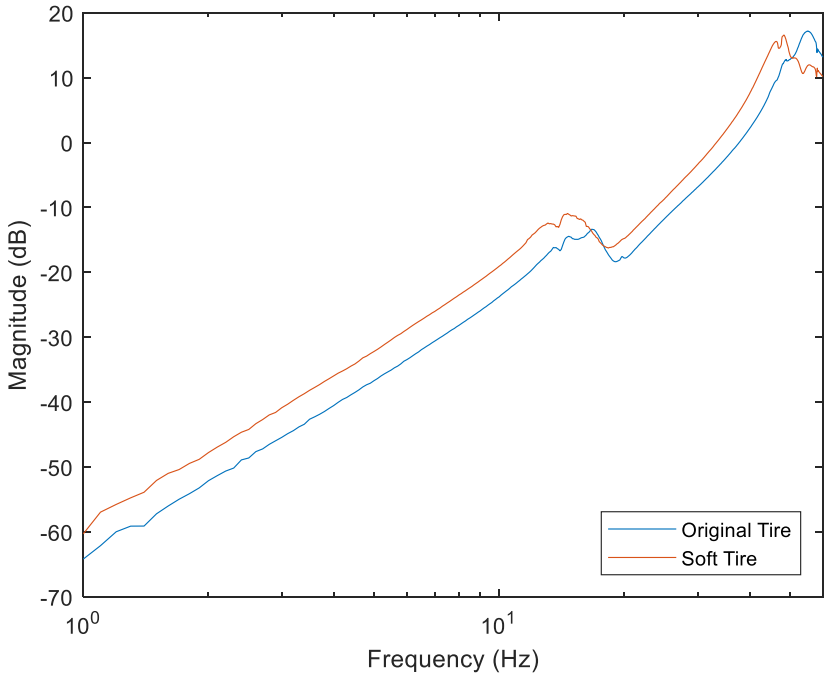

Figure 109: Comparison of unsprung mass response for quarter car system with original tire and with softer tire

The response of the two systems is very similar over the entire range with a slight change in magnitude and lower natural frequency, both of which correspond to a decrease in effective stiffness of the tire. The test configuration of Figure 93 was restored and each tire was tested individually. FRFs for each tire are shown in Figure 110.

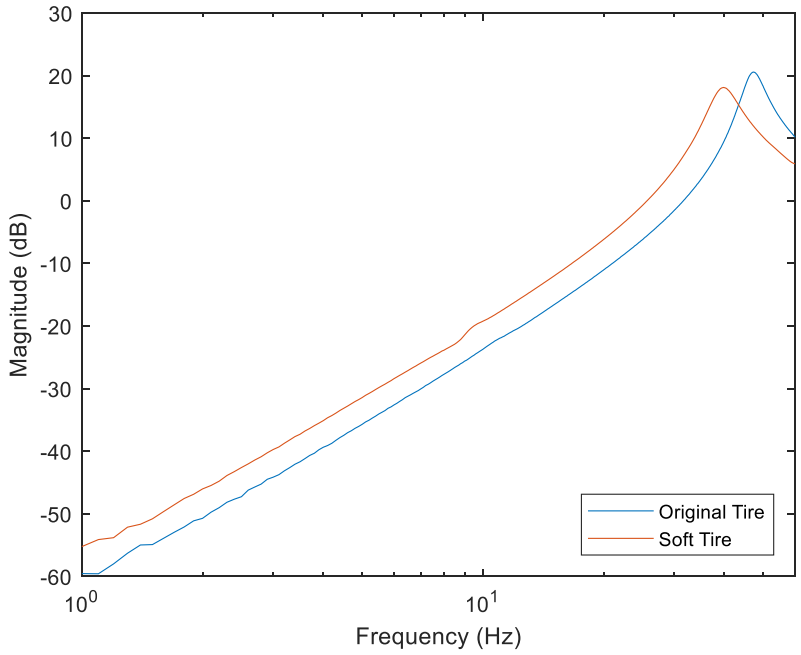

Figure 110: Comparison of FRFs for the original tire and the new, softer tire

A trend similar to that in Figure 109 is also present in Figure 110. As expected, the "soft" tire has a lower natural frequency than the original, 39.8 Hz compared to the original 47.3 Hz. Aside from confirming the assertion that the new tire is softer than the original, Figure 109 and Figure 110 show that the decoupling based on a change of tire will provide more clear results than for the change of suspension shown in the previous section. Specifically, the two suspension subsystems in the previous section (Figure 101) had very similar responses due to the most prominent dynamics arising from the control arms. In contrast, Figure 110 shows a clear change in the subsystem dynamics between the two tires. In turn, it will be easier to determine success for decoupling and subsequent recoupling for the change of tire.

Treating the tire as the known subsystem, the FRF for the original tire in Figure 110 was decoupled from the corresponding assembled system FRF in Figure 109. The resulting suspension subsystem FRF is shown in Figure 111.

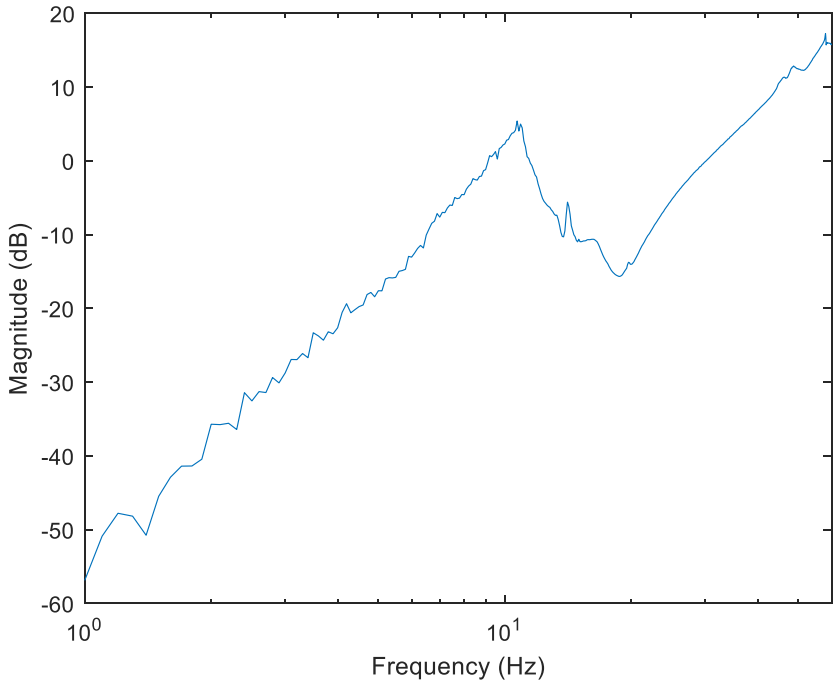

Figure 111: Suspension subsystem FRF obtained via decoupling

One item of note about Figure 111 is that the FRF is distinctly different than those which were obtained experimentally and displayed in the previous section. However, considering that the tire FRFs looked as expected in Figure 110, more confidence is placed in the results of Figure 111 than in the previous results.

The most important result, though, will be how well the recoupling matches with the experimental results for the assembled quarter car system with the soft tire (Figure 109). In that interest, the soft tire subsystem of Figure 110 was coupled with the suspension subsystem of Figure 111. A comparison of this recoupling to the experimental data for the assembled system with the soft tire is shown in Figure 112.

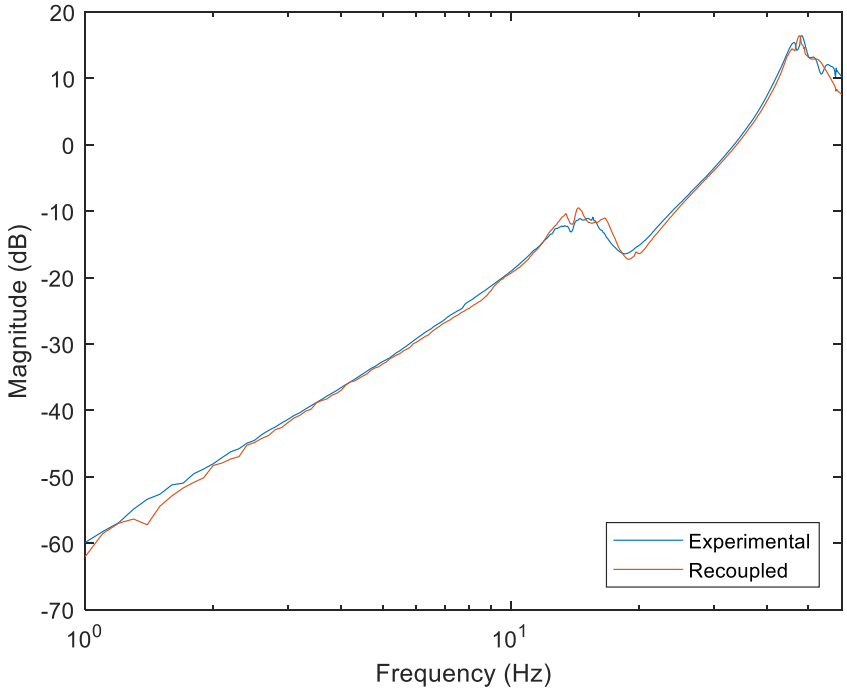

Figure 112: Comparison of FRFs for the assembled quarter car system obtained experimentally and through coupling

Figure 112 shows a strong correlation between the experimental and recoupled results for the quarter car system with the soft tire. There are some small discrepancies in the locations of the peaks which will be explored through the following figures.

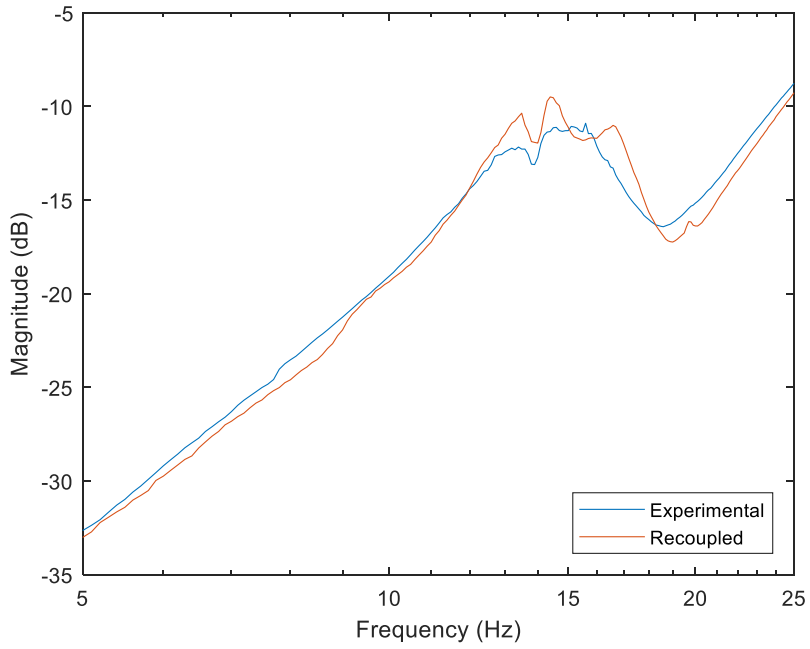

Figure 113: Zoomed view of Figure 112 between 5 Hz and 25 Hz

Though the magnitude is slightly off, the frequencies of the first two peaks in Figure 113 have been predicted closely at 13.5 Hz and 14.4 Hz. Additionally, the anti-resonance between the two peaks was predicted correctly at 14 Hz. However, the third peak is over-predicted by the coupling, at 16.7 Hz compared to 15.6 Hz (a 6.6% difference). Before an overall assessment of the coupling can be given, the neighborhood around 45 Hz must be inspected. Figure 114 shows this range.

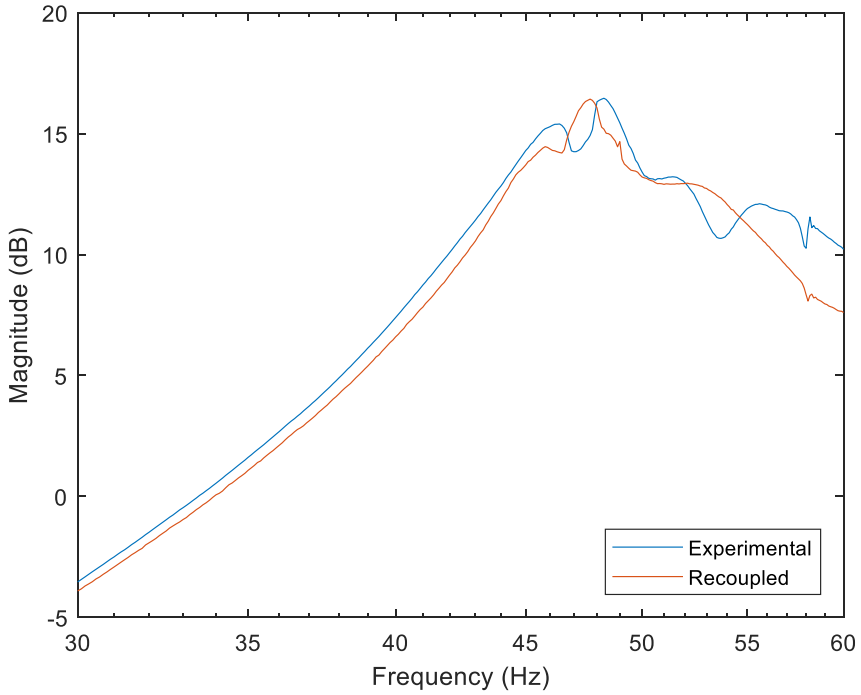

Figure 114: Zoomed view of Figure 112 between 30 Hz and 60 Hz

Again, there is some discrepancy between the experimental and coupled FRFs, but the major frequencies are predicted well overall. In particular, the frequency of the highest peak of the system, that corresponding to the stiffness of the tire, is predicted to within 1.3% of the measured value (47.7 Hz predicted, 48.3 Hz measured). Moreover, the magnitude of this highest peak is predicted exactly at 16.43 dB.

There is a somewhat higher discrepancy between the coupled and experimental FRFs from 55-60 Hz. As discussed in previous sections, the peaks in this region are caused by bending modes of the plastic control arms. Much more in depth testing or modelling of the suspension subsystem would be required to fully describe the behavior, and thus the accuracy of the coupling, in the 55-60 Hz frequency range. For the present work, the result of the coupling shown in Figure 114 provides a

good approximation for the first dominant peaks in the 40-60 Hz range while the discrepancies between 55 and 60 Hz occur around 5 dB less than the dominant peak of the system.

Overall, Figure 112 through Figure 114 demonstrate the success of the recoupling process. By using the suspension subsystem FRF of Figure 111, which was itself obtained through decoupling, and coupling that with the FRF for the soft tire, a close approximation of the corresponding experimental system was obtained. The maximum offset between the natural frequencies predicted by the coupling and those observed experimentally was 6.6%. This close agreement between the predicted and observed values provides confidence in application of the methods developed in this work.

Further, the successful application of these methods to the experimental quarter car system highlights the importance of the present work. First, the successful application shows that the novel experimental setup developed specifically for this research meets the particular testing requirements. Second, it demonstrates the power of the techniques presented in this work in regards to the ability to speed up the design and evaluation processes. Specifically, for the frequency resolution and range of Figure 112, the experimental FRF took more than half an hour to obtain via testing. In contrast, once the necessary subsystem FRFs were obtained, the "recoupled" FRF of Figure 112 was obtained in a matter of seconds.

By demonstrating a successful application of the coupling methods presented in this work to an experimental small-scale quarter car system, the preceding discussion shows the vast potential for improving and shortening the tire design process. The individual successes with the experimental data and simulated data opens the door for the possibility of combining the two. As was discussed in **Chapter 2**, part of what makes FBS such a powerful technique is the ability to couple data from

different sources together (i.e. simulated/modeled and experimental). This ability will allow for high fidelity tire models (for a full scale vehicle) to later be couple with experimental data. In that interest, the next steps of this research would be to expand upon the analytical models and scale up the experimental procedures for a full sized quarter car system. These and other developments will be discussed in **Chapter 6 – Conclusions and Future Work**.

Chapter 6 – Conclusions and Future Work

6.1 Conclusions

The primary goal of this research was to develop an appropriate method to apply Frequency Based Substructuring (FBS) techniques to a quarter car system in order to improve and shorten the tire design process. Application of FBS techniques to the quarter car system is non-trivial due to the significant nonlinearities of the tire and specific experimental design required to obtain the necessary data.

To achieve the stated objective, a thorough literature review of the most up to date advancements on both theoretical and experimental FBS techniques was conducted. Methods were then developed to apply these techniques to varying levels of quarter car models as well as to experimental data. Several levels of analytical quarter-car models were discussed in Chapter 3. Namely these models are: 1) a base level model using equations of motion (EOM); 2) a generalized model coupled at a single point; and 3) a generalized model coupled at three points.

Decoupling with each of these models brings its own contributions and benefits:

1. The decoupling of the model with the EOMs served both as a proof of the decoupling concept, a simple demonstration of advanced techniques, and a potential source of validation.
2. The generalized model coupled at a single point serves as the simplest model which could actually be applied to experimental results. It allows for decoupling the FRFs of the tire and suspension assuming a single connection at the center of the tire.

3. The generalized model coupled at three points is the most complete of the three current models. Instead of assuming coupling at a single point in the center of the bolt pattern, this model assumes coupling at three points along the circumference of the circle circumscribing the bolt positions. This use of three coupling points allows for a more complex model without using five points (the number of bolts), but still accounts for potential coupling applications in future work. Using translations at the three points, along with dimensional spacing information, rotations and moments present in coupling can be accounted for in addition to the translations and forces.

Due to experimental limitations, the only model which could be fully validated was the generalized model coupled at a single point. In order to validate that generalized model, more complex analytical models, with damping included, were developed and numerically populated. Then, simulations were conducted with a nonlinear rigid ring tire model and the decoupling process was applied assuming the generalized coupling model at a single point. These results highlighted the development of a testing procedure which will allow the process to work, despite significant nonlinearities in the tire.

The intention was to validate the process developed with the rigid ring tire model on the full-scale quarter car test rig in the Center for Tire Research (CenTiRe). After much experimental planning and design work on the rig, that test plan had to be suspended due to issues with the hydraulic actuation system. Instead, a novel small-scale quarter car test rig was developed in order to validate the processes on experimental data. This small-scale test rig had some differences from the full-scale system, but was specifically designed to meet the unique testing requirements for this research. Through this testing, it was discovered that the process which was developed for the full-scale quarter system was not the most effective process for the small-scale system. Instead, a new

process was developed for the small-scale system in which the tire was treated as the known subsystem and tested independently. This process proved to be effective, both for decoupling the tire from the assembled quarter car system and for recoupling a new tire to obtain an FRF for a different assembled system. The recoupled system was compared to experimental data for the same system and was shown to accurately predict the quarter car dynamics.

The success with the small-scale system provides a baseline approach for applying the same process to a full-scale quarter car system. Though there are significant differences between the dynamics of the two systems, the testing on the small-scale system provides insight into the work which must be done when switching to full-scale. As mentioned in previous chapters, the nonlinearity in the stiffness of a typical radial tire limits the possibility of testing the tire subsystem independently. Thus, one of the most important findings (in terms of scaling up) from the present work, is the necessity of a well-designed suspension support for testing the suspension subsystem. Furthermore, the testing approach used in this work is shown in **Chapter 4** in a generalized manner that is applicable to both full and small-scale quarter car systems.

Finally, by successfully applying the techniques developed in this research to the experimental quarter car system, the results of this work have the potential to improve the tire design process and shorten design times.

6.2 Future Work

There are several improvements and extensions of the present research which should be considered for any future work.

In regards to the small scale-setup, the sprung mass should be increased in order to reduce the effective damping ratio of the system and make the effect of the vertical vibration more prominent

in the system response. In order to accomplish this increase in sprung mass, the plastic components of the small scale system should be replaced with geometrically similar, metal components. The replacement of the plastic components will also eliminate the effect of the flexing of the control arms. Furthermore, detailed CAD or multi-body models should be developed and validated for the small-scale suspension system. These models will provide more insight into the behavior of the suspension subsystem and will also provide FRFs which could be used in place of experimental data in the decoupling process.

For the full-scale quarter car test rig, the hydraulic actuation system must first be repaired once resources are available. Once the hydraulic system is working, the design improvements detailed in the present work should be continued and subsequently implemented on the test rig. With full-scale rig functional, the simulations performed in this work for the rigid ring tire model should be validated experimentally against the corresponding test tire. Assuming successful validation has been completed, the simulations should be expanded to include additional degrees of freedom (of which the rigid ring model is capable) and those results used for coupling/decoupling. Again, these results should be validated against experimental data from the test rig. Finally, the entire process should be repeated for a rolling tire, both in simulation and experimentally, when possible.

As a further extension to the work on the full-scale quarter car system, the process detailed in this work could then be applied to a full car model. The use of the full car model, which could incorporate the aforementioned rigid ring model, will introduce pitch and roll modes which can then be included into the coupling/decoupling. Testing a full vehicle will be the biggest challenge of this work. Ideally, some variation of a 4-post shaker would be used to simultaneously excite the unsprung mass at all four wheels. It may be possible to excite at only a single wheel and conduct the analysis again on just a quarter car system, but this time with pitch and roll dynamics included.

The same general testing progression described for the quarter car systems could be applied to the full car system as well. Specifically, a first step of this testing would be to excite and measure response only in the vertical direction. By its very nature, the use of the full car for testing will introduce roll and pitch modes into the experimental data. Then, the testing can be expanded to include input force in x, y, and z-directions with responses measured in all three directions as well. Aside from introducing roll and pitch dynamics, the testing of the system as part of a full car will provide a more realistic view of how the suspension behaves when connected to the rest of the vehicle, as opposed to a test rig. This final testing should utilize the generalized coupling model developed in this work for nine DOFs across three coupling points. The nine DOF coupling model will include camber or other such changes in the decoupling and recoupling processes.

Finally, the most difficult aspect of testing will be to test the suspension subsystem separately. Many aspects of testing the suspension subsystem as part of the full vehicle model will be similar to those described in the previous paragraph for when tires are attached. However, testing of the suspension subsystem will additionally require some type of isolation table/platform at each wheel location. Overall, the equipment and setup required for testing the full vehicle model represents a significant time and monetary investment, which should be taken under serious consideration before this future work is undertaken.

References

[1] J. Y. Wong, *Theory of ground vehicles*. John Wiley & Sons, 2001.

[2] T. D. Gillespie, "Fundamentals of vehicle dynamics," SAE Technical Paper1992.

[3] D. E. Goldman, *A review of subjective responses to vibratory motion of the human body in the frequency range 1 to 70 cycles per second*. Naval Medical Research Institute, National Naval Medical Center, 1948.

[4] R. A. Lee and F. Pradko, "Analytical analysis of human vibration," SAE Technical Paper0148-7191, 1968.

[5] F. Pradko and R. A. Lee, "Vibration comfort criteria," SAE Technical Paper0148-7191, 1966.

[6] P. DONAT, A. Grosjean, P. Mistrot, and L. Roure, "The subjective equivalence of sinusoidal and random whole-body vibration in the sitting position (an experimental study using the 'floating reference vibration'method)," *Ergonomics,* vol. 26, no. 3, pp. 251-273, 1983.

[7] C. Corbridge and M. Grifftn, "Vibration and comfort: vertical and lateral motion in the range 0· 5 to 5· 0 Hz," *Ergonomics,* vol. 29, no. 2, pp. 249-272, 1986.

[8] T. Fairley and M. Griffin, "Predicting the discomfort caused by simultaneous vertical and fore-and-aft whole-body vibration," *Journal of Sound and Vibration,* vol. 124, no. 1, pp. 141-156, 1988.

[9] M. Demić, J. Lukić, and Ž. Milić, "Some aspects of the investigation of random vibration influence on ride comfort," *Journal of sound and vibration,* vol. 253, no. 1, pp. 109-128, 2002.

[10] W. F. Faris, Z. BenLahcene, and F. Hasbullah, "Ride quality of passenger cars: an overview on the research trends," *International Journal of Vehicle Noise and Vibration,* vol. 8, no. 3, pp. 185-199, 2012.

[11] ISO, *Mechanical Vibration and Shock: Evaluation of Human Exposure to Whole-body Vibration. Part 1, General Requirements: International Standard ISO 2631-1: 1997 (E)*. ISO, 1997.

[12] B. S. Institution, *British Standard Guide to Measurement and Evaluation of Human Exposure to Whole-body Mechanical Vibration and Repeated Shock*. British Standards Institution, 1987.

[13] G. Hohl, "Ride comfort of off-road vehicles," DTIC Document1984.

[14] P. Els, "The applicability of ride comfort standards to off-road vehicles," *Journal of Terramechanics,* vol. 42, no. 1, pp. 47-64, 2005.

[15] D. De Klerk, D. J. Rixen, and S. Voormeeren, "General framework for dynamic substructuring: history, review and classification of techniques," *AIAA journal,* vol. 46, no. 5, pp. 1169-1181, 2008.

[16] B. Jetmundsen, R. L. Bielawa, and W. G. Flannelly, "Generalized frequency domain substructure synthesis," *Journal of the American Helicopter Society,* vol. 33, no. 1, pp. 55-64, 1988.

[17] S. Voormeeren, "Coupling procedure improvement & uncertainty quantification in experimental dynamic substructuring," Master's thesis, TU Delft, 2007.

[18] D. De Klerk and D. Rixen, "Effektive hybride Analyse von gekoppelter mechanischer Subsysteme," 2004.

[19] C. Farhat and U. Hetmaniuk, "A fictitious domain decomposition method for the solution of partially axisymmetric acoustic scattering problems. Part I: Dirichlet boundary conditions," *International Journal for Numerical Methods in Engineering,* vol. 54, no. 9, pp. 1309-1332, 2002.

[20] D. Ewins, "Modal testing: theory, practice and application," *Research Studies Press LTD., Baldock, Hertfordshire, England,* vol. 171, pp. 415-437, 2000.

[21] A. P. V. Urgueira, "Dynamic analysis of coupled structures using experimental data," University of London, 1989.
[22] Z.-W. Wang and J. Wang, "Inverse substructure method of three-substructures coupled system and its application in product-transport-system," *Journal of Vibration and Control,* vol. 17, no. 6, pp. 943-951, 2010.
[23] D. de Klerk, D. J. Rixen, and J. de Jong, "The frequency based substructuring (FBS) method reformulated according to the dual domain decomposition method," in *24th international modal analysis conference*, 2006, vol. 36: Springer New York.
[24] Y. Ren and C. Beards, "On substructure synthesis with FRF data," *Journal of Sound and Vibration,* vol. 185, no. 5, pp. 845-866, 1995.
[25] Y. Ren, "The analysis and identification of friction joint parameters in the dynamic response of structures," 1992.
[26] Y. Ren and C. Beards, "A generalized receptance coupling technique," in *PROCEEDINGS-SPIE THE INTERNATIONAL SOCIETY FOR OPTICAL ENGINEERING*, 1993, pp. 868-868: SPIE INTERNATIONAL SOCIETY FOR OPTICAL.
[27] P. Ind and D. Ewins, "Impedance based decoupling and its application to indirect modal testing and component measurement: a numerical investigation," in *Proceedings of the Twenty First International Modal Analysis Conference, Kissimmee, FL*, 2003.
[28] W. D'Ambrogio and A. Fregolent, "Decoupling procedures in the general framework of frequency based substructuring," *Proceedings of 27th IMAC. Orlando (USA),* 2009.
[29] W. D'Ambrogio and A. Fregolent, "Direct decoupling of substructures using primal and dual formulation," in *Linking Models and Experiments, Volume 2*: Springer, 2011, pp. 47-76.
[30] P. Sjövall and T. Abrahamsson, "Substructure system identification from coupled system test data," *Mechanical Systems and Signal Processing,* vol. 22, no. 1, pp. 15-33, 2008.
[31] W. D'Ambrogio and A. Fregolent, "Promises and pitfalls of decoupling procedures," *Proceeding of 26th IMAC. Orlando (USA),* 2008.
[32] P. Ind, "The Non-Intrusive Modal Testing of Delicate and Critical Structures," *Imperial College of Science, Technology and Medicine,* PhD Thesis 2004.
[33] W. D'Ambrogio and A. Fregolent, "Prediction of substructure properties using decoupling procedures," in *Proceedings of EURODYN*, 2005.
[34] S. Voormeeren, D. De Klerk, and D. Rixen, "Uncertainty quantification in experimental frequency based substructuring," *Mechanical Systems and Signal Processing,* vol. 24, no. 1, pp. 106-118, 2010.
[35] W. D'Ambrogio and A. Fregolent, "Are Rotational DoFs Essential in Substructure Decoupling?," in *Dynamics of Coupled Structures, Volume 1*: Springer, 2014, pp. 27-36.
[36] J. Leuridan, D. De Vis, H. Grangier, and R. Aquilina, "Coupling of Structures Using Measured FRF's: Some Improved Techniques," in *13th Int. Seminar on Modal Analysis, Part I, Invited papers, paper*, 1988, no. 1-19.
[37] C. L. Lawson, "Hanson RJ Solving Least Squares Problems," ed: Prentice-Hall, 1974.
[38] D. Otte, J. Leuridan, H. Grangier, and R. Aquilana, "The use of SVD-based data reduction techniques for coupling of structures using measured FRF data," in *Proceedings of the 15th International Seminar on Modal Analysis (ISMA), Leuven, Belgium*, 1990, pp. 99-113.
[39] M. Imregun, D. Robb, and D. Ewins, "Structural modification and coupling dynamic analysis using measured FRF data," in *5th International Modal Analysis Conference (IMAC V)*, 1987.
[40] T. G. Carne and C. R. Dohrmann, "Improving experimental frequency response function matrices for admittance modeling," in *Proceedings of the Nineteenth International Modal Analysis Conference*, 2006.

[41] H. Kanda, M. Wei, R. Allemang, and D. Brown, "Structural dynamic modification using mass additive technique," in *4th International Modal Analysis Conference (IMAC IV)*, 1986.

[42] M. S. Allen, R. L. Mayes, and E. J. Bergman, "Experimental modal substructuring to couple and uncouple substructures with flexible fixtures and multi-point connections," *Journal of Sound and Vibration,* vol. 329, no. 23, pp. 4891-4906, 2010.

[43] M. S. Allen and R. L. Mayes, "Comparison of FRF and modal methods for combining experimental and analytical substructures," in *25th International Modal Analysis Conference (IMAC XXV)*, 2007.

[44] M. S. Allen, D. C. Kammer, and R. L. Mayes, "Uncertainty in experimental/analytical substructuring predictions: a review with illustrative examples," in *ISMA2010–international conference on noise and vibration engineering, Leuven*, 2010.

[45] D. C. Kammer, "Sensor placement for on-orbit modal identification and correlation of large space structures," *Journal of Guidance, Control, and Dynamics,* vol. 14, no. 2, pp. 251-259, 1991.

[46] M. S. Allen, D. C. Kammer, and R. L. Mayes, "Metrics for diagnosing negative mass and stiffness when uncoupling experimental and analytical substructures," *Journal of Sound and Vibration,* vol. 331, no. 25, pp. 5435-5448, 2012.

[47] D. Nicgorski and P. Avitabile, "Conditioning of FRF measurements for use with frequency based substructuring," *Mechanical Systems and Signal Processing,* vol. 24, no. 2, pp. 340-351, 2010.

[48] J. O'Callahan, P. Avitabile, and R. Riemer, "System equivalent reduction expansion process (SEREP)," in *Proceedings of the 7th international modal analysis conference*, 1989, vol. 1, pp. 29-37: Union College Schnectady, NY.

[49] D. Nicgorski and P. Avitabile, "Experimental issues related to frequency response function measurements for frequency-based substructuring," *Mechanical Systems and Signal Processing,* vol. 24, no. 5, pp. 1324-1337, 2010.

[50] S. Voormeeren and D. Rixen, "Substructure decoupling techniques—a review and uncertainty propagation analysis," in *27th International Modal Analysis Conference, Orlando, FL*, 2009.

[51] D. C. Kammer and D. Krattiger, "Propagation of uncertainty in substructured spacecraft using frequency response," *AIAA journal,* vol. 51, no. 2, pp. 353-361, 2013.

[52] T. K. Hasselman, J. D. Chrostowski, and T. J. Ross, "Propagation of modeling uncertainty through structural dynamic models," in *35th Structures, Structural Dynamics, and Materials Conference*, 1994, pp. 72-83.

[53] E. Balmes and L. Billet, "Using expansion and interface reduction to enhance structural modification methods," in *IMAC-XIX: A Conference on Structural Dynamics*, 2001, vol. 1, pp. 615-621.

[54] E. D'Amato, F. Durante, and W. D'Ambrogio, "Distributed structural modification using local interface model," in *ISMA 2002-International Conference on Noise and Vibration Enguineering*, 2002, pp. 1731-1739.

[55] W. D'Ambrogio and A. Sestieri, "A unified approach to substructuring and structural modification problems," *Shock and Vibration,* vol. 11, no. 3-4, pp. 295-309, 2004.

[56] D. de Klerk, D. Rixen, S. Voormeeren, and F. Pasteuning, "Solving the RDoF problem in experimental dynamic substructuring," in *26th International Modal Analysis Conference (IMAC XXVI), Orlando, FL*, 2008.

[57] F. Pasteuning, "Experimental Dynamic Substructuring and its Application to Automotive Research," *Master's Thesis, TU Delft, Department of Engineering Mechanics,* 2007.

[58] D. De Klerk, *Dynamic response characterization of complex systems through operational identification and dynamic substructuring-An application to gear noise propagation in the automotive industry*. TU Delft, Delft University of Technology, 2009.

[59] R. L. Mayes, "Tutorial on experimental dynamic substructuring using the transmission simulator method," in *Topics in Experimental Dynamics Substructuring and Wind Turbine Dynamics, Volume 2*: Springer, 2012, pp. 1-9.
[60] R. L. Mayes and M. Arviso, "Design studies for the transmission simulator method of experimental dynamic substructuring," in *International Seminar on Modal Analysis (ISMA2010)*, 2010.
[61] R. L. Mayes, M. S. Allen, and D. C. Kammer, "Correcting indefinite mass matrices due to substructure uncoupling," *Journal of Sound and Vibration,* vol. 332, no. 22, pp. 5856-5866, 2013.
[62] D. J. Rixen and P. L. van der Valk, "An impulse based substructuring approach for impact analysis and load case simulations," *Journal of Sound and Vibration,* vol. 332, no. 26, pp. 7174-7190, 2013.
[63] M. Česnik, J. Slavič, P. Čermelj, and M. Boltežar, "Frequency-based structural modification for the case of base excitation," *Journal of Sound and Vibration,* vol. 332, no. 20, pp. 5029-5039, 2013.
[64] J. R. Crowley, A. L. Klosterman, G. T. Rocklin, and H. Vold, "Direct structural modification using frequency response functions," in *Proceedings of the second international modal analysis conference*, 1984, pp. 58-65.
[65] T. Kranjc, J. Slavič, and M. Boltežar, "An interface force measurements-based substructure identification and an analysis of the uncertainty propagation," *Mechanical Systems and Signal Processing,* vol. 56, pp. 2-14, 2015.
[66] T. Horiuchi, M. Inoue, T. Konno, and Y. Namita, "Real-time hybrid experimental system with actuator delay compensation and its application to a piping system with energy absorber," *Earthquake Engineering & Structural Dynamics,* vol. 28, no. 10, pp. 1121-1141, 1999.
[67] M. Nakashima and N. Masaoka, "Real-time on-line test for MDOF systems," *Earthquake engineering & structural dynamics,* vol. 28, no. 4, pp. 393-420, 1999.
[68] S. J. Kim, R. E. Christenson, S. F. Wojtkiewicz, and E. A. Johnson, "Real-time hybrid simulation using the convolution integral method," *Smart Materials and Structures,* vol. 20, no. 2, p. 025024, 2011.
[69] Z. Jiang, S. J. Kim, S. Plude, and R. Christenson, "Real-time hybrid simulation of a complex bridge model with MR dampers using the convolution integral method," *Smart Materials and Structures,* vol. 22, no. 10, p. 105008, 2013.
[70] R. Botelho and R. E. Christenson, "Real-time hybrid substructuring of a physical mass-spring system coupled to a fluid-loaded analytical substructure," *The Journal of the Acoustical Society of America,* vol. 135, no. 4, pp. 2351-2351, 2014.
[71] R. M. Botelho and R. E. Christenson, "Mathematical Equivalence Between Dynamic Substructuring and Feedback Control Theory," in *Dynamics of Coupled Structures, Volume 4*: Springer, 2015, pp. 31-40.
[72] P. van der Valk, J. van Wuijckhuijse, and D. de Klerk, "A benchmark test structure for experimental dynamic substructuring," in *Structural Dynamics, Volume 3*: Springer, 2010, pp. 1113-1122.
[73] A. Culla, W. D'Ambrogio, A. Fregolent, and A. Schiavone, "Problems in using experimental data for dynamic substructuring of a lumped parameter system," 2010 2010.
[74] A. Culla, W. D'Ambrogio, A. Fregolent, and A. Schiavone, "Smoothing experimental data in dynamic substructuring of built up systems," in *Linking Models and Experiments, Volume 2*: Springer, 2011, pp. 89-109.
[75] E.-T. Lee *et al.*, "647. FRF based substructuring and decoupling of substructures," *Journal of Vibroengineering,* vol. 13, no. 3, 2011.
[76] K. Larsson, S. Barrelet, and W. Kropp, "The modelling of the dynamic behaviour of tyre tread blocks," *Applied Acoustics,* vol. 63, no. 6, pp. 659-677, 2002.
[77] K. Cuppens, P. Sas, and L. Hermans, "Evaluation of the FRF based substructuring and modal synthesis technique applied to vehicle FE data," in *PROCEEDINGS OF THE INTERNATIONAL SEMINAR ON MODAL ANALYSIS*, 2001, vol. 3, pp. 1143-1150: KU Leuven; 1998.

[78] S. D. Ochcsner and R. J. Bernhard, "Application of a component mobility modeling technique to automotive suspension systems," *Noise Control Engineering Journal,* vol. 43, no. 3, pp. 73-82, 1995.
[79] T. Lim and J. Li, "A theoretical and computational study of the FRF-based substructuring technique applying enhanced least square and TSVD approaches," *Journal of Sound and Vibration,* vol. 231, no. 4, pp. 1135-1157, 2000.
[80] A. Berman and W. G. Flannelly, "Theory of incomplete models of dynamic structures," *AIAA journal,* vol. 9, no. 8, pp. 1481-1487, 1971.
[81] M. Corus, E. Balmes, and O. Nicolas, "Using model reduction and data expansion techniques to improve SDM," *Mechanical Systems and Signal Processing,* vol. 20, no. 5, pp. 1067-1089, 2006.
[82] W. D'Ambrogio and A. Sestieri, "Analysis of coupled structures using combined expe rimental and theoretical models," *Universita de L'Aquila-Dipartimento di Energetica,* 1992.
[83] J. Gordis, R. Bielawa, and W. Flannelly, "A general theory for frequency domain structural synthesis," *Journal of Sound and Vibration,* vol. 150, no. 1, pp. 139-158, 1991.
[84] B. Jetmundsen, "On frequency domain methodologies for prescribed structural modification and subsystem synthesis," Ph. D. thesis, Rensselaer Polytechnic Institute, New York, 1986.
[85] A. L. Klosterman, *On the experimental determination and use of modal representations of dynamic characteristics*. University of Cincinnati., 1971.
[86] E. Pagnacco, C. Gautrelet, J. Paumelle, and S. Lambert, "Frequency Based Substructuring without R-Dof Measurements: A Two-Beam Test Case," in *20th International Congress of Mecahnical Engineering*, 2009.
[87] P. Peeters, T. Tamarozzi, F. Vanhollebeke, and W. Desmet, "A robust approach for substructure decoupling," in *Proceedings of the International Conference on Noise and Vibration Engineering ISMA 2014*, 2014, pp. 3907-3921.
[88] S. Perrier, Y. Champoux, and J.-M. Drouet, "Using substructuring to predict the human hand influence on a mechanical structure," in *Topics in Experimental Dynamics Substructuring and Wind Turbine Dynamics, Volume 2*: Springer, 2012, pp. 33-44.
[89] A. Puchalski, "A technique for the vibration signal analysis in vehicle diagnostics," *Mechanical Systems and Signal Processing,* vol. 56, pp. 173-180, 2015.
[90] B. Smith, P. Bjorstad, and W. Gropp, *Domain decomposition: parallel multilevel methods for elliptic partial differential equations*. Cambridge university press, 2004.
[91] J.-S. Tsai and Y.-F. Chou, "The identification of dynamic characteristics of a single bolt joint," *Journal of Sound and Vibration,* vol. 125, no. 3, pp. 487-502, 1988.
[92] M. V. van der Seijs, D. de Klerk, D. J. Rixen, and S. Rahimi, "Validation of current state frequency based substructuring technology for the characterisation of steering gear–vehicle interaction," in *Topics in Experimental Dynamic Substructuring, Volume 2*: Springer, 2014, pp. 253-266.
[93] S. Voormeeren and D. Rixen, "A dual approach to substructure decoupling techniques," in *Structural Dynamics, Volume 3*: Springer, 2011, pp. 601-616.
[94] S. Voormeeren and D. Rixen, "A family of substructure decoupling techniques based on a dual assembly approach," *Mechanical Systems and Signal Processing,* vol. 27, pp. 379-396, 2012.
[95] S. N. Voormeeren, *Dynamic substructuring methodologies for integrated dynamic analysis of wind turbines*. TU Delft, Delft University of Technology, 2012.
[96] S. Weng, Y. Xia, X.-Q. Zhou, Y.-L. Xu, and H.-P. Zhu, "Inverse substructure method for model updating of structures," *Journal of Sound and Vibration,* vol. 331, no. 25, pp. 5449-5468, 2012.
[97] D. J. Inman and R. C. Singh, *Engineering vibration*. Prentice Hall Upper Saddle River, 2001.
[98] O. Døssing, *Structural testing*. Brüel & Kjær, 1988.

[99] P. Castellini, N. Paone, and E. P. Tomasini, "The laser doppler vibrometer as an instrument for nonintrusive diagnostic of works of art: application to fresco paintings," *Optics and Lasers in Engineering,* vol. 25, no. 4, pp. 227-246, 1996.
[100] P. Zhang, X. Tang, B. Shan, J. Brandon, and A. Kwan, "Analytical and experimental modal analysis for operational validation and calibration of a miniature silicon sensor," *Journal of sound and vibration,* vol. 214, no. 5, pp. 903-913, 1998.
[101] P. Castellini, G. Revel, and L. Scalise, "Measurement of vibrational modal parameters using laser pulse excitation techniques," *Measurement,* vol. 35, no. 2, pp. 163-179, 2004.
[102] S. Vanlanduit, F. Daerden, and P. Guillaume, "Experimental modal testing using pressurized air excitation," *Journal of sound and vibration,* vol. 299, no. 1, pp. 83-98, 2007.
[103] D. Guan, L. Yam, M. Mignolet, and Y. Li, "Study of experimental modal analysis on tires," in *SEM*, 1999.
[104] D. Guan, L. Yam, M. Mignolet, and Y. Liy, "Techniques: experimental modal analysis of tires," *Experimental Techniques,* vol. 24, no. 6, pp. 39-45, 2000.
[105] R. Pieters, "Experimental modal analysis of an automobile tire under static load," *Bachelor Project, Eindhoven University of Technology,* 2007.
[106] J. Qiao, Y. Du, and P. Zhao, "Three-Dimensional Modal Parameters of Tire," in *Topics in Modal Analysis I, Volume 7*: Springer, 2014, pp. 225-230.
[107] L. Yam, D. Guan, and A. Zhang, "Three-dimensional mode shapes of a tire using experimental modal analysis," *Experimental mechanics,* vol. 40, no. 4, pp. 369-375, 2000.
[108] J. Vervoort, "Experimental modal analysis of an automobile tire," *Bachelor final project report No, DCT,* 2007.
[109] P. Sakthivel, K. N. Rao, and R. K. Kumar, "Operational Modal Analysis of tyre road interaction using Abaqus Explicit and Operational Modal Analysis," in *Proceedings of the ISMA 2012 International Conference on Noise and Vibration Engineering, Leuven, Belgium*, 2012.
[110] C. Patil, "Antilock Brake System Re-design and Control Prototyping using a One-Fifth Scaled Vehicle Setup," MS Thesis, The University of Texas at Austin, Aug, 2003.
[111] R. G. Longoria, A. Al-Sharif, and C. B. Patil, "Scaled vehicle system dynamics and control: a case study in anti-lock braking," *International journal of vehicle autonomous systems,* vol. 2, no. 1-2, pp. 18-39, 2004.
[112] A. A. Al-Sharif, "Design and Development of a Scaled Test Laboratory for the Study of ABS and other Active Vehicle Systems," University of Texas at Austin, 2002.
[113] P. Kachroo and K. Ozbay, "Microprocessor-controlled small-scale vehicles for experiments in automated highway systems," *The Korean Transport Policy Review,* vol. 4, no. 3, pp. 145-178, 1997.
[114] W. Witaya, W. Parinya, and C. Krissada, "Scaled vehicle for Interactive dynamic Simulation (SIS)," in *Robotics and Biomimetics, 2008. ROBIO 2008. IEEE International Conference on*, 2009, pp. 554-559: IEEE.
[115] S. Brennan and A. Alleyne, "Robust scalable vehicle control via non-dimensional vehicle dynamics," *Vehicle System Dynamics,* vol. 36, no. 4-5, pp. 255-277, 2001.
[116] C. van Maren and J. Sika, "Scaled Vehicle Dynamics of DAVINCI Project," *Delft University of Technology,* 2001.
[117] P. Hoblet, R. O'Brien, and J. A. Piepmeier, "Scale-model vehicle analysis for the design of a steering controller," in *System Theory, 2003. Proceedings of the 35th Southeastern Symposium on*, 2003, pp. 201-205: IEEE.
[118] A. T. Glumac, "Scale tire modeling and experimentation on a rolling roadway simulator," Pennsylvania State University, 2006.

[119] Y. Siramdasu, "Discrete Tire Model Application for Vehicle Dynamics Performance Enhancement," Virginia Tech, 2015.
[120] P. W. A. Zegelaar, *The dynamic response of tyres to brake torque variations and road unevenesses*. TU Delft, Delft University of Technology, 1998.
[121] R. Taylor, L. Bashford, and M. Schrock, "Methods for measuring vertical tire stiffness," *Transactions of the ASAE,* vol. 43, no. 6, p. 1415, 2000.
[122] E. Vinesse, "Tyre vibration testing from modal analysis to dispersion relations," in *Proceedings of ISATA*, 1988, vol. 88.
[123] C. Yue, T. Butsuen, and J. Hedrick, "Alternative control laws for automotive active suspensions," *Journal of Dynamic Systems, Measurement, and Control,* vol. 111, no. 2, pp. 286-291, 1989.
[124] J. K. Hedrick and T. Butsuen, "Invariant properties of automotive suspensions," *Proceedings of the Institution of Mechanical Engineers, Part D: Journal of Automobile Engineering,* vol. 204, no. 1, pp. 21-27, 1990.
[125] H. E. Tseng and D. Hrovat, "State of the art survey: active and semi-active suspension control," *Vehicle system dynamics,* vol. 53, no. 7, pp. 1034-1062, 2015.
[126] H. Akçay and S. Türkay, "Influence of tire damping on mixed H2/H∞ synthesis of half-car active suspensions," *Journal of Sound and Vibration,* vol. 322, no. 1, pp. 15-28, 2009.
[127] J. Levitt and N. Zorka, "The influence of tire damping in quarter car active suspension models," *Journal of dynamic systems, measurement, and control,* vol. 113, no. 1, pp. 134-137, 1991.
[128] S. Türkay and H. Akçay, "A study of random vibration characteristics of the quarter-car model," *Journal of sound and vibration,* vol. 282, no. 1, pp. 111-124, 2005.
[129] S. Taheri, C. Sandu, and S. Taheri, "Finite Element Modeling of Tire Transient Characteristics in Dynamic Maneuvers," *SAE International Journal of Passenger Cars-Mechanical Systems,* vol. 7, no. 2014-01-0858, pp. 221-230, 2014.
[130] Y. Siramdasu and S. Taheri, "Discrete tyre model application for evaluation of vehicle limit handling performance," *Vehicle System Dynamics,* vol. 54, no. 11, pp. 1554-1573, 2016.
[131] A. J. C. Schmeitz, "A semi-empirical three-dimensional model of the pneumatic tyre rolling over arbitrarily uneven road surfaces," 2004.
[132] W. F. Milliken and D. L. Milliken, *Race car vehicle dynamics*. Society of Automotive Engineers Warrendale, 1995.